Coupled electrokinetic fluxes in a single nanochannel for energy conversion

Preeti Sharma

Communauté
UNIVERSITÉ Grenoble Alpes

THÈSE

Pour obtenir le grade de

DOCTEUR DE LA COMMUNAUTE UNIVERSITE GRENOBLE ALPES

Spécialité : NANOPHYSIQUE

Arrêté ministériel : 25 mai 2016

Présentée par

Preeti SHARMA

Thèse dirigée par **Elisabeth CHARLAIX,** et
codirigée par **Frank FOURNEL et Cyril PICARD**

préparée au sein du **Laboratoire Interdisciplinaire de Physique**
dans **l'École Doctorale Physique**

Coupled electrokinetic fluxes in a single nanochannel for energy conversion

Thèse soutenue publiquement le **14 Avril 2017,**
devant le jury composé de :

Monsieur Eric DROCKENMULLER
PROFESSEUR, Université Claude Bernard, Président
Monsieur Jean Luc REBOUD
PROFESSEUR, Université Grenoble Alpes, Examinateur
Madame, Marie-Caroline JULLIEN
CHARGE DE RECHERCHE, GulliverUMR 7083–MMN ESPCI Paris, Rapporteur
Madame, Anne-Laure BIANCE
CHARGE DE RECHERCHE, ILM Université Claude Bernard Lyon1, Rapporteur
Madame, Marie-Charlotte AUDRY-DESCHAMPS
MAITRE DE CONFERENCES, Institut des nanotechnologies de Lyon, Invité

Contents

Abstract

Coupled electrokinetic phenomena within nanochannel are of interest for energy harvesting and production of electricity based on the controlled mixing of river water with sea water known as "blue energy". The origin of the phenomena is related to interaction with charged walls and transport of ions within the so called Debye layer. This work aims at a better understanding of the physics and transport phenomena in presence of electrolyte confined in nanochannels.

A specific instrumentation has been developed during this thesis to study the mechanisms governing coupled nanofluidic fluxes. The goal is to characterize simultaneously the mass transport within a nanochannel and the electrical current driven through the nanochannel by the application of either a salinity difference, a pressure difference or a voltage difference across the channel.

The electrokinetic measurement cell has been qualified by performing electrical measurements under applied thermodynamic forces, taking the benefit of commercially available nanoporous Nafion membrane. Later on, the cell is qualified by performing electrical measurements in a sample having single solid state nanochannel. We have presented an easy way to prepare the freestanding silica membranes suspended on silicon wafer, afterwards pierced by focused ion beam for the realization of single nanopore. The electrical as well as mechanical characteristics of these suspended membranes are presented.

Finally, a method for the development of a pico-flow cell to perform direct and in-situ measurements of flow rate within a single nanochannel is presented. This measurement approach combined with the electrical current measurement, could be used, in presence of pressure, voltage or salinity gradient. This approach allow us to measure the flow rate and the electrical current across a single nanochannel simultaneously and independently.

Acknowledgements

First and foremost, I would like to express my deepest gratitude to my supervisors Professor Elisabeth CHARLAIX and Co-supervisors Dr. Frank FOURNEL and Dr. Cyril PICARD for their continuous support during my thesis. Their valuable time, constructive advice, and willingness to share their knowledge have been stimulating in all the time of my research and writing of the thesis. The enthusiasm they had for research was always motivational, even at tough times during my Ph.D. I thank them for welcoming me in the lab as an intern, and providing me a chance to learn and contribute towards the development of the project. Without their precious support, it would not have been possible to conduct this research project.

I would like to thank my thesis committee members starting from Dr. Marie-Caroline JULLIEN and Dr. Anne-Laure BIANCE for evaluating my thesis and providing their insightful comments. I would like to thank the other jury members Professor Jean-Luc REBOUD and Professor Eric DROCKENMULLER for accepting to judge my Ph.D. Thesis.

I would like to thank all the faculties at my masters level in India, as well as France for providing me rich scientific background. A word of special thanks goes to Professor S. ANNAPOORNI, University of Delhi, and Professor Philippe PEYLA, Université Joseph-Fourier for exposing me with the scientific knowledge and research opportunities in France. I would specially like to thank Dr. Cyril PICARD and Dr. Benjamin CROSS for helping me in learning the skills to develop the experimental tools. I will always be indebted to your valuable inputs. I would like to thank Jean-Francois MOTTE and Gwenaelle JULIE for helping me in carrying out the nanofabrication at Institute Neel, Grenoble and for their valuable discussions. Thank you to Jérome GIRAUD in helping to design and develop the flow cell.

I thank the Communauté de Research Academique (ARC) for their financial support during this work. I would like to thank the administrative department for their assistance throughout my stay at LIPhy. My time in Grenoble and LIPhy was made enjoyable in large part due to the many colleagues and friends I had. I am grateful to my friends for all the fun we had, for backing me up whenever I felt low, and for their love and support towards the fulfillment of my thesis. Thank you very much for your support and friendship.

Lastly, I would like to thank my family for all their love and encouragement. I thank my parents who raised me with the ability to pursue what I wanted and

their constant support in my life. Thanks to my brother M. Amit SHARMA and my sister Miss Archana SHARMA for their motivational support during all ups and downs in my PhD duration. Thanks for always believing in me. Thank you!

Introduction

The transport of molecules through nanopores is common place in biology [1]. The biological cell is filled with all types of nanopores that control the trafficking of ions and water molecules. For instance, transmembrane acquaporins are able to transport selectively water in a particularly efficient manner [2]. Although, these complex mechanism remains partly understood, they demonstrate the possibility to play with electro-osmotic phenomena with a high energetical efficiency. In the context of process engineering, these electro-osmotic phenomena revealed to be of particular interest to harvest energy related to the mixing of sea water and river water [3, 4]. However, up to now, all the attempts to extract this "blue energy" failed because of their low power density and their low efficiency with respect to the thermodynamical limits.

In 1974, Loeb showed theoretically that the energy based on the osmotic pressure between sea water and fresh water could be recovered as a mechanical work through pressure retarded osmosis (PRO)[3]. In this process, water transports across a semipermeable membrane from fresh water compartment to salt water compartment, creating a hydrostatic pressure difference that is converted into electrical energy. One year later, Weinstein explained how to convert directly this osmotic energy in electric energy using reverse-electrodialysis (RED)[5]. RED consists of a stack of alternating cation and anion exchange membranes, allowing a selective transport of ions across the membrane. The compartments between the membranes are alternately filled with sea water and freshwater. The salinity gradient is the driving force in transporting counter-ions across the membranes that results in electric potential generated across each membrane [6, 7, 8, 9, 10]. These processes are currently of interest as they would allow to harvest the "blue energy" of river water mixing with sea water to produce renewable electrical power: using 10 % of available river water flow rate could produce up to 150 GW, or the electrical consumption of half a billion people.

RED is originated from the physical phenomena involved within a double layer of ions at the vicinity of charged walls of nanopores or nanochannels [11]. At the nanoscale, the physics of liquid flow, the flux of ions and the electrostatics arising from the electric charge at the solid-liquid interface are coupled. Application of a thermodynamic force such as voltage difference, pressure difference or concentration difference across the nanochannel results in well known phenomena such as electro-

osmosis, streaming currents and diffusio-omosis [12, 13]. The forces and the fluxes are coupled to each other [14]. Taking benefit from this coupling, the conversion of energy from one form to another (mechanical, electric, chemical) is possible when a thermodynamic gradient (pressure gradient, electric potential gradient or chemical potential gradient) is applied across a nanochannel [3, 4, 12, 15, 16].

Recently, it has been shown by Siria *et al.* [13] that the electrical current density generated from diffusio-osmosis through a single boron nitride nanotube is three orders of magnitude larger than the one obtained with nanoporous membranes used in RED process [17, 18, 19]. This experiment is promising for large power density, nevertheless, remains the question of energy efficiency. This calls for, the development of the experimental tools to precisely characterize various forces and fluxes employed in the transport within a nanodevice.

To study the fundamental properties of nanofluidic transport and its related coupling, tailored solid-state nanochannels or nanopores have been used [15, 16]. Membranes actually are not the best choice for this due to non-reliable geometric parameters of nanopores or nanochannels present in membranes. It is difficult to control the shape and size of the pores/channels in membranes. This problem can be overcome by the fabrication of single solid-state nanometric pore/channel. The geometry of such structures is usually known and well defined which makes it convenient to model the transport properties.

Another interesting phenomena observed in nanofluidic devices is the rectification of fluxes which can be correlated to the current rectification in semiconductor diodes. Current rectification properties in solid state nanochannels or nanopores, either of conical shape or having assymetrically charged walls, have been previously illustrated by various groups [20, 21, 22, 23, 24, 25]. In contrast to the classical semiconductor diode, the nanofluidic diode does not only allow current rectification, but also flow rectification that could stem numerous applications. One such application is the directional valve. Another application involves the purification of water based on osmotic diodes where water flows against the salinity gradient [26]. However, a better understanding of these complex electrokinetic phenomena calls for experimental investigation as well as development of nanofludic devices. This forms the basis for our experimental goals to achieve during the thesis.

Measurements of the coupled fluxes at the level of a single nanochannel is, however, challenging and scarcely reported in the past. Owing to this, the present thesis focuses at developing a versatile nanofluidic device to probe coupled transport in a single nanochannel. The objective of this device is to characterize simultaneously and independently: the liquid flow rate, the electrical current and the voltage difference, by the application of either one of the thermodynamic force, pressure difference, concentration difference and voltage difference across the nanochannel.

Part I of the thesis introduces the basics concepts related to coupled transport phenomena in nanofluidic devices.

Part II of the thesis presents a basic home-made flow cell and discusses the

optimization of the experimental conditions in order to control and measure the fluxes and forces. Then, the capability of the cell and whole set-up to carry out nanofluidic electrical measurements under applied pressure or salinity gradient are presented using a commercially available nanoporous Nafion membrane.

Part III of the thesis focuses on preparation of a solid state nanochannel/nanopore sample. This sample is in the form of a single macroscopic piece which can be manipulated and adapted to the electrokinetic cell under application (cell prepared in part II or pico-flow cell in part IV of the thesis). The method presented here is globally based on two steps; first, the preparation of micro-metric freestanding silica membrane suspended on silicon and second piercing the membrane with focused ion beam milling. The membrane preparation step is based on an easy and low cost wet chemical etching process. These suspended silica membranes are characterized by AC impedance measurements in order to obtain their dielectric capacitance and further tested for their mechanical robustness. The presence of the nanopore in the membrane is also verified by the electrical conductance measurement of the nanopore.

Part IV of the thesis is devoted to the development of a method for the direct flow rate measurement in a single nanochannel. At first, the principle of method of flow measurement is elaborated. Subsequently, the development of the device and challenges faced during the development are elaborated. Later on, the capabilities of the developed device (pico-flow cell) are presented. Afterwards, the very first results for the demonstration of the flow measurement method are presented.

Part I

State of the art

Chapter 1

Linear coupled transport in nanofluidics and energy conversion

Contents

The state of the art presented here is intended to introduce the theoretical concepts which have been used to interpret the experimental results obtained in this thesis. Chapter1 presents the basics of linear coupled transport phenomena in nanofluidic devices and their standard application to energy conversion. We use the results of this chapter in part II for guiding and interpreting the experimental results performed for testing our measurement cell with a Nafion membrane. Chapter2 is devoted to a short introduction to rectifying effects in nanofluidic transport in relation to part III and part IV of the thesis.

1.1 Surface induced coupled transport in electrolyte solutions

1.1.1 Surface charge and electrostatic double layer (EDL)

Solid surfaces charge naturally when they come in contact with an aqueous solution. The charging of surfaces is due to either ionization, dissociation of the surface groups or adsorption of ions from solution [27]. A charged region of liquid rich in ions of opposite charge (that we will call later-on "counter ions" in general) develops close to the solid-liquid interface due to electroneutrality [11]. The ensemble of the charged surface and of the nearby charged diffuse layer in the solution, is called the electrostatic double layer (EDL) because of its analogy with a plane capacitor. The potential difference between the charged surface and the bulk solution is given in the case of a weak or moderate surface charge Σ by:

$$V_o = \frac{l_d \Sigma}{\epsilon_0 \epsilon_r} \tag{1.1}$$

valid for $V_o \leqslant 25$ mV, with l_d the Debye length:

$$l_d = \sqrt{\frac{\epsilon_0 \epsilon_r kT}{2 n_0 e^2}} \tag{1.2}$$

with ϵ_0 the permittivity of free space, ϵ_r the relative permittivity of medium, k the Boltzmann constant, T the absolute temperature, n_o the ionic concentration in m^{-3} and e the elementary charge.

Another typical length scales we would like to introduce are the Bjerrum length and the Dukhin length. The Bjerrum length l_b is defined as the distance between two charged species becomes equal to the thermal energy kT.

$$l_b = \frac{z^2 e^2}{4\pi \epsilon_r \epsilon_0 kT}$$

with z the valency of ion. At ambient temperature l_b=0.7 nm. In the following we will always use electrolyte concentration for which the distance between nearest neighbor ions is larger than l_b.

The Dukhin length is important in nanochannels, nanopores and membranes. It is defined as:

$$l_{DU} = \Sigma/(e n_o) \tag{1.3}$$

which characterizes the channel height or pore size below which the average concentration of counter-ions is larger than the bulk electrolyte concentration. For a channel aperture smaller than l_{DU}, the conductance is dominated by the counter-ions.

The EDL is at the origin of various electrokinetic phenomena. Here, in the following section we are going to discuss more particularly electro-osmosis and its symmetric phenomena called streaming currents. In section 1.1.3, a phenomena called diffusio-osmosis, is discussed.

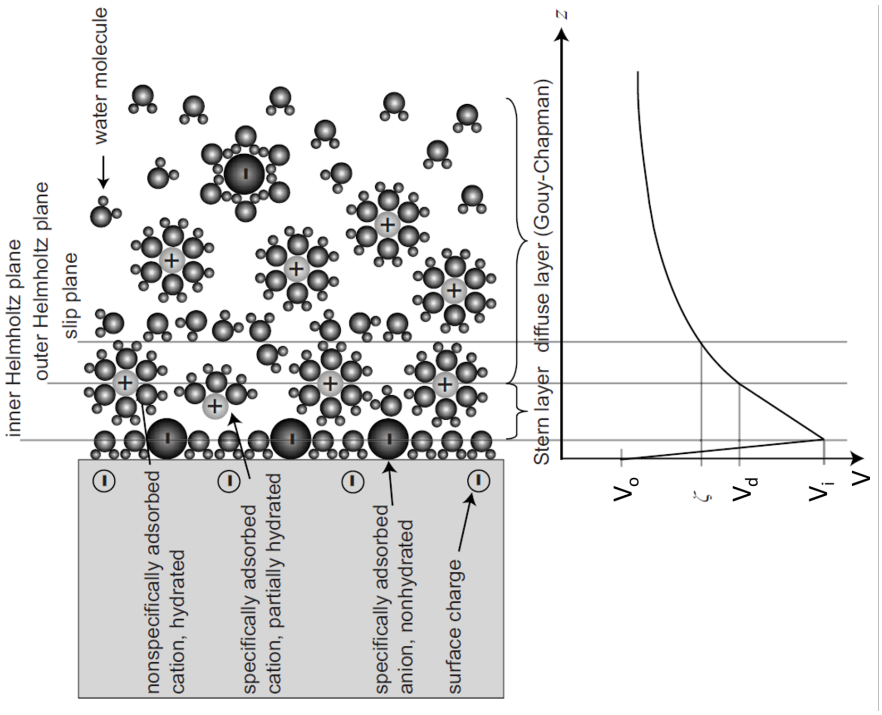

Figure 1.1: Representation of the electric double layer. A charged surface is contacted with an electrolyte. The diffuse layer and the Stern layer constituting the double layer are represented on this figure. The corresponding electrical potential is associated with the positions of the different layers [11].

1.1.2 Electro-osmosis and streaming currents

Electro-osmosis is the phenomena by which the motion of the liquid is induced by an applied electric field parallel to the surface. For a negatively charged surface, the net excess of positive ions in the electric double layer (EDL) will draw the liquid resulting in a flow from left to right (figure 1.2). The flow velocity along the surface (x-direction) can be derived from the stationary Stokes equation :

$$\eta \frac{\partial^2 v_x}{\partial z^2} + \rho_e E_e = 0 \tag{1.4}$$

with ρ_e the volumetric charge density and E_e the electric field applied along the charged surface.nUsing Poisson equation, $\nabla^2 V = -\rho_e/\epsilon$ in eq. (1.4):

$$\frac{\partial^2 v_x}{\partial z^2} = \frac{\epsilon E_e}{\eta} \frac{\partial^2 V}{\partial z^2} \tag{1.5}$$

This equation needs to be integrated twice with two boundary conditions: the derivative of velocity far from the wall is zero (plug flow) ie. $\partial_z v_x = 0$ at $z = \infty$ and the velocity at the wall is zero (no slip boundary condition) ie. $v_x = 0$ at $z = 0$. This results in:

$$v_x(z) = -\frac{\epsilon E_e}{\eta} \left(-V(z) + \zeta\right) \tag{1.6}$$

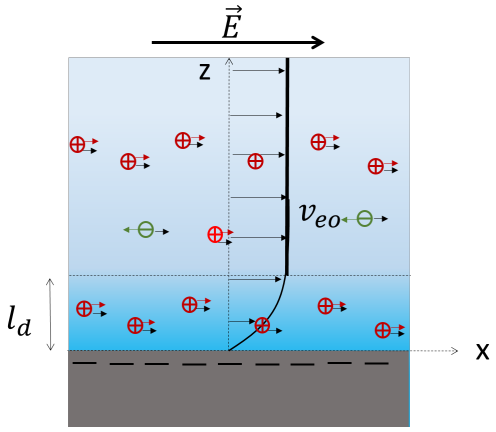

Figure 1.2: Schematic of an electro-osmotic flow profile induced by an electric field from left to right, in black arrows. Additional electrophoretic ion velocity is denoted in red for positive ions and in green for negative ions.

with ζ electrostatic potential at the no-slip plane and V(z) potential difference along the z axis between the point of interest and the bulk solution at the same x-abscissa.

In the diffuse layer, more counter ions are conducted in the direction of the electric field and by driving effect, the surrounding fluid is entrained with the ions. This effect is stopped when the number of cations become equal to the number of anions, that is, out of the EDL or far from the charged surface, resulting in a constant velocity called the electro-osmotic velocity. This is termed as plug flow velocity v_{eo}, first described by Smoluchowski [28] :

$$\boxed{v_{eo} = -\frac{\epsilon \zeta E_e}{\eta}} \tag{1.7}$$

A reverse effect of electro-osmotic flow is seen when a tangential stress τ_{xz} is applied along the surface [28]. A shear flow $v_x(z) = \tau_{xz}/\eta \times z$ is induced and drags the ions along the surface. This results in a net current density I_{str}/w, per unit length of the y-axis, called streaming current (I_{str}):

$$I_{str}/w = \int_0^\infty \rho_e(z) v_x(z) dz \tag{1.8}$$

Using Poisson equation $\nabla^2 V = -\rho_e/\epsilon$, the above equation reformed into:

$$I_{str}/w = -\int_0^\infty \epsilon \frac{\partial^2 V}{\partial z^2} v_x(z) dz \tag{1.9}$$

With boundary conditions; at $z = \infty$, $\partial V/\partial z = 0$ and at z=0, $v_x = 0$ and $V = \zeta$, the above equation results in:

$$\boxed{\frac{I_{str}}{w} = \frac{\epsilon \tau_{xz}}{\eta}(-\zeta)} \tag{1.10}$$

The electro-osmosis and streaming currents are reverse phenomena of each other: the cross-product $v_{eo} \times \tau_{xz}$ and $I_{str}/w \times E_e$ are indeed the power dissipation per unit surface area by viscous dissipation and Ohm's law respectively.

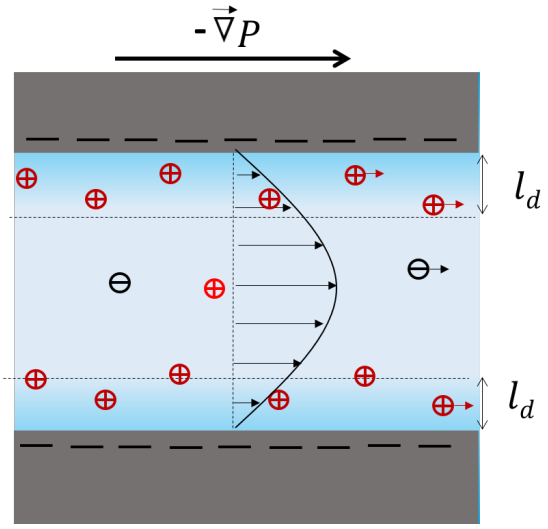

Figure 1.3: Schematic showing pressure driven flow within a channel of negatively charged walls. l_d is the Debye layer thickness.

In the case of a channel, the shear stress is induced by a pressure gradient such that $\tau_{xz}\mathcal{P} = -A \times dP/dz$ with $\mathcal{P}$ and A the perimeter and area of the channel's section. The fluxes and forces are then related by the Onsager matrix [14]:

$$q_{eo} = -\frac{\epsilon\zeta A}{\eta}\overrightarrow{E} - K\overrightarrow{\nabla}P$$
$$I = \frac{\epsilon\zeta}{\eta}A\overrightarrow{\nabla}P + G\overrightarrow{E}$$

with K the hydraulic permeability and G the electrical conductivity of the channel (note, $\overrightarrow{E} = -\overrightarrow{\nabla}V$).

1.1.3 Diffusio-osmosis

In the diffuse layer of ions close to the charged surface, the concentration of ions is not same as that of the bulk. The local concentration profile of each type of ion in the diffuse layer follows a Boltzmann distribution:

$$n_{\pm} = n_o \exp\left(\mp eV/kT\right) \tag{1.11}$$

where n_+ and n_- are local cation and anion concentrations and n_o is the bulk concentration in m^{-3}. This results in a non-compensated osmotic pressure difference: $kT\left[n_+(x,z) + n_-(x,z) - n_o(z)\right]$ build in the Debye layer. When a concentration gradient along the wall of the channel is applied, the diffuse layer is set in motion,

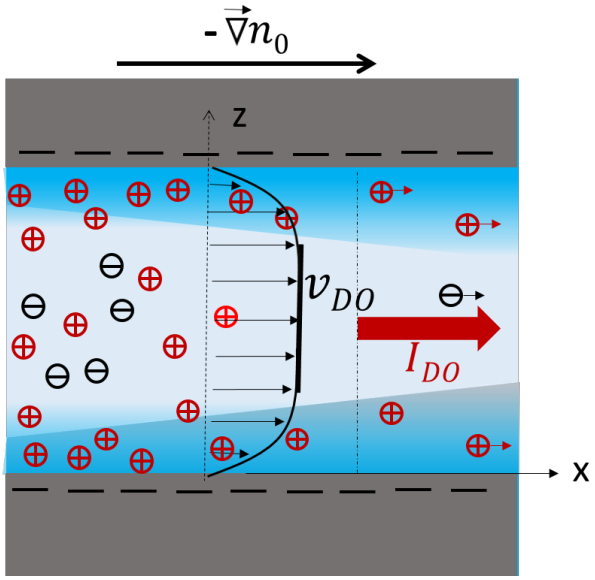

Figure 1.4: Schematic showing diffusio-osmotic flow within a channel of negatively charged walls. v_{DO} is the diffusio-osmotic velocity and I_{DO} is the diffusio-osmotic current. The blue contrast close to the walls is the Debye layer.

inducing a net flow in the channel called the diffusio-osmotic flow v_{DO}, and the current carried by the diffused ions is called diffusio-osmotic current I_{DO}, figure 1.4. Following ref. [29], the expression of the diffusio-osmotic velocity is derived to [13]:

$$\boxed{v_{DO} = \frac{kT}{2\pi\eta l_b}\ln(1-\gamma^2)\nabla\ln(n_o)} \tag{1.12}$$

with k the Boltzmann constant, T the temperature, η the liquid viscosity and l_b is the Bjerrum length. $\gamma = \tanh\left(\frac{eV_o}{4kT}\right)$ with V_o the surface charge.

The diffusio-osmotic current is derived to:

$$\boxed{\frac{I_{DO}}{w} = \frac{\epsilon_0\epsilon_r(kT)^2}{\pi e\eta l_b l_d}\left(\sinh\frac{\psi_o}{2} - \frac{\psi_o}{2}\right)\nabla\ln(n_o)} \tag{1.13}$$

with the relation between surface potential and surface charge

$$\sinh(\psi/2) = \sinh(eV/2kT) = 2\pi\Sigma l_d l_b/e \tag{1.14}$$

where Σ is the surface charge and l_d is the Debye length. For $\Sigma > \Sigma_c = e/(2\pi l_b l_d)$, the expression of diffusio-osmosis current reduces to:

$$\boxed{I_{DO}/w = \frac{\Sigma kT}{2\pi\eta l_b}\nabla\ln(n_o)} \tag{1.15}$$

In diffusio-osmosis phenomena, the current originates from the pressure difference generated along the wall of the channel, which can be quiet large. For example, for 1 molar salinity difference, a pressure difference upto 50 bar is generated (from

$p_0 = 2kT\Delta n_0$). This makes the mechanism of current generation different from the RED process where the mechanism is based on an ion selection [10].

Although, the streaming current and diffusio-osmotic current both are originated at the vicinity of the charged surfaces, the diffusio-osmotic currents can reach to much larger values as experimentally investigated by Siria *et.al.* [13]. They have measured the diffusio-osmotic current in a highly charged single boron nitride nanotube, resulting in a current density of 8×10^5 A.m^2 (for a concentration ratio of 1000).

1.2 Application to power generation in linear nanofluidic systems

1.2.1 General formulation of linear electrokinetic phenomena

Osterle *et al.*[30] and more recently Brunet and Ajdari [14], have generalized the coupled transport equations in the case of a general geometry and arbitrary number of ion species; provided that the system stays in a linear response regime (the condition for this is not being specified). As in this thesis we have used only potassium chloride as an electrolyte, we focus here on the transport of these ions, assuming that they are the only ones that play role in transport. Let J_{K^+} be the flux of K^+

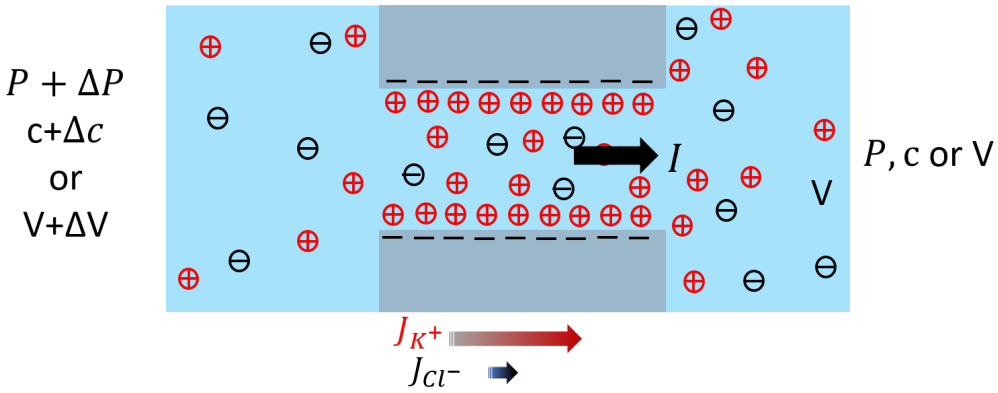

Figure 1.5: Schematic of the transport in a nanochannel or membrane under the application of pressure difference, concentration difference or voltage difference. J_{K^+} and J_{Cl^-} represent the fluxes of K^+ and Cl^- ions through the nanochannel.

ions and J_{Cl^-} be the flux of Cl^- ions through the channel/membrane. Then the electrical current within the channel is

$$I = e(J_{K^+} - J_{Cl^-}) \tag{1.16}$$

We can define the total solute flux by the sum of the fluxes as:

$$J_d = J_{K^+} + J_{Cl^-} \tag{1.17}$$

Ajdari and Brunet related the flux of ions and the volume flux of the solution to the driving forces:

$$\begin{aligned}\Delta\mu_+ =&\Delta\mu + e\Delta V\\ \Delta\mu_- =&\Delta\mu - e\Delta V\\ \Delta\Pi =&\Delta P - \Delta p_o\end{aligned} \tag{1.18}$$

with $\Delta\mu = kT\Delta\ln(\mathrm{n})$ the chemical potential gradient, $\Delta n = N_A\Delta c$ the concentration difference between the two reservoirs with N_A Avogadro constant, ΔP is the static pressure difference and $\Delta p_o = 2kT\Delta n$ is the osmotic pressure drop given by the famous van't Hoff formula. By the symmetry, justified in annex B, of Onsager's matrix:

$$\begin{bmatrix} J_{K^+} \\ J_{Cl^+} \\ Q \end{bmatrix} = \begin{bmatrix} L_{++} & L_{+-} & L_{+P} \\ L_{+-} & L_{--} & L_{-P} \\ L_{+P} & L_{-P} & L_{PP} \end{bmatrix} \begin{bmatrix} \Delta\mu_+ \\ \Delta\mu_- \\ \Delta\Pi \end{bmatrix} \tag{1.19}$$

Here, L_{++}, L_{--} and L_{PP} are the coefficients associated with the direct force terms and L_{+-}, L_{+P} and L_{-P} are the off-diagonal coefficients. Onsager symmetry is applied on these off-diagonal i.e., $L_{ij} = L_{ji}$ [14].

Combining the equations (1.18) and (1.19) and feeding them into equation (1.16) and (1.17), a linear relationship between the ionic fluxes and corresponding driving forces exist in the limit of small forces [31, 30]. The associated equation of fluxes can be written in the form of following matrix:

$$\begin{bmatrix} J_d \\ I \\ Q \end{bmatrix} = \begin{bmatrix} L_{CC} & L_{CE} & L_{CP} \\ L_{CE} & L_{EE} & L_{EP} \\ L_{CP} & L_{EP} & L_{PP} \end{bmatrix} \begin{bmatrix} \Delta\mu \\ \Delta V \\ \Delta\Pi \end{bmatrix} \tag{1.20}$$

where L_{CC}, L_{EE} and L_{PP} are the direct terms, linking each flux with their natural force, solvent flow with the pressure gradient, the ionic flow with the salt gradient and the ionic current with the voltage gradient respectively. L_{CE}, L_{CP}, L_{CE}, L_{EP}, L_{PC} and L_{PE} are the cross terms (off diagonal) which are related to the couplings between hydrodynamics, ion diffusion and electrostatics. For example L_{CE} is the coefficient related to the salt flux generated under the electric potential gradient and reversely the current generated under the salt gradient (osmotic current).

$$\begin{aligned} L_{CC} =&\quad L_{++} + L_{--} + 2L_{+-}, && L_{EE} = e^2(L_{++} + L_{--} - 2L_{+-}),\\ L_{CE} =&\quad L_{EC} = e(L_{++} - L_{--}), && L_{CP} = L_{PC} = L_{+P} + L_{-P},\\ L_{EP} =&\quad L_{PE} = e(L_{+P} - L_{-P}) \end{aligned} \tag{1.21}$$

In energy applications it is of interest to characterize fluxes and power densities. For a device of area A and thickness L, the above matrix can also be written as

$$\begin{bmatrix} J_d/A \\ I/A \\ Q/A \end{bmatrix} = \begin{bmatrix} l_{CC} & l_{CE} & l_{CP} \\ l_{CE} & l_{EE} & l_{EP} \\ l_{CP} & l_{EP} & l_{PP} \end{bmatrix} \begin{bmatrix} \Delta\mu/L \\ \Delta V/L \\ \Delta\Pi/L \end{bmatrix} \tag{1.22}$$

For instance, in the case of a nanochannel or membrane with a pore size r_{nc} larger than the Debye length, we expect that the previous mechanisms lead to a first approximation of the transport matrix coefficients as:

$$\begin{aligned} l_{EE} &= \sigma_e, & l_{EP} &= \frac{\epsilon\zeta}{\eta}, \\ l_{CE} &= \frac{2\Sigma}{\pi r_{ch} h l_b \eta}, & l_{PP} &= \frac{K}{\eta}, \\ l_{CP} &= 2n_0 l_{PP} + \frac{\ln(1-\gamma^2)}{2\pi\eta l_b} \end{aligned} \tag{1.23}$$

σ_e, the effective conductivity of the electrolyte in the nanopore, ζ the zeta potential of the pore walls and Σ the surface charge (higher than Σ_c), K the permeability of the pore/membrane. Note that the first term in l_{CP} accounts for the bulk convection transport of solute.

1.2.2 Electrical modelization: electromotive force, current source

From the electrical current equation in equation (1.22), the expression for the voltage difference is

$$\Delta V = \frac{I}{L_{EE}} - \left(\frac{L_{CE}}{L_{EE}} \Delta\mu + \frac{L_{EP}}{L_{EE}} \Delta\Pi \right) \tag{1.24}$$

From this we can see that the nanochannel is equivalent to a generator delivering a current I with a tension U available at this current output equal to:

$$U = -\Delta V = -R_{ch} I + \varepsilon_s \tag{1.25}$$

with nanochannel resistance defined as $R_{ch} = 1/L_{EE}$ and an electromotive force (e.m.f.) denoted by ε_s:

$$\boxed{\varepsilon_s = \frac{L_{CE}}{L_{EE}} \Delta\mu + \frac{L_{EP}}{L_{EE}} \Delta\Pi} \tag{1.26}$$

The equation (1.25) represents a battery of potential ε_s with an internal resistance R_{ch}. The electro-motive force is provided by ε_s in order to put energy into an external load connected between the inlet and outlet of the nanochannel.

From the above equation (1.25), in general, the equivalent electrical circuit of a nanochannel can be viewed as a voltage source ε_s in series of a channel resistance R_{ch}. (as adopted in Majumdar*et al.* [15] and Ouyang *et al.* [32]). An alternative electrical circuit is made of the current source I_s given by equation (1.27) in parallel to the nanochannel resistance R_{ch}. This model has been used by Siria *et al.* [13] where the origin of the current source has been attributed to the diffusio-osmotic current.

$$\boxed{I_s = \frac{\varepsilon_s}{R_{ch}} = (L_{CE}\Delta\mu + L_{EP}\Delta\Pi)} \tag{1.27}$$

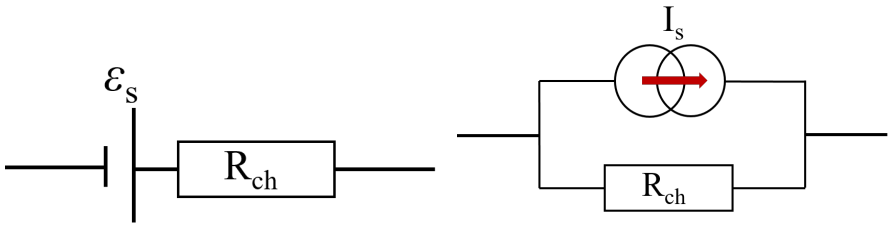

(a) (b)

Figure 1.6: Schematic of the equivalent electrical circuit of a nanochannel as (a) a voltage source ε_s in series with channel resistance R_{ch}, or (b) current source I_s in parallel with channel resistance R_{ch}.

1.2.3 Power generation

If the electrodes placed at the inlet and outlet of the channel are connected to an external load resistor, the electrical power can be harvested from the nanochannel. The electrical power captured at the load R_L is:

$$P_{out} = U \times I = \frac{R_L \varepsilon_s^2}{(R_L + R_{ch})^2} \tag{1.28}$$

The maximum power will be delivered under the condition $R_L = R_{ch}$, resulting in:

$$\boxed{(P_{out})_{max} = \frac{\varepsilon_s^2}{4R_{ch}} = \frac{1}{4} I_s^2 R_{ch}} \tag{1.29}$$

1.2.4 Reference cases

Here we will discuss some particular cases corresponding to typical experimental situations. This allows us to access the cross coupling coefficients. In each case we formulate the electromotive force and current source intensity as well.

Case 1: Electrokinetic power generation, $\Delta\mu = 0$.
In this case, $\Delta\Pi = \Delta P$, as there is no concentration gradient. Thus, the driving force is only the pressure difference applied across nanochannel. This mode of operation is called electro-osmosis and the flux of current and flow are given by:

$$\begin{aligned} I &= L_{EE}\Delta V + L_{EP}\Delta P \\ q &= L_{EP}\Delta V + L_{PP}\Delta P \end{aligned} \tag{1.30}$$

The electromotive force is

$$\boxed{\varepsilon_s = V_{str} = \frac{L_{EP}}{L_{EE}}\Delta P = S_{str}\Delta P} \tag{1.31}$$

with $S_{str} = l_{EP}/l_{EE} = R_{ch}L_{EP}$, the streaming coefficient in V/bar. Equation (1.25) is rewritten as:

$$U = -R_{ch}I + S_{str}\Delta P \tag{1.32}$$

If $I = 0$, then $U = V_{str} = S_{str}\Delta P$ gives the expression of the streaming voltage. This is the case when the end reservoirs are not electrically connected to an external circuit. The ions travelling downstream accumulate in the end reservoirs and build the streaming potential. The streaming current is compensated by a conduction current through the nanochannel.

If $U = 0$ then $I = I_{str} = L_{EP}\Delta P$, with L_{EP} the streaming current coefficient in A/bar. The maximum power delivered in this case is

$$(P_{out})_{max} = \frac{(S_{str}\Delta P)^2}{4R_{ch}} = \frac{R_{ch}\,(L_{EP}\Delta P)^2}{4} \tag{1.33}$$

Therefore, increasing the pressure difference across the nanochannel results in an increase in the maximum power delivered by the channel.

We can use the simplified approach as presented in the beginning of the present section for a first qualitative estimation. For instance, in a membrane of conductivity σ_e=0.1 S.cm^{-1} (see section 4.3), the streaming coefficient could be estimated from: $S_{str} = \frac{l_{EP}}{l_{EE}} = \frac{\epsilon\zeta}{\eta\sigma_e}$. For a zeta potential ($\zeta$) of 100 mV (considered as a high ζ potential), we get : $S_{str} = 640$ μV.bar^{-1}. The maximum possible power in an electrokinetic conversion of mechanical energy, would then be: $P_{out}/A = \frac{S_{str}^2\sigma_e}{4L}(\Delta P)^2$. For a thickness L=60$\mu$m of a Nafion 112 membrane, this amounts to 17 mW/m^2/bar^2.

Case 2: Electrical power generation for salinity gradient, $\Delta\Pi = 0$ The driving force are the chemical potential ($\Delta\mu$) and the voltage difference ΔV across the nanochannel. The flux equations are given as follows

$$\begin{aligned} J_d &= L_{CC}\Delta\mu + L_{CE}\Delta V \\ I &= L_{CE}\Delta\mu + L_{EE}\Delta V \end{aligned} \tag{1.34}$$

The electromotive force, required to provide the energy into an electrical circuit is expressed as:

$$\varepsilon_s = V_{diff} = \frac{L_{CE}}{L_{EE}} kT\Delta \ln c = \frac{l_{CE}}{l_{EE}} kT\Delta \ln c \tag{1.35}$$

This electromotive force can be expressed in terms of a transference number as sometimes used in the literature [15, 32]. The transference number is defined as the fraction of the current that is carried by a certain type of ion in a conductivity experiment (only ΔV is applied across the membrane, Δc=0, ΔP=0).

$$t_+ = \frac{J_{K^+}}{J_{K^+} - J_{Cl^-}} = 1 + t_- \tag{1.36}$$

and

$$t_+ = \frac{L_{++} - L_{+-}}{L_{++} + L_{--} - 2L_{+-}} \tag{1.37}$$

The difference of the transference numbers of the two types of ions across the nanochannel is always one ie. $t_+ - t_- = 1$. The ratio of coefficients L_{CE}/L_{EE}

can be formulated in terms of the transference number as follows:

$$\frac{L_{CE}}{L_{EE}} = \frac{L_{++} - L_{--}}{e(L_{++} + L_{--} - 2L_{+-})} = \frac{1}{e}(2t_+ - 1)$$

which gives

$$\boxed{V_{diff} = (2t_+ - 1)\,\frac{kT}{e}\Delta \ln c} \tag{1.38}$$

Note that the transference number is not the ratio of the K^+ ion flux in any experimental condition. It is defined as this ratio only in the condition of equation (1.36). Note that the transference number is not bounded to unity.
The maximum electrical power transferred from the salinity gradient is:

$$(P_{out})_{max} = \frac{(V_{diff})^2}{4R_{ch}} \tag{1.39}$$

Therefore, increasing the diffusion potential across the nanochannel is favorable to increase the output power. We can use the simplified approach to perform a first quantitative estimation. In this simplified approach the electromotive force induced by a salinity product is:

$$V_{diff} = \frac{l_{CE}}{l_{EE}}\Delta \ln(c) = \frac{2\Sigma kT}{\pi r_{ch} l_b \eta \sigma_e}\Delta ln(c) \tag{1.40}$$

We can take for instance the case of nanochannel of surface charge Σ=10 mC/m^2 (typical surface charge for silica), of radius 10 nm and of effective conductivity $\sigma_e = 0.1$ S.m^{-1}, corresponding to an average KCl concentration of 10^{-2} M (see table 4.1 in part II). This gives diffusion potential V_{diff}=70 mV/decade of concentration in the salinity gradient. The maximum electrical power harvested from this salinity gradient is than

$$\frac{(P_{out})_{max}}{A} = V_{diff}^2 \frac{\sigma_e}{L} \tag{1.41}$$

For a channel of length 150 μm (i.e. the experiment of Mjaumdhar *et al.* [15]), we get 3 W/m^2/pC^2, with pC=$\Delta \log_{10}$c. This evaluation fo V_{diff} and the harvested power are the typical magnitude found by Mjaumdhar *et al.* [15].

For a membrane such as Nafion (see part II section 4.3) with $r_{nc} = 1$ nm, $\sigma_e = 10$ S.m^{-1} and L=60 μm, with the same surface charge, the expected electromotive flux an maximum power density are 7mV/pC and 10 W/m^2/pC^2.

The very first estimation shows that the chemical energy of salinity gradient might give higher electrical power density than mechanical energy, when harvested by nanofluidic devices.

Case 3: When $\Delta P = 0$

This is the case of our experiments presented in the first part of the thesis. There is no static pressure applied across the membrane, but an osmotic pressure difference exists. In this case, the equation of current flux is written as follows:

$$I = L_{CE}\Delta\mu + L_{EE}\Delta V + L_{EP}(-\Delta p_o)$$

(1.42)

The electromotive force to provide the energy into an electrical circuit is expressed as:

$$\boxed{\varepsilon_s = \frac{L_{CE}}{L_{EE}} kT\Delta \ln c - \frac{L_{EP}}{L_{EE}} \Delta p_o} \tag{1.43}$$

Chapter 2

Nonlinear transport in nanofluidics

Contents

In the previous chapter we have discussed the coupled transport phenomena in nanofluidic devices in the limit of the linear response. The linear response is always expected for small enough driving forces. However, as stated in Ajdari and Brunet 2004, in the general case there is no simple criterion which defines the limiting driving forces below which the linear response is actually obtained.

Non-linear effects, and more specifically rectification effects, have been predicted and studied in nano-pores and nano-fluidic devices in which Debye layers overlap [33, 23]. We present here a very quick overview of rectifying effects in electrical and osmotic transport through asymmetric nanopores. We limit this presentation to the material needed for the interpretation of our experiments on the electrical conductance of conical shape solid-state nanopores presented in part III, and for the estimation of the flow rate resolution needed to study rectified electro-diffusio-osmotic flows in solid-state nanopores, in part IV.

2.1 Nonlinear effects in nanofluidic systems: ionic current rectification

Non-linear I-V characteristics in asymmetric nanochannels, displaying a rectified electrical current, have been reported and studied by various groups [21, 22, 33, 23]. For instance figure 2.1 represents an IV characteristics of a conical nanopore in polyethylene terephthalate (PET), from reference [33]. PET is a thermoplastic polymer. The surface charge is regulated by pH of the KCl solution (zero at pH 3

and negative with increase in pH). In one direction the current is recorded higher as compared to the other direction (when polarity has been changed, see figure 2.1). Similar types of asymmetric I-V characteristics have been observed from the nanofluidic device equipped with asymmetrically charged walls, illustrated by Karnik *et al.* [20].

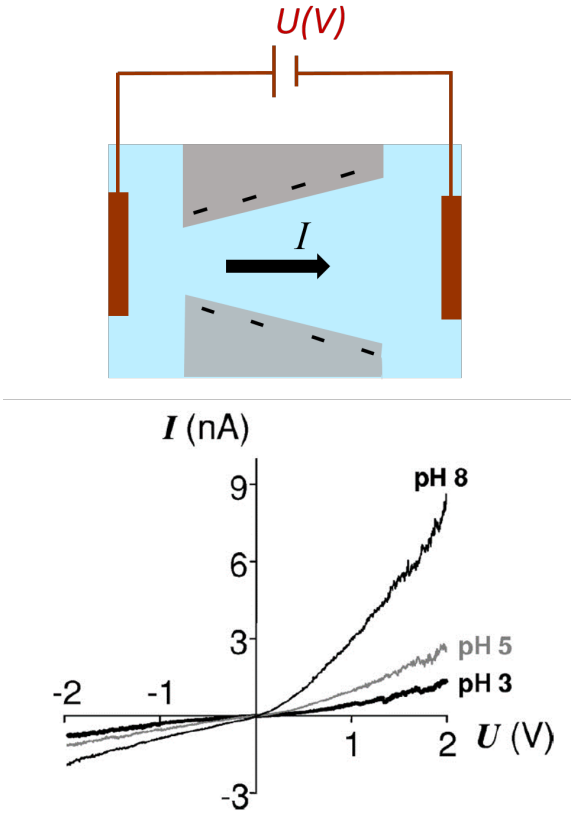

Figure 2.1: I-V characteristics of a conical nanopore at various pH values From ref [22]. On top, a schematic of a negatively charged conical pore in forward bias configuration.

These rectifying effects in the conductance of nanofluidic devices are somewhat similar to that observed in solid-state semi-conductor diodes, and have lead to the term *nanofluidic diode*. The analogy with semi-conductor diodes stems from the so-called Donnan equilibrium first developped in the context of membranes, for describing the exclusion/enrichment in ions in a nanochannel of aperture h not very large compared to the Debye length [34]. The Donnan's equilibrium is a thickness-averaged approach to determine the potential in a nanochannel in contact with a reservoir of electrolyte concentration n_o:

$$n_{eq}^{+} = n_o e^{-eV_D/kT}, \qquad n_{eq}^{-} = n_o e^{eV_D/kT}, \quad n_{eq}^{+} n_{eq}^{-} = n_o^2 \tag{2.1}$$

$$n_{eq}^{+} - n_{eq}^{-} = -\frac{2\Sigma}{eh} \tag{2.2}$$

$$\sinh\frac{eV_D}{kT} = \frac{l_{Du}}{h}, \qquad l_{Du} = \frac{\Sigma}{en_o} \tag{2.3}$$

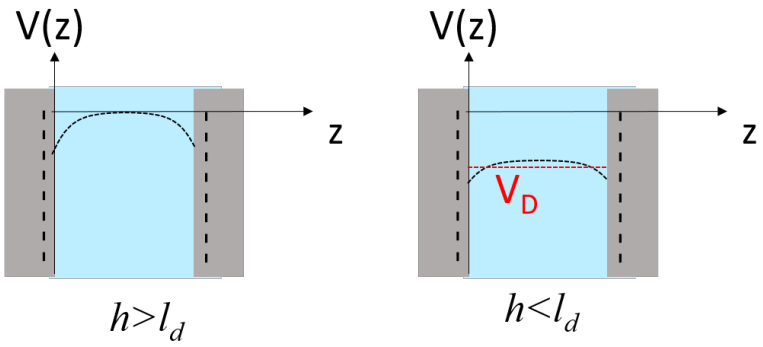

Figure 2.2: Schematic showing potential in a nanochannel for $h > l_d$ on the left, and $h < l_d$ on the right.

The Donnan potential V_D describes the potential difference between the inside of the nanochannel and the surrounding reservoir. The analogy between the Donnan equilibrium and the equilibrium of charge carriers in doped semi-conductors (SC) lies equations (2.1) and (2.2), which are also obeyed by the electron density and the hole density in SC. Here, the electrolyte density n_o should be replaced by the carrier density in the intrinsic (non-doped) SC, while the surface charge in the nano-channel (more precisely the ratio Σ/h) actually acts as the concentration of dopant impurities, delivering additional carriers. A positive surface charge $\Sigma > 0$ corresponds to donors (N-doped SC) and a negative charge $\Sigma < 0$ to acceptors (P-doped SC). The Donnan potential is then the analogous of the shift in the Fermi energy due to impurities.

A nanofluidic system analogous to a P-N junction is then constituted by the junction of two nanochannels of negative and positive surface charge. Karnik *et al.* studied such a configuration, by functionnalizing a 30nm thick nanochannel half with avidin (ie positive surface charge) and half with biotin (neutral surface charge) [20]. Other configurations are conical shape nanopores, which display a gradient in the "dopant" parameter Σ/h.

The rectifying effect in such a nanofluidic system is similar to the one in a P-N junction: the factor limiting the current is the energy jump that carriers have to undergo at the junction. In the case of a conical shape charged nanopore as studied in Part III (see figure 6.10) the rectifying behavior comes from the dissymmetry of the junctions with the reservoir. For a negative surface charge, the majority carriers are positive ions. In the case of a forward voltage bias, the positive current is limited by the energy jump that the positive ions have to perform at the widest extremity of the pore. This energy barrier is lower than the one to overcome in the case of a reverse bias, where the positive ions have to exit the pore at its narrow end, with a higher energy jump. Therefore, the forward conductance of the pore is larger than its conductance under reverse bias.

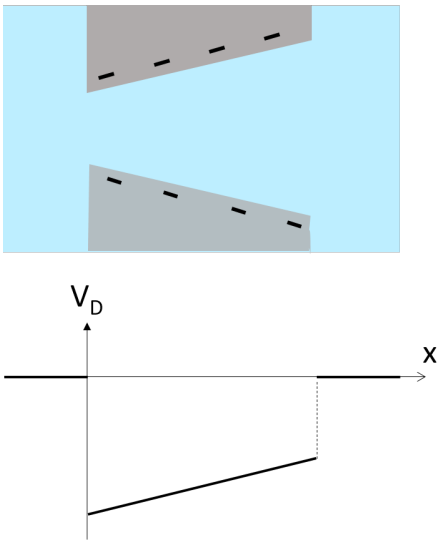

Figure 2.3: Schematic showing Donnan potential along a conical nanopore of negative surface charge. The majority carriers in the pore are positive ions, whose energy $E = eV_D < 0$ has the same sign as on the plot.

2.2 Flow rectification: the osmotic diode

The nanofluidic diode is able to mimic the behavior of a semiconductor diode but it presents also specific features that distinguishes if from its solid state counterpart. Unlike in doped semiconductors, where mobile charges diffuse through a fixed crystalline structure, the motion of ions, in a nanofluidic diode, is coupled with the transport of the fluid solvent within which they are solubilized. The coupling between the charge transport and the fluid flow originates from electrostatic forces that behave as an apparent osmotic pressure. As a result, beyond electrical current rectification, a nanofluidic diode should also rectify electroosmotic flow and as such behave as an osmotic diode. Such an osmotic diode is appealing to control fluid flow at the nanoscale and more precisely built valves at this scale without any moving parts.

The non-linearity required to produce such a flow rectification at low Reynolds number, responsible for inertial less behavior common to nanofluidic, comes from the coupling between momentum balance and charge transport through a non-linear electrostatic contribution. Non-linear behavior in flows are usually observed either at large Reynolds number in the turbulent flow of a Newtonian fluid or at low Reynolds number because of the visco-elastic behavior of a non-Newtonian fluid. The Donnan equilibrium, keystone of the osmotic diode, provide an additional framework to obtain non-linear behavior in creeping flows of Newtonian fluid at the nanoscale.

In this framework, few works suggests the ability of an osmotic diode to rectify flows. In the case of a diode made of a cylindrical pore presenting a discontinuity in surface charge, an analytical expression of the rectifying osmotic pressure has been

proposed by Picallo et al [26]:

$$\Delta\Pi_{app} = 2\left(1 - \frac{1}{\delta}\right)(n_L - n_R) - \frac{\alpha - 1}{\alpha\delta}\frac{n_R}{n_o}\left(n_L \exp\left(e\Delta V/kT\right) - n_R\right) \tag{2.4}$$

with n_L, n_R the concentrations of left and right side of the channel, ΔV the difference of potential across the channel, $\delta = \Sigma/(ehn_o)$ the Dukhin number, and α a numerical coefficient characterizing the jump of surface charge as illustrated in figure 2.4a. In the absence of pressure gradient, the flow is supposed to be proportional to $\Delta\Pi_{app}$ and as a result, its rectification described by the equation (2.4) and illustrated in the figure 2.4b

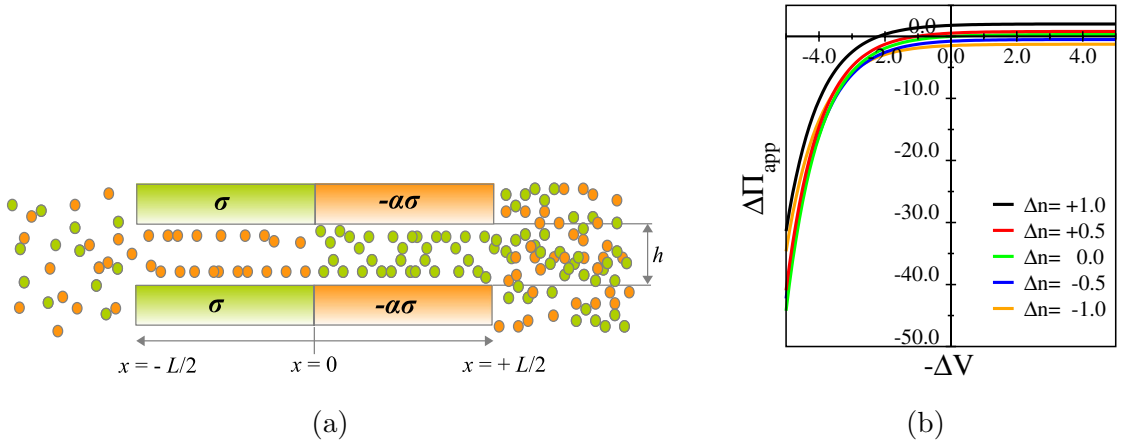

Figure 2.4: (a) Schematic of an asymmetrically charged nanochannel with two different salt concentrations applied on the left and right side of the nanochannel from [26]. (b) apparent osmotic pressure variation with applied voltage difference for several concentration differences from [26].

In the numerical work by Laohakunakorn et al [25] electroomotic flow through glass conical nanopore where studied with finite element simulation (figure 2.5a). The typical diameter of the pore is of the order of $d = 50$ nm. The flow rate according to the difference of electrical potential across the nanopore is shown in figure 2.5b. The considered surface charge is of the order of $\Sigma = 10$ mC.m^{-2} and the concentration of the electrolyte solution is $C = 100$ mM. In this framework, the Dukhin length $l_{Du} = \Sigma/(eC) = 1$ nm is small with respect to the nanopore diameter which explain the slight rectification observed by the authors.

In the experimental work by Jin et al [35], mica membranes with pyramidally shaped pores were prepared by the track-etch method (figure 2.6a). In this study, the author imposes a constant electrical current of 100 µA through the membrane and they follow indirectly the flow through the membrane according to the sens of the current using phenol as an electrically neutral tracer whose concentration increases due to convective transport is measured according time (figures 2.6). As the angle of the pyramidal pore can be adjusted, the authors were able to compared the case of asymmetric pores (figure 2.6b A) and symmetric pores (figure 2.6b B).

From the strong change in slope of the linear increase of the phenol concentration, in the asymmetric case, according to the current direction it can be inferred that indeed a strong rectification has been obtained.

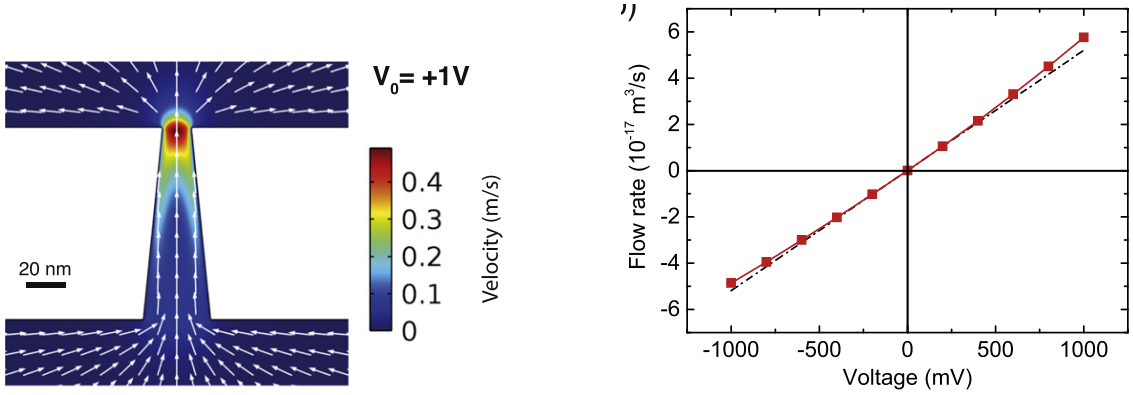

(a) (b)

Figure 2.5: Finite-element simulation of transport through a nanopore from [25]. (a) Typical flow profiles through a pore arrows indicate flow direction and colours indicate flow magnitude. (b) Flow rate rectification according to the applied difference of potential.

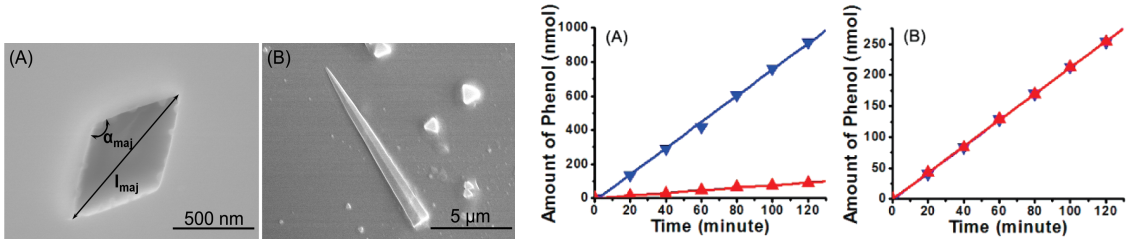

(a) (b)

Figure 2.6: Transport rectification through mica membranes with pyramidally shaped pores from [35]. (a) Electron micrographs of (A) the base opening of a pore in a mica membrane and (B) a carbon replica of a pyramidal mica pore. (b) Plots of phenol amount transported versus time through two mica membranes. (A) Asymmetric-pore membrane: Transport from base to tip (blue); transport from tip to base (red). (B) Membrane containing symmetrical pores.

Nevertheless, the rectification of an electroosmotic flow through a nanofluidic diode has never been demonstrated experimentally. In order to estimate the typical scale of the flow rate to be measured, the numerical study, Laohakunakorn *et al* provide a first direct quantitative values of the electro-osmotic flow through a conical nanopore made of glass with a typical diameter of the order of $d = 50$ nm according to the difference of electrical potential across the nanopore. The considered surface charge is of the order of $\Sigma = 10$ mC.m^{-2} and the concentration of the electrolyte solution is $C = 100$ mM. In this framework, the Dukhin length is $l_{Du} = \Sigma/(eC) = 1$ nm which is limited with respect to the nanopore diameter and results in the limited rectification observed by the author.

The elecroosmotic flow obtained through the nanopore is of the order of 40 fL.s^{-1} as shown in figure 2.5b, or 2 pL.min^{-1}, for a difference of potential of 1 V. This value can be compared to a typical electroosmotic flow rate based on the electroosmotic velocity given in relation (1.7) in previous chapter. Considering a surface potential of $\zeta = 10$ mV, a viscosity of 10^{-3} Pa.s, and the dielectric permittivity in water $\epsilon \sim 7.10^{-10}$ F.m^{-1}, the order of magnitude of the flow q_{eo}, through a nanopore of length $L = 1$ µm for a difference of potential of $\Delta V = 1$ V , is $q_{eo} \sim d^2\zeta\epsilon\Delta V/\eta L \sim 2.10^{-17}$ m^3.s^{-1} or 2 pL.min^{-1} which is the same order of magnitude obtained by Laohakunakorn et al.

The measurement of such a flow rate is a challenge as it is 3 orders of magnitude smaller than the current sensitivity available with the best commercial flow sensors. It is possible to gain one order of magnitude in the flow rate multiplying the nanopore diameter by 4 while keeping in play the physics of interest by a reduction of the electrolyte concentration. Nevertheless, if the maximum flow rate to be measured is of the order of 30 pL.min^{-1}, a sensitivity and a resolution of the order of 1 pL.min^{-1} is still required. The part IV of this work is focused on the development of a direct flow rate sensor able to reach such a sensitivity. A second requirement is the ability to use easily the flow sensor with any type of solid state nanopore.

Part II

Preparation and test of a electrokinetic flow cell

Chapter 3

Electrokinetic cell and set-up

Contents

Herein, I will describe the electrochemical cell and setup which is further used to study the electrokinetics within nanochannels. The electrochemistry of electrodes used to convert ionic current from the solutions into electrical current in an external circuit is summarized.

3.1 Design of the fluidic cell

A home made electrochemical cell was designed and build in polyether ether ketone (PEEK). This semi-crystalline thermoplastic is well known for its robustness due to excellent mechanical and chemical resistant properties with respect to organic and aqueous solvents. Thus, using PEEK as a material for designing the flow cell allows us to avoid the risk of creation of any kind of pollutant which can foul the nanochannels.

A schematic of the fluidic cell is depicted in figure 3.1. The fluidic cell consists of two disc type pieces each one having three ports: one inlet, one outlet (each having a diameter of 3.3 mm) and a port for electrode connection. Two tight fitting manual valves in PEEK (P732) from Upchurch Scientific are used for each half cell in order to control the flow within it. Three metal screws are used for clamping the PEEK pieces together. The sample can be pressed against two o-rings fixed at the inner circular perimeter of the PEEK pieces. Nitrile o-rings are used for this purpose as they are chemically inert and resistant to water, electrolytes and oils. The exposed area of the sample to the electrolyte solutions is slightly overestimated as 0.283

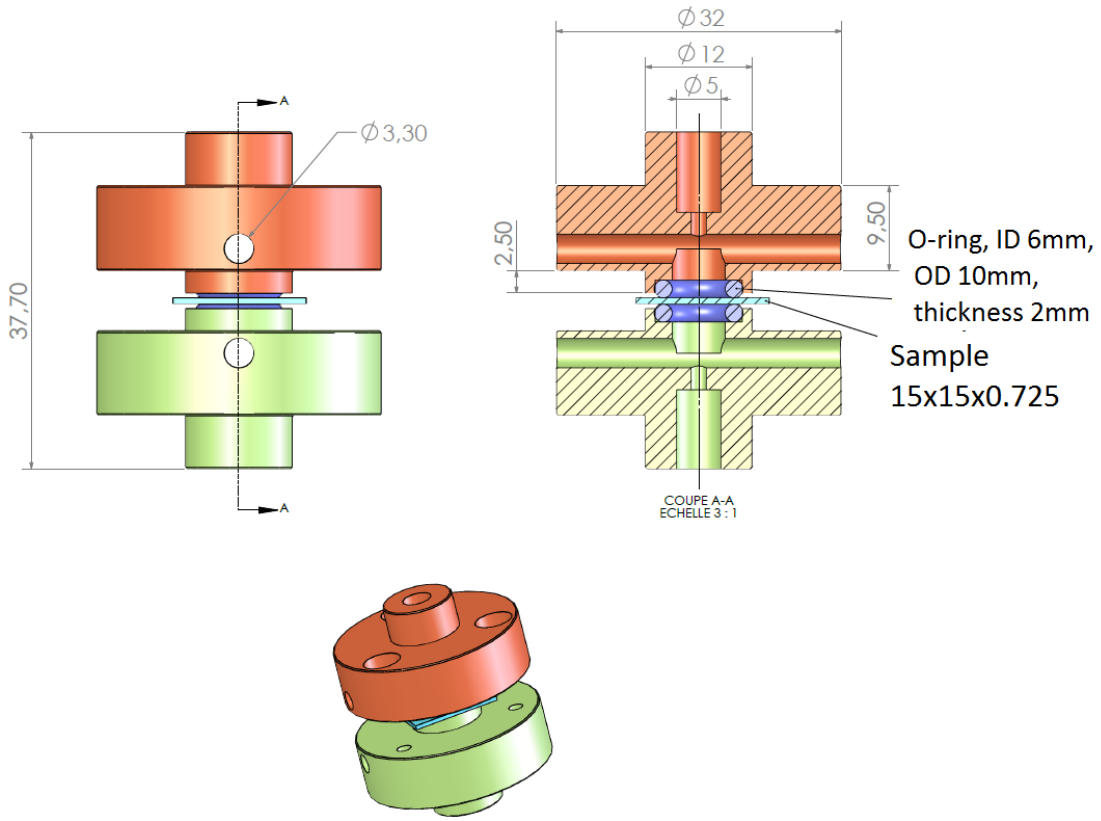

Figure 3.1: Schematic of the flow cell made in PEEK. The side view on the left indicates the inlets/outlets of dimensions 3.3 mm in circles. On the right, a cross sectional cut of the cell shows the dimensions of the fluidic paths, o-ring and sample to be used. At the bottom, a 3D view of the cell.

cm^2 (calculated from the nominal inner diameter of the o-rings equal to 6 mm). While placing the sample within the flow cell, it is required to be sure not to trap bubbles. This is achieved by filling the whole cell with liquid before clamping the sample. Later on when the sample is clamped, the solution is allowed to circulate back and forth within the cell leaving all four valves open. The electrolytes prepared are degassed in a desiccator for half an hour and then filtered by a 0.2 μm nylon membrane syringe filter before using them in experiments.

All the experiments were performed with KCl electrolyte. The KCl electrolyte was prepared by dissolving KCl salt (bought from Sigma Aldrich) into deionized water (18.2 MΩ-cm).

3.1.1 Control of the electrolyte concentration

The presence of an inlet and an outlet in each half cell allows us to apply a continuous flow of electrolyte on each side of the sample (figure 3.2). The cell is filled with the same concentration or different concentrations (c_1 and c_2) depending on the requirement of the experiment. This experimental arrangement minimizes the

concentration gradient inside the electrolyte. The flow is applied and controlled by a peristaltic pump, REGLO Digital MS 4/12-100.

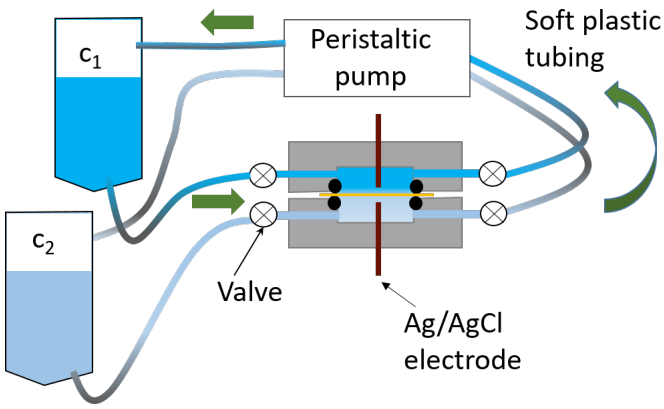

Figure 3.2: Schematic of the flow cell connected to the peristaltic pump for continuous circulation of the electrolyte on each side of the sample. Green arrows indicate the direction of the electrolyte flow.

3.1.2 Pressure control

In this work, a pressure difference across the sample in the cell has been applied upto 1 bar. For this purpose a N_2 gas flow is applied to one of the falcon tube connected to the inlet and outlet of the cell (figure 3.2).

The incoming N_2 gas, via an external source (approximately 2 bar, figure 3.3), is allowed to pass across the fluidic path. Herein, the pressure can be controlled by two knobs, shown in figure 3.3. This pressure can be read directly from the pressure gauge above the knob 1 with a precision of 0.1 bar. A piezoresistive pressure sensor (Keller, Series 23 Y) is used to measure the pressure with a precision of ± 1 m-Bar. This pressure sensor is fed by a 15 V DC source and the output in terms of voltage is recorded via a National Instruments data acquisition system board. From this arrangement, the pressure difference across the sample is applied upto 1 bar when required, and controlled with a precision of 1 m-bar.

3.1.3 Electrical measurements

In the following, we perform two types of electrical measurements. Alternating current measurements (a.c.) are performed with a SR830 lock-in amplifier. The source of the amplifier is used to apply an a.c. potential to the circuit, and the inlet of the amplifier records the voltage across a load resistance in series with the electro-chemical cell under test, so as derive the a.c. current intensity.

For direct current (d.c.) measurements, we use a multimeter (Keithley 2750) to measure the current intensity through the sample in a range 10 nA-3 A or the voltage

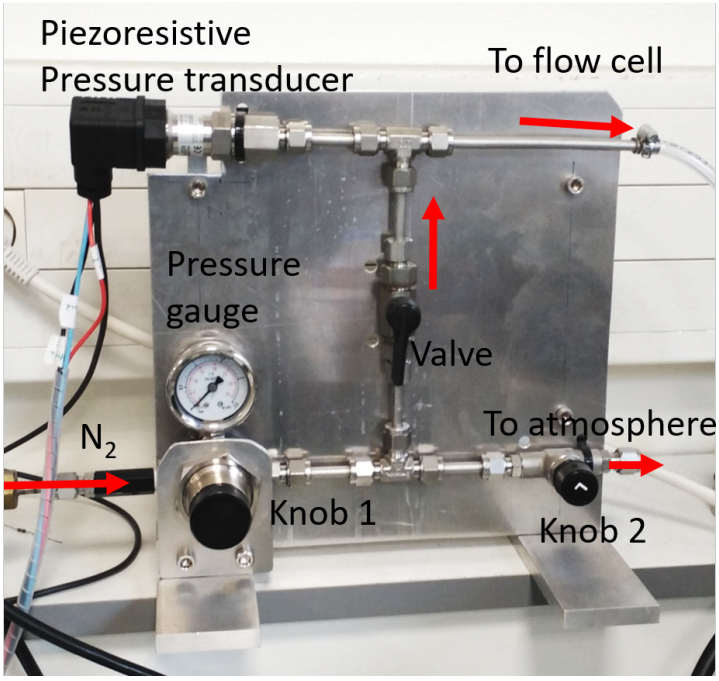

Figure 3.3: A picture of the N_2 pressure adjustment. The fluidic path is shown in red arrows. Knob 1 and knob 2 are used to adjust the N_2 pressure which can be read from the pressure gauge above knob1. A Piezoresistive pressure sensor at the top left is connected to the circuit in order to measure the pressure with a precision of 1m-bar.

difference across the sample in a range 0.1 μV-1000 V. We also use a patch-clamp amplifier RK300 to measure much smaller currents in the range 1 pA-50 nA.

Patch clamp is a well known technique in electrophysiology used to study single or multiple ion channels in cell membranes. Usually "patch" refers to patching a small piece of cell membrane and clamp refers to imposing on a membrane patch a defined voltage ("voltage-clamp") with the purpose of measuring the resulting current and of calculating the patch conductance. Clamping could also mean forcing a defined current through a membrane patch ("current-clamp") with the purpose of measuring the voltage across the patched membrane. Herein, the patch clamp technique is used to measure small ion currents across solid state nanochannels.

A simplified schematic of the patch clamp technique is presented in figure 3.4. A voltage $V_{applied}$ is applied resulting in a current flowing within the nanochannel. The same amount of current flows in the feedback resistor in order to compensate the channel current. The measured output voltage V_o from the operational amplifier is recorded by a National instruments data acquisition system board, the channel current can be calculated as $I_{ch} = \frac{V_o}{R_o}$. Consequently, the conductance of the channel can be measured ($G_{ch} = I_{ch}/V_{applied}$).

The electrokinetic experiments in different types of samples, e.g. single nanochannel or commercially available membranes are performed due to the ability of measur-

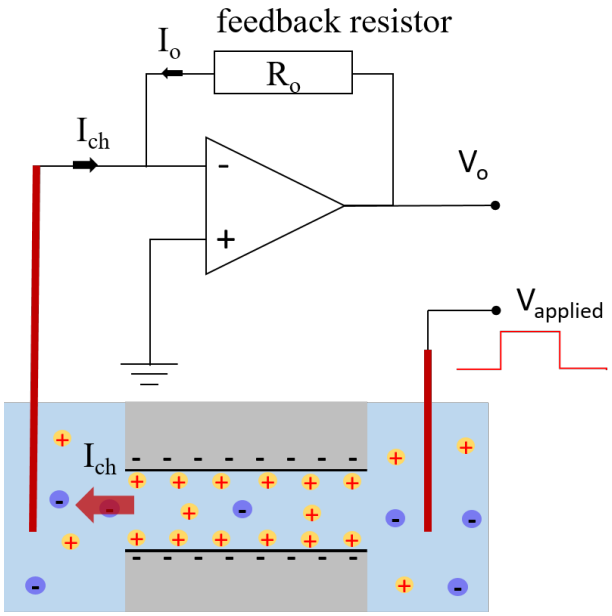

Figure 3.4: Schematic of the patch clamp technique used to measure a small ion current intensity in nanochannel by the application of a voltage $V_{applied}$. The output voltage V_o across the feed-back resistor R_o is measured and the channel current is calculated knowing the value of the feedback resistor.

ing current and voltage in a broad range. All the instruments are remotely controlled by a computer via Labview programs.

3.2 Theory and preparation of electrodes

In a typical electrokinetic cell, the motion of ions is responsible for the charge transport within the electrolyte while in the electrodes the charge transport occurs via the motion of electrons. For converting the ion current into electron current, a redox reaction usually occurs at each electrode resulting in the oxidation and the reduction of chemical species. When a metal surface comes in contact with an electrolyte, electrons enter into the metal and metal ions diffuse into the electrolyte. The resistance associated in this charge transfer process is called charge transfer resistance R_{ct} and the absolute value of the current per unit area is called the exchange current density I_{d0} [11].

In addition to this charge transfer resistance, there exists an impedance due to the formation of an EDL at electrode-electrolyte interface. The current is infact the sum of the Faradaic current linked to the charge transfer (across electrode-electrolyte interface) and a capacitive current linked to a electrical double layer (EDL) formed at electrode electrolyte interface. Therefore, these two components can be assumed to occur in parallel to each other and the relative impedance of the two components decides the behavior of the electrodes. If $R_{ct} \rightarrow 0$, the electrodes are called non-

polarizable (Ag/AgCl electrodes) and the current will be only Faradic current. If $R_{ct} \to \infty$ electrodes are polarizable (Pt electrodes).

Diffusion of ions also creates an impedance known as the Warburg impedance. This impedance depends on the frequency of the potential perturbation. At high frequencies, the Warburg impedance is small since diffusing reactants don't have to move very far. At low frequencies the reactants have to diffuse within much longer distances, thereby increasing the Warburg impedance. For infinite diffusion layer thickness, the equation for the Warburg impedance is [36]:

$$Z_W = \frac{\sigma_w (1 - i)}{\sqrt{\omega}} \tag{3.1}$$

where σ_w is a coefficient named Warburg coefficient which depends on the physico-chemical parameters of the system under investigation and ω is angular frequency.

In this work, two types of the electrodes are used: platinum (Pt) electrodes and Ag/AgCl electrodes. We are going to discuss the working principle and preparation process of these two types of electrodes.

Pt electrodes: If a DC voltage is applied at planar Pt electrodes, the current follows a decay with the square root of time, described in chronoamperometry by the Cottrell equation [36]:

$$I(t) = nFAc_R\sqrt{\frac{D_R}{\pi t}} \tag{3.2}$$

where n is the number of electrons needed to reduce/oxide one molecule of analyte, A is the electrode surface, c_R is the concentration of the reduced species R, and D_R is the diffusion coefficient of the reduced species R. The current I results from oxidation and reduction reactions at the platinum electrodes. Those reactions are not symmetric: On one electrode there is a formation of O_2 while on other one formation of H_2.

$$2H^+ + 2e^- = H_2(g), \qquad O_2^- = O_2 + 2e^- \tag{3.3}$$

The creation and consumption of species results in a diffusion limited current which can be avoided by application of AC measurement. In AC measurements diffusion limited currents cannot occur. Chemical reactions are not induced because of the alternating electric field, therefore these electrodes are suitable for AC measurements.

In this work the Pt electrodes are prepared in the form of thin film directly over the nanochannel sample. The detailed description of the preparation is presented in the part III of the thesis.

Ag/AgCl electrodes While using Ag/AgCl electrode on DC applications, the following reversible oxidation and reduction reactions take place on the electrodes:

$$AgCl + e^- \leftrightarrows Ag + Cl^- \tag{3.4}$$

These reactions are ideally quick and it is considered that they do not lead to a charge transfer resistance. Therefore, the Ag/AgCl electrodes are not polarizable and do not have a significance impedance. However, a Warburg resistance can be present due to the K^+ ions transported by the electric field in the solution but are not transferred at the interface (see Annex A).

Usually, at one of the Ag/AgCl electrodes, there is a diminution of the AgCl layer (becasue AgCl converts into Ag) while on the other electrode there is a diminution of Ag (Ag turns into AgCl). Because of this the electrodes degrade with time and can not be used in a repeatable manner until repairing the AgCl coating. Therefore, platinum electrodes are another choice of electrodes that we have used in this work, because of their non-corrosive behavior.

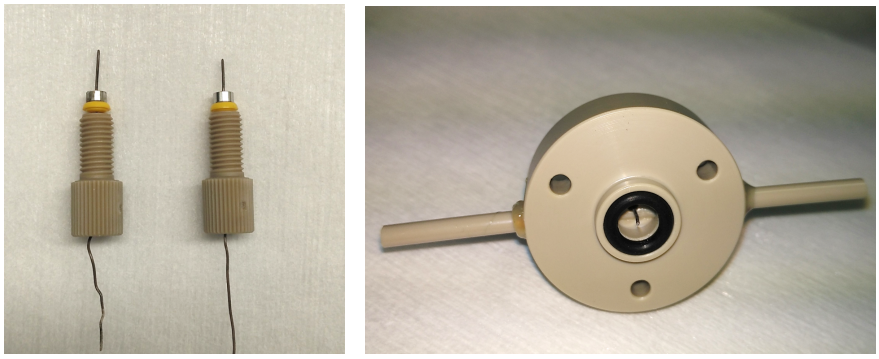

(a) (b)

Figure 3.5: (a) Ag/AgCl electrodes prepared in bleach solution and fitted in a PEEK connector. (b) This PEEK connector with embedded Ag/AgCl electrode is fixed within the flow cell vertically in the middle of the o-ring.

Here, in this part of the thesis, Ag/AgCl electrodes are used. Ag/AgCl electrodes are prepared with 0.5 mm thick silver wire bought from Sigma Aldrich. The wire is cut in a 6 cm length and rinsed with isopropanol in order to remove oil contamination and dust remaining on the wire surface. Afterwards, Ag wire is immersed in 30% NaClO (Clorox bleach) solution for half an hour. Then, the wires are rinsed with deionized water and isopropanol.

If the electrode surface is unclean or corroded, the previous layer of AgCl can be gently removed by a sandpaper and a new layer of AgCl can be formed onto it by immersing them within the bleach solution.

These prepared electrodes are embedded within PEEK connectors as shown in figure 3.5a. The PEEK connectors are connected to the custom made flow cell as described above. This allows us to remove and replace the electrodes easily when it is required. The electrodes are kept in bleach solution for 10 minutes every day before starting a new experiment.

Chapter 4

Cell operation

Contents

In the last chapter, we have presented the custom made cell which can adapt various kind of samples e.g. soft organic membrane or solid state nanopore or nanochannel sample to study electrokinetics. Prior to using it for studying nanofluidic transport, this cell needs to be tested first, from the point of view of controlling and measuring current fluxes under the three driving forces, pressure difference, chemical potential gradient or potential gradient. In this chapter, we first study the conductance and electrical impedance of the bare cell without sample, but equipped with the Ag/AgCl electrodes. Afterwards, we test the cell with a commercially available inexpensive well-known Nafion membrane, whose electrokinetic properties are available in the literature [37].

4.1 Estimation of the cell resistance

The overall conductivity of the cell equipped with the sample depends basically on

- the resistance of the nanopore/nanochannel or the membrane under test,

- the resistance of the electrolyte solutions,

- and on the shape and position of the two electrodes.

Depending on the resistance of the sample under investigation and the resistance of the solution, there is a voltage drop across the sample as well as a voltage drop due to the solution resistivity. In order to study the characteristics of a sample, it is required to have an estimation about these resistances.

4.1.1 Conductivity of potassium chloride electrolyte

The conductivity of an electrolyte solution is usually determined by its molar conductivity defined as the conductivity per molar concentration of solution. The molar conductivity of an electrolyte depends on its concentration non-linearly and is modelled theoretically by the well known Kohlrausch's law [36]:

$$\Lambda_m = \Lambda_m^o - K\sqrt{c} \tag{4.1}$$

where, Λ_m^o is the molar conductivity at infinite dilution, and c is the molar concentration.
The experimental values of the molar conductivity (Λ_m) at 25°C for KCl electrolyte, in the range of concentrations between 0.5 mM-1 M are tabulated in table 4.1 extracted from the ref [36]. In the following we interpolate these values to estimate the KCl electrolyte conductivity.

Table 4.1: Molar conductivity of KCl electrolyte (Λ_m in S.mol^{-1}.cm^2) for concentrations from 1 molar to 0.5 mM taken from ref. [36]. Conductivity of the electrolyte, σ_{el} in S.cm^{-1}.

Concentration(M)	Λ_m(S.mol^{-1}.cm^2)	σ_{el}(S.cm^{-1})
1	112	0.112
0.5	117	0.585
0.2	122	0.0244
0.1	129	0.0129
0.05	133	0.00665
0.01	141	0.00141
0.005	143	7.15×10^{-4}
0.001	147	1.47×10^{-4}
0.0005	148	7.4×10^{-5}

4.1.2 Cell resistance in the absence of sample

Here, two approaches for estimating the cell resistance are presented. The first approach is based on calculating the resistance of the bulk solution considering

planer electrodes placed on the walls of the cell as shown in figure 4.1a In this configuration, the cell resistance is calculated from $R_{sh} = 2h/(\sigma_{el}A)$, where 2h is height of the cell ($h = 7$ mm) and A is the area of electrode equal to the cross section of the cell of diameter 6 mm. This estimated cell resistance R_{sh} is tabulated in table 4.2.

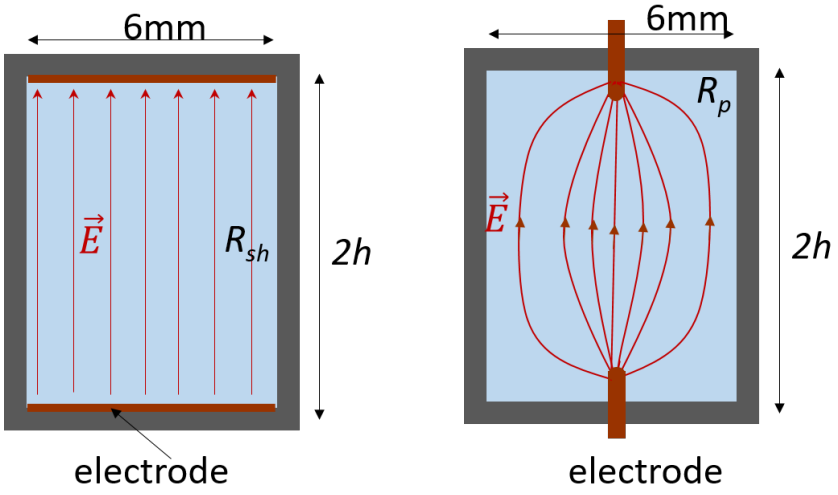

(a) (b)

Figure 4.1: Schematic showing distribution of electric field with (a) two planar electrodes placed in plane of the top and bottom wall of the cell and (b) two cylindrical electrodes pointing towards each other.

The second approach is based on positioning two cylindrical electrodes pointing towards each other within the cell as shown in figure 4.1b. For simplicity, the electrodes can be assumed as point electrodes. The field lines converges or diverges towards the hemispherical tip of the electrode of diameter 0.25 mm (figure 4.1b). The current density across this half hemispherical surface is given as follows:

$$\vec{j} = \sigma_{el}\vec{E} \Rightarrow \frac{I}{2\pi r^2} = -\sigma_{el}\frac{dV}{dr} \tag{4.2}$$

The expression of the potential difference between this surface and infinitely placed point ie. $r >> r_{elect}$, is given by integrating above equation from $r = r_{elect}$ to $r = \infty$:

$$V(r) = \frac{I}{2\pi r_{elect}\sigma_{el}} = I \times R \tag{4.3}$$

where, $R = 1/2\pi r_{elect}\sigma_{el}$. This gives an expression for the cell resistance R_p,

$$R_p = 2R = \frac{1}{(\pi r_{elect}\sigma_{el})} \tag{4.4}$$

The value of the cell resistance R_p is calculated for each concentration taking into account the electrolyte conductivity from table 4.1 and the radius of the electrode, r_{elect}=0.25 mm. It is tabulated in table 4.2.

Table 4.2: The cell resistance values calculated for planar electrode approach (R_s) and point electrode approach R_p.

Concentration(M)	R_{sh} (Ω)	R_p (Ω)
1	44	114
0.5	84	218
0.2	202	522
0.1	384	988
0.05	744	1915
0.01	3512	9030
0.005	6926	17806
0.001	16842	86600
0.0005	33684	1.72×10^5

In the whole thesis, two types of samples are studied: a commercially available Nafion membrane (in the present part of the thesis) and solid state single nanochannel samples (in part III of the thesis).

The resistance of the nafion membrane is less than few ohms and is always smaller than that of the bare cell resistance, calculated from the above two approaches. To the contrary the solution resistance is negligible in the case of a nanochannel whose resistance lies in the $G\Omega$ range (see chapter 6 in part III). Therefore, the cell is actually appropriate to study nanochannels without significant corrections due to ions transfer in the reservoirs. In the case of membranes, these effects will dominate the current intensity. Nevertheless, we proceed in testing the cell with a Nafion membrane in order to check the validity of our estimations for the cell resistance and to qualify the operation of the cell.

4.2 Measurement of the cell electrochemical impedance

Experimental set-up and modeling: The cell conductivity in the absence of any sample is measured by AC impedance measurements. The concentration of KCl solution is 1 Molar during the experiments. A load resistance R_L is connected to the electrochemical cell in series as shown in figure 4.2. A small AC excitation signal V_e of amplitude 4mV and 10mV is applied within a range of frequency 10Hz-100kHz, by a lock-in amplifier, Stanford Research SR830. The response is an AC current within the circuit, resulting in an AC voltage drop V_o across the resistor R_L. This voltage, V_o is measured by the input terminal of the Lock-in. A Labview program is built in order to apply a frequency sweep between 10 Hz-100 kHz and to record the voltage (V_o) across R_L.

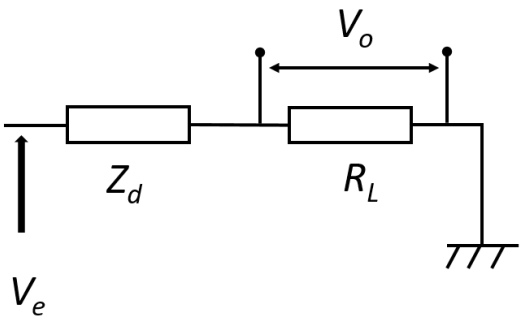

Figure 4.2: Circuit diagram of the cell of impedance Z_d in series with a load resister R_L. V_e is the AC voltage applied to the circuit and V_o is the output voltage to be measured across the load R_L.

Following the circuitry, the impedance of the cell Z_d can be evaluated as follows:

$$Z_d(\omega) = \left(\frac{V_e(\omega)}{V_o} - 1\right) R_L \tag{4.5}$$

where ω is the angular frequency. Separating real and imaginary parts of the device impedance:

$$Re\,(Z_d) = \left(\frac{V_e(\omega)(V_o)_r}{(V_o)_r^2 + (V_o)_i^2} - 1\right) \times R_L,\ Im\,(Z_d) = -\left(\frac{V_e(\omega)(V_o)_i}{(V_o)_r^2 + (V_o)_i^2}\right) \times R_L \tag{4.6}$$

The absolute value of the impedance can be calculated as $\mid Z \mid = \left[Re\,(Z_d)^2 + Im\,(Z_d)^2\right]^{1/2}$.

Results and discussion: Figure 4.3 represents a Nyquist plot, where the opposite of the imaginary part of the cell impedance is plotted against its real part (figure 4.3a) and a plot of the phase shift vs frequency (figure 4.3b). At high frequencies typically higher than 10 kHz, negative values in the real part of impedance are observed (figure 4.3a). These negative values are not physical, they are probably due to the impedance of the coaxial cable which was not taken into account in the model (figure 4.2). For the moment, we neglect the frequencies higher than 10k-Hz and focus on the linear part of figure 4.3a.

The Nyquist plot, figure 4.3a is typical of a finite resistance in series with a Warburg impedance Z_W. Warburg impedance is a purely diffusional impedance which can not be ignored at small frequencies because ions are not able to diffuse from the bulk to the electrode interface fast enough at small frequencies [36].

The frequency dependence of Warburg impedance is $(i\omega)^{-1/2}$, equation (3.1). This frequency dependence is not usually observed in experiments. Electrode impedances display more general power laws, named "constant phase element", corresponding to:

$$Z_{CPE} = \frac{1}{Y_0\,(i\omega)^n} \tag{4.7}$$

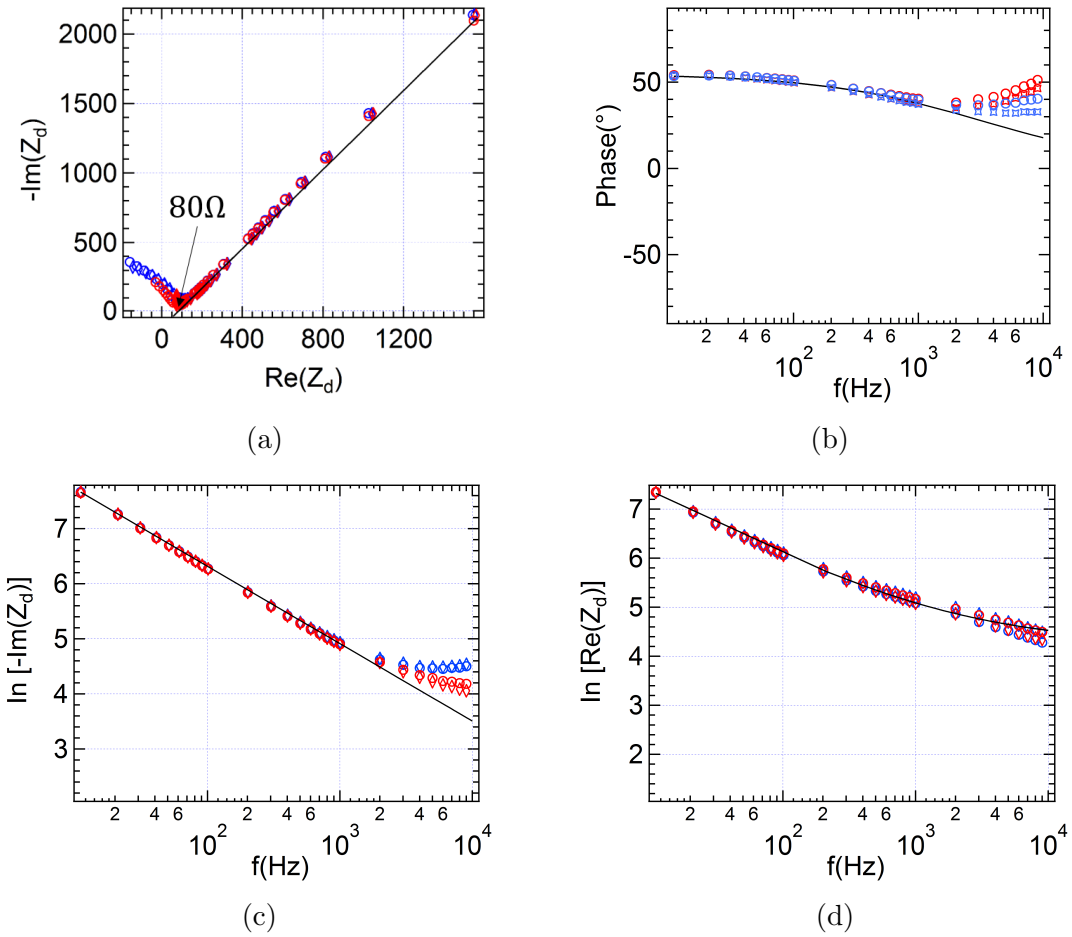

Figure 4.3: Impedance of the cell filled with 1 molar KCl concentration, measured with a load resistance R_L=10 kΩ. Blue symbols: V_e=4 mV, red symbols: V_e=10 mV. The black continuous line corresponds to a model with a constant phase element in series with solution resistance, see eq. (4.8). (a) Nyquist plot, (b) phase versus frequency, (c) natural logarithm of opposite of Im(Z_d) vs frequency and (d) natural logarithm of Re(Z_d).

with $1/2 < n < 1$. There are various models providing such constant phase elements [38], usually involving the roughness of the electrode surface. In our experiment, we find that the cell impedance is well described as:

$$Z = R_{elec} + 1/(Y_0(i\omega)^n) \tag{4.8}$$

with n=0.61 and Y_0=2.9×10^{-5}. This expression is plotted as a continuous black line in figure 4.3.

Note that the offset term R_{elec} which is obtained at large frequencies when the diffusion layer is negligible, should be the pure electrolyte resistance in the cell. This value is obtained from the intercept of the Nyquist plot with the x-axis. We find R_{elec} is 80 Ω.

The value of the solution resistance obtained experimentally can be compared to the expected value of the solution resistance ie. R_{sh} or R_p, from table 4.1. We found the values of R_{sh} and R_p to be 44 Ω and 114 Ω respectively. In reality, the

electrodes are cylindrical wires of 0.5 mm diameter pointing towards the sample. Therefore, it is expected that the cell resistance should lie in between 44 Ω and 114 Ω. Our experimental determination is in excellent agreement with this estimation.

We can conclude that, the fluidic cell behaves as two elements in series; the resistance of the electrolyte R_{elect} which can be estimated from the two approaches presented in earlier section, and the electrodes impedance $Z_{electrodes} = 1/(Y_0(i\omega)^n)$, with n=0.61 and Yo=$2.9\times10^{-5}$ USI.

4.3 Electrokinetic transport in a Nafion membrane

Here, we test our cell with a sample which is inexpensive, a Nafion membrane displaying electrokinetic and diffusio-osmosis properties.

Nafion membrane Nafion is a perfluorosulphonated polymer widely used in a variety of applications [39], and best known being used in fuel Cells [40]. A large amount of work has been carried out in view of elucidating the various properties of these membranes. Nafion membranes are identified based on the variety of their thicknesses. In fuel cells they are use as proton exchange membranes, permitting hydrogen ion transport while preventing electron conduction. They feature selective permeability to water and small cations, in particular protons [41]. Nafion 117, Nafion 115, Nafion 212 and Nafion 211 membranes are types of non-reinforced films where the numbers after the name is related to their thickness. The structure building blocks are the same for each kind of membrane.

Various models have been proposed in order to describe the structure of the Nafion membranes [41]. It has been explained in terms of cluster channels or cluster network model with narrow channels [42, 43]. The presence of a connected network of rod-like nanochannel structure has been also proposed [44, 45]. Although the

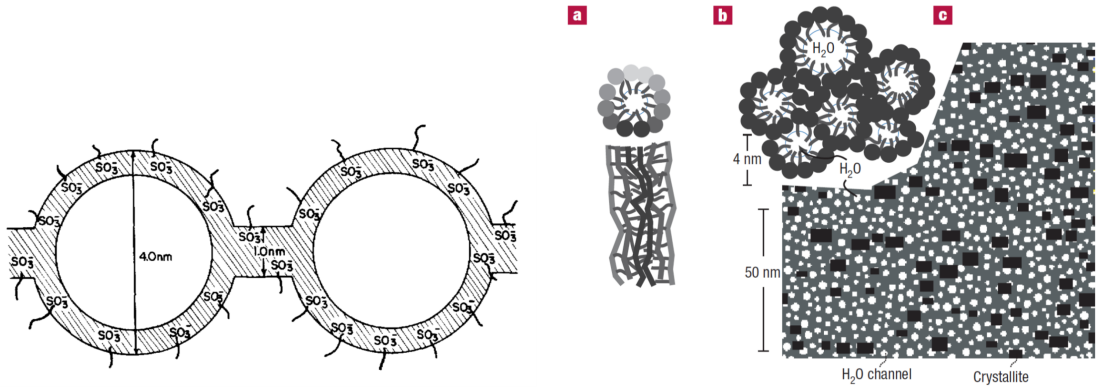

(a) (b)

Figure 4.4: (a) Cluster network model described in [43] and (b) parallel cylinderical nanochannels model presented by Schmidt *et al.*[46]

detailed structure of Nafion is controversial, recent measurements based on small-

angle X-ray scattering and nuclear magnetic resonance carried out by Schmith *et al.* have revealed the presence of parallel water nanochannels of diameter ranging between 2-5 nm, figure 4.4 from ref. [46]. Despite the differences in the structure presented by various groups, there is a general agreement on the fact that fluid transport occurs through an interconnected network of nanopores having diameters between 2 to 5 nm. This allows one to study the electrokinetic properties of these membranes as illustrated in ref. [37].

When a Nafion membrane is mounted on the cell, it is equivalent to a 1D geometry because all the area in cell including membrane is conducting, figure 4.5. The conductivity of Nafion 112 membrane from literature is known to be 0.1 S.cm^{-1} [47]. Taking into account the area of the membrane equivalent to the cross section area of our experimental cell (0.283 cm^2) and the thickness of the membrane 60 μm, the resistance of the Nafion 112 membrane is estimated to be R_m=0.2 Ω.

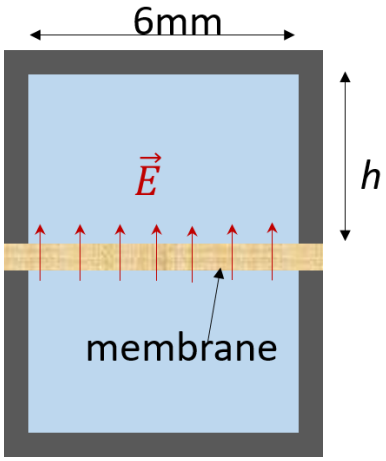

Figure 4.5: Schematic showing the distribution of the electric field within a Nafion membrane when mounted on the cell.

Cleaning procedure of Nafion membranes: A Nafion-112 membrane has been bought from Ion Power Inc. (USA). The thickness of the membrane is 50 μm. The membrane is cut into small circular pieces of 12 mm diameter. These pieces are cleaned following the chemical treatment described in [48]. First these pieces of Nafion are boiled in 3% H_2O_2 (from Sigma Aldrich) solution for 60 minutes in order to remove possible cations (K^+, Na^+) occupying the SO_3^- sites. Then the membrane pieces are immersed in boiling water for 15 minutes. After washing the membrane pieces thoroughly with deionised water, the membranes are treated with 0.5 M H_2SO_4 water solution at 90°C for 60 min. Finally, they are washed and boiled again with deionized water three times. The membrane pieces are dipped into deionized water until using them for experiments. When the membrane is cleaned it looks transparent as shown in figure 4.6.

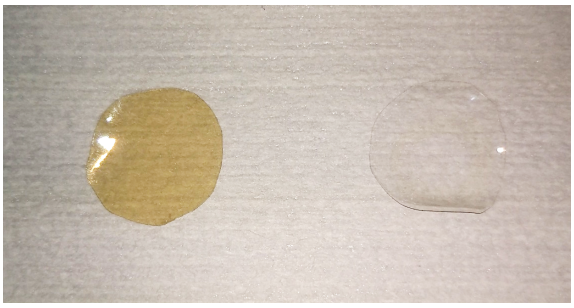

Figure 4.6: Nafion 112 membranes: before cleaning (on the left) and after performing the cleaning procedure (on the right).

4.3.1 Streaming voltage and current measurements

Measurements of the streaming voltage and current due to a pressure driven flow across a piece of membrane are performed at 100 mM KCl concentration. At first, the voltage between the electrodes is measured in the absence of applied pressure, and then a pressure is applied in one step for the duration of 1-3 minutes, figure 4.7a. Three sets of experiments are performed in the same manner and a mean value of the streaming voltage is calculated and plotted against the applied pressure as seen on figure 4.7b. From this experiment, the measured streaming potential is found to increase linearly with the applied pressure, with a value of the electro-osmotic coefficient $S_{str} = 352$ μV/bar. We find that this value is in close agreement with the one reported in the review [37].

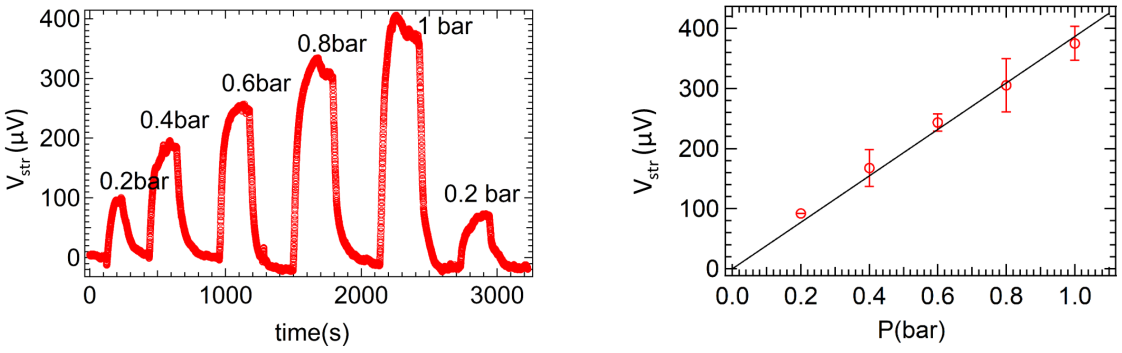

(a) (b)

Figure 4.7: Evolution of the streaming voltage measured across the membrane for 100 mM KCl as a function of (a) time and (b) pressure applied across the membrane. The black line is a linear fit with slope 352 μV/bar.

In another experiment, the output current I_o generated by an applied pressure is measured. Figure 4.8 shows the output current as a function of the applied pressure. The linear dependency corresponds to a coefficient of 0.122 μA/bar.

In these experiments the membrane can be modelled as an active element in series with a cell resistance R_c (taking all effects into account). The electro-kinetic

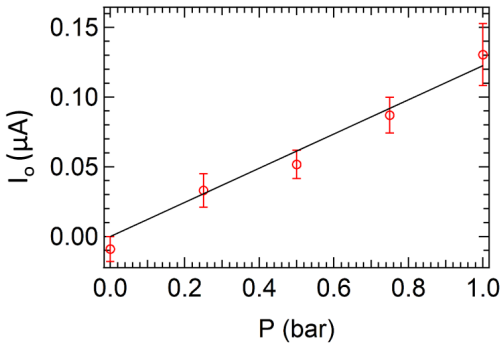

Figure 4.8: The current generated by an applied pressure was measured, for a 100 mM KCl electrolyte solution as a function of the pressure applied across the membrane. The black line is a linear fit with slope 0.112 μA/bar.

transport across the membrane writes

$$I = I_o = I_{str}\frac{R_{ch}}{R_{ch}+R_c} - \frac{V_m}{R_{ch}+R_c} \tag{4.9}$$

with $I_{str} = S_{str}\Delta P$ the electro-kinetic streaming current source and R_{ch} the membrane resistance.

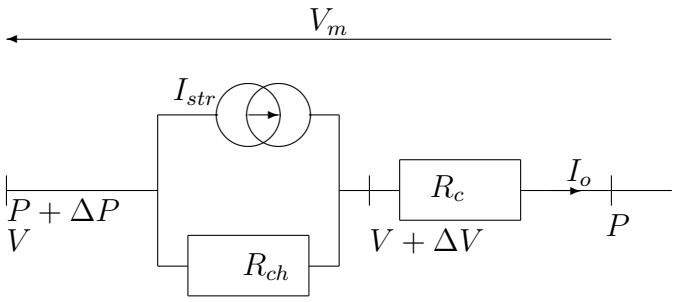

Figure 4.9: Electrical equivalent circuit of the cell during streaming voltage and current measurements.

In the streaming voltage measurement, the circuit is left opened so that $I = 0$. Then the measured voltage is $V_m = -\Delta V$ and the coefficient $\Delta V/\Delta P = S_{str} = 352$ μV/bar. In the current measurement, the circuit is effectively shortcut, so $V_m = 0$ and $\Delta V = R_c I_o$. One measures then $I_o/\Delta P = S_{str}/(R_{ch}+R_c) = 0.122$ μA/bar. The ratio between the two coefficients is 2885 $\Omega = R_{ch} + R_c \simeq R_c$, which is close to the value of the cell resistance R_p for 100 mM concentration in table 4.2.

These experiments demonstrate the use of our set-up for streaming voltage and current measurements.

4.3.2 Stability of measurements under salinity gradients

An experiment is performed in order to probe the stability of voltage measurement when a concentration difference is applied across the membrane. The open circuit voltage across Ag/AgCl electrodes is measured as a function of time with an acquisition rate of 30 points/s. Figure 4.10 represents the open circuit voltage variation with time. In the absence of flow applied on both sides of the membrane (figure 4.10a), the open circuit voltage (V_m) drops quickly with a rate of 0.2 mV/s presumably due to concentration polarization. When a flow of about 30 mL.min^{-1} is applied on both side of the membrane, the measured voltage V_m is stabilized with a small negative drift of about 0.23 μV/s. This experiment demonstrates the requirement of a continuous constant flow on both sides of the membrane for experiments involving a salinity gradient across the membrane. For this purpose a peristaltic pump is used in order to circulate the electrolytes continuously with a constant flow rate of about 30 mL.min^{-1}.

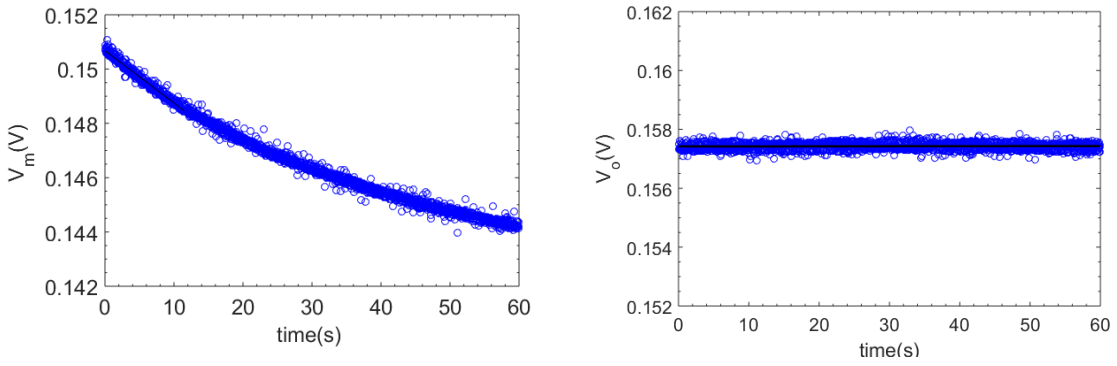

(a) (b)

Figure 4.10: The open circuit voltage measured for c_1=100 mM, c_2=2.5 mM, (a) without circulation of electrolytes and (b) with circulation of about 30 mL.min^{-1} on both sides of the membrane. The black line is a linear fit evaluating the drift in measurement.

4.3.3 Diffusion potential measurements: static approach

A concentration difference across the membrane is applied by flowing two concentrations c_1 and c_2 of KCl electrolyte in cell and the potential difference across the electrodes is measured. As the current flowing in the circuit is zero, it is called static approach.

In these experiments, an osmotic pressure given by Van't Hoff equation $p_o = 2kT\Delta n$ with n the concentration in m^{-3}, exists across the membrane, case:3 in chapter 1. Recalling the equation (1.43) of electromotive force in this particular case:

$$\varepsilon_s = \frac{L_{CE}}{L_{EE}} kT\Delta \ln c - \frac{L_{EP}}{L_{EE}} \Delta p_o = \frac{L_{CE}}{L_{EE}} kT\Delta \ln c - S_{str}\Delta p_o$$

The experimentally measured streaming voltage coefficient $S_{str} = 352\ \mu V/\text{bar}$ in the earlier section, allows us to estimate the contribution of the second term in the above expression of the electromotive force. For instance, for a ratio of concentration 100:2.5 the osmotic pressure is calculated to be 4.8 bar resulting in the second term in the above equation 4.3.3 equal to 1.7 mV. It is 2% of the value of diffusion potential (80 mV) we obtained experimentally, that we are going to see later on. This means that the osmotic contribution to the measured diffusion voltage across the membrane is negligible. Therefore, the potential difference across the membrane is equal to the diffusion potential $\varepsilon_s = V_{diff}$, case:2, equation (1.38):

$$V_{diff} = (2t_+ - 1)\,\frac{kT}{e}\Delta \ln c \tag{4.10}$$

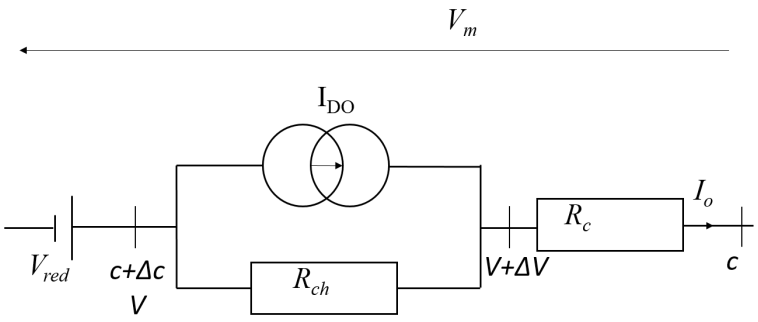

Figure 4.11: Electrical equivalent circuit of cell during diffusion potential measurements across the membrane.

During the experiments, the concentration c_1 is fixed to 100 mM and c_2 is varied from 2.5 mM-70 mM. In these experiments the membrane can be modelled as an active element in series with a cell resistance R_c and redox potential V_{red}. The electro-kinetic transport equation of current can be written as

$$I = I_o = \frac{I_{DO}R_{ch} + V_{red}}{R_{ch} + R_c} - \frac{V_m}{R_c + R_{ch}} \tag{4.11}$$

with R_{ch} the membrane resistance, I_{DO} the diffusio-osmotic current source and V_{red} the redox potential build up on the Ag/AgCl electrodes due to an unequal chloride concentration, with a thermodynamic expression given by:

$$V_{red} = \frac{kT}{e} \ln \frac{\gamma_1 c_1}{\gamma_2 c_2} \tag{4.12}$$

with γ_1 and γ_2 the mean activity coefficients of ions. For an open circuit configuration the effective current $I_o = 0$, results in:

$$V_m = I_{DO} \times R_{ch} + V_{red} = V_{diff} + V_{red} \tag{4.13}$$

with $V_{diff} = I_{DO} \times R_{ch}$.

The values of the redox potential are tabulated in table 4.3, taking into account the mean activity coefficients from references [49, 50, 51]. The diffusion potential is calculated by subtracting the redox potential from the experimentally measured voltage. Each experiment is repeated three times and a mean value and standard deviation of measured voltage across the electrodes is calculated (table 4.3).

Table 4.3: Mean activity coefficients of KCl electrolyte from reference [49, 50, 51] and redox potential V_{red} of Ag/AgCl electrodes calculated from equation 4.12. V_m is the measured voltage across the electrodes in open circuit configuration. V_{diff} is the diffusion potential calculated from equation 4.13.

C_1 (mM)	C_2 (mM)	γ_1	γ_2	V_{red} (V)	V_m (V)	V_{diff} (V)
100	70	0.816	0.830	0.0088	0.0194± 0.0002	0.0066± 0.0002
100	50	0.816	0.850	0.0169	-	-
100	35	0.816	0.872	0.0254	0.0486± 0.0002	0.0191± 0.0002
100	10	0.816	0.927	0.0554	0.1065±0.0008	0.0462± 0.0008
100	5	0.816	0.947	0.0737	0.14±0.002	0.0623± 0.002
100	2.5	0.816	0.961	0.0913	0.174±0.001	0.0787± 0.001
100	1	0.816	0.971	0.115	-	-

Figure 4.12a shows the diffusion potential extracted from the measured potential as a function of the concentration ratio. As expected from eq. (4.10), the dependency of V_{diff} with $\ln(c_1/c_2)$ is essentially linear. From the slope of the best linear fit (0.021 V), we find an average transference number t_+=0.91, which is consistent with the transference number 0.89 given in literature [52] for Nafion 112 membrane. This shows that the Nafion membrane is indeed highly selective and that the flux of Cl^- ions across it is negligible compared to the one of the cations.

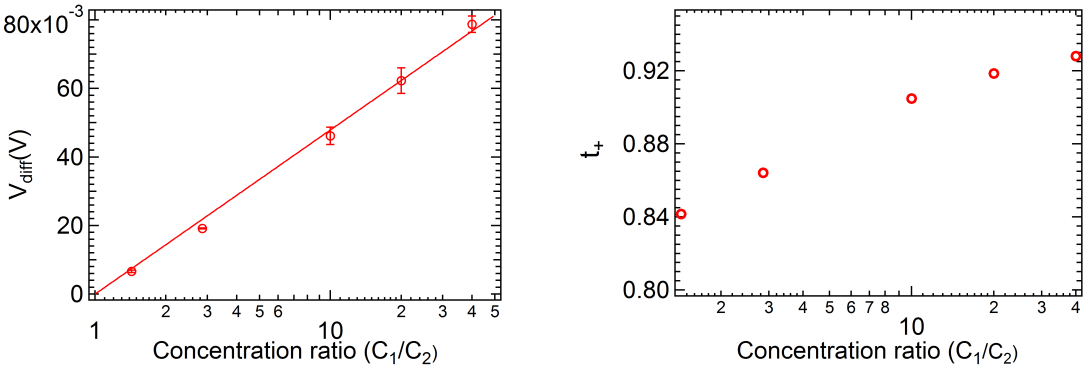

(a) (b)

Figure 4.12: (a) Variation of the diffusion potential with the ratio of concentration. The red line is a linear fit. (b) Variation of the local value of the transference number calculated from equation (4.14), with the concentration ratio.

Finally, using the same equation, we can calculate a local value of the transference

number t_+ as follows:

$$t_+ = \frac{1}{2}\left[V_{diff}\left(\frac{kT}{e}\Delta \ln c\right)^{-1} + 1\right] \tag{4.14}$$

We find a small increase in t^+ as a function of the salinity gradient (see figure 4.12b). Increasing the concentration ratio is indeed diminishing the concentration c_2 from 70 mM to 2.5 mM, while concentration c_1 remains 100 mM. The increase in the t_+ value in figure 4.12b is consistent because the influence of the surface charge on ion transport are more pronounced with decrease in the ion concentration c_2 which leads to increased ion selectivity. In other words, the Dukhin length increases with decrease in concentration. Usually, ion selectivity of nanochannel is dependent on the Dukhin length $l_{Du} \sim \frac{|\Sigma|/e}{n_o}$, where Σ is the surface charge density, e is elementary charge and n_o is the ionic concentration in m^{-3} [53]. This length characterizes the channel scale below which surface conductance dominates over the bulk conductance. If the size of the membrane pores or nanometric channels are smaller than the Dukhin length, the conductance within the membrane is dominated by surface properties, implying larger transference number.

4.3.4 Diffusion potential measurements: dynamic approach

Here in this section we study the electrical current generated by the salinity gradient. For this, four KCl concentrations of 100 mM, 50 mM, 10 mM and 1 mM are prepared and filtered with a standard nylon syringe filter of 0.2 μm pore size. At first, the higher concentration is fixed at 100mM on one compartment of the cell and the lower concentration is varied from 1 mM to 10 mM and 50 mM. The Ag/AgCl electrodes embedded within the fluidic cell are connected to a load resistance (R_L). The current generated by salinity gradient flow in circuit and a voltage drop across the load is measured with a Keithley multimeter, Series 2750. A continuous flow of electrolyte is applied during each experiment by a peristaltic pump in order to reduce the effects due to concentration polarization.

The load resistance is varied from 50 Ω- 1 MΩ for each ratio of concentration and a mean value of the voltage is evaluated for an experiment of about one minute. These mean values of measured voltages are plotted against the load resistance. In this approach the current I_o generated from the cell, is never zero, therefore, we call it a dynamic measurement.

Figure 4.14 represents the three experimental graphs each corresponding to the three concentration ratios, 100 mM: 50 mM, 100 mM: 10 mM and 100 mM:1 mM.

We use the equivalent electrical circuit depicted in figure 4.13. The equation of the current in the circuit is given as follows:

$$I_o = \frac{R_{ch}I_{DO} + V_{red}}{R_L + R_{ch} + R_c} \tag{4.15}$$

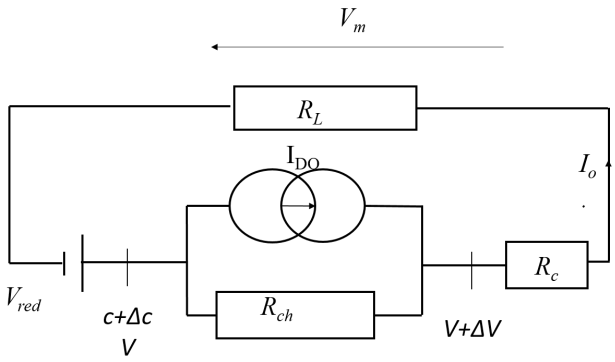

Figure 4.13: Equivalent circuitry of the cell equipped with the nafion membrane under salinity gradient.

Consequently, the output voltage across the load resistance R_L is:

$$V_m = I_o \times R_L = \frac{R_L}{R_L + R_{ch} + R_c} (R_{ch} I_{DO} + V_{red}) \tag{4.16}$$

This equation can be reformed into the following equation:

$$V_m = \frac{R_L}{R_L + R_d} (I_{DO} R_{ch} + V_{red}) \tag{4.17}$$

with $R_d = R_{ch} + R_c$ named as device resistance.

In figure 4.14, the behavior of the voltage vs load resistance can be understood from equation (4.16) intuitively. For small values of load resistance ($R_L << R_d$), most of the current flow across R_L. Therefore, the current I_o in outer circuit is given by:

$$I_o = \frac{R_{ch} I_{DO} + V_{red}}{R_d} \tag{4.18}$$

For large values of load resistance ($R_L >> R_d$) a big amount of the current I_{DO} generated by the Nafion membrane is flowed back in the membrane itself. In this situation from equation (4.17), the measured voltage is given by:

$$V_m = V_{red} + R_{ch} \times I_{DO} = V_{red} + V_{diff} \tag{4.19}$$

A fitting function presented by the equation (4.17) is used to fit the experimental points in figure 4.14. In this fitting function, the redox potential values are evaluated from the references [49, 50, 51] and tabulated in table 4.3. The coefficients V_{diff} and $R_d = R_c + R_{ch}$ are the two fitting parameters, evaluated for each set of concentration. These values are tabulated in table 4.4.

Figure 4.15 represents the variation of diffusion potential with respect to the ratio of concentration c_1/c_2 (c_1=100 mM). The value of V_{diff} evaluated from these experiments in dynamic approach are plotted in blue diamonds and the value of V_{diff} from static approach, described in previous section are plotted in red circles. The diffusion potential values measured in two different experimental approaches

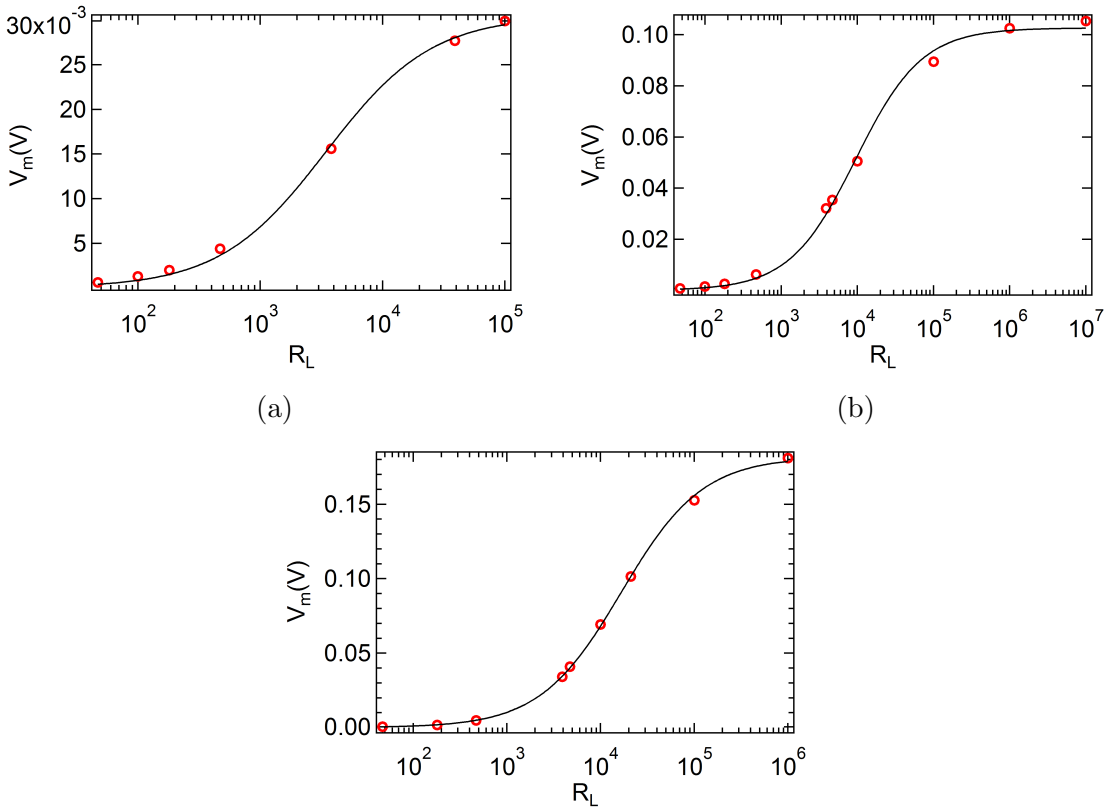

Figure 4.14: Measured voltage across the load resistance. The concentration differences across the membrane are (a) c_1=100 mM, c_2=50 mM, (b) c_1=100 mM, c_2=10 mM, (c) c_1=100 mM, c_2=1 mM. On each plot, the black continuous line is the best fit with eq. (4.17). The values of the fitted parameters are listed in Table 4.4

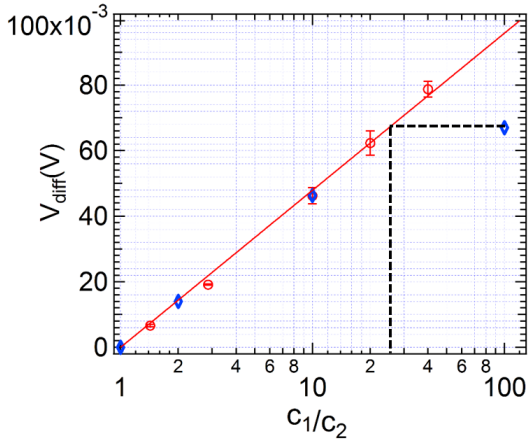

Figure 4.15: Variation of V_{diff} with ratio of concentration. The blue diamonds are the experimental points from dynamic approach and red circles are experimental points from static approach experiment (section 4.3.3). The red line is a linear fit on red data points.

are found to be coinciding each other, following a linear trend with a slop of 0.02 V

Table 4.4: The values of fitting coefficients V_{red}, V_{diff} and R_d and the calculated value of the transference number t_+ and diffusio-osmosis current I_{DO}. The value of V_{red} is calculate from equation (4.12) and V_{diff} and R_d are obtained by fitting equ. (4.17). The value of t_+ is calculated from equation (1.38), I_{DO} is calculated taking into account the resistance R_{ch}=0.2 Ω for Nafion 112 membrane from literature [47].

Conc. ratio	V_{red}	V_{diff} (V)	$R_d(\Omega)$	t_+	$I_{DO}(A)$
100:50	0.0169	0.014±0.0005	3436±264	0.91	0.07
100:10	0.0554	0.0463 ±0.0014	9480±590	0.92	0.22
100:1	0.115	0.067±0.0014	16620±432	0.80	0.32

with $\ln(c_1/c_2)$. This is in good agreement of the value of slop 0.021 V, obtained in static approach. These measurements shows the robustness of our cell.

As seen in the same figure at concentration ratio 100:1, V_{diff} does not follow the linear behavior. This could be attributed to the effect of concentration polarization.

Indeed, as ions are transported through the membrane, a concentration flux occurs in the same time as the current flux. This concentration flux has to be evacuated by diffusion in each half cell. This requires a concentration gradient essentially similar in each half cell, and therefore, a difference Δc in the concentration very close to the membrane with respect to the nominal one imposed by the feeding flow. Because of this concentration polarization, the real driving force is kT/e $\ln(c_1 - \Delta c)/(c_2 + \Delta c)$. When Δc becomes of the same order of magnitude as c_2, the magnitude of the driving force is significantly reduced, leading to a sub-linear growth of V_{diff} with respect to $\ln(c_1/c_2)$.

From figure 4.15, when the nominal concentration ratio is 100, we obtained a diffusion potential of 0.067 V experimentally. If the growth of V_{diff} was linear in $\ln(c_1/c_2)$, this value of V_{diff} would have been observed for a concentration ratio of 30 (see figure 4.15). This corresponds to a value of the concentration close to the membrane in the lower concentration reservoir, equal to 3 mM instead of 1 mM.

The value of device resistances R_d, tabulated in table 4.4 can be compared with the estimated values R_p from table 4.2. The values obtained for ratio of concentrations 100:50 and 100:10, are quiet close to the estimated values. For concentration ratio 100:1, device resistance R_d is much lower than the estimated resistance 85 kΩ. This discrepancy could be also due to concentration polarization. If the concentration has been increased from 1 mM to 3 mM, it results in a decrease of the resistance by a factor of about 3 (about 25 kΩ), which is comparable to the measured resistance R_d.

4.4 Discussion

Taking into account the resistance of the Nafion 112 membrane R_m=0.2 Ω from literature [47], and the diffusion potential measured in our experiments, the amount

of diffusio-osmosis current can be estimated (see table 4.4). Correspondingly, the maximum power delivered by the membrane can be calculated by $I_{DO}^2 R_m/4$. For a ratio of concentration 100:1, the maximum power that could be delivered by the membrane is estimated to be 5 mW with a 0.285 cm^2 piece of membrane. This results in a power density of $\sim$ 200 $W.m^{-2}$ which is significantly a high number as compared to the 1-7 $W.m^{-2}$, usually reported in literature, in classical reverse electrodialysis (RED) with alternative exchange membranes [17, 18, 54]. But, the power generation in RED highly depends on the spacing between the membranes. A significant part of power is dissipated due to the solution resistance, as seen in our experiments also. On the contrary, in case of a single solid state nanochannel, much higher power density upto 7 $kW.m^{-2}$ have been obtained, reported by Siria *et al.*[13] in a single boron nitride nanotube. The resistance of cell is negligible as compared to the nanotube resistance, therefore it is easier to access the intrinsic capabilities and maximum power density of a single nanopore or nanotube than that of a membrane.

Part III

An easy approach of nanochannels sample preparation

Chapter 5

Preparation of freestanding membrane and nanochannel sample

Contents

Solid state nanopores and nanochannels are well known for their application in multiple domains, particularly in biomolecule sensing such as DNA or protein [55], but also in the field of generation of electrical current [12, 56, 15, 13]. In this context they provide an ideal laboratory to study the fundamental properties of nanofluidic transport and related coupling phenomena.

The commonly used techniques employed in nanofluidics for the fabrication of nanostructures and nanochannels are illustrated in references [57, 58]. The most common nanochannel structures are parallel nanochannel arrays carved in-plane of the substrate as described by Majumdhar *et al.*[15], or nanopores milled in a thin insulating freestanding membrane as presented by Dekker *et al.*[59]. In an in-plane approach the nanochannels are etched onto the substrate via reactive ion etching technique interconnected between two micro-channels; later on closed from the top with a cover by anodic bonding. Another method for in-plane nanochannel fabrication is the so called sacrificial layer method [60, 61]. Sacrificial layers are nanometric layers, which are deposited onto the substrate of choice. These can be

etched off by wet etching, to create the void of dimensions equivalent to the sacrificial layer.

In the second approach, the nanochannels are fabricated by milling a thin free-standing dielectric membrane, supported on a substrate (silicon on insulator, SOI) [59]. These type of suspended membranes are usually prepared by wet etching. They are of particular interest to make nanochannels of short length called nanopores where the diameter of the nanochannel is comparable to its length. The small pore length makes it possible to reach large gradients in thermodynamic forces, such as voltage, concentration, or pressure difference are applied on opposite side of the membrane. The diameter of the milled nanohole is highly dependent on the thickness of the membrane. Reducing the thickness of the membrane upto 10nm can result the milled nanopores of 2 nm diameter as presented by Dekker *et al.*[59].

The freestanding membrane is also used as the basic building block to prepare a nanodevice following an approach presented in the work of Siria *et al.*[13]. In this device a separately prepared boron nitrite nanotube is inserted into a milled hole of 150 nm wide, in a 50-100 nm thick freestanding silicon nitride membrane, and the free space between the nanohole and the nanotube was blocked with Napthelne. The whole process is performed by nano manipulators under high vacuum while observing the performed steps by scanning electron microscopy. This prepared nanotube sample has been used to study electrokinetics for energy conversion applications.

From the above discussion, it can be realize that fabrication technologies do not limit the realization of nanostructures, but to access them, a connection to the macroscopic world is required. In this chapter we present a method that we have used for preparing solid state nanopores. The fabrication approach described here, allows us to prepare a sample with a single nanopore, directly connected to the macroscopic world. The overall fabrication process is performed in two steps: first, the preparation of micrometer thick freestanding silica membranes suspended over silicon by wet etching process, and second, milling a nanohole in the membrane by Focused Ion Beam technique.

This nanochannel sample is ready to be incorporated directly into the cell presented in chapter 3, figure 3.1 in order to study electrokinetic. This sample is also adaptable in the pico-flow cell that has been developed in this thesis (see part III). The novelty of this approach is that the process of the membrane fabrication can be performed under a standard chemical hood. It neither requires an ultra-clean platform such as clean room facilities, nor any sophisticated instrumentation. This makes the whole process of nanochannel sample preparation, a low-cost and time-efficient technique as a lot of the samples with suspended membranes can be prepared at once.

5.1 Preparation of freestanding silica membrane

5.1.1 Freestanding membrane sample geometry

The samples are prepared in a Silicon wafer (100) orientation p-type, 5 Ω-cm. This wafer has a thermally grown silica layer of thickness 1.5 μm on both sides. The silica layer is first grown at 950°C under steam and then annealed at 1100°C for 1 hour. The thickness of the overall substrate with silica layer is 725 μm, thick enough to be pressed between the o-rings in the cell, presented in the earlier part of the thesis.

The preparation process has been started with the etching of silica layer on one side of the sample, figure 5.1. An opening in silica layer is performed and then silicon is etched. The etching of silicon takes place in a pyramid shape with an angle of 54.7° due to anisotropic etching (explained in detail in the following section). The size of the opening in the silica layer is chosen so that the pyramid structure in silicon is truncated by the silica layer present at the bottom of the sample. From this we get a freestanding silica membrane of size a_m given as follows:

$$a_m = a_o - 2x_m = a_o - 2 \times \frac{t}{\tan(54.7^o)} \tag{5.1}$$

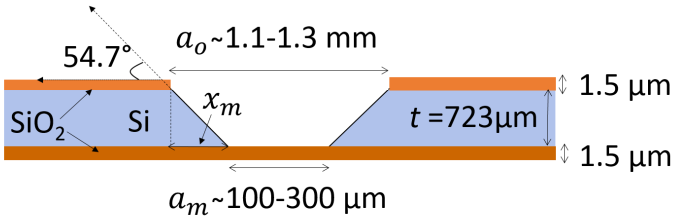

Figure 5.1: Schematic of the freestanding silica membrane suspended on silicon wafer. The size of the sample is 1.5 cm× 1.5 cm.

The size of opening in the silica layer is chosen to approximately 1.1-1.3 mm in order to end up with a silica membrane of size about 100-300 μm. A detailed protocol of preparation is presented in the following section.

5.1.2 Etching processes

The etching techniques are divided in two main categories: dry etching and wet etching. In both the techniques, etching can be isotropic or anisotropic. At first, we will introduce the isotropic and anisotropic etching and then dry *vs* wet etching technique is discussed.

Isotropic and anisotropic etching: In etching process, usually a part of the wafer is protected from the etchant by depositing a "masking" layer over the wafer.

For example, a layer of silica or silicon nitride acts as masking layer for silicon in wet etching process.

In isotropic etching the surface of the substrate is etched in all the directions (figure 5.2a). However, in anisotropic etching the sample is etched with different rates in different crystallographic planes (figure 5.2b) for example etching in silicon substrates. The bonding energy of Si atoms are different in various crystal planes. This allows the etchants (for example, TMAH and KOH) to etch silicon much faster in certain directions as compared to others [62]. On a (100) oriented silicon wafer, wet anisotropic etching produces a pyramidal structure with an angle of 54.7° with respect to the (100) plane as shown in figure 5.2b. An undercut below the masking layer usually takes place in both the isotropic and anisotropic etching, resulting in cavities with sloping sidewalls. Usually, this undercut is small in anisotropic etching of silicon substrates as it is dependent on the ratio of the etch rate for plane (111) to (100) (figure 5.2b). The higher this ratio is, the larger is the undercut.

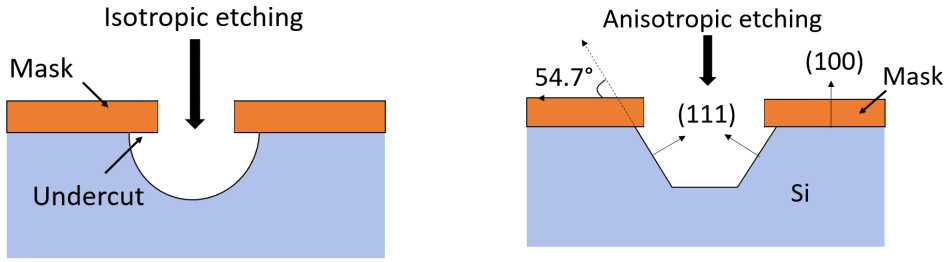

(a) (b)

Figure 5.2: Schematics showing (a) isotropic etching of any arbitrary substrate, and (b) anisotropic etching of a silicon substrate oriented towards the (100) plane. An undercut below the masking layer can be seen to form cavities with sloping sidewalls.

Dry etching: Dry etching processes are based on either high energized particles such as ions, electrons, or photon beam to etch off the substrate atoms (physical dry etching) or etchant gases which react with the substrate material and produce a dry chemical etching [63]. For example (CF_4), O_2 and N_2 are some gases used in chemical dry etching for silica or silicon nitride [64]. For performing the dry etching process, specialized conditions such as ultra high vacuum and heavy instrumentation are required.

Wet etching: In wet etching process liquid chemicals (etchants) are used to remove materials. The basic requirements in this process is a container with a liquid solution that will dissolve the material in question.

The wet and dry etching processes have unique characteristics depending on the field of requirement [65]. Performing dry etching process is an expensive process including heavy equipments while wet etching is a low cost and easy to implement

technique for selectively targeting the materials to be etched. The combined process of these two techniques is also of interest to fabricate freestanding nanoporous silicon based membranes [66] and complex 3-D structures for micro and nanofluidic applications [67]. Herein, we follow the wet etching approach for the preparation of freestanding membrane.

Selection of etching chemicals and required experimental parameters: In order to etch the silicon down to the bottom silica layer of our samples (see figure 5.1), we have to produce a hole at first in the top silica layer. This hole is produced by wet etching. Hydrofluoric acid (HF) is a good etchant, widely used in silicon wafer cleaning technology with fast and aggressive action on the oxide layers [68]. It is a solution of hydrogen fluoride in water, able to dissolves silicon dioxide according to the following chemical reaction:

$$SiO_2 + 6HF \rightarrow H_2SiF_6 + 2H_2O \tag{5.2}$$

The etch rate of silica directly depends on the concentration of HF. In this work, as we are dealing with 1.5 μm thick silica layer, a nominal concentration of the hydraulic acid of 10% volume was used, having a typical etch rate of 60 nm.min^{-1}. It takes about 30 min to etch the 1.5 μm silica layer.

For silicon, TMAH (tetramethylammonium hydroxide) is a commonly used chemical for anisotropic etching, with a typical etch rate of 0.6 μm.min^{-1} at 85°C. Usually, the etch rate of (100) plane of silicon decreases with increasing the concentration or decreasing the temperature, while the ratio of etch rates for the planes (111) and (100) increases with decreasing TMAH concentration [69, 70]. This ratio describes the undercut of the masking layer which eventually forms cavities with sloping sidewalls (figure 5.2b). Another key feature of TMAH etchant is its high selectivity for silicon as compared to silica. The selectivity is 6000 times larger for silicon compared to silica for 25% TMAH solution at 80°C. It decreases with decrement of either the temperature or the concentration of TMAH [71].

5.1.3 Protocol for membrane preparation

Cutting and cleaning of substrate: The samples are prepared in a wafer of (100) oriented silicon substrate (p-type, 5 Ω-cm), with grown silica layers as described above. This wafer has been cut into 1.5 cm×1.5 cm square pieces. At first, these pieces have been cleaned by successive sonication in soap solution, ultra pure water (18.2 MΩ.cm, Millipore) and then in isopropanol at 50°C in order to remove oil and organic residues that could remain on surfaces.

Opening of the masking layer of silica: In order to perform the very first step, opening in the masking layer of silica is required. For this an another mask is required to do an opening in the silica layer in a controlled manner.

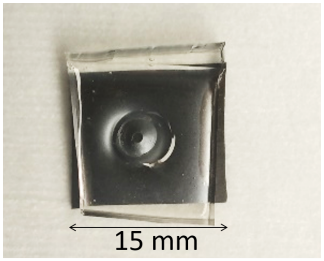

(a)

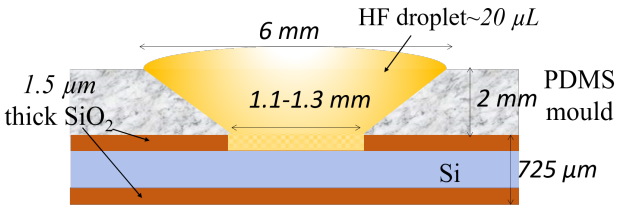

(b)

Figure 5.3: Schematic showing the PDMS mould over the silicon sample for HF etching, (a) top view and (b) a side view.

For this purpose a PDMS mould was prepared with a conically grooved center with ending diameter of 1.2 mm, as shown in the figure 5.3a. PDMS is a good candidate for this purpose because it is easy to bond it on a clean silicon substrate. The bonding is strong enough to prevent the spreading of HF sideways and hence the opening size of the silica layer is controlled. A droplet of HF 10% has been left within the mould bonded to the clean substrate figure 5.3b. This process of etching takes about 30 minutes to remove 1.5 μm thick silica and stops automatically when it reaches to silicon. After this, the samples have been washed thoroughly with deionized water. With this type of prepared PDMS mould, the opening of the silica masking layer is between 1.1-1.3 millimeters.

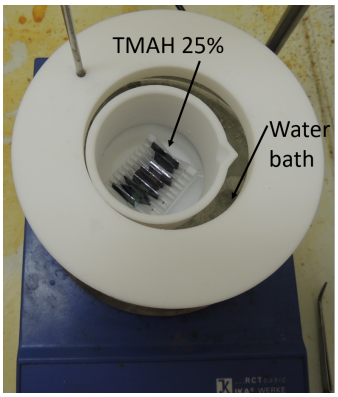

Figure 5.4: Schematic showing the experimental arrangement for TMAH manipulation in order to etch silicon.

Etching of silicon: The washed samples have been left in a beaker filled with tetramethylammonium hydroxide solution TMAH 25% (from Sigma Aldrich) to selectively etch the silicon. A small set-up has been arranged with a water bath at a regulated temperature of 85°C, as shown in figure 5.4. The samples have been kept in a teflon beaker filled with TMAH 25%, placed within the water bath. A maximum of 10 samples can be prepared at once from this experimental arrangement. At the end of the process, the samples have been washed thoroughly with deionized water,

then with isopropanol, and then dried with N_2 air. Figure 5.5 shows a micrometric

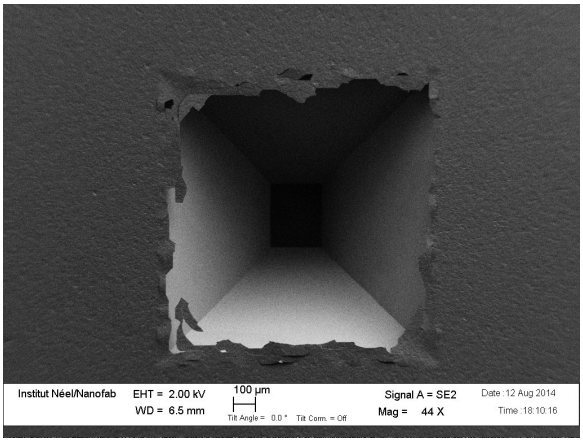

Figure 5.5: Scanning electron microscopy image of the etched sample with pyramidal cavity present in silicon and free standing silica membrane at the bottom (dark part in the middle of cavity).

view of the pyramidal well in the sample because of the anisotropic etching of silicon. At the bottom of this, there is a free standing silica membrane. With this wet etching process, it is possible to prepare membranes of various sizes with the largest edge size of about 410 μm and the minimum edge size of about 30 μm.

The size of membrane depends highly on the opening of the masking layer which is eventually decided by the opening of the conical apex in the PDMS mould. Figure 5.6 represents the microscopic view of the prepared silica membranes in a variety of sizes. The presence of a spider shaped structure in figure 5.6d is due to the stress present in the suspended membrane, as discussed in detail in the next section.

The etching process of silicon from TMAH 25% is a slow process (about 0.6 μ m.min^{-1}) and takes about 21-22 hours to reach the bottom silica layer. Although decreasing the TMAH concentration increases the etching rate of silicon, it results in defects in the silica layer as shown in figure 5.7a. These defects are of the order of 0.5 mm (maximum) and has been observed on both sides of the sample. These are not acceptable as these defects will provide an electrical leak while the sample will be used for electrokinetic experiments. In addition, most of the sample membranes have been found broken at the end of the protocol while the TMAH concentration was lowered to 10%. In order to obtain the best sample, no defect on the masking layer of silica, the typical values of the concentration and temperature have been chosen to 25% TMAH and 85°C respectively. At these parameters, also no breakage in the suspended silica membrane occurred at the end of the protocol.

All this protocol with the chemicals has been performed under a chemical hood with highly ventilated system to avoid any exposure of fumes or chemicals. All the safety regulations have been followed during the manipulation of HF 10% and TMAH 25% solutions.

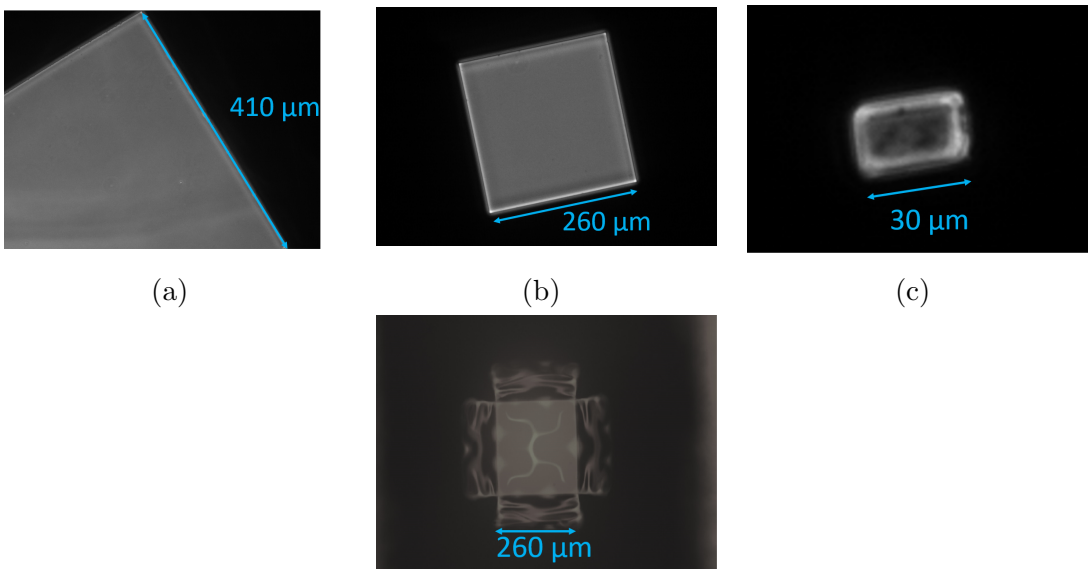

(a) (b) (c)

(d)

Figure 5.6: Microscopic images of various sized silica membranes prepared by wet etching process (a) 410 μm (b) 260 μm (c) 30 μm. (d) The presence of a spider shape structure in the membrane is due to the relaxation of stress in silica.

(a) (b)

Figure 5.7: Schematic showing a freestanding silica membrane sample (a) with defects on masking layer in red circles (etched in 10% TMAH) and (b) without defects (etched in 25% TMAH).

5.2 Shape of the membrane: a profilometry measurement

The presence of a spider shaped structure as shown in figure 5.6d has been observed for all the prepared membranes. This is due to the relaxation of stress within silica. The silica layer has been grown over silicon at a temperature of 950°C and annealed at a temperature of 1100°C for an hour. When it is cooled, the membrane is stressed due to the difference in the coefficient of thermal expansion for silicon and silica. In order to know the exact shape of this stressed membrane an optical profilometry measurement has been performed.

The bending of a membrane results from the balance between the difference of

pressure p_m across the it, and the three intrinsic mechanical contributions, namely the bending moment, the residual stress within the membrane and the straining of the neutral fiber of the membrane. For a square membrane under uniform residual stress Σ, this balance can be approximated as [72]:

$$p_m = \frac{d_m w_0}{a_m^2}\left(k_w \frac{E_m}{1-\nu_m^2}\frac{d_m}{a_{m^2}} - k_r\Sigma + k_f \frac{E_m}{1-\nu_m^2}\frac{w_0^2}{a_m^2}\right) \tag{5.3}$$

with w_0 the deflection at the center of the membrane, d_m the thickness of the membrane, a_m the width of the membrane, E_m the Young's modulus of the membrane material, ν_m its Poisson ratio and three coefficients $k_w = 62.9$, $k_r = 13.9$ and $k_f = 36.9$. In the presence of tensile residual stress, that is negative values of Σ, the membrane remains perfectly flat in the absence of difference of pressure. On the contrary in the presence of a compressive residual stress, that is positive values of Σ larger than a critical value, the membrane buckles. This buckling results in a spontaneous deflection of the membrane in the absence of pressure difference. Such a membrane is bistable as it can snap from one deflected state to the opposite state if a pressure large enough is applied to force the transition from one state to the other.

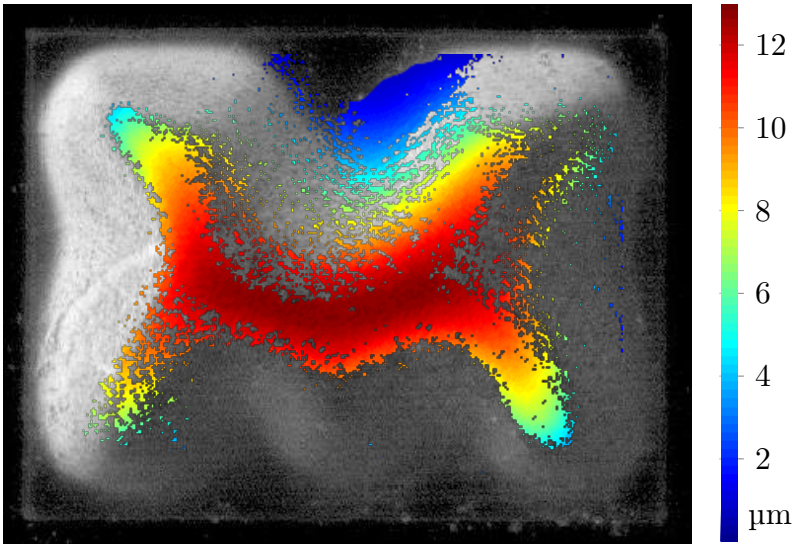

Figure 5.8: Profilometric measurement of the spontaneous deflection of a membrane superimposed on an microscopy picture of the membrane. The colorbar indicates the scale of the deflection perpendicularly to the plane of the membrane.

Our silica membrane are known to present a compressive residual stress $\Sigma = 300$ MPa while the Young modulus $E_m = 75$ GPa and $\nu_m = 0.2$ [72]. The thickness of the membrane is of the order of 1 µm while the width of the membrane is of the order of 200 µm. In this framework the contribution of the compressive stress $k_r\Sigma$ is 2 orders of magnitude larger than the bending moment $k_w E_m/(1-\nu_m^2)d_m/a_{m^2}$. The bending moment being negligible, a spontaneous buckling is observed characterized by the balance between the residual stress and the straining of the membrane

$k_f E_m/(1-\nu_m^2)w_0^2/a_m^2$. The maximum deflection w_0 of the membrane observed at its center is estimated from this balance as [72]:

$$w_0 = \sqrt{\frac{k_r \Sigma (1-\nu_m^2)}{k_w E_m}} \tag{5.4}$$

The deflection of a membrane of 312 x 228 µm^2 and 1.35 µm in thickness has been characterized by optical profilometry (Veeco profilometer) as shown in figure 5.8. The maximum measured deflection is 13 µm, which is of the same order of magnitude of the value of 11 µm obtained from the equation 5.4.

5.3 Nanochannel fabrication: focused ion beam milling

The freestanding silica membranes are milled by focused ion beam milling in the clean room NanoFab facilities, Néel Institute. The interest is to make transverse nanochannels of cylindrical as well as conical shape. Focused ion technique is based on the principle of milling the surface with a beam of ions. Usually, a focused primary beam of gallium (Ga^+) ions hits the sample surface and sputters an amount of material. As a result secondary electrons are created while Ga^+ ions raster on the sample surface. These secondary e^- are captured to form an image.

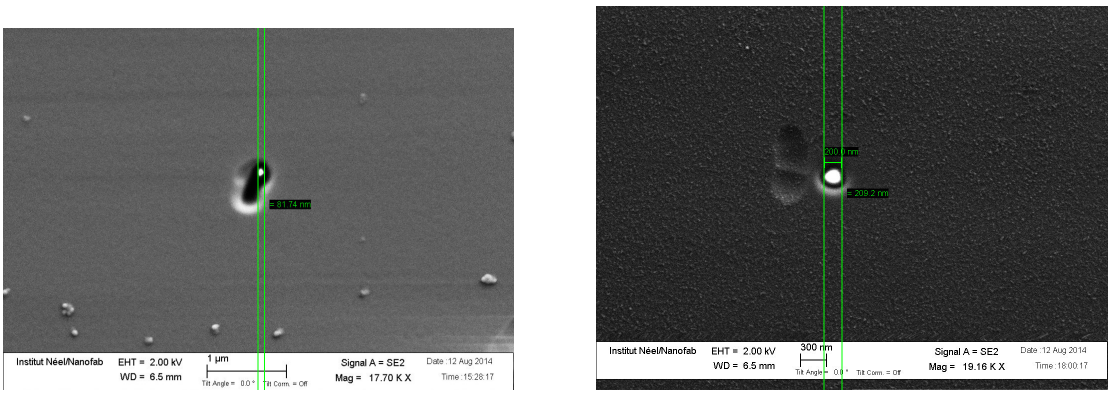

(a) (b)

Figure 5.9: (a) SEM image of a hole drilled in the silica membrane without Al coating and (b) with an Al coating of 10 nm.

Figure 5.9a shows a freestanding membrane of silica, prepared as described in the previous section and milled by FIB. The milled nanometric hole is not circular but elongated due to the deflection of the ion beam while milling. The Ga^+ ions of incident beam tend to embed into the silica membrane because of their heavy mass. This results in a coulombic repulsion between the embedded ions and the incident ions that deflects the incoming beam and results in a non circular hole.

In order to avoid this problem, it is required to coat the surface by a thin layer of metal such as aluminum (Al). This allows a uniform distribution of potential on the whole surface when Ga^+ ions are embedded.

A 10 nm thick layer of Al has been coated by sputtering machine on the sample. This coating has been etched from the sample after milling a nanohole. The presence of the nanochannel has been again verified from SEM, in order to be sure not to be blocked by some residue of etched Al.

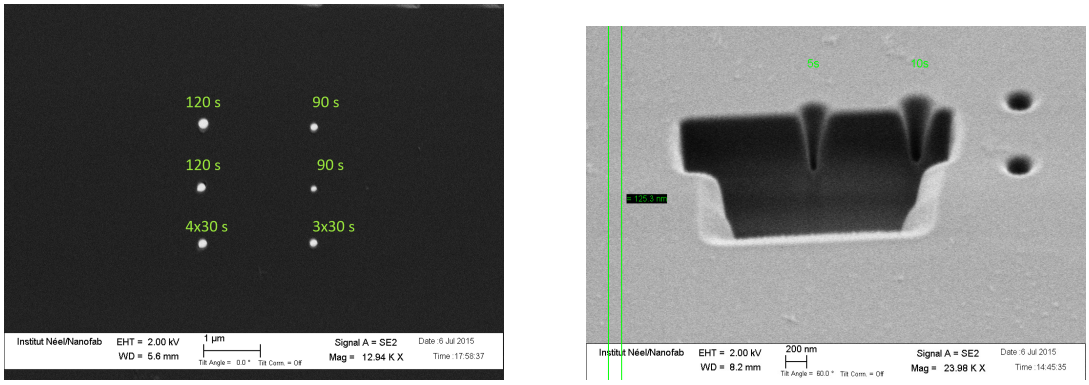

(a) (b)

Figure 5.10: Schematic showing (a) the effect of variation of the milling time and (b) the image of a cross section cut of the milled area by FIB.

Parameters for controlling the size and shape of the nanopore are investigated. At first, the optimum value of the time and the beam intensity required to pierce the thickness of silica of 1.35±0.05 μm are investigated. For a beam of current intensity 17 pA, the optimized time is about 90 s. Higher is the time, wider is the opening of the hole (figure 5.10a). The shape of the milled holes is also confirmed by a cross section cut from FIB (figure 5.10), showing a conical shape. The diameter of the pore opening is then controlled by keeping track on the measured current intensity across the membrane. Usually, the current is zero when milling is started. Current increases abruptly as soon as the membrane is pierced. Increasing the time of milling after piercing, attributes to the wide ending diameter of nanochannel. Usually we stop the milling as soon as the membrane is pierced. From this approach the size of the nanochannel ending diameter is controlled upto 50±5 nm. Figure 5.11 represents SEM images of a small nanopore ending diameter (55±5 nm) and a wide ending diameter (233±5 nm). The nanopores fabricated from this approach are always conical with a cone angle 8-10°. The current intensity of beam used for the fabrication of small holes is 6pA and for large pore is 30 pA.

From the above protocol the length of the channel is always 1.35±0.05 μm (the thickness of the freestanding membrane). It has been also possible to fabricate nanochannels of shorter length. For this, the membrane is thinned in the middle at first by etching silica from FIB at the ion beam current intensity 1.8 nA. Thereafter, the membrane is pierced to fabricate a nanochannel. Figure 5.12a represents a

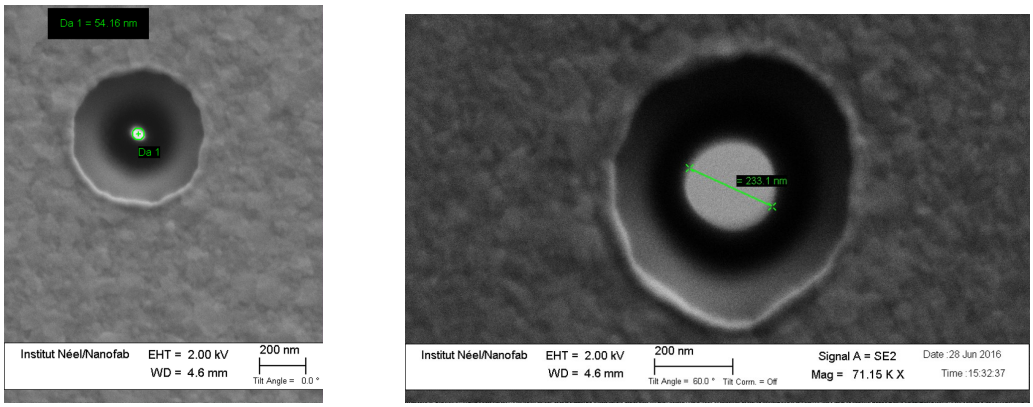

(a) (b)

Figure 5.11: SEM images of FIB milled nanoholes (a) opening diameter 566 nm and ending diameter 55 nm and (b) opening diameter 630 nm and ending diameter 233 nm.

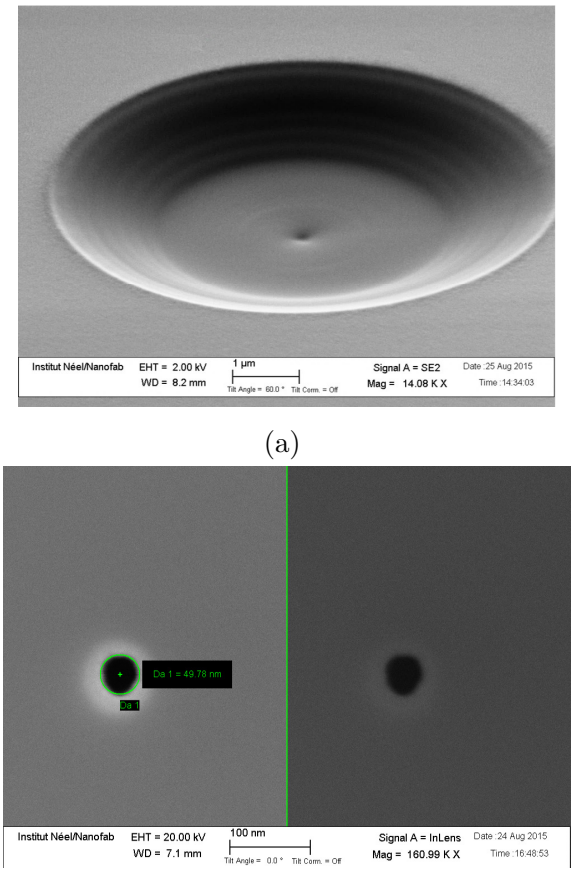

(a)

(b)

Figure 5.12: SEM images of (a) the silica membrane locally thinned by FIB milling and (b) a nanochannel milled in the middle of thinned membrane.

thinned silica membrane after performing vertical digging into the membrane (seven steps in a circle form, starting diameter of about 15 μm). Subsequently, a pore of 50±5 nm diameter has been milled into it, figure 5.12b. The disadvantage of this approach is that the thickness of the membrane left after thinning the freestanding

silica membrane is not precisely known, only can be estimated. For this precise sample in figure 5.12b, the membrane has been thinned upto 700-900 nm resulting in the length of the nanochannel to be 700 nm-900 nm.

5.4 Electrode deposition on the nanochannel sample chip

Placing the electrodes as close as possible to the nanochannel increases the sensitivity of the electrical measurements in solution [11]. For this purpose, a pair of electrodes has been deposited on both sides of the membrane before milling the nanochannel. The thickness of the deposited electrodes should be minimum in order to not to perturb the clamping of the sample in the custom made electrokinetic cell while pressed against the o-rings. At the same time it should be thick enough to be sensitive for electrical measurements.

The coating of electrodes has been performed by a deposition machine recently installed by our group, in Liphy. The principle of coating is based on cathodic pulverization method. This technique uses a metallic target to be sprayed. A potential difference (power 80 W) between the cathode named target and the walls of the whole device in a rarefied atmosphere (some 10^{-3} m-bar) creates a cold argon plasma. Under the electric field, the plasma cations are bombarded at high velocity towards the target. Their high kinetic energy allows the ions to tear away the atoms of the target which are then ejected at high speed. The atoms then follow a ballistic trajectory and cover all the surfaces present above the target, including the samples. A detailed description of the instrumentation and deposition capabilities is demonstrated in the reference [73].

The deposition of electrodes has been done directly over the freestanding membranes prepared by chemical etching process as described in the earlier section. At first, a Cr adhesion layer of about 20 nm has been deposited, thereafter a Pt layer of 50 nm. Subsequently, nanochannels have been drilled into the Pt coated membrane by FIB milling as described above. Figure 5.13 shows the Pt electrode coated nanochannel sample. The electrical connections to the electrodes has been done by silver glue (from RS component) as shown in figure 5.13b.

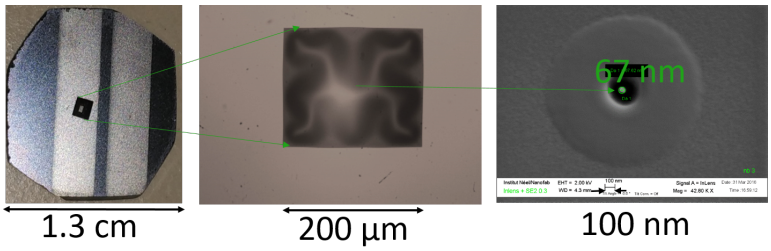

(a)

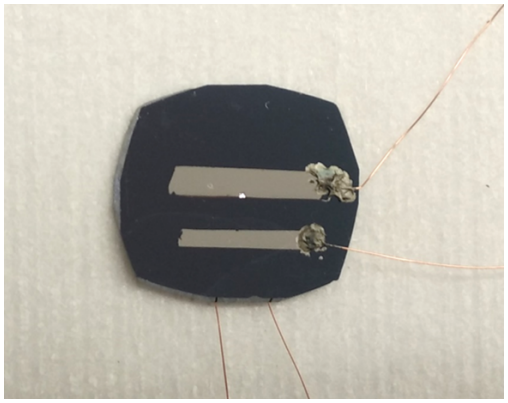

(b)

Figure 5.13: Schematic showing (a) a nanochannel sample with a deposited pair of electrodes (20 nm Cr+50 nm Pt); a macroscopic view on the left, a microscopic view in the middle and a nanometric view on the right. (b) A macroscopic view of the final prepared nanochannel sample chip with electrical connections to the deposited electrodes.

Chapter 6

Characterization of the freestanding membrane and the nanochannel

Contents

6.1 Electrical characterization of the freestanding membrane

6.1.1 Electrochemical cell and set-up

A home made fluidic cell in PEEK, described in chapter 3 figure 3.1 is used for the experiments. The sample is placed in the cell and is pressed against O-rings of $6mm$ inner diameter allowing 0.283 cm^2 area of sample to be exposed to the electrolyte. The concentration of the KCl solution is 1 Molar during all the experiments. A load resistance R_L of 330 Ω is connected to the electrochemical cell in series as shown in figure 6.1.

A small AC excitation signal V_e of 80 mV is applied within a range of frequency 10 Hz-100 kHz by a lock-in amplifier (Stanford Research SR830). The response of this is an AC current within the circuit resulting an AC voltage V_o across the resistor

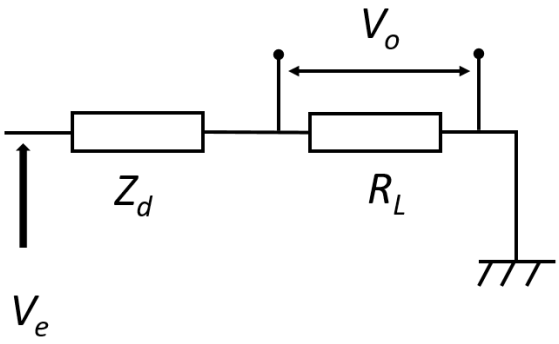

Figure 6.1: Circuit diagram of the electrochemical cell of impedance Z_d in series with a load resister R_L. V_e is the AC voltage applied to the circuit and V_o the measured voltage across the load R_L.

R_L. This voltage , V_0 is measured by the input terminal of the lock-in. A Labview program has been built in order to apply a frequency sweep between 10 Hz-100 kHz and to record the voltage (V_o) across R_L.

6.1.2 Results

Following the circuitry depicted in figure 6.1, the impedance of the electrochemical cell Z_d can be evaluated as following:

$$Z_d(\omega) = \left(\frac{V_e(\omega)}{V_o} - 1\right) R_L \tag{6.1}$$

where ω is the angular frequency. Separating real and imaginary parts of the device impedance:

$$Re\,(Z_d) = \left(\frac{V_e(\omega)(V_o)_r}{(V_o)_r^2 + (V_o)_i^2} - 1\right) \times R_L,\ Im\,(Z_d) = -\left(\frac{V_e(\omega)(V_o)_i}{(V_o)_r^2 + (V_o)_i^2}\right) \times R_L \tag{6.2}$$

The absolute value of the impedance can be calculated as $\mid Z \mid = \left[Re\,(Z_d)^2 + Im\,(Z_d)\right]^{1/2}$.

Three samples are studied under same experimental conditions:

- Bare sample: a 725 μm thick silicon (p doped, 1-14 Ω.cm) substrate with 1.5 μm thick oxide layer on both sides.
- HF treated sample: silica has been etched locally by HF treatment, on one side of the sample
- and the freestanding silica membrane sample.

Figure 6.2 represents the frequency response of the real and imaginary parts of the impedance for these three samples. In order to determine the capacitance due to the oxide layer of silica/membrane, it is required to fit the experimental data with an appropriate equivalent electrical circuit. The basic elements in the electrochemical

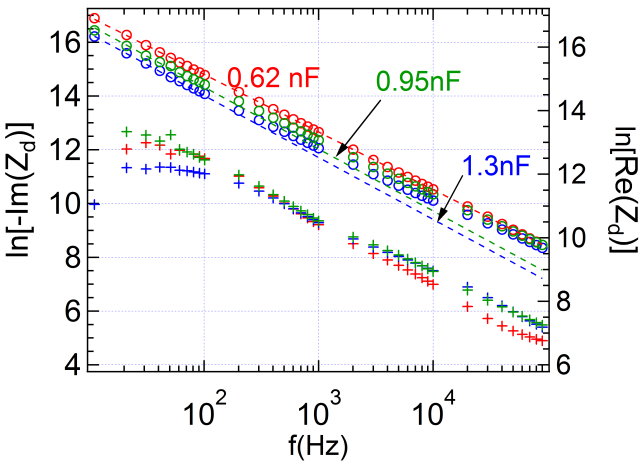

Figure 6.2: Natural logarithm of the real part Re(Z_d) in + symbols and the opposite of the imaginary part -Im(Z_d) in circles plotted as a function of the frequency (logarithmic scale). The bare sample is plotted in red, the HF treated sample in blue, and the freestanding membrane in green. The dashed lines are fits of the imaginary part with the function $X(f) = \frac{1}{2\pi f C_{SiO2}}$, corresponding to a pure capacitance.

cell are, the sample, KCl electrolyte and Ag/AgCl electrodes. Taking into account the value of silicon resistivity and assuming a uniform contribution of the sample area exposed to electrolyte (0.283 cm^2), the maximum resistance due to silicon is about 4 Ω. Therefore, a bare sample can be considered as a pure capacitor whose capacitance is the effective capacitance of two capacitor in series, each due to dielectric layer of silica of thickness 1.5 μm.

At first, we fit the experimental data, $-Im(Z_d)$ with a pure capacitance model

$$X(f) = \frac{1}{2\pi f C_{SiO2}} \tag{6.3}$$

Figure 6.2 shows that the capacitance model works very well for the Im(Z) upto the frequency 1000 Hz.

At higher frequencies deviation occurs. In addition, the pure capacitance model does not account for the finite resistance observed in figure 6.2, which is about one order of magnitude lower than the capacitance impedance.

At the concentration used (1 Molar), the calculated solution resistance is 80 Ω taking into account the conductivity value given in table 4.1. This resistance is much lower than what we are observing in the Re(Z_d). Another key point is that we have already shown in figure 4.3 that in this range of frequency, the impedance of the bare cell is not controlled by the electrolyte resistance but by the Warburg impedance or the constant phase element associated to the electrodes.

Figure 6.3 presents a plot of Re(Z_d) of the cell in presence of a sample (in + symbol) and in the absence of sample (in Δ symbol). This plot shows that the impedance of the electrodes are negligible as compared to the impedance of the sample in the frequency range 10-100 kHz.

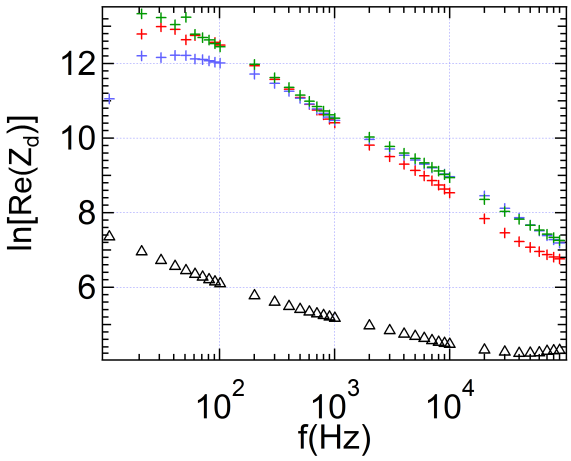

Figure 6.3: Natural logarithm of the real part $Re(Z_d)$ of the cell impedance in presence of sample (in + symbol, the bare sample in red, the HF treated sample in blue, and the freestanding membrane in green) and in the absence of a sample (in Δ symbol) plotted as a function of the frequency (log scale).

In order to refine the model, we introduce a constant phase element (CPE) in series of the pure capacitance. This constant phase element is not due to the electrodes, it is associated to the sample itself. The CPE is modelled as follows:

$$Z_{CPE} = \frac{1}{(j\omega)^{n_{CPE}} Y_0} \tag{6.4}$$

with, Y_0 the CPE capacitance, j the imaginary unit ($j = \sqrt{-1}$), ω frequency and $n_{CPE} < 1$ an empirical constant. The fitting function can be presented as the sum of the two impedances as follows:

$$Z = Z_{SiO_2} + Z_{CPE} = \frac{\cos(n\pi/2)}{Y_0(2\pi f)^{n_{CPE}}} - j\left(\frac{1}{2\pi f C_{SiO_2}} + \frac{\sin(n\pi/2)}{Y_0(2\pi f)^{n_{CPE}}}\right) \tag{6.5}$$

In the fitting function equation 6.5, the real part is independent from the silica layer capacitance C_{SiO_2}. Therefore, we first find the value n_{CPE} which fits well with the slope of Re(Z_d), keeping C_{SiO_2} fixed from the first model (pure capacitance) and Y_0 also fixed to a roughly acceptable value. Then the magnitude Y_0 is allowed to change in order to fit Re(Z_d), keeping n_{CPE} and C_{SiO_2} fixed. This allows us to find the right CPE parameters. Now, the imaginary part of the impedance can be fitted with a single fitting parameter C_{SiO_2}. Figure 6.5 represents all the three experimental data fitted with equation 6.5. The value of the CPE parameters and silica capacitance for each sample is tabulated in table 6.1.

6.1.3 Discussion

The bare sample is equivalent to two capacitors in series, each denoted by C, due to 1.5 μm thick dielectric layer of silica with area exposed to the electrolyte (figure 6.5a). The total capacitance for this sample is $C/2$. In HF treated sample, silica

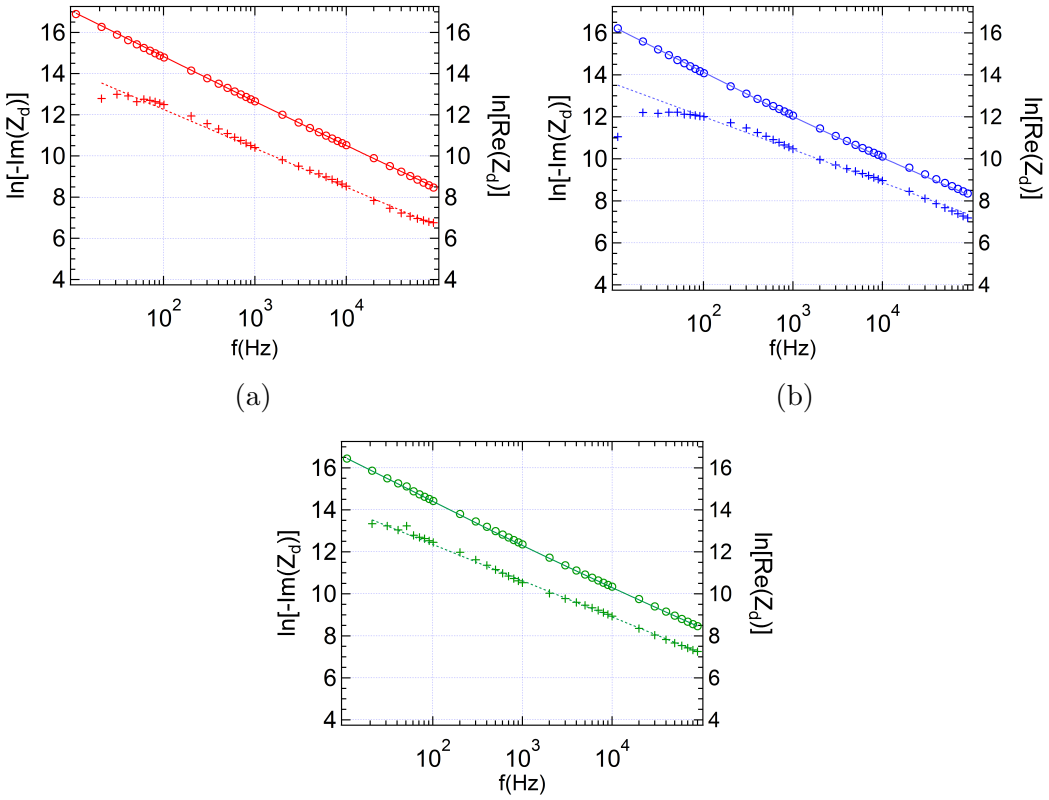

Figure 6.4: Natural logarithm of $-Im(Z_d)$ and $Re(Z_d)$ of the impedance is plotted as a function of frequency for (a) the bare sample, (b) the HF treated sample and (c) the silica membrane. $-Im(Z_d)$ is plotted in circles (o) and $Re(Z_d)$ are in plus (+). Solid lines are the fits on $-Im(Z_d)$ and $Re(Z_d)$ from equation (6.5).

Table 6.1: Value of the calculated sample capacitances, and of the fitted capacitances with the pure capacitance model and with the constant phase element model. The unit of Y_o is Ω^{-1} when ω is given in rad/s.

Sample	C_{SiO2}, calculated	C_{SiO2}, from fit eq. (6.3)	Y_0 (USI)	n_{CPE}	C_{SiO2}, from fit eq. (6.5)
Bare sample	0.33 nF	0.62 nF	3×10^{-8}	0.82	0.79 nF
HF treated	0.65 nF	1.3 nF	1.28×10^{-7}	0.68	1.55 nF
Membrane	0.72 nF	0.95 nF	5.2×10^{-8}	0.75	1.3 nF

has been etched from one side of the sample. As the doped silicon is a conductor, it is equivalent to a capacitor C figure 6.5b. The sample with freestanding silica membrane is equivalent to a capacitance $C' > C$ (figure 6.5c), as the thickness of the membrane is 1.35±0.05 μm measured by thin film reflectometry system (NanoCalc).

It can be seen from the table 6.1 that the value of the capacitance of bare sample

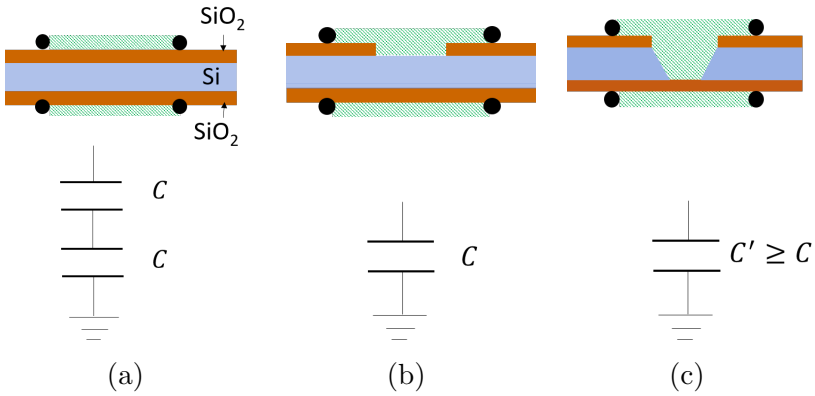

Figure 6.5: Schematic showing three samples under investigation, (a) bare sample, (b) HF treated sample and (c) freestanding silica membrane sample and their equivalence to capacitors due to the dielectric silica layers. The green shaded part is presenting the effective area of the sample in contact with the electrolyte. C is the capacitance of single silica layer (for bare or HF treated sample) and C' is the capacitance of the freestanding silica membrane sample. In a simple first analysis, C' is expected to be larger than C because the free-standing membrane is thinner than the native silica layer.

obtained from the two fitting models is about half of that obtained from the HF treated sample. This is in good agreement with what we expected as explained in the previous paragraph.

It can also be seen that, the capacitance of the sample with freestanding silica membrane is about 16% less than that of the HF treated sample. Principally, it should have been bit larger as the thickness of the silica membrane is reduced from 1.5 μm to 1.35±0.05 μm (and capacitance is inversely proportional to the thickness of dielectric layer). We attribute this lower value of the capacitance of the silica layer in the case of the free-standing membrane, to the fact that the electric field across the membrane might be not uniform, due to the difference in conductivity between the electrolyte which is in contact with one part of the silica layer, and the doped silicon which acts as electrode for the non-exposed part of the layer.

Finally, the value of the capacitance for each sample, obtained from both fitting models is about two times higher than that of calculated capacitance (taking into account the thickness of the silica layer in each sample and the area $A = 0.283$ cm^2, exposed to the electrolyte, $C_{SiO2} = \frac{\epsilon_0 \epsilon_r A}{t_{SiO_2}}$, where ϵ_0 is the permittivity of free space $\epsilon_r = 3.9$ is the relative permittivity of silica).

The above discrepancy in capacitances is probably due to the uncertainty in the area of the sample exposed to the electrolyte. If the area of the sample is wet under the o-ring periphery as well (figure 6.6), this will result in an effective area of the sample in contact with the electrolyte to 0.502 cm^2. It is approximately 2 times larger than the one we took into account for the estimation of the capacitance (C_{SiO2}, calculated in table 6.1), A=0.283 cm^2. The values of new calculated capacitances taking into account the effective area 0.502 cm^2 is given in the table 6.2.

Table 6.2: Value of the calculated sample capacitances, taking into account the effective area of the sample, 0.502 cm^2 in contact with electrolyte.

Bare sample	HF treated	Membrane
0.58 nF	1.17 nF	1.3 nF

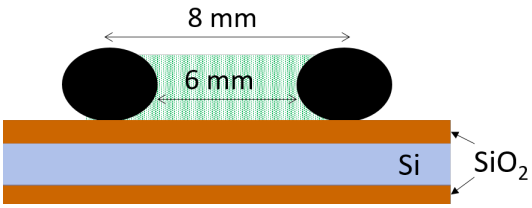

Figure 6.6: Schematic showing the side view of the o-ring placed over the bare sample.

6.2 Mechanical robustness of freestanding silica membranes

The freestanding silica membrane samples are drilled via the earlier described FIB technique to prepare the single nanochannel. A priori knowledge of the mechanical robustness of the membranes is required before drilling them as they need to be exposed to a one bar pressure difference during electrokinetic experiments.

Three experiments are performed for an applied pressure difference of 0.2 bar, 0.6 bar and 1 bar across the freestanding silica membrane sample (size of the membrane 170×170 μm^2) placed in the cell.

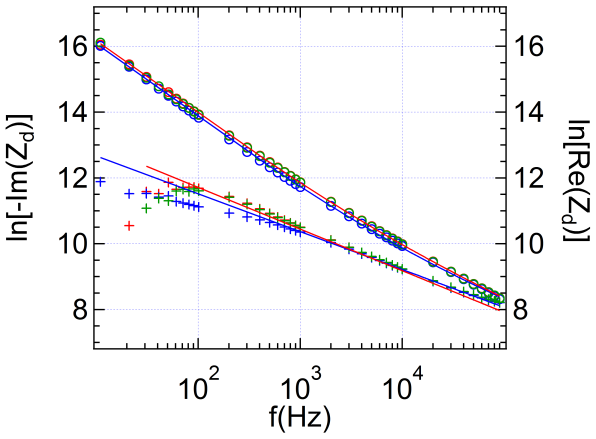

Figure 6.7: The natural logarithm of the imaginary ($-Im(Z_d)$) and real part $Re(Z_d)$ of the impedance are plotted with respect to frequency for a free standing silica membrane sample. A constant pressure difference has been applied across the membrane during measurements, P=0.2 bar in red,P=0.6 bar in green and P=1 bar in blue. Black solid lines are the fitting on $-Im(Z_d)$ and $Re(Z_d)$ from equation (6.5).

Figure 6.7 represents the variation of natural logarithm of $Re(Z_d)$ and $-Im(Z_d)$

with frequency. Equation 6.5 is used to fit the experimental data of each experiment. The fit for applied pressure 0.2 bar (in green) and 0.6 bar (in red) gives the CPE coefficients n_{CPE}=0.55, Y_0=4.2×10^{-7} and capacitance C_{SiO_2}=1.6 nF. For the experiment of applied pressure of 1 bar (in blue) the fit coefficients are n_{CPE}=0.5, Y_0=6.7×10^{-7} and C_{SiO_2}=1.7 nF.

The capacitance value is slightly higher for the 1 bar applied pressure experiment than for the values of 0.2 and 0.6 bar applied pressure. This small increase in capacitance (about 6%) could be attributed to the increase in area of the membrane, but more probably due to a change in the wetted surface area associated to the deformation of o-ring.

Even under the application of 1 bar pressure difference, no breakage of the membrane is observed. Although, it has not been possible to reach the breaking point of the membrane due to the limitation of maximum pressure applied by the N_2 gas, these types of membranes are used for milling the nanochannel and could be used for some other applications where a pressure difference upto 1 bar is required.

6.3 Single nanochannel electrical characterization

Two single nanochannel samples are tested, prepared from focused ion beam milling.

Sample 1: The first sample is a nanochannel of 50 nm diameter and length $l \approx$ 800 nm, drilled after locally thinning the silica (figure 5.12). Ag/AgCl electrodes embedded into the electrokinetic cell are used for the electrical characterization in patch clamp configuration (Chapter 3, figure 3.4).

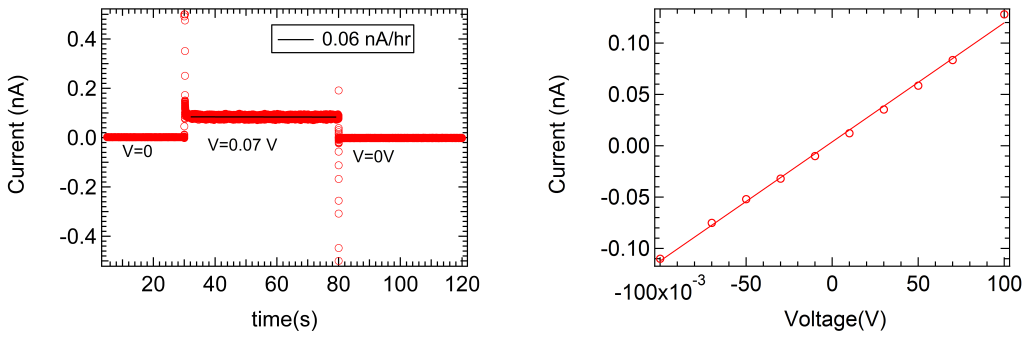

(a) (b)

Figure 6.8: (a) Current measured by the patch clamp, for an applied voltage V=0, V=0.07 V across the nanochannel. The electrolyte in the cell is 0.1 M potassium chloride (KCl). The solid black line is a small linear drift of 0.06 nA/hr.(b) I-V characteristic of the nanochannel. The solid line is a linear fit corresponding to a conductance of 1.16 nS.

Figure 6.8a represents the response of an applied voltage of 0.07 V across the nanochannel in terms of the measured electrical current. The current measured is stable upto 0.06 nA/hr.

Figure 6.8b represents the current-voltage characteristics of this first sample of nanochannel. The KCl concentration used in this experiment is 0.1 Molar. Each point on this figure is a mean value of the measured current during 30 seconds, corresponding to the applied voltage. It can be seen that the measured current increases linearly with the applied voltage between -0.1 V and 0.1 V. A linear fit on the experimental points gives us the conductance of the nanochannel; 1.16 nS. Thus this first sample behaves as a perfect resistor.

The ionic conductance in the nanochannel containing an ionic solution has essentially two main contributions: one due to the bulk conductivity of the electrolyte and one due to the excess ions because of the surface charge. For a cylindrical nanochannel the bulk conductance is given as follows:

$$G_{bulk} = \sigma_b \frac{\pi r_{nc}^2}{l} \tag{6.6}$$

with σ_b the bulk conductivity of the electrolyte solution, l the length of the nanochannel and r_{nc} the radius of the nanochannel. An addition, it is also required to take into account the conductance due to inlet and outlet effects of the nanochannel/pore. At the inlet of the nanochannel the field lines converges and at the outlet field lines diverges, figure 6.9. Therefore, the inlet/outlet of nanochannel can be considered an equipotential hemisphere cupola as an effective electrode. Proceeding in the same manner as for the cell resistance for pointing electrodes configuration in section 4.1.2 (in part II of the thesis), the inlet/outlet conductance is formulated as:

$$G' = 2\pi r_{nc} \sigma_b \tag{6.7}$$

The total conductance of nanochannel is given by:

$$G_o = \left(\frac{1}{G_{bulk}} + \frac{2}{G'} \right)^{-1} = \pi r_{nc}^2 \sigma_b \left(l + r_{nc} \right)^{-1} \tag{6.8}$$

This end effect in conductance is equivalent to adding a portion of length $r_{nc}/2$ to the nanochannel of same diameter, at it's entrance and outlet. For the nanochannel of length $l >> r_{nc}$ these end effects and negligible.

The second contribution is due to the excess ions balancing the surface charge present on the walls of the nanochannel. The nanochannel surface is charged electrically due to adsorption or dissociation of chemical species [74]. A double layer of counterions is developed close to the solid walls due to electroneutrality. The surface conductivity associated with surface charge can be first estimated as [53]:

$$\sigma_s \simeq e\mu|\Sigma| \tag{6.9}$$

with e the elementary charge, and μ the ionic mobility of K^+ and Cl^- ions (it is supposed that both ions have same mobility), and Σ the surface charge. Note that the surface conductivity has the dimension of [$\sigma_b \times$length]. Note also that the equation (6.6) assumes that the conductivity is proportional to the ion concentration, that is $\sigma_b = 2e^2\mu n_o$ with n_o the ionic concentration in m^{-3}.

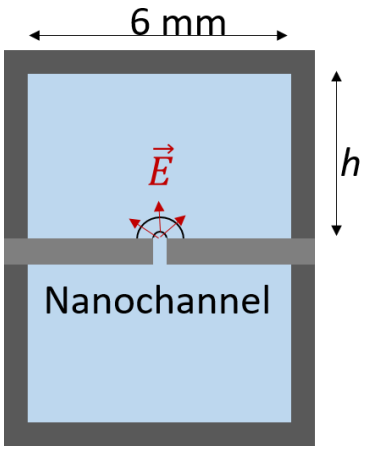

Figure 6.9: Schematic showing the distribution of the electric field within the nanopore, mounted on the cell.

The relative contribution of the surface conductivity to the bulk conductivity in the global conductance is $G_\Sigma/G_{bulk} = \mathcal{A}\sigma_s/\sigma_b$ where $\mathcal{A}$ is the specific area of the channel, that is its area per unit volume. In particular in a cylindrical nanochannel, the surface conductance is

$$G_\Sigma = \frac{\sigma_s 2\pi r_{nc}}{l} \tag{6.10}$$

The dominance of the electrical conductance due to surface charge over the bulk concentration is mainly obtained for low salt concentrations. More accurately the Dukhin length l_{Du} defines the radius of the nanochannel for which the bulk conductance and the surface conductance are equal:

$$l_{Du} = \frac{2\sigma_s}{\sigma_b} \simeq \frac{|\Sigma|/e}{n_o} \tag{6.11}$$

If Dukhin length is larger than the size of the nanochannel, surface conductance dominates over the bulk conductance. In our experiment, the Dukhin length is calculated to be 1 nm, taking into account the typical value of surface charge for silica to -10 mC.m^{-2} [53]. It confirms that in this experiment, the conductance of the channel is mainly governed by the bulk conductivity of the solution. The value of the bulk conductance is calculated to be 3.2 nS (from equation 6.6, with σ_b=0.0129 $S.cm^{-1}$ from table 4.1 in chapter4). This value is about 2.7 times higher than that of measured experimentally.

The factor of 2.7 in the calculated value of conductance can not be due to the entrance effects as the size of pore is 50 nm and length about 800 nm. The entrance and outlet effects result in an increase in length only by 25 nm (r_{nc}), which is not sufficient to lose a factor of 2.7 in calculated value of conductance. For this exact factor, the length requires to be increased 2.7 times of the length of pore (800 nm) . This results in the length of nanochannel 2.2 μm much larger than the thickness of freestanding silica membrane itself.

Similarly, the maximum possible error in the measurement of the drilled nanochannel diameter is ±5 nm. Taking into account this error, the conductance can be decreased only by 40%. In addition, electro-omosis effects should also not explain the small conductance measured because an electro-osmotic flow always enhances the electrical conductance. The only possible explanation for this discrepancy is the partial blockage of the channel by some nanometric particle, resulting in a significant diminution of the ionic current and hence of the conductance of nanochannel.

Sample 2: The second sample under investigation is a conical nanochannel with opening diameters of 200 nm and 550 nm. This sample has two Pt electrodes, deposited on both sides of the freestanding membrane before milling the nanochannel as explained in earlier chapter (section 5.4). The solution used in this experiment is deionized water. A DC voltage is applied by auxiliary output of the lock-in (Zurich instruments, HF2LI) and the current is measured by Patch clamp (as presented in Chapter 3, figure 3.4).

Figure 6.10a represents the current measured across the nanochannel in response to the applied voltage. The beginning of each applied voltage results in a start-up current peak and then a decay with the square root of time, as described by Cottrell equation [36]:

$$I(t) = nFAc_R\sqrt{\frac{D_R}{\pi t}} \tag{6.12}$$

where n is the number of electrons (needed to reduce/oxide one molecule of analyte), A is the electrode surface area, c_R is the concentration of the reduced specie R, and D_R is the diffusion coefficient of the reduced specie R.

The current with respect to $t^{-1/2}$ is plotted for each applied voltage as shown in figure 6.10b. Clearly, it is a straight line. The intercept of line with y-axis is the saturation current which is plotted vs the applied voltage in figure 6.10c. If a linear fit is performed on the experimental points, in forward bias between 0.04V to 0.1V, and in reverse bias between -0.04V to -0.1V, it results in the conductance values of 0.62 nS and 0.11 nS respectively. The value of the rectification factor at 0.1 V is calculated by $I(-0.1V)/I(0.1V)$ is 0.55.

Clearly, a rectification behavior is observed in the electrical conductance of this conical solid-state nanopore. This is expected, because of the asymmetry in the pore geometry as explained in the state of the art part I chapter 2. In passing mode, the electrical conductance of the nanopore is calculated to be 0.01 pS taking into account the bulk electrical conductivity of the deionised water (0.055 μS.m^{-1}), which is very small as compared to the experimentally measured electrical conductivity, 620 pS from figure 6.10c. From equation (6.9), calculated surface charge on pore walls is found to be -1.7 mC.m^{-2}, which is comparable with the expected typical surface charge of silica -10 mC.m^{-2} from ref.[53]. For this value of surface charge (-1.7 mC.m^{-2}), the value of the Dukhin length l_{Du} in deionized water is estimated to be 20 μm (for pH 6 of CO_2 saturated deionised water and equivalent concentration

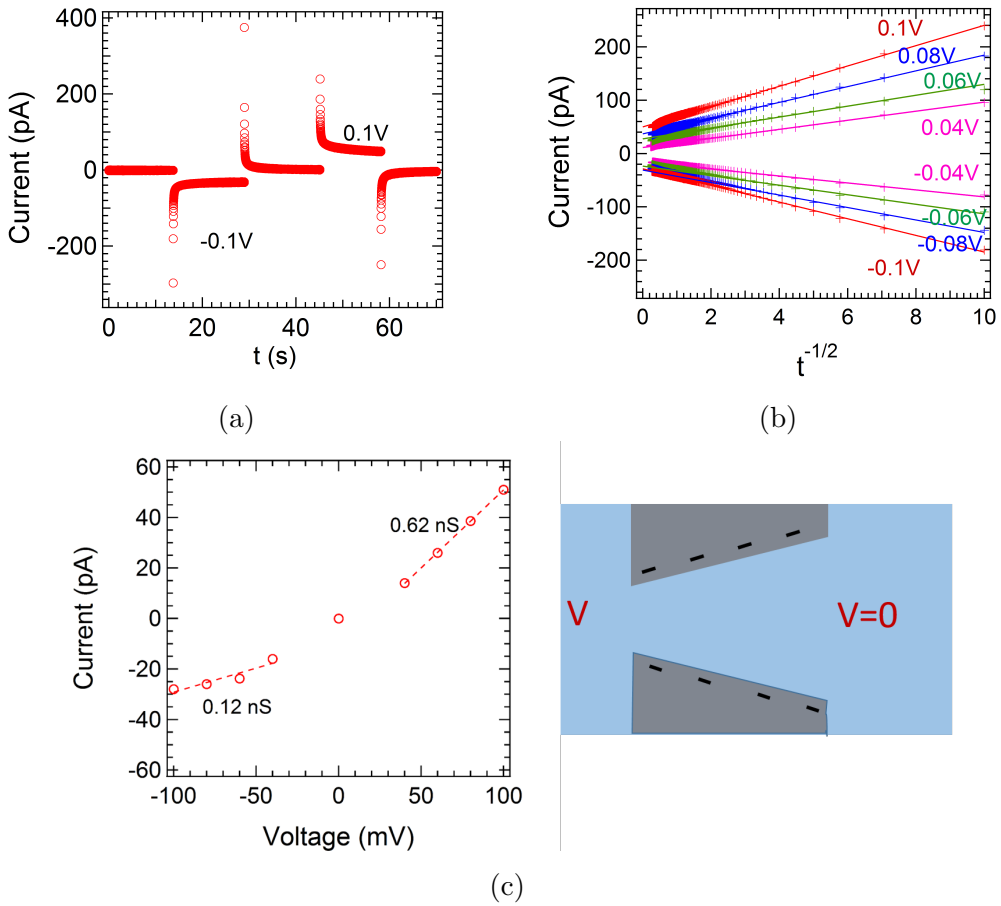

Figure 6.10: (a) Current measured across the nanochannel with the applied voltages V=-0.1V and V=0.1V .(b) The current is plotted vs $t^{-1/2}$ for each applied voltage across the nanochannel and (c) the current value obtained from the extrapolation of I vs $t^{-1/2}$ to origin, is plotted vs the applied voltage. A schematic of the nanopore with applied voltage V across it.

10^{-6} M.L^{-1}). It is very large as compared to both the opening diameters of the pore, narrow side 200 nm and wide side 550 nm. It confirms that the conductance of the pore is governed by the surface charge. In this case the Donnan potential at the inlet and outlet of the pore can be estimated from (recalling equation 2.3 from the state of the art):

$$V_D = \frac{kT}{e} \sinh^{-1}\left(\frac{l_{DU}}{h}\right) \tag{6.13}$$

The estimated values of Donnan potentials are -48 mV at wide opening of the pore and -73 mV at the narrow opening of the pore. These values of the Donnan potential correspond to the applied potential range for which the asymmetry in the I-V characteristic is observed on figure 6.10.

The phenomena of ion current rectification in asymmetric pores have already been intensively studied by various groups [23, 75, 76, 22, 24]. Here, we do not pursue on a more detailed investigation of this rectification behavior, as the purpose of this part of the thesis is to demonstrate the qualification of our method and set-up

to perform electrical measurements in single solid-state nanopore.

6.4 Conclusion

In this part we have demonstrated the feasibility of an easy method to elaborate free-standing silica membranes, ready to be embedded in a flow cell with standard o-ring sealing, and possibly equipped with platinum electrodes. The thickness of the membrane can be varied by choosing the thickness of the silica layer on the initial silicon wafer. We have tested the mechanical robustness of 1.35 ± 0.05 μm thick membranes, and found no failure up to 1 bar. These free-standing silica membranes provide a convenient tool to study nano-fluidic phenomena in solid-state nanopores drilled by FIB.

We have performed the AC electrical characterization of these silica membranes, as well as DC conductivity characterization of solid-state nanopores carved in them, with our instrumented flow cell. The results demonstrate the qualification of the whole set-up for nanofluidic electrical measurements in single nano-pore samples.

Part IV

Development of a pico-flow rate sensor

Chapter 7

Introduction to flow rate measurement techniques

The liquid flow measurement within a nanochannel is challenging as to deal with minuscule volume of liquid corresponding to a flow rate of few pico-liters to femto-liters per minute. The advancement in the fabrication techniques allow us to fabricate common nanofluidic structures for example nanopores, nanochannels, and nanopipettes [77] in which the flow rates from picolitre (pL) to femtolitre (fL) range can be achieved. Over the past few years, various techniques have been identified for probing the flow rates in micro and nanochannels [78]. The flow rate induced in wide channels typically in the sub millimeter channels can be controlled and measured easily by weighing the outcoming liquid or measuring the height of the meniscus in a micrometric tube [79, 80]. The accuracy of these measurements is directly related to the accuracy of the balance or the diameter of the tube.

Monitoring and calibrating the flow rate within sub-micrometric and nanometric channels becomes rather complicated and requires more efficient techniques to be implemented. The common approach of pumping the flow within nanochannels are pressure driven flow and electrically driven flow (electro-osmotic flow). In pressure driven flow, a flow with parabolic profile known as Hagen-Poiseuille flow is induced by generating a pressure difference pneumatically with the help of compressed air or gases for example N_2 or CO_2. While in electro-osmotic flow (EOF), a flow is induced by the application of electric voltage across the nanochannel resulting in a planar velocity profile known as plug flow. It was identified and used to probe zeta potential of channel surfaces by an easy to implement method called *current monitoring* method [81, 82]. In this method, the current through the channel connecting with two reservoirs filled with slightly different concentrations was recorded. Knowing the time of filling and the geometry of the channel, the electro-osmotic velocity and flow rate were evaluated. Further, this method was extended to probe flow rate under pressure driven flow [83].

Alternatively, a flow sensor based on micromechanical systems (MEMS) had been developed for flow rate measurement of biological fluids upto few $nL.min^{-1}$.

These sensors are based on sensing the temperature difference between two points in microchannels [84, 85]. The sensitivity and accuracy of such flow sensors rely on the environment associated in the heat transfer. Other MEMS flow transducers were proposed based on AC admittance measurement of a pair of gold electrodes in micro-channel [86, 87]. The sensitivity of these devices with implemented electrodes was to measure flow rate as low as 60 nL.min^{-1}. Subsequently, electrochemical flow sensor based on two closely spaced amperometric oxygen sensors was developed [88]. The approach was based on measuring the difference of consumed oxygen present in the solution between two closely separated oxygen sensors. A novel method based on electrical cross correlation spectroscopy was demonstrated by K. Mathwing to measure pL-min^{-1} flow rate within a nanochannel [89]. In this approach, the electrical fluctuations of the number of electrochemically active molecules at two electrodes implemented on the walls of the nanochannel are measured. The time of flight detection of the fluctuations allows to determine the liquid flow velocity. These MEMS flow sensors can measure the flow rate of the order of sub pL.min^{-1} which is hundred times more sensitive than the flow rates measured with a commercially available sensors (limited to measure the flow rate as low as 500 pL/min based on on-chip detection of heat transfer, SLG1430 Liquid Mass Flow Meter, Sensirion AG, Switzerland). In such sensors, fixing the electrodes to the nanochannel imposes limitations in the geometric confinement and to the reusability of a particular nanochannel.

Visual inspection of the velocity profile is an alternative way of flow measurement such as in particle image velocimetry [90, 91]. In this method, addition of tracer

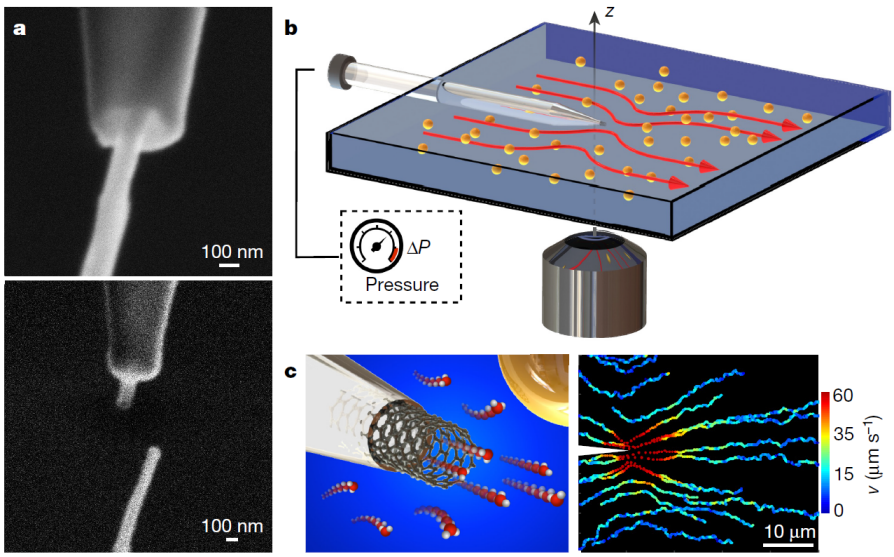

Figure 7.1: An illustration of nanojet experimental set-up in ref.[92]. (a) SEM images of carbon nanotube inserted into nanocapillary. (b) Schematic of the fluidic cell and set-up to image the motion of tracers (in orange) in response of Landau square flow (in red lines). (c) Sketch of a nanotube protruding from a nanocapillary tip. On the right, trajectories of the tracer in a Landau-squaire flow field in the outer reservoir.

particles are required which introduces additional hydrodynamic or electrostatic interaction due to invariable charge present on tracer particles itself, resulting in a complicated analysis of flow measurements. This type of problem is avoided in a technique based on Landau-squire nanojet. In this method, an electro-osmotically driven or a pressure-driven flow across a single nanotube sets up a flow in the outer reservoir called a Landau–Squire nanojet [93, 92]. The flow through the outlet of the nanochannel can be considered to be a jet from a point source. The exact solution of the Navier-Stokes equation, representing a jet from a point source was given by Landau and Square [94, 95, 96]. The resulting motion of the tracer particles in response of the jet, in the outlet reservoir is tracked out to map the velocity profile of flowing liquid as presented in figure 7.1 in ref.[92]. This method allows one to measure the unprecedented flow rate upto 0.1 fl.min^{-1}, but is limited to specifically fabricated experimental device with single nanotube, in the form of a nanofluidic needle.

Another method based on recording the fluorescent intensity of molecular dye used as a probe for the generated water flow across nanochannel is demonstrated by Lee *et al.* in ref.[97], figure 7.2. The flow generation within nanochannel submitted to salinity gradient is called diffusio-osmosis flow. The flow rate was obtained following the stationary diffusion-convection equation with a precision of 50 fL.min^{-1}.

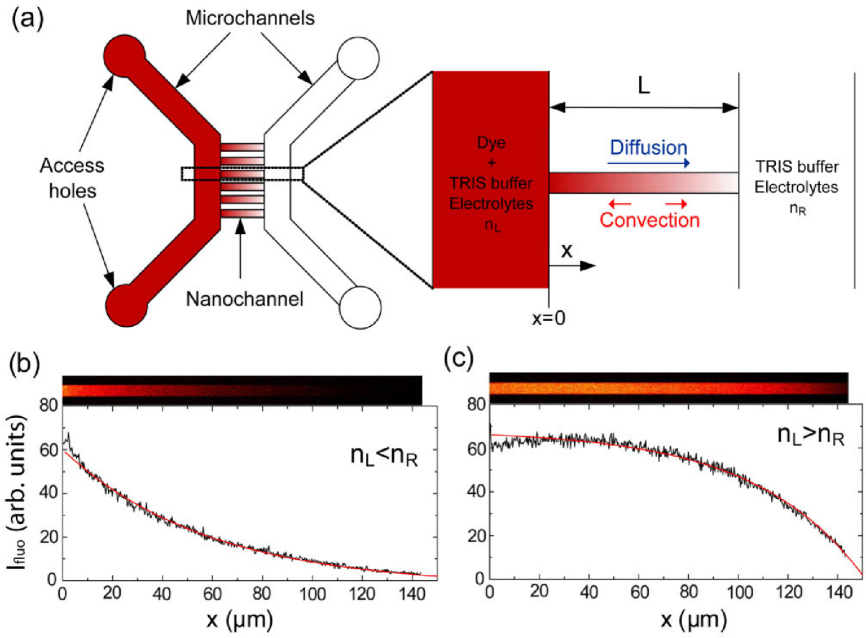

Figure 7.2: Schematic of the flow measurement principle in ref.[97]. (a) Device layout and (b) Steady state fluorescent probe intensity profiles along nanochannels for different solute (NaI) imbalances (b) $n_L < n_R$ (1 and 30 mM) and (c) $n_R < n_L$ (30 and 1 mM).

In this thesis, a method based on direct measurement of liquid flow rate across nanochannel is presented. The principle of measurement is based on in-situ detection of small volume of liquid coming out of the nanochannel connected to a rigid cavity closed with a mechanically deformable solid state silicon membrane. The change

in volume in the cavity connected to nanochannel is measured with time, giving the corresponding flow rate. The novelty of this method is that it can be used to probe the flow rate submitted to either pressure difference, voltage difference or concentration difference across the channel. This technique of measurement is free from the requirement of any tracer particle to use as a probe and hence no need of large and heavy instrumentation.

A flow cell named pico-flow cell to perform flow measurements based on detection of small change in volume is developed during this thesis. The developed cell is able to adapt the solid state single nanochannel sample prepared in chapter 5. The flow measurement combined with the electrical current measurement allows us to measure atleast two coupled fluxes experimentally, submitted to either voltage, pressure gradient or salinity gradient.

In the chapter 8, the principle of the technique used to measure liquid flow rates of the order of few $pL.min^{-1}$ is demonstrated. A detailed description on the realization of the experimental requirements for the development of technique and pico-flow cell is also illustrated.

Chapter 9 is devoted to the development and qualification of the pico-flow cell. The challenges faced during the development are also discussed.

Chapter 10 represents the very first results to demonstrate our technique of flow rate measurement, across a micrometric fused silica capillary as well as a single nanochannel sample prepared in part III of the thesis.

Chapter 8

A capacitive method to measure flow rate

Contents

8.1 Principle of the liquid flow rate measurement

The flow rate measurement method developed in this thesis is based on the measurement of a volume variation induced by a liquid flow. This approach corresponds to an integrated measurement of the flow rate, similar to the electrical current integration method, frequently used in electrical circuits to measure current in the range of pA [98].

8.1.1 Electrical analogy

In the electrical current integration method, a capacitor of known capacitance C is charged by the current i to be measured (figure 8.1a). The electric potential difference U across the capacitor increases linearly with time t according to the constant current i. The variation ΔU in voltage during a time interval $t_2 - t_1$ is:

$$\Delta U = \frac{1}{C} \int_{t_1}^{t_2} i \, dt \tag{8.1}$$

Accordingly, the value of the current i corresponds to the slope

$$i = C \times \frac{dU}{dt} \tag{8.2}$$

The same approach is developed here to built a flow rate sensor with a detection threshold of the order of the picoliter per minute. In our method an hydraulic capacitance is made from a deformable solid state membrane whose deformation accommodates the change in volume imposed by the liquid flow to be characterized (figure 8.1b). The progressive deformation of the membrane related to the liquid volume increase V results in an increase of the pressure difference p_m across the membrane. The flow rate q is proportional to the hydraulic capacitance C_h of the membrane and the time derivative of p_m, in the same way as the electrical current to the voltage:

$$\boxed{q = \frac{dV}{dt} = C_h \frac{dp_m}{dt}} \tag{8.3}$$

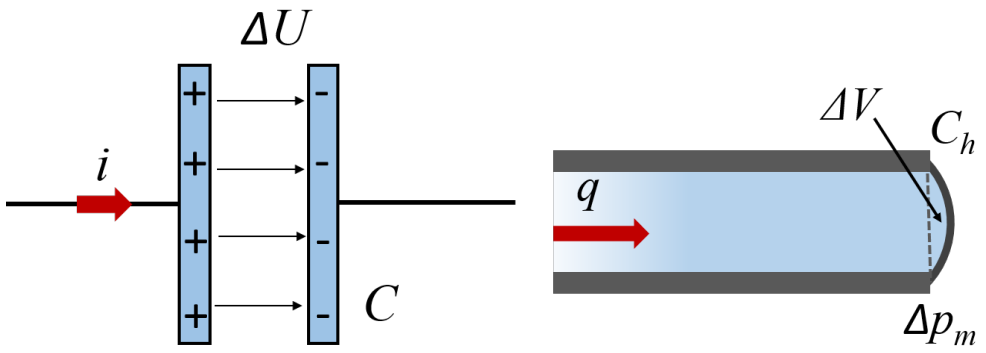

(a) (b)

Figure 8.1: (a) A capacitor of capacitance C is charged by the current i to be measured. The charging of the capacitor during a time lapse Δt results in a variation ΔU of the voltage difference between the plates of the capacitor. (b) Liquid flowing through a channel sealed by a deformable membrane of hydraulic capacitance C_h. The volume increase ΔV results in an increase in the pressure difference Δp_m across the membrane.

8.1.2 A deformable membrane as a capacitor

Here, we focus on the case of a solid membrane clamped on a rigid body on its outer edge. The deflection of such a membrane could be compared to the inflation of a rubber balloon. Such an image though corresponds to a highly nonlinear behavior which does not represent the situation of interest for our application. According to the amplitude of the deflection of the membrane with respect to its thickness, two types of behavior can be observed. The so called *thin membrane* case corresponds to large deflections in comparison to the thickness and exhibits a non linear behavior similarly to the rubber ballon. The *thick membrane* case, which is of interest for our flow rate measurement, corresponds to small deflections in comparison to the thickness of the membrane and exhibits a linear behavior. A *thick* membrane becomes a *thin* one if the magnitude of the deflection becomes larger than the thickness of the membrane

The deflection of a membrane is related to two physical quantities:

- the bending moment of the membrane.

- the strain within the membrane associated to the stretching of the neutral fiber of the membrane.

In the *thin membrane* case, with a thickness negligible in comparison to the deflection, the stress generated into the membrane due to elongation of the membrane fibers is much larger than the bending moment. Therefore, bending moments can be neglected in the thin membrane approximation and the deflection of the membrane is dominated only by the stretching of the neutral fiber. In such a case, the deflection w_0 at the center of the membrane is proportional to the power one third of the pressure generated across membrane [99] $w_0 \propto p_m^{1/3}$. In the thick membrane case, the deformation of the membrane is controlled by the bending moments and the stretching of the neutral fiber can be neglected. In this approximation, the deflection is proportional to the pressure difference $w_0 \propto p_m$. This linear case corresponds to the situation of a linear dependence between the volume and the difference of pressure as expressed in the relation (8.3). The non linear case, although it corresponds to larger pressure variations that could alter the flow to be studied, demonstrates a better sensitivity of the pressure to the membrane deflection. In the present work, we focused only on the linear case, nevertheless it could be of interest to look more carefully to this thin non linear case in a future work.

The deflection w of a thick membrane, clamped at the edges and submitted to a uniform loading depends on the shape of the membrane [99, 72]. For a circular membrane it is given by:

$$w(r) = \left(1 - \frac{4r^2}{a_m^2}\right)^2 \frac{1-\nu_m^2}{k_w E_m} \frac{a_m^4}{d_m^3} p_m \tag{8.4}$$

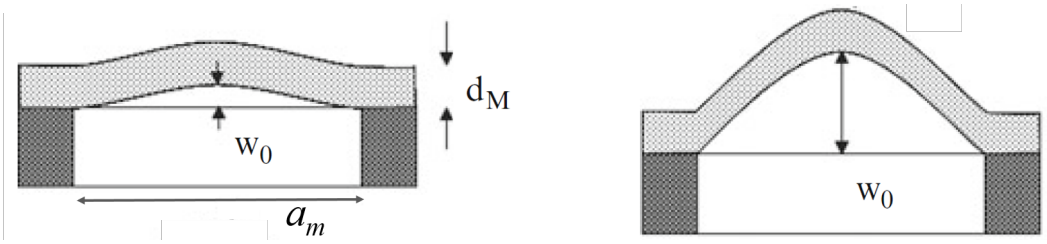

(a) (b)

Figure 8.2: Schematic of (a) thick membrane ($w_0 < d_m$) and (b) thin membrane ($w_0 > d_m$). a_m is the edge length of the square membrane. [99]

For a square membrane it is approximated by:

$$w(x,y) = \left(1 - \frac{4x^2}{a_m^2}\right)^2 \left(1 - \frac{4y^2}{a_m^2}\right)^2 \frac{1-\nu_m^2}{k_w E_m} \frac{a_m^4}{d_m^3} p_m \tag{8.5}$$

where d_m, E_m, ν_m are the thickness, the elastic modulus, the Poisson's ratio of the material of membrane, a_m either the diameter or the width of membrane and p_m the pressure difference generated across the membrane due to its deflection. The prefactor is $k_w = 256/3$ for a circular membrane and $k_w = 66$ for a square membrane.

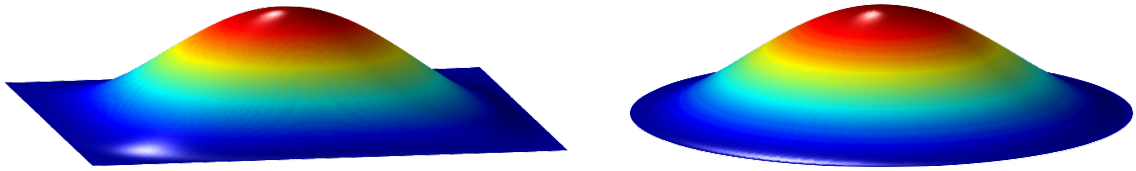

(a) (b)

Figure 8.3: Schematic of the deflection (a) a square clamped membrane and (b) a circular clamped membrane.

By a surface integration of either (8.4) or (8.5), one gets the volume associated with the deformation of the membrane from its plane state:

$$V = \iint_S w(x,y)dS = k_S \frac{a_m^6}{d_m^3} \left(\frac{1-\nu_m^2}{E_m}\right) p_m = k_S k_w a_m^2 w_0 \tag{8.6}$$

where k_S is a shape factor. For a circular membrane:

$$k_S = \frac{\pi}{1024} \simeq 3.1 \times 10^{-3}$$

For a square membrane:

$$k_S = \frac{1}{66}\left(\frac{8}{15}\right)^2 \simeq 4.3 \times 10^{-3}$$

The proportionality coefficient between V and p_m is the hydraulic capacitance C_{hm} of the membrane :

$$\boxed{C_{hm} = \frac{dV}{dp_m} = k_S \frac{a_m^6}{d_m^3} \frac{1-\nu_m^2}{E_m}} \tag{8.7}$$

This hydraulic capacitance is the key stone of our flow rate measurement approach that relies on the determination of a volume change from the measurement of the time dependent pressure difference across the membrane deformed in linear regime.

8.2 Design of the hydraulic capacitor

The hydraulic capacitance C_{hm} depends on the dimensions and mechanical properties of the membrane (equation (8.7)). The material of choice used to prepare slightly deformable membrane is generally silicon. For this material $E_m \sim 150$ GPa and $\nu_m \sim 0.3$. These two values are only order of magnitude as silicon is rarely an isotropic material. The mechanical properties being fixed, the quantities to be estimated are the thickness and the width of the membrane. These dimensions can be estimated from the calculation of the capacitance required to be able to measure a flow rate of the order of the pL.min^{-1} and imposing the supplementary constraint of a linear behavior.

8.2.1 Scaling the membrane

The hydraulic capacitance is strongly dependent on its dimensions. From equation (8.7) one can see that the hydraulic capacitance is proportional to the power 6 of the membrane width and inversely proportional to the power 3 of the membrane thickness.

To scale the membrane, the two main quantities to be estimated are the minimum detectable pressure variation Δp and the corresponding volume variation ΔV associated with the membrane deflection. We want to be able to do flow rate measurements in the presence of various field gradients namely, voltage, concentration or pressure. To be able to study voltage or concentration gradients only, it is necessary that our measurement approach does not create any significant pressure change during the measurement. A variation $\Delta p \sim 10$ Pa corresponds to a 1 mm height of water, is taken as the lower limit for the pressure detection. Such a pressure difference between the extremities of a nanochannel would drive a negligible flow rate less than 3 orders of magnitude of our reference flow rate of 1 pL.min^{-1}. The volume variation associated to the pressure change Δp, resulting from the membrane deflection, is imposed to be smaller than 100 pL. Such volume correspond to an integration time of 100 min, or 1.5 h, for a flow rate of 1 pL. The ratio of these two quantities $\Delta p/\Delta V$ gives an upper limit for the hydraulic capacitance C_{hm} of 10 pL.Pa^{-1}. The maximum width of the membrane can be estimated from this value using the relation (8.7)

$$a_m^3 = \frac{E_m}{1-\nu_m^2}\left(\frac{d_m}{a_m}\right)^3 \frac{C_{hm}}{k_S} \tag{8.8}$$

In this relation the aspect ratio d_m/a_m can be estimated from the relation (8.5). As the system is supposed to behave as in thick membrane case, the deflection in the middle of the membrane has to remain smaller than the thickness of the membrane $w_{0(max)} \ll d_m$. Considering $w_{0(max)} \sim d_m$:

$$\frac{a_m}{d_m} \sim \left(k_w^{-1} \frac{E_m}{1-\nu_m^2} p_{m(max)}^{-1} \right)^{1/4} \tag{8.9}$$

where $p_{m(max)}$ is the maximum pressure jump corresponding to the maximum deflection in the middle of the membrane $w_{0(max)}$. Considering that in linear regime the membrane is able to sustain 100 times the minimum detectable pressure variation, $p_{m(max)} \sim 10^4$ Pa. As a result, with $C_{hm} \sim 10$ pL.Pa^{-1} and $E_m/(1-\nu^2) \sim 160$ GPa:

$$a_m^3 \sim \frac{k_w^{-1/4}}{k_S} \left(\frac{E_m}{1-\nu_m^2} \right)^{1/4} p_{m(max)}^{3/4} C_{hm} \sim 10 \text{ mm}^3 \tag{8.10}$$

One should note from this last expression that the width a_m of the membrane is slightly dependent on the maximum pressure as $a_m \propto p_m^{1/4}$ and very slightly dependent on the mechanical properties of the material as a_m is proportional to the power 1/12 of the ratio $E_m/(1-\nu^2)$. From equation (8.10), one find a reference membrane width $a_m \sim 3.5$ mm and using this value in equation (8.12), a reference membrane thickness $d_m \sim 10$ µm. Figure 8.4 gives the value of the hydraulic capacitance C_{hm} according to a_m and d_m taken around their reference values. Dimensions needs to be chosen so that $C_{hm} < 10$ pL.pa^{-1}. Nevertheless, this simple theoretical model of

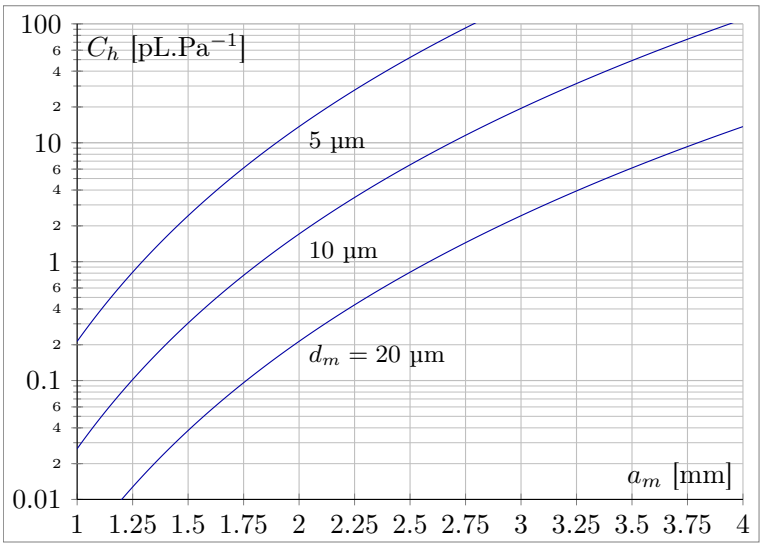

Figure 8.4: Variation of the hydraulic capacitance C_{hm} of a clamped square membrane according to its width a_m for different thicknesses d_m.

the capacitance according to the dimensions of the membrane gives only an order of magnitude of C_{hm}. Significant variations may be observed if the membrane is not a plain square membrane, for instance if the thickness of the membrane is not uniform or in presence of a significant surface stress. Another aspect that may lead to a shift

of the hydraulic capacitance from the theoretical value is the impact of the fluid compressibility. As a result, to know the real value of the hydraulic capacitance, a calibration step is compulsory, as described in paragraph 8.2.3.

8.2.2 Measuring the jump of pressure across the membrane

The pressure difference generated across a clamped membrane is directly related to the stress sustained by the deformed membrane. The strain in such a membrane is not uniform and not isotropic. The use of a strain gages deposited onto the surface of the membrane with adequate orientation has proven to be an efficient way to measure the pressure difference across the membrane.

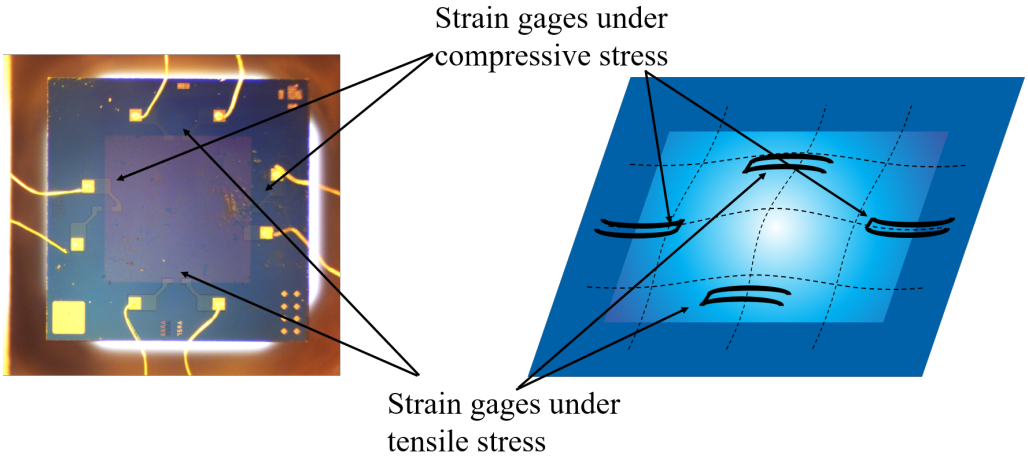

(a)

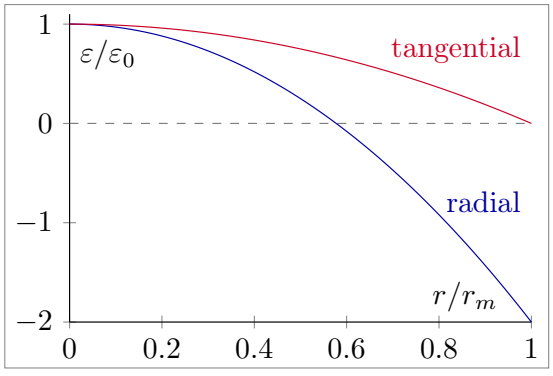

(b)

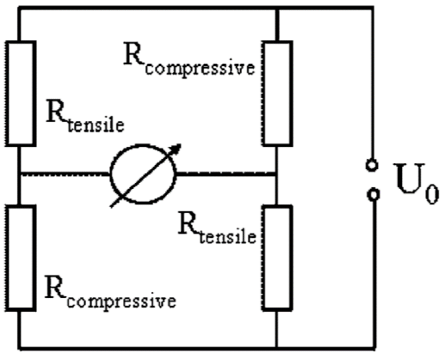

(c)

Figure 8.5: (a) An image of a membrane instrumented with four gages on it and a schematic of gages under compressive and tensile stress when membrane is deflected. (b) Dimensionless radial and tangential stress against the radial position for a circular membrane (c) Wheatstone bridge with compressive and tensile stress.

An instrumented membrane is generally equipped with four gages, mounted in pairs each of them submitted to a different strain during the membrane deflection.

The non isotropic strain increases from the rim to the center. For a circular membrane the radial and tangential strains are:

$$\varepsilon_r = \frac{3}{8}\left(1 - 3\left(\frac{r}{r_m}\right)^2\right)\frac{1-\nu_m^2}{E_m}\frac{r_m^2}{d_m^2}p_m \tag{8.11}$$

$$\varepsilon_t = \frac{3}{8}\left(1 - \left(\frac{r}{r_m}\right)^2\right)\frac{1-\nu_m^2}{E_m}\frac{r_m^2}{d_m^2}p_m \tag{8.12}$$

As shown in the figure 8.5b, the membrane is submitted to a compression at the rim and a dilation at the center while the tangential strain is purely dilational. To reveal the membrane deflection, the gage pairs are either placed with perpendicular orientation near the rim, as shown in figure 8.5a or with the same orientation at different locations, two of them close from the center and two others near the rim.

The two pairs of gages are electrically connected so as to form a Wheatstone bridge (figure 8.5c). When the membrane is at rest the Wheatstone bridge is equilibrated while under deformation the voltage difference between the two branches of the bridge is proportional to the difference of pressure across the membrane. The calibration of the sensor is made measuring the voltage difference of the Wheatstone bridge for an imposed difference of pressure across the membrane. This type of instrumented deformable membrane are commonly found in piezoresistive pressure sensors.

Such commercially available silicon instrumented membrane corresponds to our need. As we shall see, a piezoresistive pressure sensor can be converted into a flow rate sensor after a calibration step, to know the hydraulic capacitance of the sensor.

8.2.3 Calibration method for the hydraulic capacitance

The calibration can be done with the help of a capillary of known length L and radius r. When a liquid is pressurized to flow within such a capillary, the pressure drops between the inlet and outlet because of the viscosity effects. A linear relation between the pressure drop and volumetric flow rate is given by the Hagen-Poiseuille law, neglecting end effects:

$$\Delta P = \frac{8\eta L}{\pi r^4} \times Q \tag{8.13}$$

where ΔP, η, and Q are respectively the pressure drop across the channel, the viscosity of the liquid, and the flow rate through the capillary. This equation can be written as:

$$\Delta P = R_h \times Q \tag{8.14}$$

where R_h is the hydraulic resistance, analogous to the electrical resistance, defined as the ratio of the difference of pressure over the flow rate:

$$R_h = \frac{8\eta L}{\pi r^4} \tag{8.15}$$

The calibration of the membrane is done measuring the relaxation time of an hydraulic circuit constituted of the hydraulic resistance and the deformable membrane mounted in series.

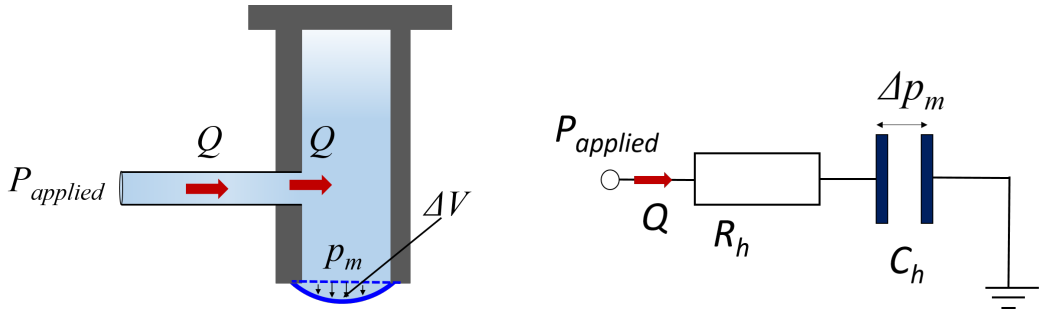

(a) (b)

Figure 8.6: (a) Schematic showing a calibration capillary connected to a cavity clamped with a deformable membrane for calibration of the membrane. Q is the flow rate, p_m is pressure difference across the membrane. (b) Equivalent hydraulic circuit for calibration. R_h is the hydraulic resistance of the capillary and C_h is hydraulic capacitance of the membrane.

Starting from a system at uniform ambient pressure p_{ext}, the inlet of the capillary is submitted at an initial time to a constant pressure $p_a > p_{ext}$. The time dependent jump of pressure across the membrane follows a first order relaxation law:

$$p_m(t) = p_0 \left(1 - e^{-\frac{t}{\tau}}\right) \tag{8.16}$$

where $p_0 = p_a - p_{ext}$ and the time constant $\tau = R_h C_h$ is equal to the product of the hydraulic resistance time the hydraulic capacitance. The hydraulic capacitance is then the product of the time constant τ times the hydraulic conductance $G_h = R_h^{-1}$ of the calibration capillary. For t<< τ, the above equation can be linearized

$$p_m(t) = p_0 \frac{t}{\tau} \tag{8.17}$$

and C_h is related to the slope of the pressure against time:

$$C_h = \frac{p_0}{R_h} \left(\frac{dp_m}{dt}\right)^{-1} = p_0 G_h \left(\frac{dp_m}{dt}\right)^{-1} \tag{8.18}$$

The hydraulic resistance is chosen so that the calibration can be done on time scale of the order of 1 min. This means that the hydraulic resistance has to be of the order of $R_h \sim \tau/C_h \sim 1$ Pa.min.pL^{-1}. The length of the capillary with respect to its diameter ϕ is $L = R_h \pi \phi^4/(128\eta) \sim \pi \phi^4 \tau/(128 C_h \eta)$ as shown in the figure 8.7.

8.3 Experimental requirements

In this section, the first experimental set-up and the results obtained with it are presented. Following this, the physical quantities that need to be carefully controlled to carry out the flow rate measurement with a limited uncertainty are elaborated.

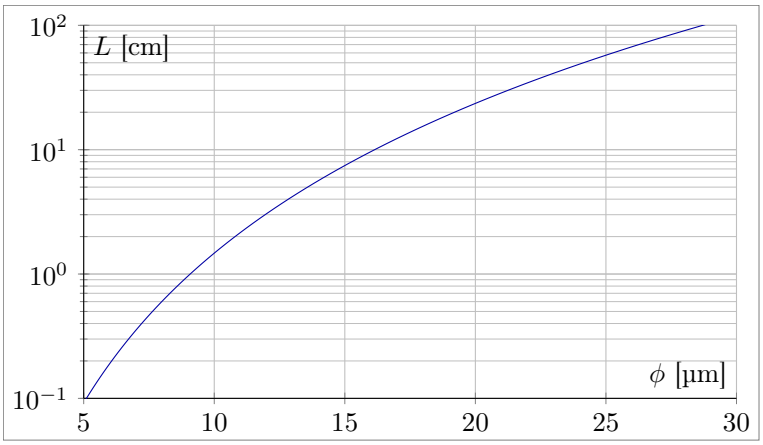

Figure 8.7: Dependance of the length of the capillary with respect to its diameter for a calibration with water to get a time constant of 1 min and for an hydraulic resistance of 1 Pa.min.pL^{-1}.

8.3.1 A tentative set-up: results and feedback

The first experimental set-up for flow measurement has been prepared adapting the custom made fluidic cell presented in chapter 3 with a piezoelectric pressure transducer (Omega, PX160 series: 163PC01D36). This sensor comprises of a silicon square membrane (3 mm width) that can measure a maximum pressure of 1200 Pa. The thickness of the membrane, measured when the sensor was broken, was approximately 10 µm. The pressure transducer is built within a thermoplastic housing having two pressure ports indicated by P_1 and P_2 (figure 8.8). Port P_1 is compatible only for dry gases because all the circuitry (gages and other electronics connections to the integrated circuit) is in connection with this port. Port P_2 is compatible for the media which does not attack on silicon and silicon based adhesives. This pressure port is constructed with a rectangular glass cuvette ($3 \times 3 \times 10mm^3$) and anodically bonded with a deformable silicon membrane instrumented on the other side (pressure port P1 side).

The external surface of the cuvette is encapsulated within a thermoplastic resin beyond the height of the glass cuvette. It is required to customize the pressure transducers by cutting the plastic head of the pressure port $P2$ until the proximity of the top of glass cuvette (figure 8.8). This facilitates filling of liquid inside the glass cuvette and avoids the trapping of air bubbles.

Preparation A half PEEK cell has been glued to the prepared sensor by epoxy based glue (Araldite) as shown in figure 8.9a. A glass substrate, sandwiched between the two half cells, has been thoroughly cleaned via successive sonication in soap solution and isopropanol prior to its use. The schematic of the whole fluidic cell and set-up is shown in figure 8.9.

The inlet of the cell has been divided into two fluidic paths by means of a four way manual valve (Upchurch Scientific). One path had a connection to a PEEK

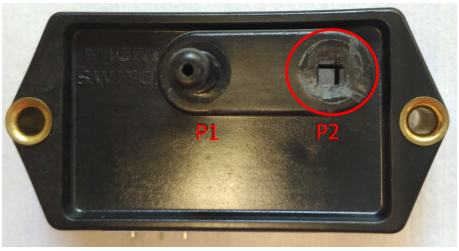

Figure 8.8: Schematic showing the pressure transducer. The top of the pressure port P_2 is cut until the glass cuvette (in red circle). The silicon membrane within the cuvette can be seen in gray colour (enclosed within the circle).

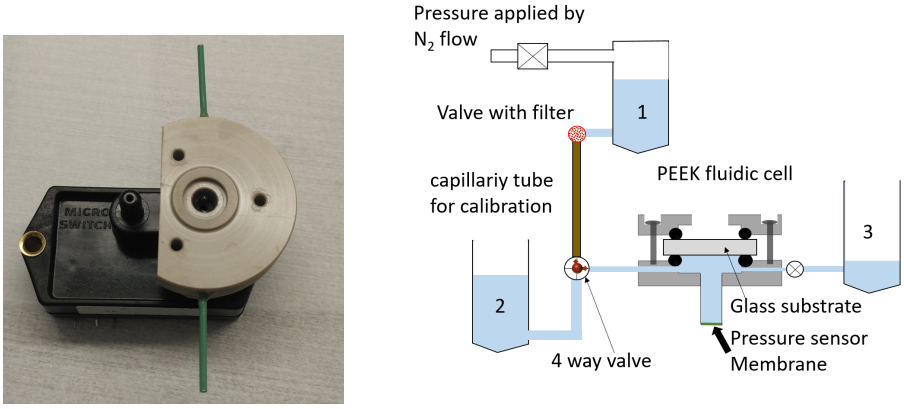

(a) (b)

Figure 8.9: Schematic showing (a) the custom made PEEK half cell glued on the top of the pressure transducer (163PC01D36) and (b) the first experimental fluidic cell set-up.

capillary tube ($ID = 25\ \mu m$, $L = 1.5\ m$, from Upchurch Scientific), used as the calibration capillary, further connected to a 15 mL falcon tube 1 filled with water. A pressure up to 1 bar can be applied to this falcon tube by means of N_2 gas flow as explained in chapter 3 in order to perform calibration for hydraulic capacitance. The second path had a connection to a second falcon tube 2, exposed to atmospheric pressure. The outlet of the fluidic cell has been connected to a tight fitting two way valve in PEEK (Upchurch Scientific) linked to the falcon tube 3. The four way valve allows the connection of the fluidic cell either to the calibration capillary under pressure or to the falcon tube filled with water, exposed to the atmosphere. If the 4 way valve is rotated by 180°(in reference to the inlet of the fluidic cell), the liquid is enclosed within the cell.

Calibration A pressure of 0.5 bar and 1 bar was applied to induce a flow within the capillary. This increases the liquid volume within the pressure sensor cuvette due to deformation of membrane. The time dependent pressure jump across the membrane of the sensor was recorded (figure 8.10). At first, the height of water in falcon tube 2 was levelled with that of the pressure sensor membrane. This sets a zero pressure difference across the membrane. The 4-way valve was rotated to

induce liquid flow through the capillary tube to the cavity of the transducer.

Figure 8.10 shows the variation of normalized pressure p_m/p_0 as a function of time. It can be seen that the normalized pressure increases linearly. The experimentally obtained curves were fitted from equation (8.17). The value of time constant τ obtained from the fit was 5890±25 s. Taking into account the value of τ, the hydraulic capacitance was calculated to be $C_h = \tau/R_h$ with R_h hydraulic resistance of the capillary. The hydraulic resistance of the calibration capillary ($L = 1.5$ m,$D = 25$ µm) was calculated to be 1.56×10^2 Pa.s.pL^{-1} using the relation (8.15).

From this experiment the hydraulic capacitance of the membrane was found to be 38±3 pL.Pa^{-1}. This value appears to be about 13 times larger than the theoretical value of 3 pL.Pa^{-1} calculated in the earlier section.

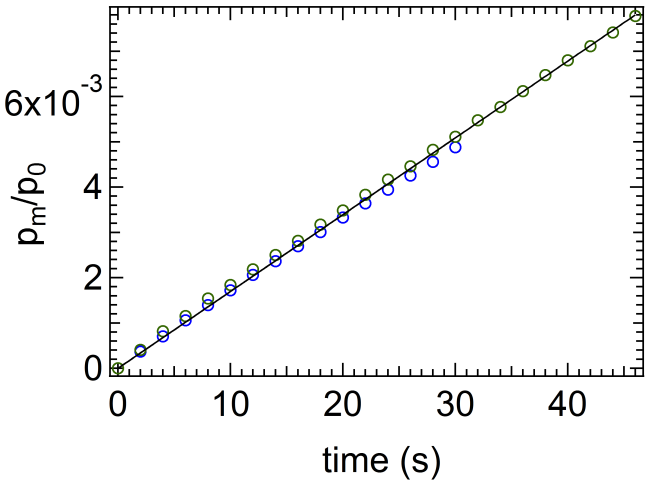

Figure 8.10: Calibration curve for an applied pressure 1 bar in blue and 0.5 bar in green. The black solid line is the fitting from equation (8.17).

Stability test After the calibration all valves were closed. Under the present set of experiments, the volume of the liquid confined within the fluidic cell is supposed to be constant. This should lead to a constant pressure difference across the membrane. This implies that no change in the pressure difference across the membrane should occur as a function of time. Thus, to validate this hypothesis a stability test was performed wherein the pressure difference across the membrane was monitored as a function of time. Figure 8.11 represents the time dependence of the measured pressure difference across the membrane.

A steady value of pressure difference at first denotes the open state of the valve, being exposed to the atmosphere. Upon closing the valve, fluctuations in the readings arise, which could be attributed to the mechanical vibrations in the set up. Over the course of the experiment, significant drifts were observed: following a steady state, p_m first increased and then decreased towards negative values with a rate of 160 Pa.min^{-1}(obtained following a linear fit between 8 and 10 minutes).

From the measured hydraulic capacitance of the sensor, this drift corresponds to a flow rate of the order of 6.10^3 pL.min^{-1}. Such a huge drift in volume is not acceptable as we would like to measure flow rate of few pL.min^{-1}.

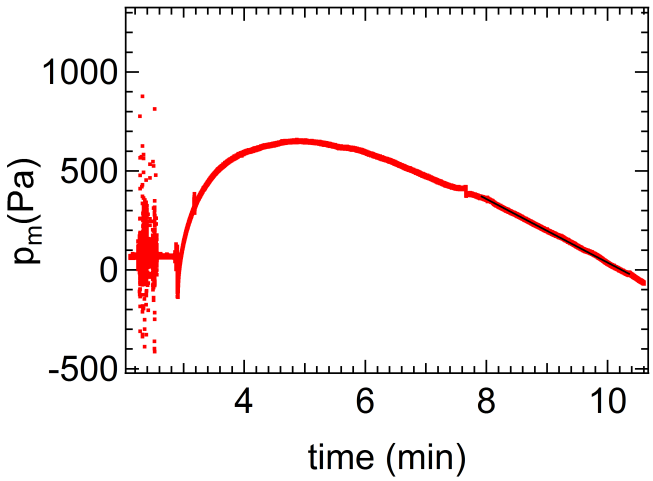

Figure 8.11: Schematic showing the variation of pressure difference across the membrane as a function of time. The black solid line is the linear fit.

Conclusion Improvements in the measurement cell are required. At first, the potential causes of the large experimental capacitance as well as lack of stability had to be identified before attempting to correct them. Three main implicit hypothesis had been made during the experiment:

- The liquid dead volume within the cuvette, supposed to be constant in time, was ignored.
- The closed cuvette was considered as infinitely rigid in comparison to the deformable membrane.
- The cuvette wall was considered as fully non permeable and non absorbent.

We shall come back on these hypothesis to identify the possible reason that may play a role in order to envision subsequent corrections.

8.3.2 Impact of the volume of liquid on the mechanical and thermal sensitivity of the sensor

Impact of the liquid compressibility Our flow rate measurement approach relies on collecting the liquid, flowing out from the nanochannel, in a rigid cavity closed by the deformable membrane used as a hydraulic capacitor. The deflection of the membrane, linked to the increase of the volume, is also responsible for an increase of the pressure of the fluid contained in the cavity. This pressure increase induces in turn a compression of the fluid.

This compression corresponds to an additional variation of the amount of fluid in the cavity all the more significant that the volume of the cavity and the compressibility of the fluid are large. More rigorously, the mass flux of fluid ρq entering the cavity is balanced by the time derivative of the product of the volume V of the cavity by the average density ρ of the fluid. This time derivative expresses as well as the sum of two terms. The first term is the time derivative of the volume of the cavity multiplied by the average density of the fluid. This term is the contribution associated to the deflection of the membrane. The second term, related to the compressibility of the fluid, is the time derivative of the average density of the fluid multiplied by the volume of the cavity.

$$\rho q = \frac{d}{dt}(\rho V) = \rho \frac{dV}{dt} + V \frac{d\rho}{dt} \tag{8.19}$$

Dividing this relation by the average mass density, the flow rate q is

$$q = \frac{dV}{dt} + V \frac{1}{\rho} \frac{d\rho}{dt} \tag{8.20}$$

that writes also:

$$q = C_{hm} \frac{dp_m}{dt} + V \chi_f \frac{dp}{dt} \tag{8.21}$$

In this relation, χ_f is the isothermal compressibility of the fluid:

$$\chi_f = \frac{1}{\rho} \frac{d\rho}{dp} \tag{8.22}$$

and $p = p_{ext} + p_m$ is the absolute pressure within the cavity with p_{ext} the pressure on the dry side of the deformable membrane. If the dry side of the membrane is in direct contact with the atmosphere, the time derivative of dp_{ext}/dt is typically of the order of 10 Pa.h^{-1} because of atmospheric tide[1] but may rich values of the order of 100 Pa.h^{-1} when weather is changing, it means the same order of magnitude as dp_m/dt. The second term of the relation (8.21), related to the compressibility of the fluid, can be seen as an additional hydraulic capacitance $C_{hc} = V\chi_f$ submitted to a pressure difference p while the membrane hydraulic capacitance is submitted to the pressure difference $p_m = p - p_{ext}$. The two capacitors and the flow source forms a star connection as depicted in the figure 8.12.

Compared to the perfect non compressible case, the additional capacitance C_{hc} contributes to an increase of the integration time for a fixed pressure sensitivity of the measurement system. The impact of the compressibility capacitance C_{hc} becomes negligible with respect to the membrane capacitance C_{hm} if $V \ll C_{hm}/\chi_f$ considering $dp/dt \sim dp_m dt$. For a cavity fully filled with liquid water of compressibility $\chi_f \sim 5.10^{-10}$ Pa^{-1} and for a membrane capacitance $C_{hm} \sim 1$ pL.Pa^{-1}, this later condition corresponds to $V \ll 2$ mL. This condition requires to work with a cavity whose characteristic dimension is much less than the cm. In the first experiment the volume was of the order of 1 cm^3 that would have contribute to an increase of the hydraulic capacitance of only 50% and can not explain the almost one order discrepancy between the theoretical and measured capacitance.

[1] regular daily fluctuation in barometric pressure of the order of 100 to 200 Pa in half a day.

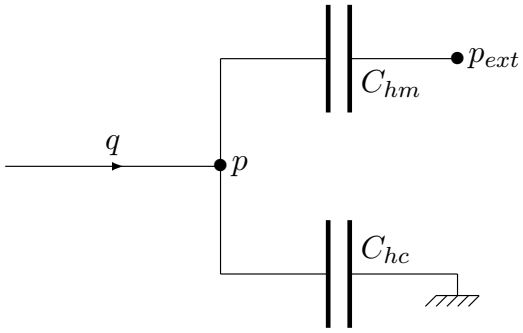

Figure 8.12: Schematic of equivalent hydraulic circuit. C_{hm} is hydraulic capacitance of the membrane and C_{hc} is compressibility capacitance. p is absolute pressure within cavity and p_{ext} is the atmospheric pressure.

Evaluation of the admissible thermal drift As the thermal dilation coefficient of solid is at least 10 times larger than liquid, the contribution of solid dilation is neglected here. We consider only in this estimation the thermal expansion of the fluid within the cuvette. The relative change in volume of liquid with respect to the temperature change is defined by the volumetric isobaric thermal expansion coefficient α_v of the liquid:

$$\alpha_v = \frac{1}{V}\frac{dV}{dT} \tag{8.23}$$

For water at room temperature $\alpha_v = 2 \times 10^{-4}$ K^{-1}. During a flow rate measurement the liquid in the cuvette might be submitted to a thermal dilation. Such a process induces a volume variation proportional to the liquid volume within the cuvette and to the temperature variation:

$$\frac{dV}{dt} = \alpha_v V \frac{dT}{dt} \tag{8.24}$$

In order to be able to carry out our flow rate measurement, the thermal dilation of the liquid should not be significantly larger than the flow rate to be measured of the order of $q_{ref} = 1$ pL.min^{-1}. Such a condition imposes that:

$$\boxed{V\frac{dT}{dt} < \frac{q_{ref}}{\alpha_v} \sim 5 \times 10^{-6} \text{ mL.K.min}^{-1}} \tag{8.25}$$

The acceptable thermal drift dT/dt is inversely proportional to the volume of the cuvette. For instance for the dead volume present in our first experiment $V \sim 1$ mL the drift should be smaller than $q_{ref/\alpha_v V} \sim 5 \times 10^{-6}$ K.min^{-1} or 0.3 mK.h^{-1}. In absence of any specific thermalization, the temperature in the experimental room shows a typical daily drift more than 3 order of magnitude larger than this target, that could at least partly explain the observed negative volume drift during the stability experiment. In order to be able to respect the criterion expressed by the relation (8.25) it is compulsory to minimize the volume V to relax the condition on the thermal drift dT/dt. **To do so we aim to work with a volume as close as possible to the minimal volume fixed by the size of the glass cuvette of the**

order of 0.1 cm^3. With such a volume the thermal drift has to be smaller than 3 mK.h^{-1}. Such a thermal drift would generate a volume variation the same order of the one resulting from the liquid flow. However, if the thermal dilation coefficient of the set up is well characterized experimentaly, it will be possible from the measurement of the temperature drift to apply a correection by subtracting the thermal dilation contribution to the measured volume increase.

8.3.3 Impact of gas inclusions

Isothermal contribution Although working with a fully degassed water, the trapping of a gas bubble during the filling of the system is highly probable, at least in the form of small voids due to the roughness of the surface itself or as a bubble as shown in figure 8.13.

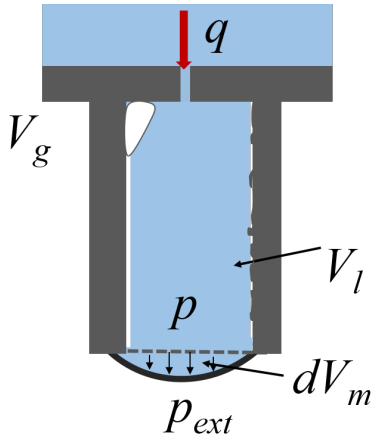

Figure 8.13: Schematic of pressure transducer cuvette with deformable membrane. The cuvette is partially filled with liquid of volume (V_l) and gas of volume V_g. The change in volume due to compressibility of bubble is denoted by dV$_g$.

For a cavity partially filled with a gas phase, a significant increase of the capacitance C_{hc} even with a limited amount of gas can be observed. The gas and liquid phases behave differently according to the pressure. In an attempt to estimate the impact of the presence of gas in the system and to which extend this amount may contribute to C_{hc}, a simple model is proposed assuming a perfect gas behavior neglecting solubilization effects. The capillary contribution is estimated considering the volume V_g is divided in a series of bubbles of radius r_b so that $V_g \propto r_b^3$.

Beyond the pure liquid case, the hydraulic capacitance C_{hc} is the opposite of the derivative with respect to pressure of the volume of fluid molecules either liquid or gas contained in the cavity at a certain time. This capacitance can be divided into two terms, one for the liquid of volume V_l and one for the gas of volume V_g:

$$C_{hc} = -\frac{\partial V_f}{\partial p} = -\frac{\partial V_l}{\partial p} - \frac{\partial V_g}{\partial p} = -\frac{\partial V_l}{\partial p} - \frac{\partial V_g}{\partial p_g}\frac{\partial p_g}{\partial p} \tag{8.26}$$

From the perfect gas law in isothermal conditions and fixed amount of gas:

$$-\frac{\partial V_g}{\partial p_g} = \frac{V_g}{p_g} \tag{8.27}$$

Using the Laplace law of capillarity $p_g = p + 2\gamma/r_b$ with γ the surface tension :

$$\frac{\partial p_g}{\partial p} = 1 - \frac{2\gamma}{r_b}\frac{1}{r_b}\frac{\partial r_b}{\partial p} = 1 - \frac{2\gamma}{3r_b}\frac{1}{V_g}\frac{\partial V_g}{\partial p} \tag{8.28}$$

Consequently:

$$\frac{\partial V_g}{\partial p} = -\frac{V_g}{p_g}\frac{\partial p_g}{\partial p} = -\frac{V_g}{p_g} + \frac{2\gamma}{3r_b p_g}\frac{\partial V_g}{\partial p} \tag{8.29}$$

As a result multiplying (8.29) by the ratio p_g/p:

$$\frac{\partial V_g}{\partial p}\left(1 + \frac{4\gamma}{3r_b p}\right) = -\frac{V_g}{p} \tag{8.30}$$

Finally

$$\boxed{C_{hc} = -\frac{dV_f}{dp} = V_l\chi_l + \frac{V_g}{p}\left(1 + \frac{4\gamma}{3r_b p}\right)^{-1}} \tag{8.31}$$

The contribution of the capillarity is significative only if $4\gamma/3r_b p \gg 1$ that is $r_b \ll 1$ µm, for $p = 10^5$ Pa and for $\gamma = 7.10^{-2}$ N.m^{-2}. In such a case, the strong curvature of the bubble limits their compression and the impact of the volume of gas on the global compressibility is damped. With bubbles larger than a few micron, the capillary effect remains negligible. In this case, the contribution of the gas phase to the compressibility capacitance is small only if $V_g/V_l \ll p_g\chi_l \sim 5.10^{-5}$ considering that p_g is close to the atmospheric pressure. If the hydraulic capacitance of the membrane is significantly larger than the compressibility contribution of the liquid, the previous condition can be relaxed and reduced to $V_g/p_g \ll C_{hm}$ that is $V_g/V \ll C_{hm}p_g/V$ as shown in the figure 8.14.

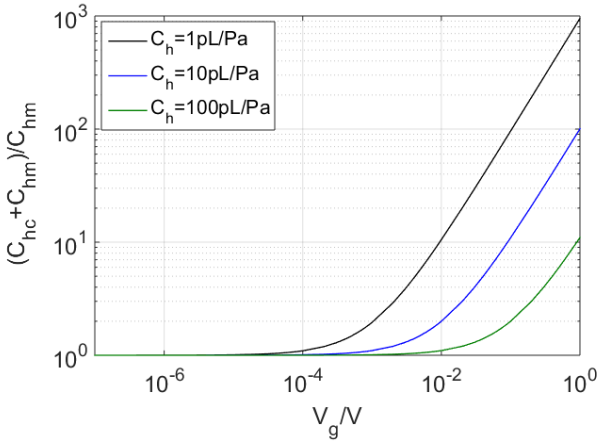

Figure 8.14: Ratio of the capacitances, in presence and absence of gas volume according to the volume fraction of gas V_g/V for $V = 0.1$ mL neglecting the capillary contribution.

Behavior in presence of a thermal drift Assuming that the behavior of the deformable membrane is not affected by the temperature, the variation of the fluid volume according to the variation of the pressure is imposed by the thermally constant membrane capacitance. Assuming the external pressure is constant $dp_{ext} = dp - dp_m = 0$ and in the absence of flow rate or phase changes, that is with fixed amount of liquid and gas:

$$\frac{dV}{dT} = C_{hm}\frac{dp_m}{dT} = C_{hm}\frac{dp}{dT} = \frac{dV_l}{dT} + \frac{dV_g}{dT} \tag{8.32}$$

From the paragraph 8.3.2 the derivative of the liquid volume with respect to temperature writes:

$$\frac{dV_l}{dT} = -\chi_l V_l \frac{dp}{dT} + \alpha_v V_l \tag{8.33}$$

Differentiating the perfect gas law for a fixed amount of gas:

$$\frac{dp_g}{p_g} + \frac{dV_g}{V_g} = \frac{dT}{T}$$

Following the derivation from equation (8.28), this leads to:

$$\frac{dV_g}{dT}p_g = p_g\frac{V_g}{T} - V_g\frac{dp_g}{dT} = p_g\frac{V_g}{T} - V_g\frac{dp}{dT} - \frac{2V_g}{r_b}\frac{\partial\gamma}{\partial T} + \frac{2\gamma}{3r_b}\frac{\partial V_g}{\partial T} \tag{8.34}$$

As a result:

$$\frac{dV_g}{dT}\left(p + \frac{4\gamma}{3r_b}\right) = \frac{V_g}{T}\left(p + \frac{2}{r_b}\left(\gamma - T\frac{\partial\gamma}{\partial T}\right)\right) - V_g\frac{\partial p}{\partial T} \tag{8.35}$$

Replacing dV_l/dT and dV_g/dT by equation (8.33) and (8.35) in equation(8.32):

$$C_{hm}\frac{dp}{dT} = -\chi_l V_l\frac{dp}{dT} + \alpha_v V_l + \frac{V_g}{T}\left(1 + \frac{2U_\sigma}{r_b p}\right)\left(1 + \frac{4\gamma}{3r_b p}\right)^{-1} - \frac{V_g}{p}\left(1 + \frac{4\gamma}{3r_b p}\right)^{-1}\frac{dp}{dT}$$

where $U_\sigma = \gamma - T\partial\gamma/\partial T = 0.11$ N/m at room temperature is the excess internal energy of the interface. Defining the dimensionless coefficient $k^*_\gamma = 1 + 2\kappa^*/3$ and $k^*_U = 1 + \kappa^* U_\sigma/\gamma$ related to the dimensionless curvature of the interface $\kappa^* = 2\gamma/(r_b p)$, the derivative of the pressure with respect to the temperature is:

$$\frac{dp}{dT} = \frac{\alpha_v V_l + V_g/T\ k^*_U/k^*_\gamma}{C_{hm} + \chi_l V_l + V_g/(pk^*_\gamma)} \tag{8.36}$$

Because of the low compressibility of the liquid and the limit volume of the cell $\chi_l V_l \ll C_{hm}$. In this limit the derivative of the volume with respect to temperature is:

$$\frac{dV}{dT} = C_{hm}\frac{dp}{dT} = C_{hm}p\frac{\alpha_v(V - V_g) + V_g/T\ k^*_U/k^*_\gamma}{C_{hm}p + V_g/k^*_\gamma} = \alpha_v V f(V_g, r_b) \tag{8.37}$$

where the function f expresses the correction from the pure liquid case. It is the dimensionless ratio of the volumetric thermal expansion in the presence of air to the thermal expansion when volume V is completely filled with liquid:

$$f(V^*_g, \kappa^*) = \frac{C^*}{C^* + V^*_g/k^*_\gamma}\left(1 + V^*_g\left(\frac{k^*_U/k^*_\gamma}{\alpha_v T} - 1\right)\right) \tag{8.38}$$

with the dimensionless quantities $C^* = C_{hm}p/V$ and $V_g^* = V_g/V$. For $V = 0.1$ mL and $C_{hm} = 1$ pL.Pa^{-1} and p equal to atmospheric pressure, $C^* \sim 10^{-3}$. For $\kappa^* \ll 1$ that is $r_b \gg 1$ µm the coefficients k_γ^{*-1} and k_U^*/k_γ^* are both of the order of the unity. In this limit and for T near room temperature, $\alpha_v T \sim 6.10^{-2}$ for water, the function f can be simplified as:

$$f(V_g^*) \sim \frac{C^*}{C^* + V_g^*}\left(1 + \frac{V_g^*}{\alpha_v T}\right) \tag{8.39}$$

In figure 8.15, $f(C^*, V_g^*)$ is plotted versus V_g^*. For small volume of gas in the cuvette:

$$f(V_g^*) \underset{V_g^* \to 0}{\sim} 1 + V_g^*\left(\frac{1}{\alpha_v T} - \frac{1}{C^*}\right) \tag{8.40}$$

For $C^* > \alpha_v T$, the function f is increasing while it is decreasing for $C^* < \alpha_v T$. The volumetric thermal expansion of the liquid-gas volume is not very significant for the ratio $V_g/V < 10^{-5}$. Under this volume of gas the thermal expansion of the system is dominated by the expansion of the liquid (the expansion of the gas is negligible) as described in paragraph 8.3.2. For large volume of gas present in the cuvette and for $C^* \ll 1$:

$$f(V_g^*) \underset{V_g^* \to 1}{\sim} \frac{1}{\alpha_v T}\frac{C^*}{C^* + 1} \sim \frac{C^*}{\alpha_v T} \tag{8.41}$$

For $C^* < \alpha_v T$ one finds $f(C^*) < 1$ while $f(C^*) > 1$ for $C^* > \alpha_v T$. For the value

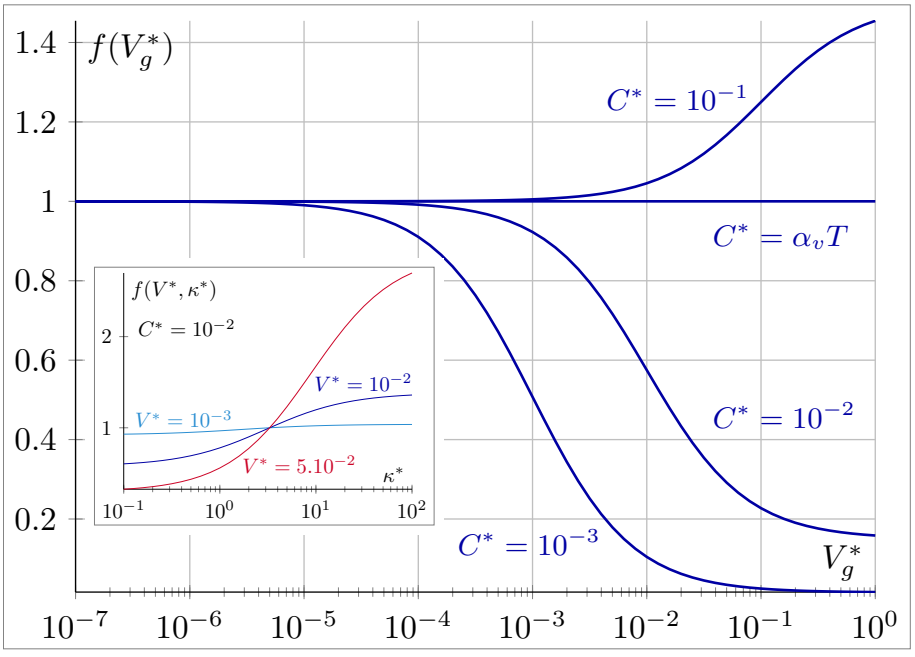

Figure 8.15: Evolution of the ratio of thermal expansion of the system in the presence and absence of gas volume with relative volume V_g^* when the capillarity contribution is neglected ($\kappa^* \to 0$) and $\alpha_v T = 0.06$. The inset shows the limited impact of κ^* on f significative only for important gas fraction V_g^* and large $\kappa^* = 100$; the value $\kappa^* = 100$ corresponds to $r_b = 14$ nm.

$C^* \ll \alpha_v T$ of interest for our measurement, the membrane is able to prevent the

thermal dilation of the gas due to its significant compressibility but it is not able to prevent the dilation of the liquid because of its negligible compressibility. As a result, the presence of gas does not emphasize the thermal drift unless in presence of a collection of sub-micrometric gas inclusions. In this case, k_{γ^*} increases linearly with the interfaces curvature while k_U^*/k_{γ^*} tends to the asymptotic value $3U_\sigma/2\gamma = 2.6$ at room temperature. For a total volume of gas inclusion large enough so that $V_g^*/\alpha T > 1$ and for curvature strong enough so that $V_g^*/k_\gamma^* \ll C^*$ the previous trend can be reversed. In this limit:

$$f(V_g^*) \underset{k_\gamma^* \gg V_\gamma^*/C^*}{\sim} 1 + \frac{3U_\sigma}{2\gamma}\frac{V_g^*}{\alpha T} \tag{8.42}$$

The inset of the figure 8.15 shows that the impact of curvature is significative only for sub-micrometric bubble radius and large amount of gas, the combination of this two characteristics being unlikely if the system is thoroughly degased. This means that the condition found in the pure liquid case is indeed the one to be taken into account for the thermal control of the system.

8.3.4 Volume drift and parasitic fluxes

Up to this point, the system was assumed to keep, at zero flow rate, a constant amount of liquid and gas within the measurement cuvette. However, diffusion fluxes that may contribute to unwanted volume changes might have to be taken into account. This fluxes can be of different natures: solubilisation/desolubiliation of the gas in/from the liquid phase, absorption of the liquid within the wall of the container, permeation of the liquid through the wall of the container. Associated to the absorption effect, one may observe a deformation of the cell walls that may compromise the rigidity hypothesis which is the key stone of our sensor.

Solubilisation effect Coming back to the perfect gas law, we consider now an isothermal behavior but a possible change of composition from a gas state to a solubilized state of gas molecule. The gas volume is the sum of a term related to gas compression and a term related to gas solubilization:

$$dV_g = \frac{RT}{p_g}dn_g - \frac{n_g RT}{p_g}\frac{dp_g}{p_g} = -\frac{RT}{p_g}dn_s - V_g\frac{dp_g}{p_g} \tag{8.43}$$

where n_g is the number of gas molecule in the gas state and n_s the number of mole in the solubilized state the sum n of the two being conserved. Using the dimensionless Henry's constant k_i relating the concentration in solubilized molecules c_{is} to the partial pressure $x_i p/RT$ for each species of fixed fraction x_i:

$$dn_s = V_l dc_s = V_l\frac{dp_g}{RT}\sum x_i k_i \tag{8.44}$$

As a result :

$$C_{hc} = -\frac{dV_f}{dp} = V_l\chi_l + \frac{V_l\sum x_i k_i + V_g}{p_g}\frac{dp_g}{dp} \tag{8.45}$$

The constant k_i are of the order of 10^{-2} for most of the gas (1.5×10^{-2} for N_2 and 3×10^{-2} for O_2) except for CO_2 for which $k = 0.8$ at room temperature. To give an order of magnitude, if p_g is close to the atmospheric pressure $\sum x_i k_i/(p_g \chi_l) \sim 10^3$. This means, considering that $dp_g/dp \sim 1$ in the equation 8.45, that the presence of a gas phase significantly increases C_{hc} through solubilization effects even if $V_s \ll Vl$. As a conclusion, although the kinetics of solubilization/desolubilization might be slow, these phenomena may contribute to a noticeable drift of C_{hc}. Our flow rate measurement systems requires to work with fully degassed liquid to avoid such a drift.

Contribution from the wall: Absorption, Permeation, Deformation Although PEEK is highly resistant to water and moisture, it still demonstrate 0.5 wt% absorption at saturation while immersed in water [100]. The slow uptake of water into our measurement cell would lead to a flow rate of the order of the one measured during our first experiment, moreover several days would be required to reach a stable state of saturation in water of the cell. In order to avoid such a long transient regime, the volume of PEEK pieces should be limited as much as possible. One major issue is the choice of the agent used to seal and bond pieces together. Three mains criterions needs to be met. The glue needs to absorb as less as possible the liquid. The swelling should be as limited as possible to avoid any consequent change of volume resulting from the displacement of bonded surfaces. The glue should present a good thermal stability to not increase the thermal drift induced by the liquid dilation. More over, after bonding, the presence of liquid should not induce any debonding between pieces. As these aspects are difficult to control in advance, we will have to proceed empirically from experimental trials.

Chapter 9

Experimental set up for pico-flow rate measurement

Contents

9.1 Control of the thermal environment

In the previous section 8.3.2, we have evaluated the thermal drift admissible during pico flow measurements of the order of 3 $mK.hr^{-1}$. This explains explicitly the need of a precise temperature measurement close to the flow cell and development of a thermally stable environment typically up to few $mK.hr^{-1}$.

9.1.1 Fluctuations in passive thermal environment

A passive thermal box is prepared in order to perform a comparative study of thermal drift in the presence and absence of insulation.

Temperature measurement

For sensitive temperature measurement, Pt100 temperature sensors were bought from RS France. The principle of operation is based on the measurement of the resistance of a platinum (Pt) element. For Pt100 the resistance of this Pt element is 100 ohms at 0°C and 138.4 ohms at 100 °C. The relationship between temperature and resistance is approximately linear over a small temperature range: for example, if we assume that it is linear over the 0 to 100 °C range, the error at 50 °C is 0.4 °C. For precision measurement, a third degree polynome is used to relate the resistance to the temperature. The linearization equation is:

$$R(T) = R_0(1 + A \times T + B \times T^2 + C \times (T - 100) \times T^3) \tag{9.1}$$

where T is the temperature in 0°C, R_0 is the resistance at 0°C, and A, B, C three numerical coefficients as follow:
A=0.391×10^{-3} K^{-1}
B=-5.77×10^{-7} K^{-2}
C=-4.18×10^{-12} K^{-3}
A four wire connection is used to measure the temperature. Two wires are used to supply the Pt sensor with a regulated current and two other to measure the potential drop across the resistance. The four wire temperature measurement is made using a multimeter (Keithley Model-2750) controlled by a Labview program.

Passive insulation

The passive thermal insulation is made in polystyrene with wall thickness of 5 cm with an interior dimensions of $14 \times 21 \times 14$ cubic centimeter. A beaker of capacity 2 liter filled with 1 liter water is placed in the middle of the box. The heat capacity of water per unit volume is largest among common liquids, therefore it is used as a thermal mass providing thermal inertia that averages thermal fluctuations. Another empty beaker of capacity 500 mL is placed within the thermal bath where the pressure sensor cell and temperature sensor are to be placed. The rest of the space within the box is filled with polystyrene beads. Three platinum sensors were implemented to measure the temperature at three different places: outside the box T1, inside the box T2 (within polystyrene) and inside the beaker T3 (figure 9.1a).

Figure 9.1b represents the temperature variation during 65 hours, outside of the box in red, within the box in black and inside the water bath in blue. At large time scale the amplitude of the temperature variation are damped to 1 K within the thermal box (inside the beaker) as compared to the amplitude outside the box of the order of 3 K. The variations are not sinusoidal: on the time course of one day, a slow decrease in temperature is observed during 18 h and followed by a rapid increase of temperature during 6 h. The drift in temperature measured inside the box is of the order of 0.1 $K.h^{-1}$ during the increase stage that is 30 time larger than what is required to be able to carry out our flow rate measurement.

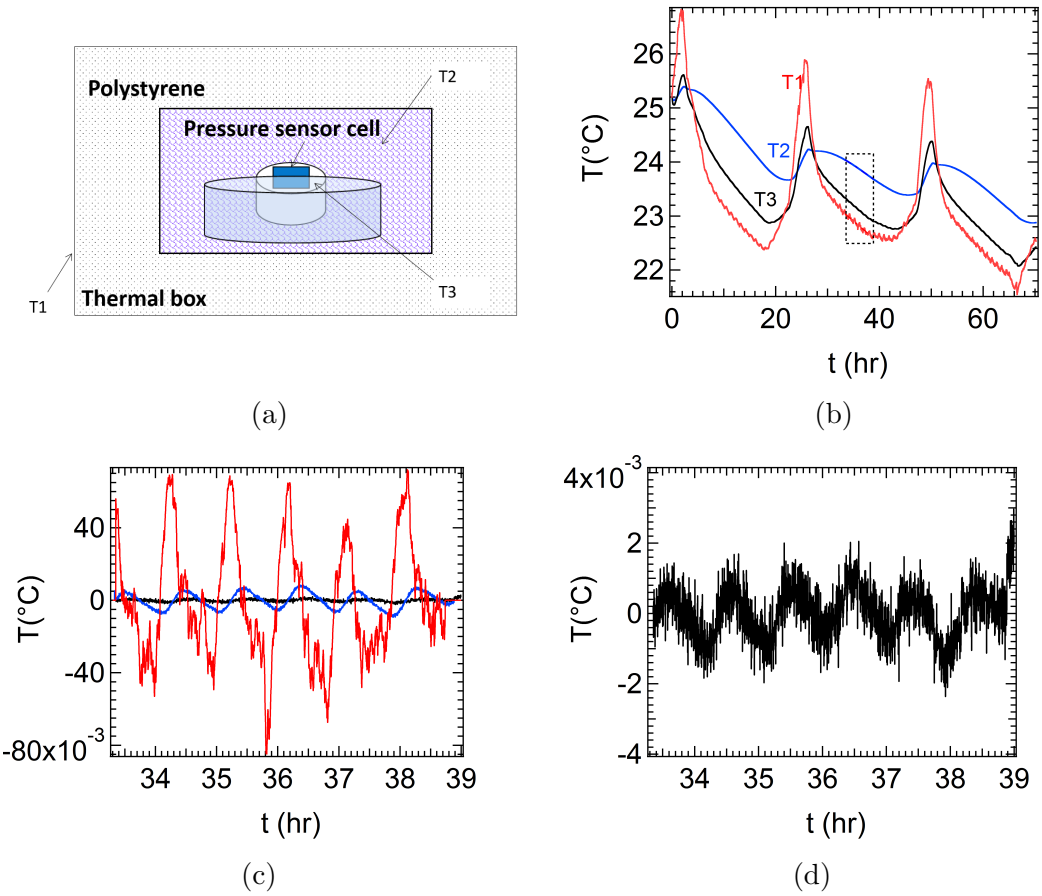

Figure 9.1: (a) Schematic showing of the passive thermal insulation. (b) Evolution of the measured temperature with time at 3 different places. The box presents the time interval where polynomial fit of $3^r d$ order was performed to extract the local fluctualtions in temperature (residuals). (c) Residuals of T1, T2 and T3 are plotted between 33-39 hr. (d) A zoom picture of the residual corresponding to temperature T3.

An additional oscillatory temperature fluctuations of approximately one hour time period is observed, presumably due to the fridge functioning present in the experimental room. Compared to the slow daily oscillation, the one hour sinusoidal oscillations are as expected much more efficiently damped. From an experimental curves fitting by a polynomial of third degree between 33 to 39 hours, these local fluctuations are extracted. Figure 9.1c and 9.1d represents these thermal fluctuations. Inside the room they are of the order of ± 200 mK while inside the thermal bath they are reduced to ± 4 mK at the time scale of one hour.

This behavior is confirmed using a simple model based on a unidimensional heat transfer in sinusoidal regime considering the thermal bath temperature as uniform. The complex temperature oscillation of the bath T_m is related to the magnitude T_o of the temperature oscillation outside of the box as follow:

$$T_m = T_o \left(\cosh(\epsilon\sqrt{i}) + N_i \epsilon \sqrt{i} \sinh(\epsilon\sqrt{i}) \right)^{-1} \tag{9.2}$$

with ϵ is the dimensionless thickness of the insulating box, expressed from the phys-

ical thickness $e_i = 5$ cm, ω the pulsation and $D_T = 1.5 \times 10^{-6}$ m^2.s^{-1} the thermal diffusivity of the expanded polystyrene insulator:

$$\epsilon = e_i \sqrt{\frac{\omega}{D_T}} \tag{9.3}$$

The product $N_i \epsilon$ is related to the ratio of the effusivities of the insulator and the thermal bath with N_i defined as:

$$N_i = \frac{mC_p}{m_i C_{pi}} \tag{9.4}$$

where $mC_p = 4200$ J is the thermal capacity of the water bath and $m_i C_{pi} = 120$ J the thermal capacity of the thermal box. The only free variable in this model is the pulsation ω.

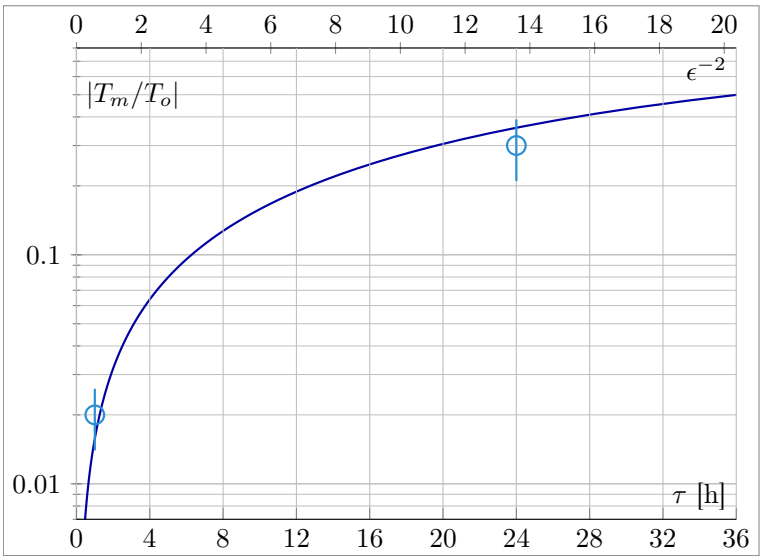

Figure 9.2: Damping of thermal oscillations according to the oscillation period τ. The square of the inverse of the corresponding dimensionless thickness of the insulator ϵ is indicating of the top axis. Markers are the 2 experimental points corresponding to daily and hour period oscillations. The plain line is the model prediction without free parameters, for our system $N_i = 35$.

Conclusion:

The above experiment gives us the typical temperature drift in the ambient atmosphere and inside the passive thermal environment. It demonstrates that the passive thermal box is able to damp by a factor larger than 50 oscillations of period smaller than 1 h and by a factor 3 oscillations of the order of one day period. This behavior is well described by 1D model without any free parameter. This experiment clarifies the requirement of a dynamic thermal regulation to be able to carry out our flow rate measurements.

9.1.2 Principle of the thermal environment stabilization

To be able to reach the thermal stability required for our experiment, the passive thermal box has been modified in order to avoid daily thermal oscillations. To do so an active control of the temperature is designed. The principle relies on the regulation of the temperature of the outer wall of the thermal bath. The thermal bath forms a water annulus contained between the outer wall of the bath and a cylindrical central container within which the sensor is placed. The regulation system may present oscillations of several minutes period around the target temperature. These fast oscillations are efficiently damped by the water layer separating the outer wall from the internal container because of the low thermal diffusivity of water $D_{Tw} = 1.4 \times 10^{-7}$ m^2.s^{-1}. On the other hand, at large time scale, the average temperature of the outer wall, which is transmitted to the internal container, has to present a drift smaller than 3 mK.h^{-1}, the limit required to be able to carry out the flow rate measurement.

Fast oscillations are efficiently damped only if water is not submitted to free convection. This hypothesis require to work with limited temperature fluctuations and a ratio of water thickness over water height small enough to stay in conduction regime. On the other hand free convection is of interest to fasten the transient regime of temperature stabilization during the start up of an experiment.

The dimensionless number that control the transition from the conduction regime to what is called the boundary layer regime is the product Ra^* of the Rayleigh number Ra multiplied by the aspect ratio of d_i/H [101]:

$$Ra^* = \frac{\alpha g \Theta}{\nu D_T} \frac{d_i^4}{H} \tag{9.5}$$

where g is the acceleration of the gravity, α the thermal dilation coefficient, ν the kinematic viscosity of water, Θ the difference of temperature between the inner wall and the outer wall, e the water thickness between the two wall and H the height of water. In permanent regime, the heat transfer is controlled by the Nusselt number $Nu = he/k_T$ where $k_T = 0.6$ W.m^{-1}.K^{-1} is the heat conductivity of water and h the heat transfer coefficient through the water layer. The typical time scale τ_t that characterizes the transient regime duration for the onset of free convection is given by:

$$\tau_t = \sqrt{\frac{e\nu}{g\alpha\Theta D_T}} \tag{9.6}$$

For a difference of temperature of 0.1 K, the typical time scale is of the order of 20 s. For periods of temperature oscillation significantly larger than 20 s, the system behave in quasi-static regime. For $Ra^* > 10^4$ free convection is observed while below $Ra^* < 10^3$ pure conduction is observed. The water annulus presents a gap $e = 3$ cm and a height $H = 9$ cm for which the conduction regime is observed for temperature difference lower than 0.01 K. In the conduction regime , the Nusselt number $Nu = 1$. As shown in figure 9.3a, beyond this temperature difference, one observes the onset

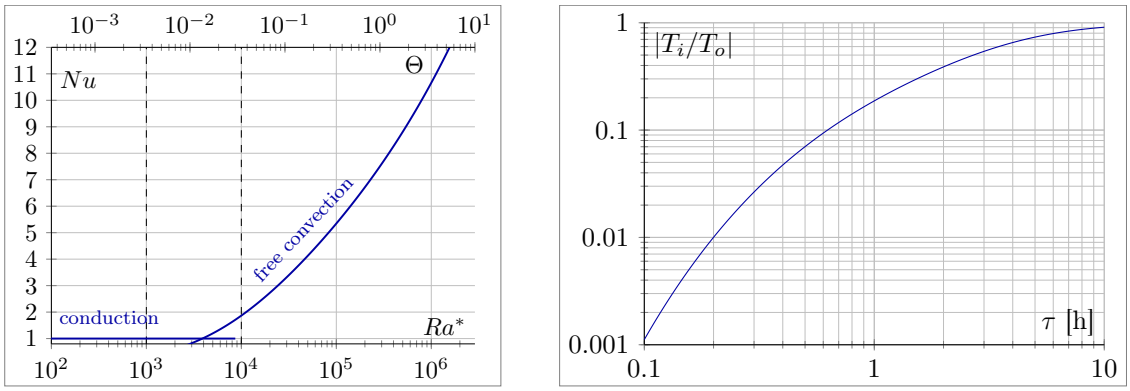

(a) (b)

Figure 9.3: (a) Dependence of the Nusselt number according to the dimensionless Ra^* number (lower axis). The associated time difference Θ is shown in the upper axis. (b) Ratio of the magnitude of the Temperature oscillation on the inner wall over the one on the outer wall.

of free convection with a noticeable increase of Nu according to the temperature that is responsible for a better heat transfer between outer and inner walls. In the free convection regime, Nu expresses as [102]:

$$Nu = \frac{hd_i}{2k_T \ln(d_o/d_i)} = \frac{1}{2\ln(d_o/d_i)} \times \frac{0.48Ra^*}{6830\,(d_i/d_o)^3 + Ra^{*3/4}} \tag{9.7}$$

In stationary regime, temperature differences between the inner and outer wall are smaller than 10^{-2} K. Such reduced temperature difference requires to limit as much as possible all power sources within the inner container. In this condition, heat transfers are purely conductive. The damping of temperature oscillations on the outer wall of the water annulus can be estimated from the relation (9.2) applied between the outer wall with temperature oscillation amplitude T_o and the inner wall with complex temperature oscillation T_i. In this configuration the thermal capacity of the inner cylinder is small with respect to the water bath and $N_i \ll 1$ so $T_i \sim T_o(\cosh(\epsilon\sqrt{i}))$ with ϵ express from relation (9.3) using the gap thickness of the water annulus and the thermal diffusivity of water. As shown on figure 9.3b, the chosen dimensions allow an efficient damping occurs for oscillation period shorter than 1 h.

9.1.3 Implementation of an active thermal box

The passive thermal box has been customized to implement the thermal regulation A flow of water at regulated temperature is circulated at the vicinity of the outer wall of the thermal bath to control its temperature. The circulation is forced within a tubing coiled along the wall. The thermalized water circulation is driven by a regulated and thermostated bath (CF31 Cryo-Compact Circulator, Julabo). The bath is able to regulate the temperature with a fluctuation smaller than 10^{-2} K

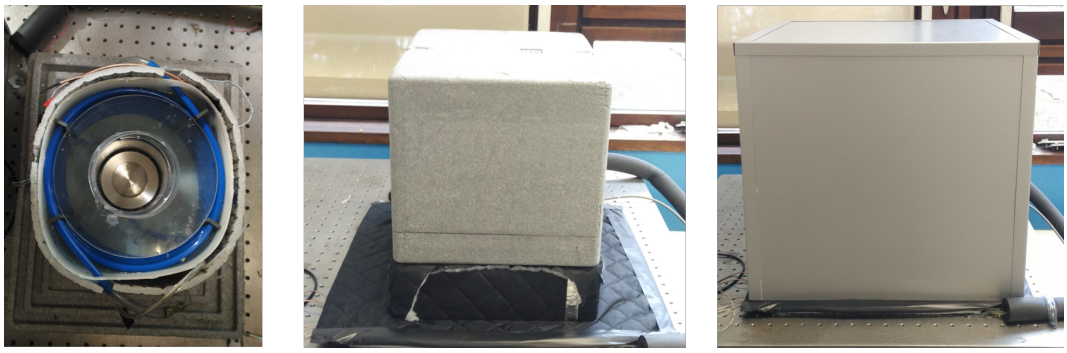

Figure 9.4: Schematic showing the active thermal regulation box. The first image is an insight of the active thermal box with thermal bath and a spiral coil in blue (further connected to the CF 31 cryo-compact water circulator to regulate temperature, not shown in picture). In the middle of blue coil free space is for the flow cell to be placed. Second and third images are of polystyrene box and prepared PU foam box to cover the set-up in first picture in order to limit the heat transfer with the ambient environment.

around the target temperature with a period oscillation of several minutes and a deviation between the average temperature measured by the regulation sensor and the target temperature smaller than 2 mK. The regulation sensor is a Pt100 resistance immersed within the water flow within the coiled tubing.

Because of the difference of temperature between the ambient environment and the inside of the box, a heat flux occurs across its insulated wall. This heat flux is counterbalanced by the energy provided by the water flow. This energy flux results in a gradient of temperature along the tube the larger that the difference of temperature between the inside and the outside is important. To limit the heat exchange with the ambient environment, the wall thickness has been increased. For this purpose a supplementary insulation box of 8 cm thick PU foam (Polyurethane) with an internal dimensions adapted to cover the polystyrene box. The thermal conductance of the final box is of the order of 0.1 $W.K^{-1}$. This means that 1 K difference between the inside and the outside of the box correspond to 0.1 W thermal flux. As the thermalized water flow rate is 10 $mL.s^{-1}$, the water temperature difference between the inlet and the outlet of the coiled tubing, associated to the heat flux compensation is of the order of 0.025 K. To compensate this potential temperature gradient in the water flow, the tubing has been coiled in a double counter rotating helix that allow the spatial averaging of the temperature on the outer wall of the thermal bath.

The use of the flow rate sensor require several electrical connections to control electrovalves needed to adjust the liquid volume within the sensor cuvette, to proceed to electrokinetic and piezoresistive flow rate measurements and finally to measure temperature. There are as well two fluidic connections via capillaries, to control the pressure and the fluid composition within the experimental cell. From a thermal point a view, in absence of flow through the capillaries, the main contribution of wiring and tubing comes from the copper wires whose thermal conductivity of 400 $W.K^{-1}.m^{-1}$ is 2.10^4 larger than the one of the insulating material of box.

The section area of all the copper wires is of the order of 10^{-6} m^2 which stands for 2.10^{-6} the surface area of the insulated box. The product of these too factors is 0.04, which means that the cable passing across the insulated box do not represent a significant thermal shortcut. For practical reason, the electrical connections and tubing pass through the horizontal base plate of the insulated box. In such a way the thermal box can be easily opened and closed with no interaction with the cables.

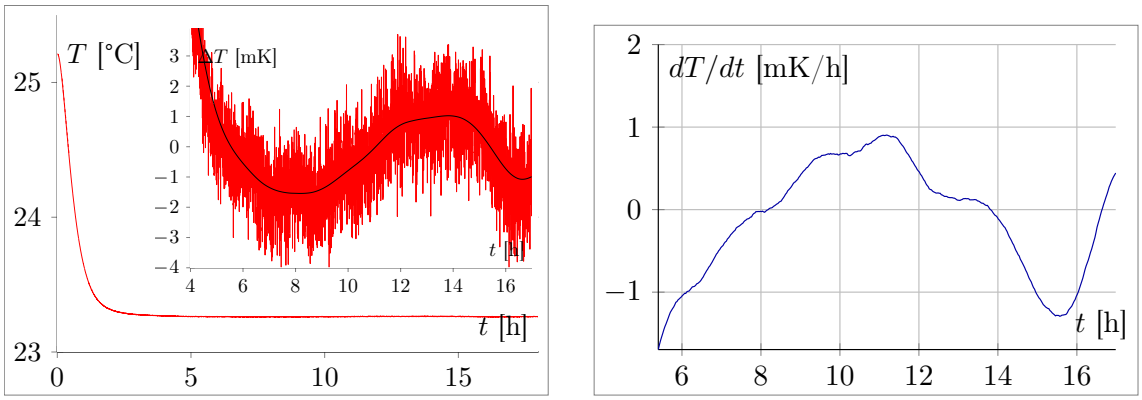

(a) (b)

Figure 9.5: (a) Temperature measured inside the active thermal box where the flow cell will be placed. The temperature has been measured by Pt100 sensor. The inset of the graph is a zoom of the temperature deviation from the mean temperature after stabilization, the line represents filtered data with a gaussian having a temporal width of 10 min. (b) Temperature derivative after stabilisation

As shown in the figure 9.5a, this home made thermalization system respect the thermal stability criterion with a thermal drift smaller than 3 mK.h^{-1} after stabilization. It takes about 2 hours to reach a stabilized temperature. After stabilization the drift is almost two order of magnitude smaller than the temperature drift measured in the passive box (figure 9.1b).

9.2 Elaboration of the measurement cuvette

The minimization of volume changes due to thermal dilation effects rely on the control of temperature as described in the previous section and on the reduction of the measurement volume as explained in the paragraph 8.3.2. To do so a pressure sensor has been chosen so that its cuvette can be directly used as the container of the measurement volume. An appropriate sealing process of the open end of the cuvette has been developed to assure rigidity and stability of the cuvette while providing an adequate structure for a future connection with nanopore samples.

9.2.1 Selection of the sensor

For the application of flow rate measurement the selection of an appropriate sensor with instrumented membrane has to present the following requirements:

- Compatibility with media to be used.
- Compact size to minimize the liquid volume.
- No integrated signal amplification or conditioning in order to minimize potential parasitic thermal drifts due to power supply.
- Pressure range and membrane dimensions in accordance with flow rate range as described in previous chapter (section 8.2.1).

The pressure transducers (163PC01D36 Omega Engineering) used during the feasability experiment includes an integrated signal amplification stage circuit whose power consumption was 0.1 W continuously. The active thermal box is able to stabilize efficiently the temperature only if the power delivered from the central container is limited enough to be evacuated through the annular water bath in conduction regime with a temperature difference between the inner and outer walls not larger than 1 mK in permanent regime. The power corresponding to this temperature difference is 0.5 mW. For this reason we focus at a compact pressure transducer pictured in figure 9.7 (PX170 Omega engineering) that includes only temperature compensated strain gages connected in Wheatstone bridge. This simple wheastone bridge can be supplied with a power much smaller than the 0.1 W previously required by the integrated circuit of the first sensor.

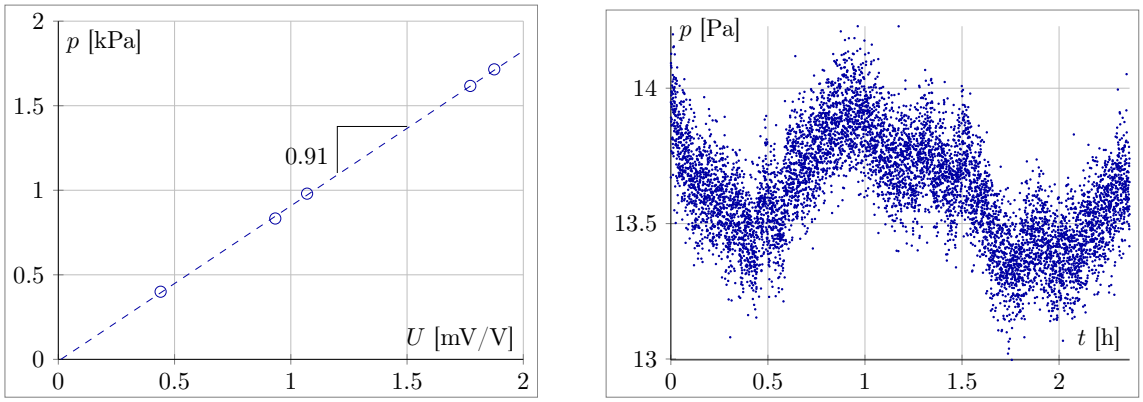

(a) (b)

Figure 9.6: (a) Calibration of the pressure sensor PX170, the signal U corresponds to the magnitude of the Wheatstone bridge voltage for a sinusoidal supply of 1 V amplitude. (b) Measurement of the pressure fluctuations delivered by a bare sensor in ambient atmosphere.

The input impedance of the bridge is 6.6 kΩ which corresponds to the resistance of each individual gage. Natively, the sensor is supposed to be supplied with 10 V dc,

which correspond to a power of 15 mW in absence of membrane deflection. In order to reduce this power while preserving the signal to noise ratio, the sensor is supplied with a sinusoidal voltage generated by a lock-in amplifier (Zurich Instruments) which is also used to measure the difference of electrical potential across the bridge. The amplitude of the sinusoidal applied voltage is 100 mV, which corresponds to a power of 1.5×10^{-6} W dissipated through the Wheastone bridge. The measurement signal is a sinusoidal voltage whose amplitude is proportional to the difference of pressure across the membrane. We work at an arbitrary frequency of 217 Hz different from a multiple of 50 Hz. This frequency is low enough so that the electrical capacitive inductance of BNC cables used to connect the sensor can be neglected in comparison to the purely resistive impedance of the sensor. As a result, the response of the system is close to the dc response, the phase shift between the input and response signals is negligible. The frequency is on the other hand high enough to allow a precise measurement of the pressure with an integration time of 0.5 s. With such a configuration, the pressure fluctuation is of the order of 1 Pa around the mean value as shown in figure 9.6b. Such a stability is compatible with the ability of measuring a difference of pressure of 10 Pa as assumed for the scaling of the membrane in paragraph 8.2.1.

The sensor has been calibrated submitting the wettable side of the sensor membrane to a precisely measured height of water. Plotting the pressure with the ratio of the magnitudes of the bridge voltage over the supplied voltage, as shown in figure 9.6a, a gain of 0.91 Pa/(µV/V) has been found for the sensor in agreement with the one given by the producer. This sensor presents a linear behavior in the range 0-3000 Pa but it is able to sustain pressures up to 0.1 bar without any damage, which is of interest for the robustness of the flow rate sensor to be developed.

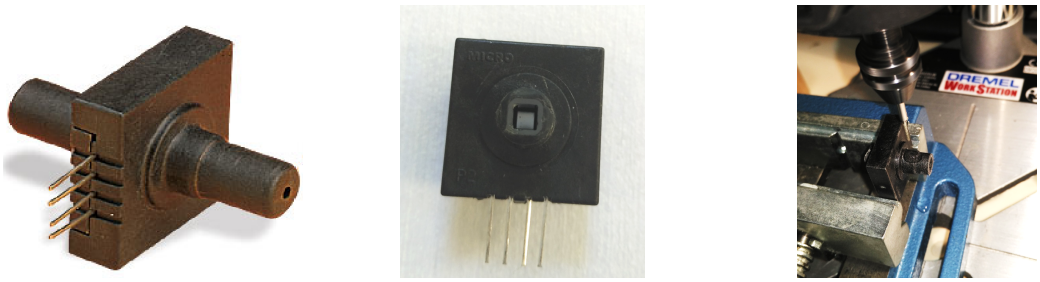

(a) (b) (c)

Figure 9.7: An image of PX170 Pressure sensor. This sensor is used in the upcoming experiments performed during the development of the pico flow cell. b) Pressure sensor (PX170) resin head cut upto the glass cuvette. c) Drilling the hole of 0.8 mm in the wall of glass cuvette of the pressure sensor with diamond drill.

The instrumented membrane of this sensor has a thickness about 13 ± 1 μm and a size 2.5×2.5 mm^2 with an uncertainty of 0.1 mm on the width of the membrane. From the relation (8.7), the theoretical hydraulic capacitance of the square membrane, calculated with $E_m/(1-\nu^2) = 160$ GPa, is $C_{hm=}3 \pm 1$ pL.Pa^{-1}, the important

uncertainty being related to the uncertainty on the dimensions of the membrane.

This sensor is of interest as the fluidic connection is made in square glass capillary compatible with the use of electrolyte solution. The glass capillary is closed on one end by the sensitive deformable membrane and opens on the other side. After removal of a protective resin around the capillary (figure 9.7b), a good access is available to fill the sensor with liquid and to visualize its content. The glass cuvette has a parallelepipedic shape with a depth of 14 mm and a square base of 3 mm width. The corresponding volume is 0.12 cm^3 in agreement with the criterion established in the paragraph 8.3.2. For these reasons, the sensor of PX170 series seems most suitable for our application for filling and mounting in the flow cell.

To get access to the glass cuvette, holes were pierced using a 0.8 mm diamond drill (Busch diamond impregnated drill bought from Diaminor). This delicate step is carried out with a droplet of water as a cooling agent while drilling (figure 9.7c). Later on, the pressure transducer is thoroughly cleaned by deionized water and isopropanol.

9.2.2 Sealing and bonding

The sensor glass cuvette has been closed using a flat pyrex substrate. This substrate is mounted in place of the PEEK cell used in the feasibility test. Several basic systems has been prepared in order to test several sealing agents to bond the pyrex substrate to the glass cuvette. After sealing, the signal delivered by a sensor has been measured with time in presence of liquid enclosed within the sealed cuvette. The stability of the pressure is a direct indication of the relevance of the sealing procedure: absorption, permeation, or deformation. These phenomena result in a deflection of the sensor membrane which is detected as a change of pressure versus time within the cuvette.

Simple epoxy glue

The cuvette of the pressure transducer has been closed with clean glass substrate with epoxy glue (Araldite). In this experiment, two soft tubing of external diameter of about 0.5 mm are allowed to pass within the glue in order to fill the sensor without any hole through the glass. Figure 9.8a represents the schematic of the pressure sensor flow cell. Filling of this type of flow cell is rather difficult due to trapping of bubbles. To solve this issue the cuvette is first saturated with CO_2 gas at atmospheric pressure. Once the cuvette is saturated by CO_2 gas, deionized water is allowed to flow within the cuvette. Due to good solubility of CO_2 in water, trapped gas progressively solubilizes within the liquid. After solubilization, deionized water is circulated long enough to expel liquid containing solubilized CO_2. Teflon valves mounted at the end of the capillaries has been closed and the sensor cell is placed inside the thermal regulation box. The temperature and the pressure are recorded with time.

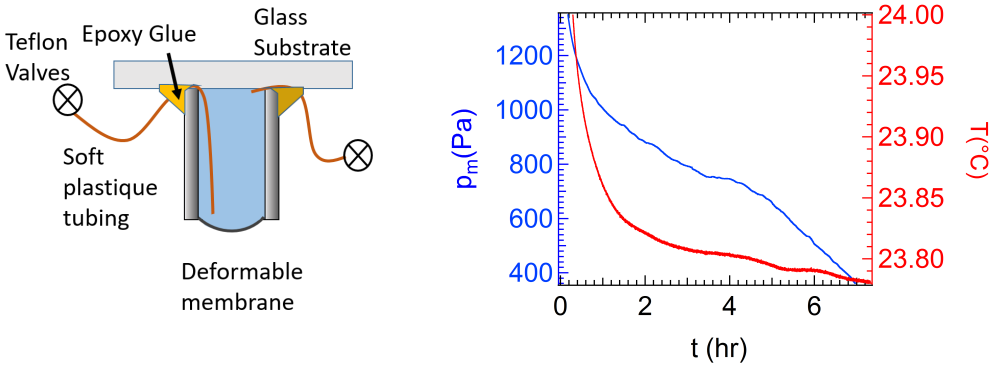

(a) (b)

Figure 9.8: (a) Schematic showing the basic pressure sensor flow cell prepared by pressure sensor and glass substrate for the stability test. (b) Evolution of pressure (in blue) and temperature (in red) with time.

Figure 9.8b represents the evolution of the pressure and temperature with time while the valves have been closed. The drifts in pressure and temperature, evaluated at two different times, are not proportional:
after 2 h, $dp_m/dt = -100$ Pa/h and $dT/dt = -0.016$ K/h
after 5.5 h, $dp_m/dt = -150$ Pa/h and $dT/dt = -0.005$ K/h.
These values of temperature and pressure drifts imply that the volume of the liquid enclosed within the pressure sensor cell decreases continuously regardless of the temperature drift with a rate 1 order of magnitude larger than the flow rate planed to be measured. The main suspect is the epoxy glue: swelling due to water absorption results in an upward motion of the pyrex substrate that manifests as an upward deflection of the membrane or a pressure decrease.

Epoxy glue plus silicon sealant

A layer of silicon sealant is placed under the glass substrate to prevent any direct contact between water and epoxy glue. The silicon for sealing while epoxy glue deposited above the silicon sealant has been used to provide rigidity between the substrate and the cuvette. Moreover to eliminate possible contribution of the capillary and valves, the cuvette has been first filled with water, then slowly closed with the siliconized glass, which is finally glued on the cuvette. Therefore, volume changes can be related only to temperature change or aging of the silicon/epoxy bond. Figure 9.9b represents the variations of pressure and temperature. In this configuration the pressure drift is still the same order of magnitude as the first experiment with a decrease of 100 Pa/h after 15 h although the pressure inside the cuvette is already 5% lower than the atmospheric pressure. This decrease in pressure is not correlated at all with the temperature.

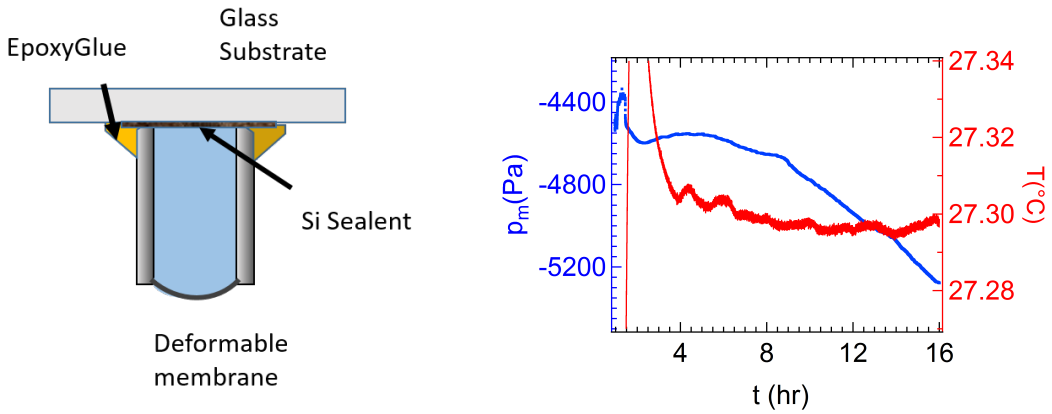

(a) (b)

Figure 9.9: (a) Schematic showing the basic flow cell prepared with pressure sensor and glass substrate for the stability test. (b) Evolution of pressure in blue and temperature in red with time.

Norland Optical UV curing glue

Figure 9.10 represents the next configuration of the pressure sensor cell based on Norland Optical Adhesives (NOA) UV curing glue regularly used in microfluidics. A

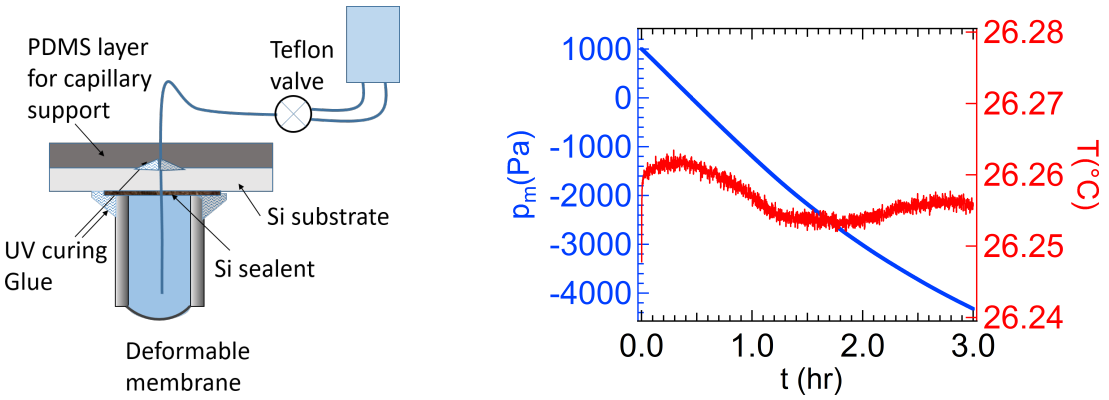

(a) (b)

Figure 9.10: (a) Schematic showing the basic flow cell prepared with pressure sensor and glass substrate for the stability test.(b) Evolution of pressure in blue and temperature in red with time.

layer of silicon sealant has been used to avoid direct contact of UV curing glue with water. To limit the amount of glue and to improve the contact between the cuvette and the substrate, a soft capillary tubing has been passed within a hole drilled in the middle of the flat substrate which is further connected to a manual valve in teflon and then to fluid container. The cuvette is filled with water and the space between the hole and tubing was filled with UV curing glue. During this procedure the teflon valve are left open so that if any change in volume takes place during the curing of UV glue it is balanced by the water flow through the tube. The valve has been

closed after curing and the pressure cell is placed inside temperature regulation box.

Figure 9.10b represents the variation of the pressure and temperature with time while the valve was closed. During this experiment the drift in pressure was 10 time large -2000 Pa/hr than the previous two experiments for a comparable thermal stability.

Stycast

STYCAST 2850 FT is a two component, thermally conductive epoxy encapsulant which is used with a variety of catalysts and shows excellent chemical resistance properties. It features a low coefficient of thermal expansion and good adhesive properties to glass too. When stycast is mixed with the catalyst 24lv, it is a black liquid of low viscosity which is able to fill all the voids or gaps. Normally, it takes 8-16 hours for curing the stycast at room temperature. We have used stycast 24lv for assembling the pressure sensor flow cell as shown in figure 9.11. Because this glue is not transparent, a more complex set up has been created to keep visibility into the cuvette from the upper substrate.

Two holes of 0.8 mm diameter has been drilled within two walls of the pressure sensor glass cuvette carefully in order to prepare connections for inlet and outlet. A rigid metal syringe needle of 0.7 mm external diameter is glued with stycast to the drilled holes. Another end of the syringes are joined to the PEEK tubing (ID-0.76, OD-1.6 mm from VWR international) then to two way tight fitting PEEK valves (from Upchurch Scientific). The final step is to glue a clean glass substrate on the top of the glass cuvette with stycast. This allows us to see within the cuvette of the pressure sensor while filled with liquid. In this prepared cell, the presence of valves allow us to connect the calibration capillary to calibrate the hydraulic capacitance of the sensor membrane.

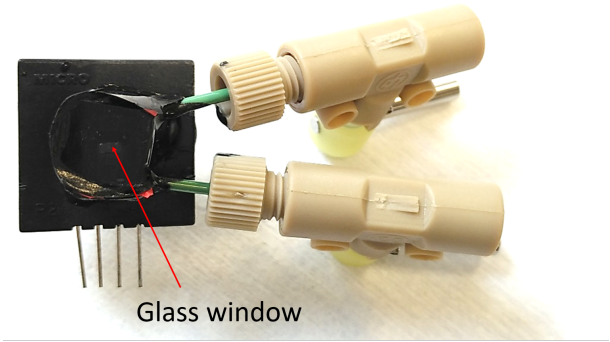

Figure 9.11: A picture of pressure sensor fluidic cell prepared with manual PEEK valves and stycast 2850.

Calibration: The pressure sensor is filled with highly degassed deionised water. A rigid PEEK capillary (Upchurch Scientific) of inner diameter 25 μm outer diam-

eter 1.6 mm and length 43 mm is used in order to calibrate the fluidic cell. This calibration capillary is connected with tight fitting valve and further to a falcon tube filled with deionized water. By means of a 4-way valve this tube can be either connected to a regulated N_2 pressure or to the atmospheric pressure, as shown in figure 8.9b in previous chapter. The flow cell with calibration capillary is placed inside the thermal box. Figure 9.12 represents the charging and discharging process of this hydraulic RC circuit for three different applied pressures. Before calibration, the membrane deflection is minimized adjusting the level of water column of the falcon tube to get a zero pressure signal. Then, a fixed N_2 pressure is applied and released once the hydraulic system is charged.

The pressure difference at any time across the membrane while charging the capacitance is given by:

$$p_m(t) = A + p_0 \left(1 - e^{\frac{-(t-t_0)}{\tau}}\right) \tag{9.8}$$

where p_0 is the applied pressure to the capillary, A is the value of pressure difference across the membrane at time t_0 when calibration is started. The time t_0 is an offset which can be set to zero. This results in a reformed equation:

$$\frac{(p_m(t) - A)}{p_0} = \left(1 - e^{\frac{-t}{\tau}}\right) \tag{9.9}$$

For t<< τ, the above equation can be linearized

$$\frac{(p_m(t) - A)}{p_0} = \frac{t}{\tau} \tag{9.10}$$

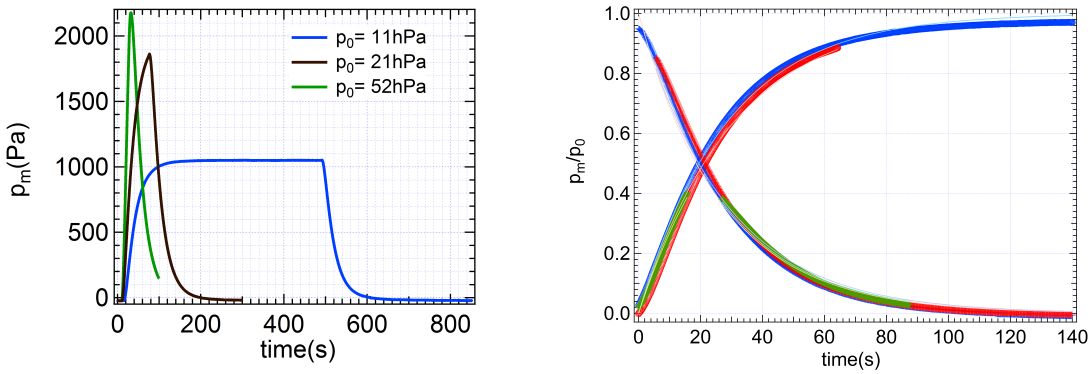

(a) (b)

Figure 9.12: (a) Charging and discharging of hydraulic capacitance for an applied pressure p_0 of 11 hPa, 21hPa and 52hPa. (b) Dimensionless pressure plotted with respect to time, during charging and discharging at three different applied pressure p_0.

Usually, A is very smalls (few pascals) and can be neglected. The above equation (9.9) gives us a dimensionalised pressure $p_m(t)/p_0$ varying with time saturating towards 1 for $p_m = p_0$. This model is used for fitting the experimental calibration curves in future.

The charging and discharging processes in figure 9.12a are plotted in terms of dimensionalized pressure $p_m(t)/p_0$ as described above and fitted with the above model. The time constant obtained from model allows us to calculated the hydraulic capacitance from $\tau = R_h C_h$ where, the hydraulic resistance of the calibration capillary is, $R_h = 4.7$ Pa.s.pL^{-1}, from $R_h = 8\eta L/\pi r^4$ with L length of the capillary, r radius and η viscosity of water. For three different charging/discharging experiments at different applied pressures, the time constants are found to be approximately the same (figure 9.12). From the mean value of theses time constants the value of the capacitance is $C_h = 6.1 \pm 0.4$ pL/Pa with the uncertainty estimated from the standard deviation of the time constants. This experimental hydraulic capacitance measured with a good reproducibility is now less than twice the theoretical value. For this value of capacitance, a flow rate of 1pL/min^{-1} or 60 pL/h is equivalent to a drift of 12 Pa/h in pressure.

Stability test: After calibration the capillary has been disconnected from the pressure sensor fluidic cell and the valves were closed. The evolution of the pressure difference across the membrane with time was recorded during 24 h.

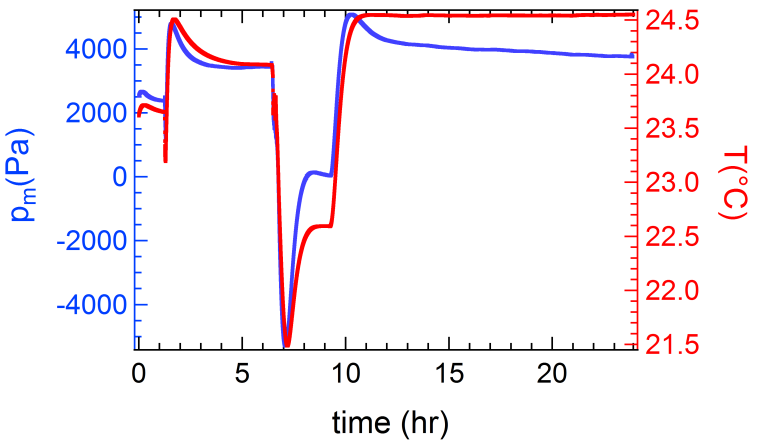

Figure 9.13: Evolution of the pressure and temperature for the pressure sensor cell shown in figure 9.16 and filled with deionised water.

A good correlation between temperature and pressure can be observed in figure 9.13. This correlation reflects the change in volume of the confined water within the flow cell. Nevertheless, after 10 h experiment, the temperature is stabilized with a positive drift of 0.5 mK/h while the pressure shows a steady negative drift of 36 Pa/h that can not be related to thermal dilation. Finally, after 48 h, debonding of the pyrex substrate has been observed as shown in figure 9.14: debonding is at the origin of the measured pressure drift.

Comparatively to other glue, Stycast is particularly attractive for its mechanical rigidity, however, degradation of bonding of glass substrate with stycast in presence of water still occurs after one day of experiment.

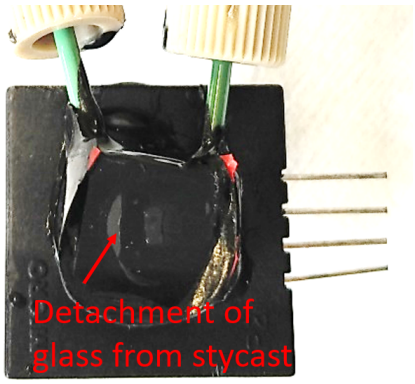

Figure 9.14: Debonding of stycasst from glass substrate in the cell shown in figure 9.11.

Discussion:

The previous set of experiments has been done with various bonding conditions. Complementary experiments lead to similar results. The following table 9.1 summerizes the average drifts in pressure measured in each configuration.

Table 9.1: Summery of the stability test in various pressure sensor cell prepared with glues.

Pressure Cell configuration	Drift [Pa/h]	Comment
Epoxy Glue with capillary	-130	Strong negative drift
Si sealant and epoxy glue	-110	Strong negative drift
Si sealant+ UV curing glue	-2800	Huge negative drift
Stycast	-36	Limited negative drift compatible with measurement

Except with stycast strong drifts have been observed. This drift is always negative and could be attributed to absorption of water and possible subsequent swelling of the glue. The presence of a large water bath in our thermal regulation system ensures that the atmosphere around the pressure sensor is saturated in water. As a result water permeation across the glue should not happen. The drift is generally not linear and comprises a periodic contribution with a magnitude of the order of 20 Pa that superimpose on the average drift of the order of 100 $Pa.h^{-1}$. This periodic contribution is regularly of the form of a relaxation process that could corresponds to bubble nucleation. This is in particular the case in presence of thin wall plastic

capillaries within which bubbles are often observed after a few days. A relaxation process could also be attributed to a delamination of the glue.

The drift in pressure reflects a complex process that originates probably from the coupling of several phenomena. We didn't fully analysed this process as the bonding with stycast seems to provide a reasonable pressure stability and good rigidity as revealed from the sensor calibration.

9.2.3 Liquid compatibility

From the previous experiment with cell prepared with stycast, debonding of glass substrate from the top of the cuvette has been observed. A first hypothesis can be related to the presence of chemical residue on glass surface when Stycast is deposited. It can be either surfactant molecules remaining from the cleaning process or on the contrary adsorbed molecules that haven't been removed by the cleaning process. However, a well established protocol is used for cleaning, based on degreasing in ultrasonication bath with a soap solution and then rinsing first with deionized water and then isopropanol.

A second hypothesis is related to a potential chemical attack of the Stycast by deionized water. This is quite unlikely as stycast is known for its stability in presence of water and its in particular low water uptake.

A third hypothesis is the dissolution of the pyrex by deionized water. It is known that the dissolution rate of pyrex in pure water correspond to 10^{-11} cm.s^{-1} at room temperature resulting in 10 nm Pyrex dissolved in 28 hours [103, 104]. Such an attack may results in a progressive delamination of the stycast from the glass.

In order to check if the reason behind degradation is related to the cleaning process, three glass substrates have been prepared as follows:

- The first substrate is cleaned by sonication in soap solution and deionized water and rinsed with ultra-pure water thoroughly.
- The second substrate is cleaned by successive sonication in soap solution, ultra-pure water and isopropanol.
- The third substrate is plasma oxidized followed by the cleaning as in step two.

The above three substrates has been dipped inside deionised water for three days. The debonding of stycast at the boundaries within 48 hours for each sample has been observed at the boundaries of the stycast and glass substrate as shown in figure 9.15. As all the samples have been cleaned with various processes and the debonding have seen in each sample in almost equal amount, it seems that the cleaning procedure is not the reason behind bonding degradation. Later on, the same test has been performed on a HF treated glass substrate resulting in the same degradation time.

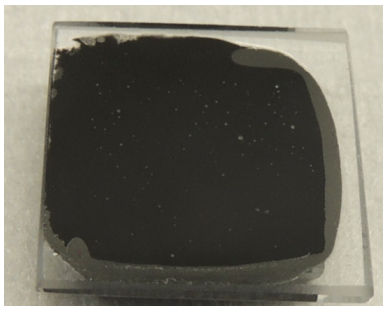

Figure 9.15: Schematic showing the debonding of stycast from glass substrate prepared by following cleaning in water and soap solution. The debonding of stycast is seen at the boundaries of the stycast on glass substrate in gray colour.

The same test has been performed in the propylene carbonate liquid and silicon oil (50 cst). Propylene carbonate is an organic compound which is used as a polar, aprotic solvent. After dipping two sample in each liquid, the sample has been quickly washed many times in isopropanol and then dried to observe the glass-stycast boundary. In these two samples no detachment of substrate was observed even within three weeks. This experiment does not explicitly explain the reason behind degradation of bonding in water but allows us to carry demonstrative measurements with one of these liquids.

9.3 Set up of picoflow rate sensors

To complete the preparation of the flow rate sensor the system needs to be controlled remotely so that calibration and measurements can be done without the need of manual intervention and opening of the thermal box. Compact electrovalves assembled to the measurement cuvette allowed us to obtain a picoflow rate sensor. This sensor can be directly connected to a substrate pierced with a nanopore in order to characterize flows generated in different manner, by a gradient of pressure, a gradient of salinity, or a gradient of eletrical potential.

9.3.1 Fluidic components

Compact components were sought in order to minimize dead volume, as well as absorption problem in resin or plastic material. Moreover, low power actuation is required to limit temperature drift. In order to be able to fill in liquid into the picoflow rate sensor, to relax the pressure when needed and to proceed to the calibration of the sensor, the system is equipped with two electrovalves and a connexion to a calibration capillary that one has to be able to change easily.

Electrovalves

In order to limit the number of elements connected to the measurement cuvette, it is equipped only with 2 electrovalves. One of the valve, called calibration valve, allows the calibration capillary to connect or not to the measurement volume. The second valve, called relaxation valve, allows to relax the pressure within the measurement cuvette when the membrane is fully deflected after a series of measurements.

The calibration valves, needs to be either opened or closed with no limitation of time, to be able to work in measurement or calibration mode. Electrovalves characterized by a normally opened (or closed) state, need to be fed continuously in electrical power to switch to the close (or open) state and hold this state. Such an electrovalve would suit our need, only its electrical power should be smaller than 0,5 mW to avoid parasitic heating, which is particularly challenging. Another approach is to look for a bistable valve that requires power only during the short time of switching from one state to the other. With such a strategy the power of the valve is less important, as the finite energy produced by the valve during actuation will diffuse through the thermal bath. The relaxation valve, on the other hand, is open for a short amount of time.

A supplementary constraint is the minimization of the pumping volume of the valve that corresponds to the displaced volume of liquid induced by the actuation of the valve. Such a pumping volume has to be significantly smaller than the maximum deflection volume than can bare the measurement membrane or the sample membrane.

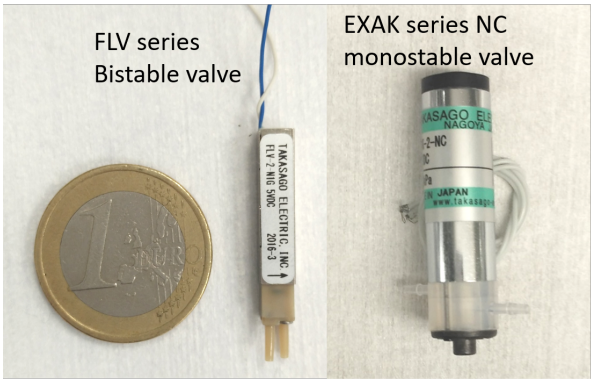

Figure 9.16: An image of electrovalves. Bistable valve (in the middle), normally closed monostable valve on the left.

Respecting both the low electrical power constraint and the low pumping volume constraint for a single miniaturized electrovalve is complex. This double constraint can however be relaxed combining a bistable valve that may present a non-negligible pumping volume for the calibration, with a zero-pumping volume valve that needs to be continuously feed by power to be open, for the relaxation. Doing so it is always possible to actuate temporarily the relaxation valve at the same time as the bistable valve so that any volume displaced by the bi-stable valve, when it is changing state,

can be expelled through the relaxation valve.

Following this approach, a bi-stable latching valve based on a solenoid actuation was purchased for the calibration (FLV-2-N1G, Takasago fluidic systems). This valve requires a 2.4 W power during its 0.1 s actuation. This valve is based on the displacement of a diaphragm to open and close the valve which induce a pumping volume when the valve is actuated. The latching behavior is based on permanent magnets that allow the diaphragm to be maintained either in open or close position without power supply. The pumping effect is compensated by the use of the limited pumping volume rocker valve for the relaxation process (EXAK-2-NC, Takasago fluidic systems) based as well on a solenoid actuation. This valve presents a normally closed state, used during measurement and calibration and can be open under continuous power supply of 0.94 W.

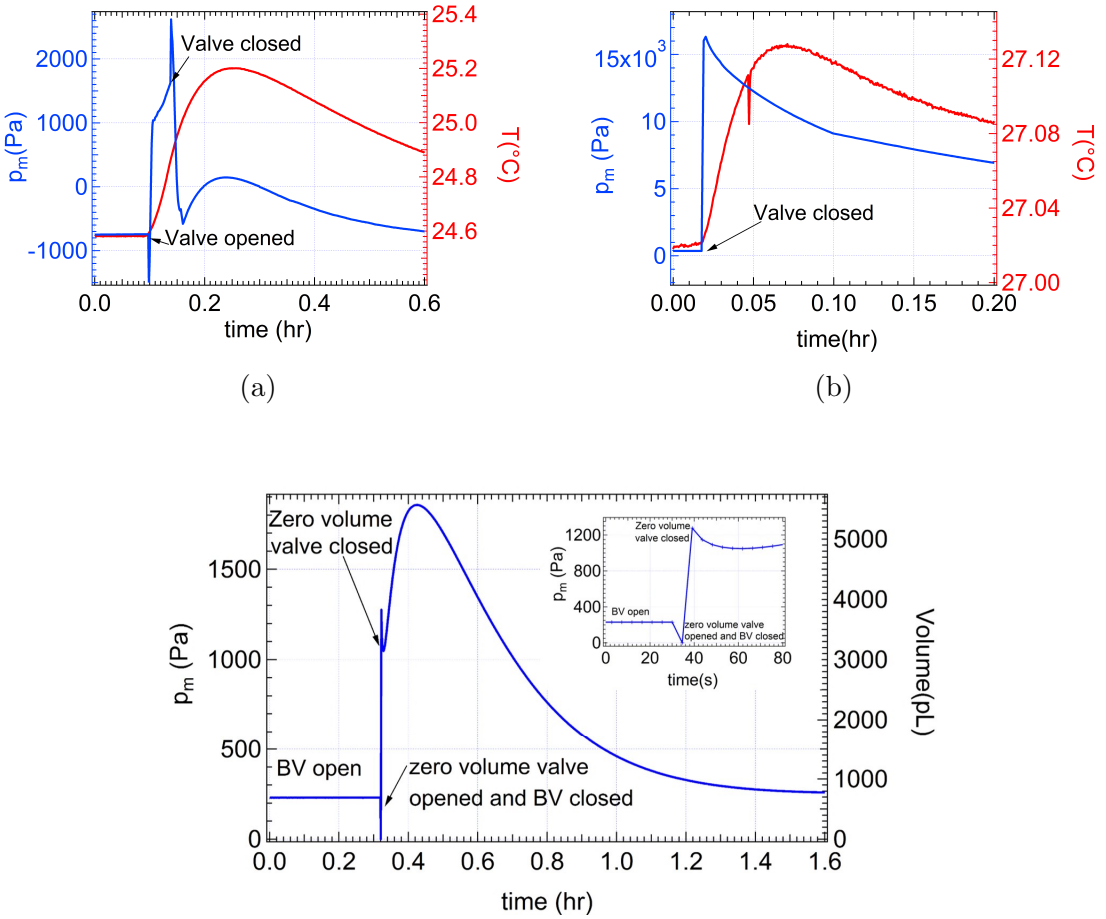

Figure 9.17: Presssure and temperature variation while operating (a) normally closed (NC) valves and (b) bistable valve (BV). (c) Time evolution of the pressure and equivalent change in volume (on right scale) for a combination of bistable and zero volume valves. Inset is showing the jump in pressure while operating two valves.

As shown in the figure 9.17b the pumping-volume of the bi-stable valve induces

a large pressure jump within the measurement cuvette, which is of the same order of magnitude of the maximum pressure that the membrane of the sensor can bare. The pressure jump induced by the state change of the rocker valve is ten times smaller as shown in 9.17a. A significant drift in pressure is nevertheless visible when this valve remains open because of the temperature increase related to the thermal power delivered by the solenoid.

As shown in figure 9.17c the combination of the two valves allow to switch the latching valve from the open state to the closed state with a pressure variation of less than 100 Pa after a transient regime of 1h related to the heat produced by the valve actuation. The control of the valve actuation is done using a set of relay controlled by a home made Labview programm that allow to adjust the duration of the electrical actuation of each valve.

Calibration capillary and connectors

In order to perform calibration experiment with different fluids within a time scale of 1 min, different calibration capillaries are prepared. Based on the calculation of the paragraph 8.2.3 and the on the figure 8.7, 5 mm long glass capillaries of 10 ± 2 μm internal diameter have been bought from Hilgenberg GmbH. For an easy implementation on the cell, these capillaries are carefully glued with stycast at the extremity of 1.6 mm external diameter PEEK tubing, paying attention to not to block the capillary by glue. Such a tubing can be easily mounted on the measurement cell and replaced if needed using a connector glued on the inlet of the bi-stable diaphragm valve, the outlet of the valve being directly connected to the measurement cell. For the calibration with more viscous oil, PEEK capillaries of 25 μm internal diameter and 24 mm length have been used (Upchurch scientific) that can be directly mounted in the above mentioned connector.

Figure 9.18 represents a global view of the prepared capillaries (in figure 9.18a) and microscopic image of a section of glass capillary in figure 9.18b and PEEK capillary in figure 9.18c. As the hydraulic resistance is inversely proportional to

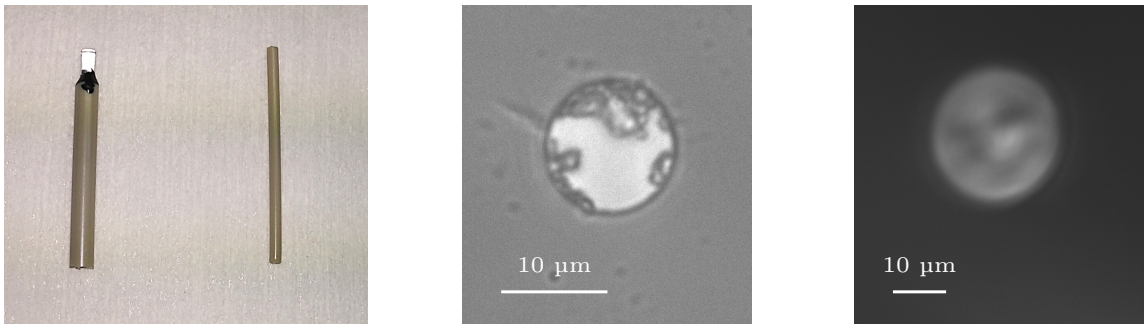

(a) (b) (c)

Figure 9.18: (a) An image of a glass capillary mounted at the end of a PEEK tubing (left) and a 25 µm internal diameter calibration PEEK capillary (right). Microscopic images of the section of (b) a glass capillary and (c) a PEEK capillary.

the power four of the capillary diameter, it needs to be measured precisely. Mean values obtained from the measurement on three glass capillaries and three PEEK capillaries are 12±0.2 μm and 25±0.3 μm respectively. The corresponding hydraulic resistance for these two capillaries for 20 cSt silicon oil are 3.3 Pa.min.pL^{-1} and 0.83 Pa.min.pL^{-1} respectively.

9.3.2 Assembling steps

To set up fluidic connections to the measurement cuvette, two 1.2 mm holes were drilled within the cuvette using a diamond drill as explained in paragraph 9.2.1. These holes are used to connect the electrovalves to the cuvette. One side of the sensor is glued with the bi-stable diaphragm valve with its connector used for the calibration. The other side of the sensor is connected to the rocker valve.

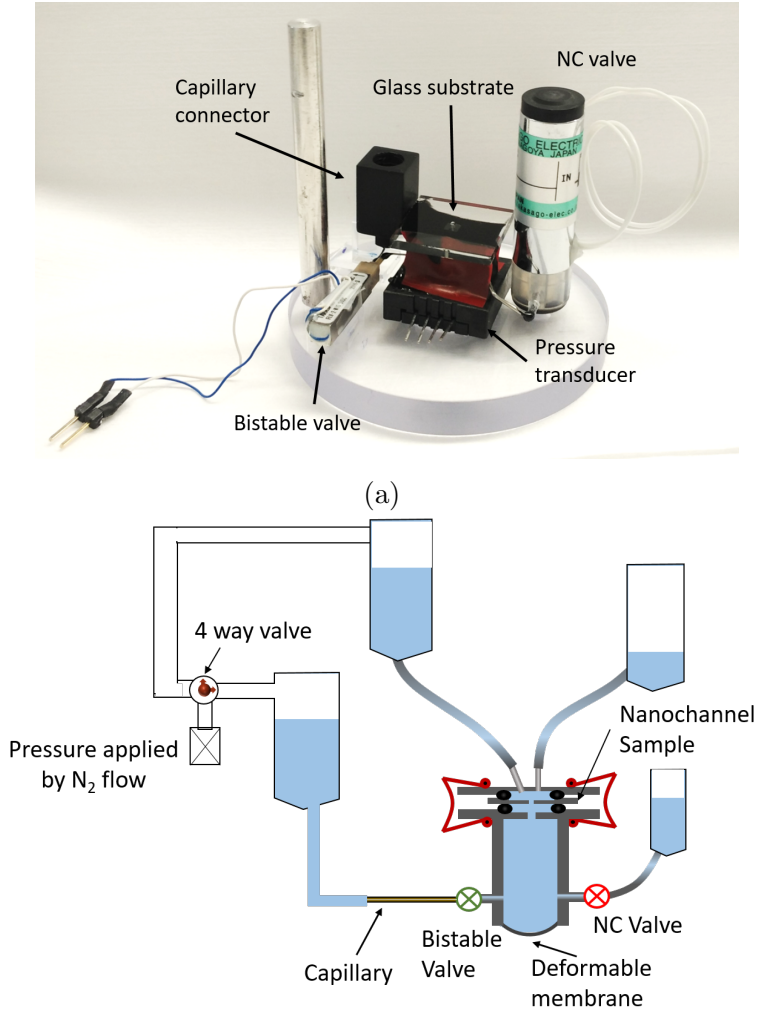

Figure 9.19: A picture of (a) Pico-flow cell (GS cell) and (b) a schematic of Pico-flow cell fluidic set-up.

The assembly of the pressure sensor, valves and supplementary pieces is per-

formed step by step on a circular disk as shown in figure 9.19 in such a way that it is compact and easy to handle while placing it within the thermal regulation box. All the electrical connections (for valves and Pt100) were also prepared individually before the assembly of the pico-flow cell.

A first pico-flow cell was made with a glass substrate as shown in figure 9.19a pierced at its center with a 1.2 mm hole and glued with stycast onto the open side of the cuvette. Sealing between the glass substrate and the sample equipped with a nanopore is made using a nitrile o-ring.

A second pico-flow cell was prepared with a substrate in PEEK of 20×20 mm^2 and 3 mm thickness fabricated with a 2 mm hole at the center with and a groove for the positioning of the o-ring used for sealing. This substrate was glued as well with stycast.

A supplementary PEEK piece was made to be able to feed liquid in the upper side of the sample. This square piece comprises a small cavity connected to two PEEK tubings used as inlet and outlet for the filling in liquid into the cavity and circulation or exchange of liquid. An o-ring is positioned around the cavity for sealing.

The sample is sandwiched between the substrate attached to the sensor and the upper PEEK circulation piece, with o-rings between each pair of surfaces as shown in figure 9.19b. This ensemble is clamped using two binder clips placed on two opposite sides of the substrate. It is of importance to limit the spatial extension of any mechanical piece to limit the sensitivity to thermal expansion. This fixation method with binder clips allows both a compact and rigid mechanical assembly.

A Pt100 sensor is also fixed within stycast onto the external wall of the cuvette in order to measure the temperature as close as possible from the liquid volume. The electrical current used for the temperature measurement is low enough not to induce any heating effect.

A full schematic of the pico-flow cell placed within thermal regulated box and with electrical connections is shown in annex C.

9.3.3 Qualification

The two sensors were calibrated with 20 cSt silicone oil (Sigma Aldrich). The silicon oil is degassed and filtered (nylon filter, pore size 0.2 µm) before filling of the cell. After filling the system was degassed one more time to remove any trapped gas during the filling. This supplementary degassing revealed to be useful as bubbles are observed coming out of the cell during the process (figure 9.20).

Once thoroughly degassed, the system was closed by a plain glass substrate and a nitrite o-ring clamped on top of the cell with the help of binder clips. During these different steps, in particular during clamping, the bi-stable diaphragm valve was kept open to avoid any over-pressure within the cuvette. The calibration capillary was then filled in silicon oil and mounted in its connector paying attention to not trap

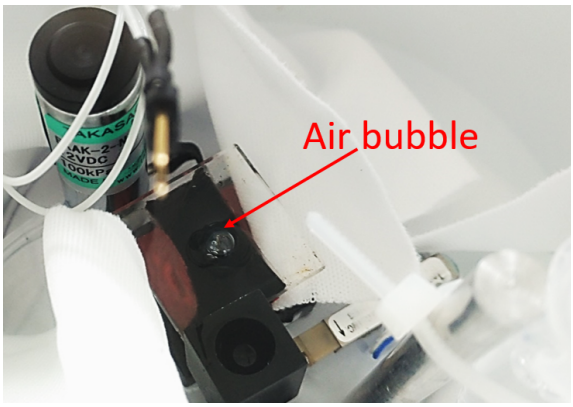

Figure 9.20: An image of the pico-flow cell while degassing by vacuum pump. The bubbles are visible coming out of the device.

any bubble. The cell was then placed within the thermal active box until thermal stabilization. The rocker valve was open temporarily if needed to relax the pressure subsequent to the thermal dilation of the system during the transient regime of temperature stabilization.

The calibration curves for the two cells are shown in figure 9.21. The two cells present capacitances of the same order of magnitude: $C_h = 3.4$ pL.Pa^{-1} for the glass substrate (GS) cell, figure 9.21a, and $C_h = 2.5$ pL.Pa^{-1} for the PEEK substrate (PS) cell. The two values are in good agreement with the theoretical estimate of 3 ± 1 pL.Pa^{-1}. The difference in structure of the upper part of the two sensors may explain the difference of measured capacitance.

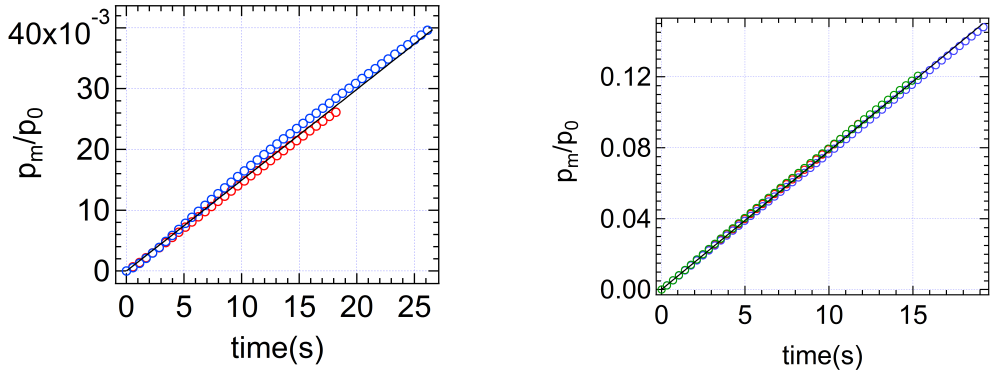

(a) (b)

Figure 9.21: Calibration curves for (a) pico-flow cell GS cell at applied pressure of 0.5 bar (in red) and 0.1 bar (in blue) and (b) pico-flow cell PS at applied pressures 0.1 bar (red and green) and 0.05 bar (in blue). Black line is the fitting model from equation 9.10.

The two cell demonstrate also a linear dependence between volume and temperature changes as shown in figures 9.22. This dependence has been characterized measuring the volume drift when the two valves of a sensor are closed after calibration. An estimation of the thermal expansion β is obtained considering only the

expansion of the silicon oil whose thermal expansion coefficient is 9.10^{-4} K^{-1}. Neglecting the dead volume within tubing and valves in comparison to the volume of the cuvette of 120 µL as calculated in paragraph 9.2.1, a dependence of $\beta = 100$ nL.K^{-1} has been found. This value is larger than the experimental values obtained with the two cells (see figure 9.22). The dependence for the GS cell is $\beta = 60$ nL/K which is twice larger than the dependence for the PS cell of $\beta = 30$ nL/K. These values suggest that the expansion of the solid body forming the cell may have a non negligible contribution. The discrepancy between the theoretical and experimental values could be also attributed to the presence of gas traces within the cell, nevertheless, as explained in paragraph 8.3.3, in such a case a significant increase of the capacitance should be also observed. This means that the difference of behaviors between GS and PS cells, not explained at the moment, is nevertheless probably not related to gas inclusion in the GS cell. This difference might reflect differences in solid bodies between the two cells that are difficult to evaluate due to the complex structure of the system, comprising the valves, the o-ring and binding clips. The knowledge of the experimental thermal expansion dependence allows us to further correct volume variations and remove the impact of temperature drift $\beta\Delta t$ on the measured volume variation ΔV in order to extract the contribution ΔV_f due to flow rate only: $\Delta V_f = \Delta V - \beta\Delta T$.

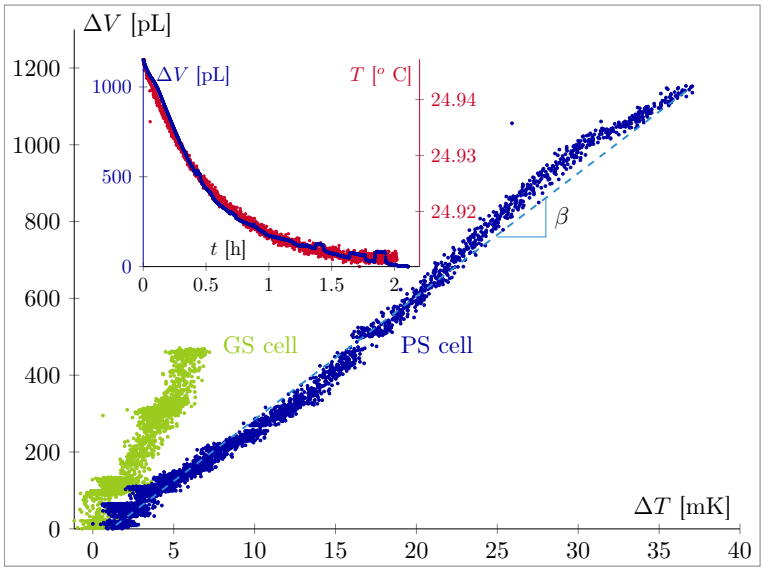

Figure 9.22: Variation of the volume measured by the GS cell (in green) and the PS cell (in blue) with temperature. Light blue line is a linear fit evaluating the coefficient β. The inset is showing the variation of the measured volume ΔV by the PS cell and the temperature with time.

Chapter 10

Towards the direct measurement of pico-flow rate through nanopores

Contents

10.1 Measurement capabilities

Signal acquired in the absence of flow and corrected by the thermal drift have been used to estimate flow rate measurement threshold according to the integration time. Two types of measures are envisioned, depending on the duration of the transient regime to startup a flow with respect to the typical fluctuation periods of the ground signal. We will distinguish the study of permanent flow that need several minutes to be launched from sudden starting flows that need less than a minute to be launched.

10.1.1 Ground signal

Figure 10.1a shows a typical ground signal acquired with the PS cell in absence of flow after correction by the thermal drift. Although irregular, this signal presents

often long time oscillations with periods of the order of several minutes with amplitude of the order of 4 Pa. These oscillations correspond to a wide pick centered at 5 h^{-1} in the Fourier transform of the signal presented in figure 10.1b. The physical origin of these slow oscillation is not clear yet. However these oscillations, resemble to a relaxation process that might originates from thermal dilation. During a half period oscillation, the average slope of the signal, of the order of 1 $pL.min^{-1}$, evolves slowly. For the duration of the order of one minute, much shorter than the period of the large scale fluctuations, the signal can be linearized. After subtraction of the average slope of the signal, the residual noise presents an amplitude of the order 0.2 pL, as shown in the inset of the figure 10.1a.

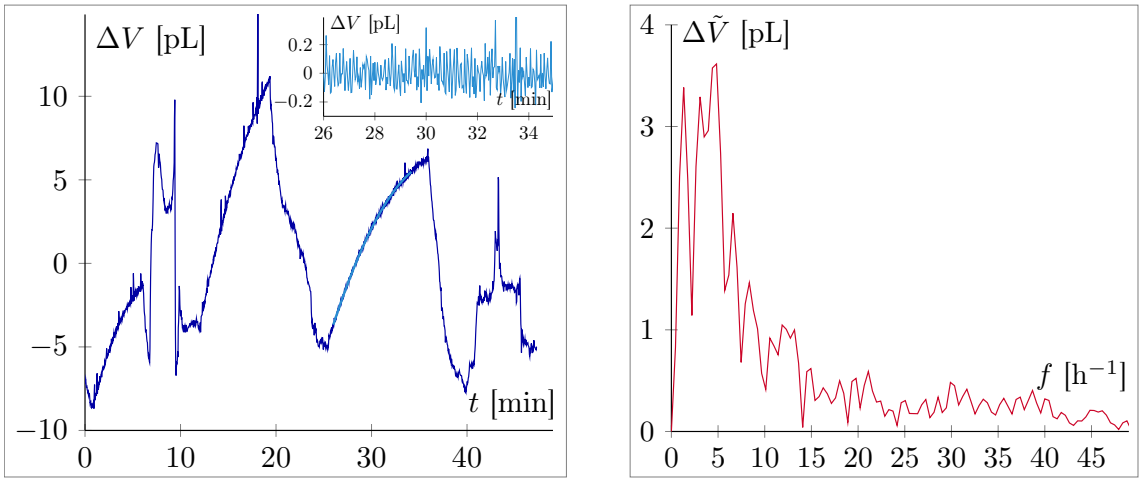

(a) (b)

Figure 10.1: Volume measured by PS pico-flow cell after correction by thermal drift (a) with respect to time and (b) with respect to inverse of time (Fourier transform). Inset of figure presents volume signal after subtraction of average slop of volume signal between 26-36 min.

According to the typical duration of the transient regime needed to launch a steady flow, the integration time will have to be either of the order of a minute or an hour.

10.1.2 Integration time and sensitivity

Our flow rate sensor is based on an integrated measurement. The integration time to be used depends on the flow rate to be measured and on the magnitude of the noise time slope of the ground signal. For the characterization of permanent flows that corresponds to a volume drift significantly larger than the local slope of the ground signal, of the order of the pL/min, the integration time is only limited by the signal to noise ratio. This is the case for flow rate larger than 10 pL/min. For the characterization of permanent flows that corresponds to a volume drift smaller than the typical slope of the ground signal, the integration time has to be larger than the typical duration of large scale fluctuations of the ground signal. For the

characterization of flow rate of the order of 1 pL/min for instance the integration time has to be larger than several tens of minutes to cover at least several large scale fluctuations. Figure 10.2a simulates the drift induced by several flow rates superimposed to the ground signal. The data used to plot the base line, shown in gray, are the ground signal data of the figure 10.1a. For flow rates of the order of one pL/min an integration time larger than 45 min is required.

However, if the flow can be quickly started so that permanent regime is reached on time scale much shorter than the duration of large scale fluctuations, much more precise measurement can be obtained. It is the case, for instance, with pressure or voltage driven flow that can be launched on time scale of the order of a few seconds. Because of the limited noise of the ground signal at short time scale and slowly varying slope it is possible to detect sudden changes in slope induced by sudden flow. In figure 10.2b, the base line in gray corresponds to a one minute ground signal, starting at time $t = 30$ min in the figure 10.1a, from which the local linear drift has been subtracted. Any quick starting flow induces a noticeable deviation from the base line. In this situation, a 1 pL/min flow rate could be detected with a 1 min integration time.

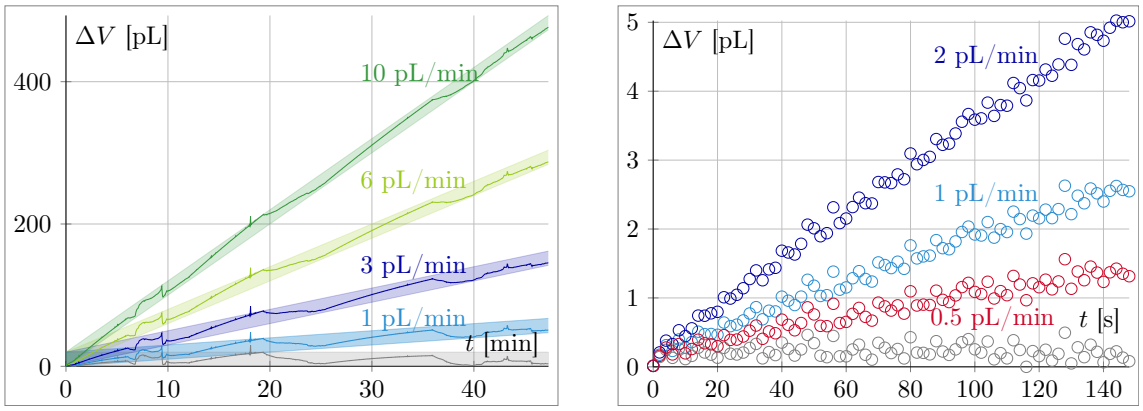

Figure 10.2: (a) Simulated volume drift plotted for several flow rates. The colored background behind each curve corresponds to the noise estimated from the background signal. Time is in minutes (b) Simulated shift of the volume drift induced be an Heaviside flow. The gray base line correspond to the ground signal from which the local slope has been substracted. Time is in seconds.

10.2 Pressure driven flow characterization

To demonstrate the capabilities of our flow rate sensors, pressure driven flow have been measured through a fused silica capillary and through nanopores prepared as described in part III of the manuscript. The measurements have been done with 20 cSt silicon oil with a series of pressure gradients across the capillary or the nanopores.

10.2.1 Flow through a fused silica capillary

Polyimide coated fused silica capillary tubing of 10 μm internal diameter were bought from Polymicro Technologies. These capillaries are flexible fused silica capillary tubing which can be cut in desired length and used in various applications.

A ceramic cleaving stone was used to cut the capillary of length $L = 27$ mm. A scratch was made on the capillary tubing to form a small flaw on its surface and then the capillary was bent up to breakage. The surfaces of this piece of capillary were cleaned thoroughly with deionized water and isopropanol and then glued with stycast as shown in figure 10.3a within a PEEK tubing piece for connection purpose to the flow sensor. The end of the fused silica capillary tubing was cut again on both sides at the proximity of PEEK tubing by cleaving stone just before connecting it to the pico flow cell for measurements.

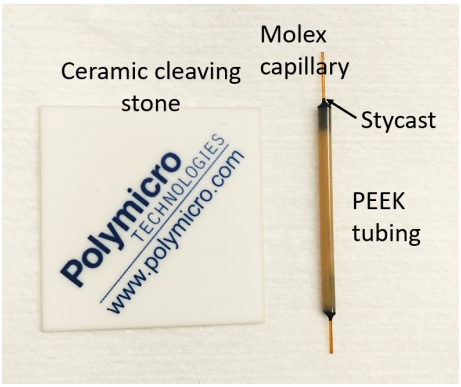

(a)

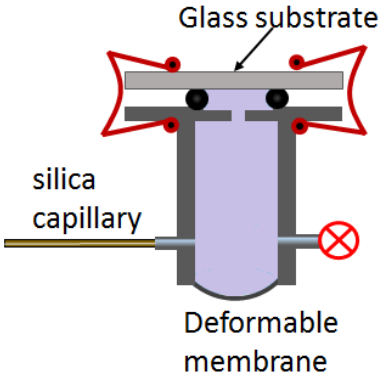

(b)

Figure 10.3: (a) Fused silica capillary tubing preparation. Stycast is used in order to fill the space between the PEEK tubing and capillary. (b) Illustration of cell equipped with fused silica capillary after performing calibration experiment. At the top, the cell is closed with a glass substrate with clamping clips against o-ring.

After calibration of the PS cell detailed in the previous paragraph, the fused silica capillary was mounted in place of the the calibration capillary (figure 10.3b). The pressure at the inlet of the capillary was controlled by pressurized N_2 gas as explained previously in figure 9.19b using the pressure regulation system presented in Chapter 3 paragraph 3.1.2. Before the experiment, the level of liquid within the inlet container was adjusted so that to minimize the deflection of the membrane.

Figure 10.4 represents the volume measured by pico-flow cell according to time for a series of applied pressure across the capillary. The pressure is released after each measurement to limit the average membrane deflection. The inset of the figure shows the volume increase measured for a pressure difference of 10 hPa, which is not visible on the main graph. For each measurement the pressure difference is applied suddenly so that it can be considered as an Heaviside function. The increased volume, measured by the sensor, corresponds to the response to this function. Due

to the large hydraulic resistance of the capillary, the time constant of the system is significantly larger than the measurement time for each pressure. As a result, for each applied pressure, one observes a linear increase of the volume with time as shown in figure 10.5.

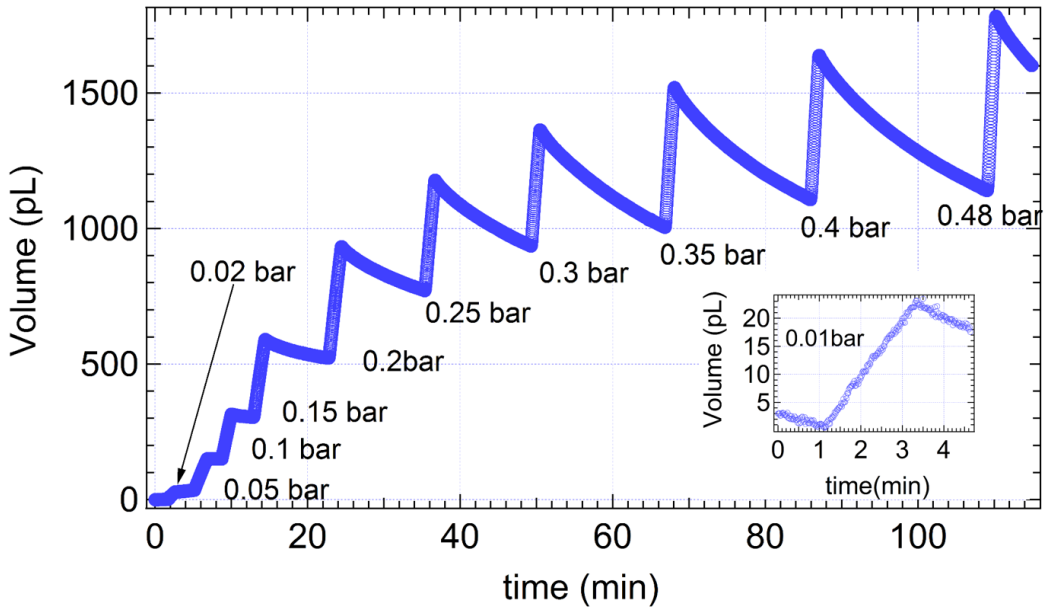

Figure 10.4: Volume measured with time in a single experiment corresponding to various applied pressures.

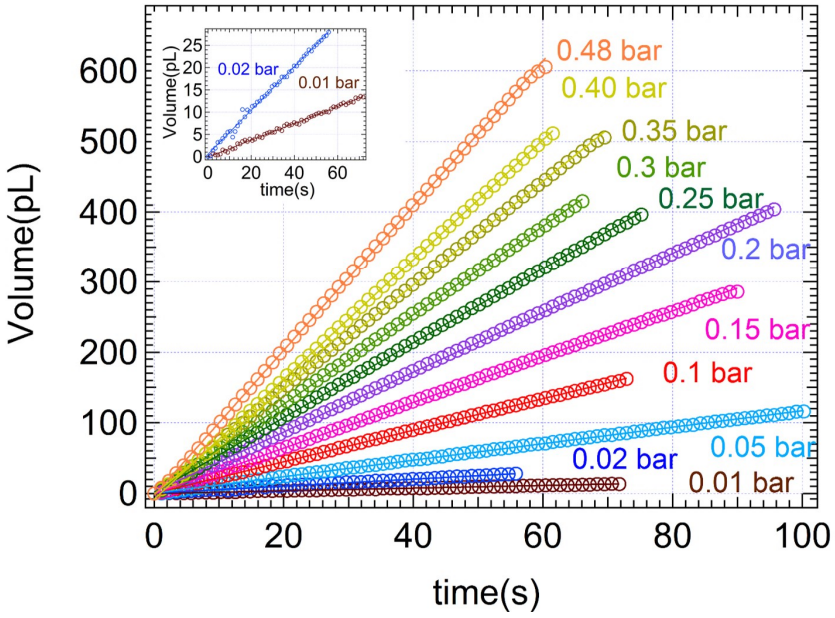

Figure 10.5: Corrected volume plotted with time for each applied pressure.

The linear increase in volume, measured for the two smallest pressure differences, corresponds to flow rates of 10 pL/min and 20 pL/min respectively, have been

magnified in the inset of the figure 10.5. From the residual of the linear fit of the volume increase, the sensitivity of the measure can be estimated to be 0.5 pL/min in agreement with the observation carried out from ground signal experiments. The flow rate through the fused silica capillary is the slope of each curve after correction of the residual thermal drift. Each flow rate has been characterized two times following two series of experiments, each of them consisting in successive increases of pressure form 10 hPa to 480 hPa. Figure 10.5 shows the volume increase measured for one of these experiments. The all measured flow rates are presented according to the applied pressure in figure 10.6.

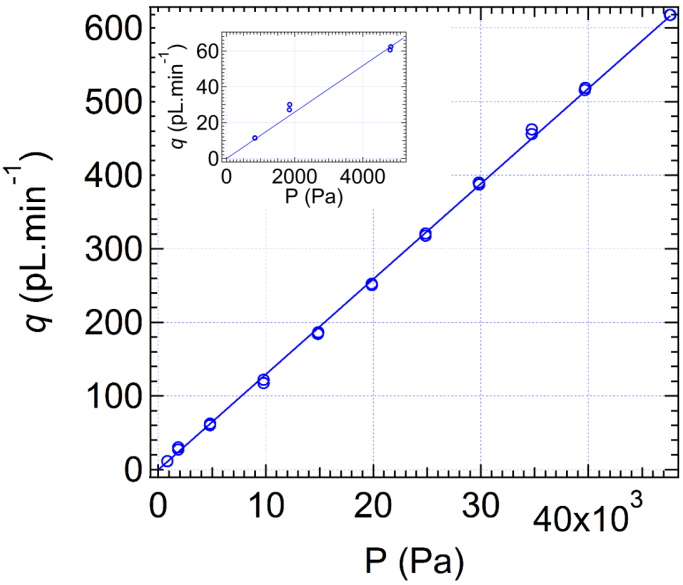

Figure 10.6: Flow rate (the slop of each experiment) in fused silica capillary plotted against corrected pressure.

As expected, the flow rate increases linearly with the pressure even for the smaller measured flow rates as shown in the inset of the figure 10.6. The slope of the linear fit equals to 1.26×10^3 pL.min^{-1}.bar^{-1}, corresponds to the hydraulic conductance of the capillary. From this value of the hydraulic conductance, the internal diameter of the fused silica capillary found to be 8.3 µm in good agreement with the value 10±2 µm provided by the supplier.

This first experiment demonstrates the ability of the sensor to measure, with a single system, almost 2 decades of flow rates with an integration time of the order of 1 min even for the smallest measured flow rate of 10 pL/min. The sensitivity of the sensor, for this integration time is of the order of 0.5 pL/min.

10.2.2 Flow across a single nanochannel

The following demonstrative experiment has been carried out with the GS cell to characterize a pressure driven flow of 20 cSt silicon oil across a single nanochannel,

prepared as described in the chapter 5 by focused ion beam milling. This approach gives us the ability to jump efficiently from our macro scale to the nanoscale.

For such a characterization, the glass substrate closing the measurement cell is replaced by a silicon substrate having a nanopore as shown in figure 10.7. As explained in the paragraph 9.3.1, this sample is clamped between the upper rigid substrate of the cell and a feeding substrate using two nylon o-rings, the all assembly being pressed with the help of two standard paper clamps. Before clamping, the different pieces need to be maintained in place while avoiding at the same time to touch and break the sample membrane as well as to trap any air bubble below the lower surface of the sample. The final compression step with the binder clips has to be done delicately to avoid any sudden overpressure within the cell cavity and subsequent sensor or sample membrane breakage. The bistable valve is let open to allow a free displacement of the liquid, nevertheless the 0.4 mm diameter of the valve can not accommodate a sudden displacement of liquid without a significant pressure difference. All in all this assembling process requires to develop a good know-how, but once mastered, it is possible to switch from one sample to another in half an hour.

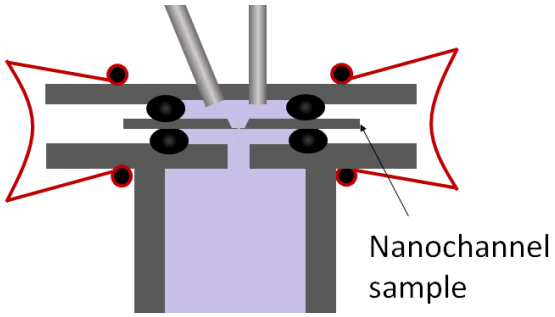

Figure 10.7: Schematic of nanochannel sample clamped against two o-rings, between the rigid glass substrate of pico-flwo cell and an addition glass substrate (on the top).

Despite a thorough cleaning of container and filtration of liquids through 0.2 µm filter, the few experiments carried out with nanopores revealed they are prompt to clogging. The origin of the element that may block the nanopore is not identified at present. The results shown below have been obtained with a single nanopore that presents a conical profile. The radius of its circular section increases from $r_1 = 130$ nm to $r_2 = 200$ nm. However, the precise dependence of the radius according to the axial position is not known. The thickness of the membrane, that corresponds to the length of the nanopores is 1.35 µm, measured by thin film reflectometry System, NanoCalc.

Calibration

A 5 mm glass capillary tubing of 12 µm internal diameter was used for the calibration carried out once the sample with the nanopore has been installed on the cell. The hydraulic resistance of the nanopore is at least 3 order of magnitude larger than

the resistance of the calibration capillary. The flow through the nanopore placed in parallel of the calibration capillary is consequently negligible compared to the flow through the calibration capillary during the calibration. Figure 10.8a represents the three experimental calibration curve at applied pressure of 0.1 bar, 0.2 bar and 0.3 bar. The mean value and standard deviation of the capacitance is evaluated from the three hydraulic capacitances values to be 16 pL/pa. The good superimposition of the three dimensionless calibration curves confirms the absence of leak. This value is 5 times larger than the one obtained during the qualification experiments. This factor would suggest that a bubble or a collection of bubbles have been trapped during the assembling process. From the figure 8.14 the volume of gas would be at least of the order of one percent of the total volume that is 1 mm^3. The volume might be larger if the gas is in the form of sub-micrometric bubbles.

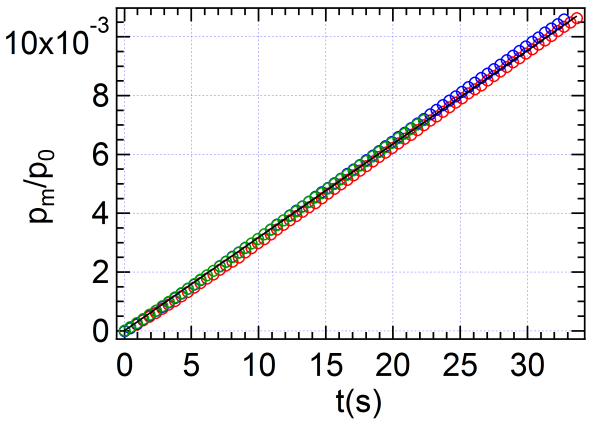

(a)

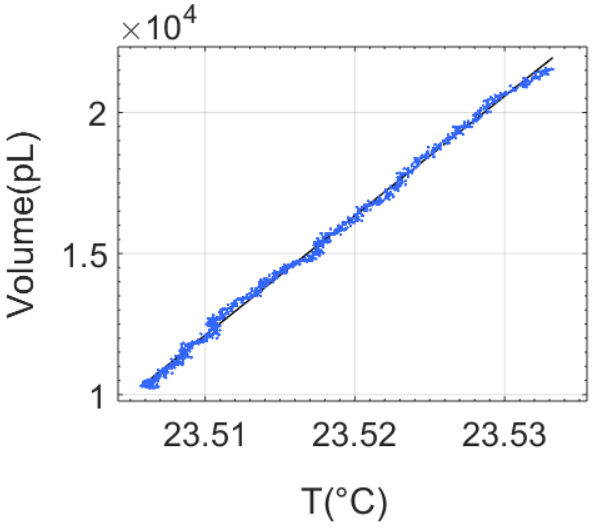

(b)

Figure 10.8: (a) Calibration experiments for the pico-flow cell when a nano channel sample is mounted on the cell. The solid black line is a linear fit from which the hydraulic capacitance was calculated. (b) Volume plotted vs temperature. Solid black line is a linear fits from which correction coefficient is evaluated to 410 $nL.K^{-1}$.

The temperature sensitivity has been characterized as shown in the figure 10.8b that represents the variation of volume of liquid confined in the cell versus temperature when the cell is closed. A linear behavior is observed with a slope of 410 nL.K^{-1}. This slope is 3 times larger than the theoretical value corresponding to the pure liquid expansion as detailed in the paragraph 9.3.3. From the figure 8.15 such an increase can be associated to the presence of gas within the cell only under the form of nanometric bubbles. The formation of such a large amount of nanobubbles is difficult to envision. The bubbles could have been formed at the outlet of the nanochannel during the clamping process, however a pressure at least 10 times larger than the atmospheric pressure would have been required, and still the size of the bubble could not be small enough to explain this large thermal expansion value.

Moreover, the thermal coefficient is 7 time larger than the value obtained during the qualification test with this same cell. The contribution of sorption or solubilisation effects could be at stakes, however, surfaces and liquid have been degassed before both experiments. This large discrepancy suggests again that the solid structure of the cell is probably much more important that initially envisioned. In particular, the contribution of the o-ring that presents a thermal expansion coefficient of the same order of magnitude of the liquid might be of importance.

Flow measurement

Figure 10.9 shows the volume variations, after thermal drift correction, measured for three pressure differences successively, applied to the nanopore between its extremities. After these three measurements, the breakage of the sample membrane due to an accidental over pressure put an end to further characterization with this sample.

For each pressure, after a transient initial regime, a linear increase of the volume is observed with respect to time. This linear regime indicated with colored marks in the figure, corresponds to a constant flow rate through the nanopore. The transient initial regime that will be discussed later is initiated by a positive jump of volume that is equal in amplitude to a negative jump of volume observed at the end of each experiment when the pressure is released.

The average slope evaluated during the linear increase of volume, is indicated in the figure 10.10a for each pressure difference. A linear dependence of the flow rate with the applied pressure is observed with a slope of 92 pL.min^{-1}.bar^{-1}, that can be related to the pressure drop associated to the flow through the nanopore between the two reservoirs.

For the largest measured flow rate, the Reynolds number based on the larger radius r_2 is $Re = 2q\rho/(r_2\pi\eta) = 5.10^{-4}$ that corresponds to the regime of creeping flow. In this regime, the pressure drop through a cylindrical orifice of radius r_p and finite length L is proportional to the flow rate as [105]:

$$\Delta p = \frac{8\eta L}{\pi r_p^4}\left(1 + \frac{3}{8}\frac{r}{L}\right) q \tag{10.1}$$

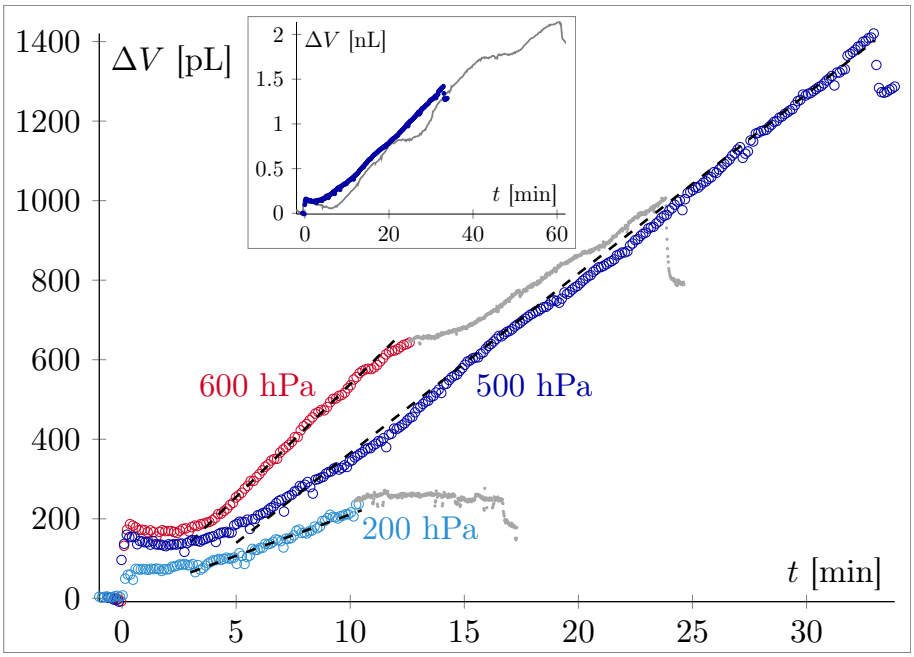

Figure 10.9: Volume variation with time corrected after thermal drift for applied pressure, 200 hPa, 500 hPa and 600 hPa (in gray and in colored curves). The inset is presenting two experiments of volume variation at applied pressure of 500 hPa. The dashed black line on each colored curve is linear fit to evaluate the corresponding flow rate.

The correction associated to the flow within the reservoirs becomes negligible compared to the Poiseuille flow dissipation for aspect ratio $r/L \ll 1$ which is the case of our nanopore. For the largest radius, the term $3/8\ r_2/L \simeq 0.06 \ll 1$. The dissipation is mainly related to the Poiseuille flow that strongly depends in our case on the conical profile of the pore. For a pure linear cone such that the radius varies linearly with the axial position as $r(x) = r_1 + (r_2 - r_1)x/L$, the hydraulic conductance can be approximated as:

$$G_{h_{cone}} = \left(\int_0^L \frac{8\eta}{\pi r(x)^4} dx \right)^{-1} = \frac{3\pi(r_2 - r_1) r_1^3 r_2^3}{8\eta L \left(r_2^3 - r_1^3\right)} = 51 \text{ pL/min/bar} \qquad (10.2)$$

While the conductance of a full cylindrical pore of radius r_2 would be 140 pL/min/bar. The measured hydraulic conductance is comprised between these two values. This suggests that the pore radius might be in average larger than the radius of a simple linear cone. Our experimental value is compared in the figure 10.10b to the hydraulic conductance of a pore with a basic hybrid geometry consisting in a simple association of a cylindrical portion of radius r_2 and a conical portion. In the framework of this simple approach, our measured value would correspond to a nanopore for which 60% length is cylindrical and 40% conical as depicted by the central schematic of the figure 10.10b.

While the flow rate remains constant for more than 30 min during the experiment at 500 hPa, a change of slope is observed during the experiments at 600 hPa and 200 hPa after 10 min approximately. This change of slope, that reveal a change in

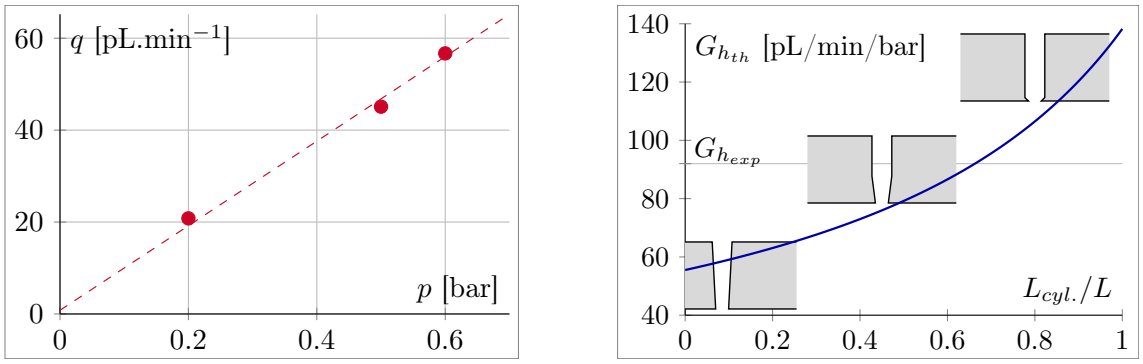

(a) (b)

Figure 10.10: (a) Flow rate measured from the slope of the linear volume increase shown in figure 10.9 for the three different applied pressures. Dashed line is the linear fit corresponding to the nanopore hydraulic conductance 92 pL.min^{-1}.bar^{-1}. (b) Variation of the calculated hydraulic conductance with the ratio of cylindrical length to the total length of the nanopore (L_{cyl}/L).

flow rate, is presumably not related to clogging. Clogging is not reversible while in our case a stop of the flow corresponding to a plateau is always followed by a spontaneous starting up of the flow after several minutes. In the inset of the figure 10.9, the constant flow measurement obtained at 500 hPa, is compared to a second measurement done at the same pressure that clearly exemplify this stop and start phenomenon.

The potential reduction of the flow due to the passage of nanometric particle is also unlikely. For the smallest measured flow rate of 20 pL/min, the average velocity within the nanopore is larger than 2.5 cm/s. This velocity corresponds to a residence time of 0.5 ms within the nanopore. It seems difficult to relate this short residence time with the several minutes duration of the observed plateau.

In the end, the origin of these plateau might be related to the origin of the initial transient regime as we shall see below.

Transient regimes

The pressure driven flow characterization done with nanopore distinguishes from the measurement carried out with silica capillary by the presence of a noticeable positive jumps of volume subsequent to the pressure application at the beginning of the measurement and a negative jump of volume of the same amplitude when the pressure is released. The initial pressure jump is systematically followed by a flat or even a small decrease in volume that seems more pronounced when the pressure is larger. After this initial transient regime, that is reminiscent of a relaxation process, become visible the volume increase associated to the flow injected in the sensor. As shown in the figure 8.5 the amplitude of the initial volume jump is proportional to the applied pressure with a slope of 3 fL.Pa^{-1}. Considering that the jump of volume is associated to the deflection of the sample membrane this slope should be equal

to the hydraulic capacitance of the silica membrane containing the nanopore. The silica membrane is a rectangle of 280 µm by 360 µm. In the framework of a linear deflection of the membrane, as described in the paragraph 8.1.2, the deflection w_0 at the center of the membrane is related to the volume V associated to the deflection by the relation (8.6): $w_0 = k_v^{-1} V/a_m^2$ with $k_v = k_w k_S = (8/15)^2 \simeq 0.28$ for a square membrane. The value of k_v results from the use of the the shape function introduced in the relation (8.5) that has to be consider only as an approximation of the shape of our buckled membrane.

For an applied pressure of 0.6 bar, the observed volume jump of 200 pL would correspond to a deflection $w_0 \simeq 7$ µm, for an average width $a_m = 320$ µm. Such a deflection, which is 7 time larger than the thickness of the membrane, is well beyond the range of validity of the linear thick membrane approach.

As explained in the chapter 5 the silica membrane is under a compressive stress of 300 MPa, 2 orders of magnitude larger than the bending moment of the membrane. Because of this large compressive stress the membrane behaves as a thin membrane and presents a non-linear behavior with a spontaneous buckling, in absence of pressure jump, of the order of $w_b = 10$ µm. If the membrane is submitted to a pressure jump, its deflection is altered by an additional amount δw that contributes to an additional volume variation $\delta V = k_v {a_m}^2 \delta w$. The value of δw is obtained rewriting the relation (5.3), neglecting the bending moment contribution with respect to the compressive stress and considering the central deflection of the form $w_0 = w_b(1+\delta w/w_{b)}$:

$$p_m = k_r \Sigma \frac{d_m w_b}{a_m^2} \frac{\delta w}{w_b} \left(1 + \frac{\delta w}{w_b}\right) \left(2 + \frac{\delta w}{w_b}\right) \tag{10.3}$$

The value of $k d_m \Sigma w_b / a_m^2$ = is significantly larger than the applied pressure smaller than 6.10^4 Pa. As a result the dimensionless additional deflection $\delta w/w_b$ is significantly smaller than one. In this framework, the membrane should present a linear behavior described by the relation (10.3) linearized at the first order:

$$p_m = 2 k_r \Sigma \frac{d_m}{a_m^2} \delta w = 2 \frac{k_r \Sigma d_m}{k_v a_m^4} \delta V \tag{10.4}$$

The corresponding hydraulic capacitance C_{hs} of the sample membrane is:

$$C_{hs} = \frac{k_v a_m^4}{2 k_r \Sigma d_m} = 0.26 \text{ fL.Pa}^{-1} \tag{10.5}$$

This value is one order of magnitude smaller than the slope of volume jump with respect of the applied pressure. As the buckling amplitude is well predicted, it would be surprising that the capacitance C_{hs} could be wrong of one order of magnitude even if the shape of the buckeld membrane is certainly approximately modeled.

This means that the membrane deflection represents only a minor contribution of the measured jump of volume. Apart from the membrane itself, the other region of the system that is directly submitted to the pressure jump is the space limited by the silicon substrate and the upper PEEK cover sealed on the side by an o-ring.

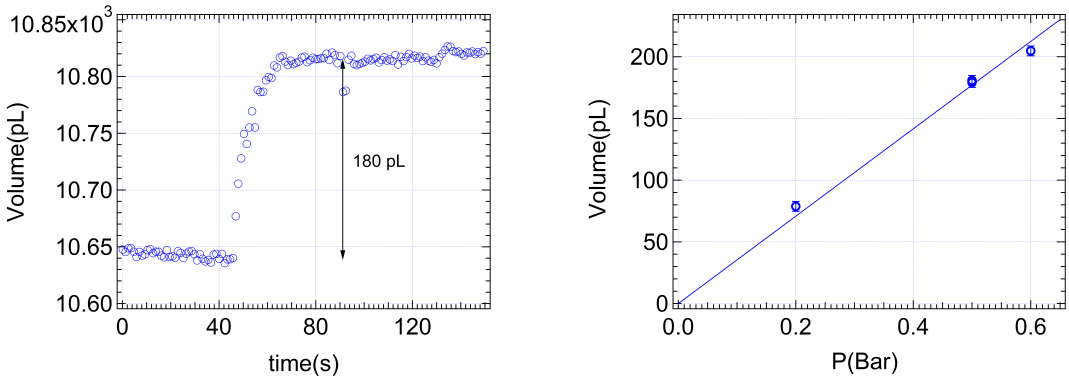

(a) (b)

Figure 10.11: (a) Pressure variation with time for 0.5 bar applied pressure to induce flow (b) Volume change due to sample membrane deformation when external pressure is applied in order to induce flow through nanochannel.

When the pressure is applied, it contributes to compensate the force exerted by the binder clip. As a result the thickness of this upper space is slightly enlarged while the thickness between the glass substrate and the silicon substrate is slightly decreased as illustrated in the figure 10.12c. This process results in a negative vertical displacement of the silicon susbstrate compensated by a deflection of the measurement membrane visible as a volume jump. From the measured volume jump and the wetted area of the silicon substrate of 10 mm^2, the displacement of the silicon substrate should be of the order of 40 nm/bar. This displacement contributes to a slight relaxation of the upper o-ring and simultanesously to an increased squeezing of the lower o-ring. When the pressure is released the reversed process should be observed inducing a negative jump of volume in our measurement. The plateau

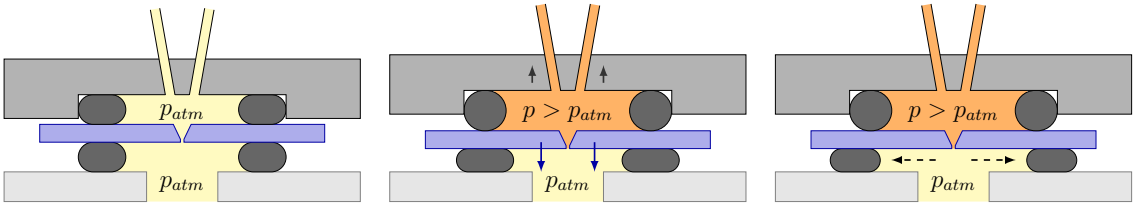

(a) (b) (c)

Figure 10.12: Schematic of the displacement of the clamped elements when a pressure larger than the atmospheric pressure is suddenly applied in the upper part of the system. The binder clip are not shown for clarity reason. (a) Clamped system at atmospheric pressure. (b) Displacement of the sample and cover as well as deformation of the o-rings subsequent to the pressure application. (c) Slow relaxation of the lower o-ring squeezed between the glass substrate and the silicon sample.

visible after the compression might results from the slow relaxation of the o-ring toward a new equilibrium position after squeezing as shown in figure 10.12c. Because

of the clamping of the o-ring between the two surfaces, its displacement might be hindered resulting in a slow stick and slip evolution. During slip, the motion of the o-ring would contribute to a slow down of the volume increase visible as a plateau, while under stick the the motion stops and the volume increase reflects again the liquid flow rate. This explanation remains nevertheless an hypothesis that have to be further tested in particular to explain the observed plateau.

10.3 A strategy to work with water

The pico-flow cell developed in the present work has limitations to work with silicon oil or solvents which does not affect bonding of various pieces of pico-flow cell with stycast. In order to be able to work with water there are two approaches:

- First approach is based on working with water-oil meniscus as explained in figure 10.13a. The pico-flow cell is filled with silicon oil upto the top of the substrate glued over cuvette, then leaving a drop of water/electrolyte within the volume available in the middle of the o-ring (about 15μL).

- Second approach is based on making the interior of the pico-flow cell cuvette hydrophobic in order to protect the bonding of various pieces of pico-flow cell against water (figure 10.15a). This can be done by chemical vapor deposition of fluorinated parylene (Parylene-F) which displays highly hydrophobic properties with respect to water and salt solutions.

10.3.1 The water on oil approach

Calibration: A calibration experiment was performed in the configuration of first approach as shown in figure 10.13a. The flow cell was closed with a glass substrate on the top after leaving a degassed water droplet carefully in the space available within the o-ring.

The time constant obtained from fitting model (equation 9.10) is 163±1 s. It gives the hydraulic capacitance of the cell to be 3.25±0.02 pL.Pa^{-1}. This value of hydraulic capacitance is very close to the one obtained from model (3 pL.Pa^{-1}, equation 8.7) as well as the capacitance of cell obtained previously (2.5 pL.Pa^{-1}, section 9.3.3) when the cell was filled with silicone oil completely.

Stability test: After calibration the two valves were closed and the evolution of the volume with time was measured as shown in figure 10.14. There is an average negative drift of 1.25 pL.min^{-1} in 12 hours. For this time scale the oscillations in volume are of the order of ±40 pL. Corresponding to these oscillations, in order to observe a significant change in volume for flow rate of 1 pL.min^{-1}, two hours would be sufficient. The inset of figure 10.14 represents the simulated volume evolution

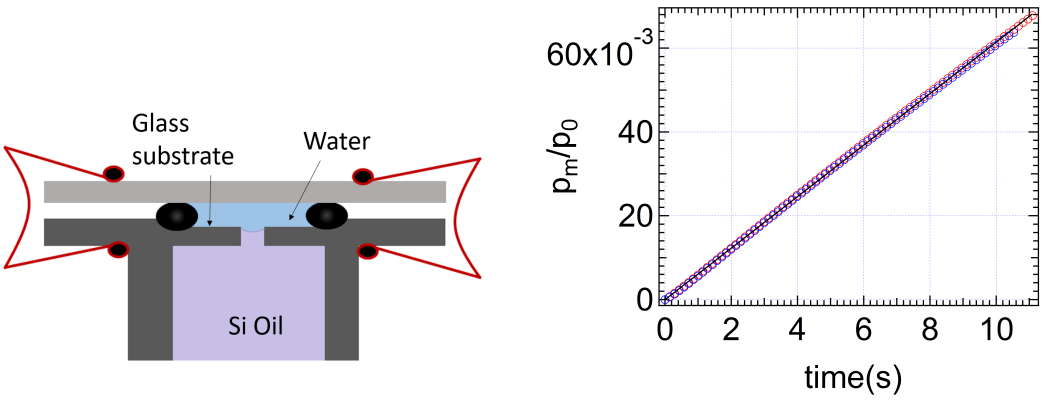

(a) (b)

Figure 10.13: Schematic of (a) water on oil approach in which water-oil meniscus is present at the proximity of enterance of flow cell cuvette, and (b) Calibration experiment in this configuration. Two experimental calibration curve corresponding to applied pressure of 0.15 bar(in red) and 0.1 bar (in blue).The solid line is the linear fit from model equation

for the flow rates of 1 pL.min^{-1}, 5 pL.min^{-1} and 10 pL.min^{-1} with respect to the corrected volume measured by the cell (after subtraction of the negative drift from the measured volume signal in blue).

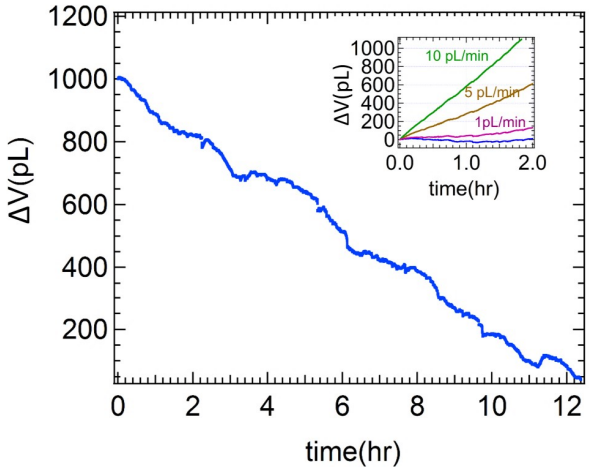

Figure 10.14: Evolution of volume measured by the cell in the configuration of first approach (with a water-oil meniscus). The inset presents simulated evolution of volume for flow rates of 1 pL.min^{-1}, 5 pL.min^{-1} and 10 pL.min^{-1} with respect to the corrected volume signal.

10.3.2 The parylene protection approach

This approach is based on making the walls of pico flow cell cuvette hydrophobic in order to not to wet the surfaces of cell by water/electrolyte (figure 10.15a). This can

be done by chemical vapor deposition of fluorinated parylene (Parylene-F) displaying highly hydrophobic properties with respect to water and salt solutions.

At first, a test was performed with a 100 nm thick coating of parylene at the interior of the cell. Figure 10.15b represents the variation of measured volume in blue and temperature in red.

A decrease in the volume measured by the cell can be observed in figure 10.15b, which does not follow the temperature. This implies that the drift in volume (in average 60 pL.min^{-1}) is attributed to the presence of leak in cell due to degradation of stycast bonding. This experiment implies that 100 nm thick coating of parylene is not sufficient to protect the surfaces.

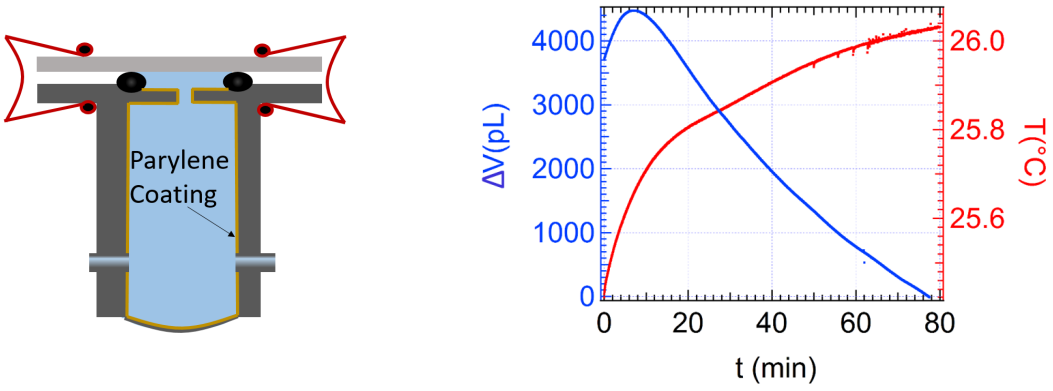

(a) (b)

Figure 10.15: (a) Schematic of parylene protection approach in which a micrometric hydrophobic layer of parylene-F (in orange) is present at the interior of flow cell. (b) Variation of volume (in blue) and temperature in red for a cell coated with 100 nm thick parylene.

In order to optimize the required thickness of Parylene for protecting the bonding against deionized water or salt solution, we have performed another simple test. Two clean glass substrates were prepared with a small drop of Stycast and reticulated for 16 hours. Consequently, 2 μm and 10 μm thick Parylene-F was deposited by chemical vapor deposition technique in Institute Neel. These samples were immersed into deionized water and pictures were taken to analyze stycast-glass bonding. In this experiment no degradation of stycast was found within 4 weeks for both of the parylene coated samples.

In conclusion of the above performed tests, the required optimum thickness of parylene to protect the bonding lies between 100 nm -2 μm. However, it is required to perform a calibration test of the cell in this configuration in order to be sure that introducing the parylene coating does not change the hydraulic capacitance significantly. This test provide a possibility to work with water or salt solutions in pico-flow cell.

Chapter 11

General conclusion and future perspectives

The basic understanding of transport in nanochannel is crucial as the efficiency of energy conversion process, based on mixing of salinities, relies on the transport mechanism of ions. The work presented in this thesis is focused on the experimental investigation of coupled transport in nanofluidic devices. The following key points are covered during the period of the thesis:

- A home-made flow cell has been prepared. Then, the capabilities of the cell and whole set-up to carry out nanofluidic electrical measurements under applied pressure or salinity gradient have been presented using a commercially available nanoporous Nafion membrane. The effect of various experimental parameters such as solution resistance and electrodes on the electrical current produced by the membrane exposed to a salinity gradient have been discussed.

- We have demonstrated the feasibility of a method to realize free-standing silica membranes on silicon substrate. The thickness of the membrane can be varied by choosing the thickness of the silica layer on the initial wafer (Si). We have tested the mechanical robustness of the prepared membranes of thickness 1.35±0.05 μm , and found no failure up to 1 bar. The electrical characterization of the so called suspended freestanding silica membrane and then a single nanohole milled within it has been illustrated. In addition, the rectification behavior observed in conical nanopore has been discussed also.

- A pico-flow cell and an experimental platform to be able to perform direct flow rate measurements across single nanochannel have been developed. Various experimental challenges faced during the development of this cell have been addressed. Also, the very first flow measurements in order to demonstrate the technique have been presented. The results of the flow rate measurement across a micrometric fused silica capillary are in agreement based on the dimensions of the capillary. This experiment demonstrates the ability to measure flow rate as low as 10 pL.min^{-1} with a sensitivity of the order of 2

pL.min^{-1}. The results on single nanochannel are also promising. Hydraulic conductance calculated theoretically taking into account the geometrical shape of nanochannel meets with the experimental outcome.

At this stage of this project, several perspectives are open. The very first future objective is to find the best configuration of the pico-flow cell to be able to work with water or salt solution based on approaches presented at the end of chapter 10.

Another important perspective will be to combine the electrical measurements with the flow rate measurements. This will allow us to probe the flow rate as well as electrical current (when they are coupled) by the application of either potential difference, pressure difference and concentration difference. This approach allow one to measure and control the fluxes which could have applications to develop the fluidic devices for harvesting the electrical energy with higher efficiency.

A further goal will include to measure the flow rate in diode configuration such as electro-osmotically driven flow across a conical pore. Afterwards, the flow rate measurement submitted to a concentration gradient across a nanochannel can also be performed.

Appendix A

Warburg impedance of electrodes

Transport equations

Here, we treat a 1D problem between infinite planar electrodes separated by a distance L. The electrolyte concentration is $c_\pm(x) = c_o(x) + \delta c_\pm(x,t)$. In the following we assume c_o uniform, that is we do not take into account eventual static surface charge at the electrodes and associated Debye layers. The electric potential is $V = V_{dc} + V_{ac}(x,t)$. Here, also we choose $V_{dc} = 0$: no superimposition of dc and ac experiments. All time dependencies are harmonic, and we note only here the complex amplitudes, that depend only on x.
Flux of ions

$$\begin{aligned} j_\pm &= -D\frac{\partial c_\pm}{\partial x} \pm e c_\pm \frac{D}{kT}\left(-\frac{\partial V}{\partial x}\right) \\ j_\pm &= -D\frac{\partial \delta c_\pm}{\partial x} \pm e c_o \frac{D}{kT}\left(-\frac{\partial V_{ac}}{\partial x}\right) \end{aligned} \tag{A.1}$$

Mass conservation

$$\frac{\partial j_\pm}{\partial x} = -\frac{\partial \delta c_\pm}{\partial t} = -i\omega \delta c_\pm \tag{A.2}$$

Poisson equation:

$$\Delta V_{ac} = \frac{\partial^2 V_{ac}}{\partial x^2} = -\frac{e(\delta c_+ - \delta c_-)}{\epsilon} \tag{A.3}$$

We define

$$\begin{aligned} \delta n = \delta c_+ + \delta c_- \qquad & \delta q = \delta c_+ - \delta c_- \\ \delta c_+ = \frac{1}{2}(\delta n + \delta q) \qquad & \delta c_- = \frac{1}{2}(\delta n - \delta q) \end{aligned} \tag{A.4}$$

We get

$$\begin{aligned} \frac{\partial (j_+ + j_-)}{\partial x} &= -i\omega\delta n = -D\frac{\partial^2 \delta n}{\partial x^2} \\ \frac{\partial (j_+ - j_-)}{\partial x} &= -i\omega\delta q = -D\frac{\partial^2 \delta q}{\partial x^2} + \frac{2e^2 c_o}{\epsilon kT}\delta q \end{aligned}$$

Taking the Debye length $l_D = \epsilon kT/2e^2c_o$ we get the set of equation

$$\frac{\partial^2 \delta n}{\partial x^2} = \lambda^2 \delta n \qquad \frac{\partial^2 \delta q}{\partial x^2} = \nu^2 \delta q$$

$$\lambda^2 = \frac{i\omega}{D} \qquad \nu^2 = \frac{i\omega}{D} + \frac{1}{l_D^2} = \frac{1}{l_D^2}(1 + i\tau) \quad \tau = \omega l_D^2/D \tag{A.5}$$

The solutions of these equations are

$$\delta n = A\mathrm{ch}\lambda x + B\mathrm{sh}\lambda x \qquad \delta q = C\mathrm{ch}\nu x + E\mathrm{sh}\nu x \tag{A.6}$$

From which we get the potential

$$\Delta V_{ac} = -\frac{e\delta q}{\epsilon} = -\frac{e}{\epsilon\nu^2}\Delta\delta q \qquad V_{ac} = -\frac{e}{\epsilon\nu^2}\delta q + Gx \tag{A.7}$$

Boundary conditions

The distance between the electrodes is L. At the Ag/AgCl electrodes, the K^+ ions do not interact:

$$j_+ = 0 \quad \text{at} \quad x = \pm L/2 \tag{A.8}$$

The Cl^- ions exchange freely with the $AgCl$ precipitate, so that their concentration at the electrodes is constant

$$\delta c_- = 0 \quad x = \pm L/2 \tag{A.9}$$

Using (A.6) and (A.9) we get

$$A\mathrm{ch}\lambda\frac{L}{2} + B\mathrm{sh}\lambda\frac{L}{2} - C\mathrm{ch}\nu\frac{L}{2} - E\mathrm{sh}\nu\frac{L}{2} = 0 \qquad A\mathrm{ch}\lambda\frac{L}{2} - B\mathrm{sh}\lambda\frac{L}{2} - C\mathrm{ch}\nu\frac{L}{2} + E\mathrm{sh}\nu\frac{L}{2} = 0$$

That is

$$A\mathrm{ch}\lambda\frac{L}{2} = C\mathrm{ch}\nu\frac{L}{2} \qquad B\mathrm{sh}\lambda\frac{L}{2} = E\mathrm{sh}\nu\frac{L}{2} \tag{A.10}$$

Using (A.1), (A.4) and (A.7)

$$2j_+ = -D\left(\frac{\partial\delta n}{\partial x} + \frac{\partial\delta q}{\partial x}\right) - \frac{2c_o eD}{kT}\left(-\frac{e}{\epsilon\nu^2}\frac{\partial\delta q}{\partial x} + G\right)$$

$$= -D\frac{\partial\delta n}{\partial x} - D\frac{\partial\delta q}{\partial x}\left(1 - \frac{1}{l_D^2\nu^2}\right) - \frac{GD\epsilon}{el_D^2}$$

$$2j_+ = -D\frac{\partial\delta n}{\partial x} - D\frac{\lambda^2}{\nu^2}\frac{\partial\delta q}{\partial x} - \frac{GD\epsilon}{el_D^2}$$

Using the boundary condition (A.8) and (A.6) we get

$$-\frac{G\epsilon}{el_D^2} = A\lambda\mathrm{sh}\lambda\frac{L}{2} + B\lambda\mathrm{ch}\lambda\frac{L}{2} + \frac{\lambda^2}{\nu^2}C\nu\mathrm{sh}\nu\frac{L}{2} + \frac{\lambda^2}{\nu^2}E\nu\mathrm{ch}\nu\frac{L}{2}$$

$$-\frac{G\epsilon}{el_D^2} = -A\lambda\mathrm{sh}\lambda\frac{L}{2} + B\lambda\mathrm{ch}\lambda\frac{L}{2} - \frac{\lambda^2}{\nu^2}C\nu\mathrm{sh}\nu\frac{L}{2} + \frac{\lambda^2}{\nu^2}E\nu\mathrm{ch}\nu\frac{L}{2}$$

that gives

$$-\frac{G\epsilon}{el_D^2} = B\lambda\mathrm{ch}\lambda\frac{L}{2} + \frac{\lambda^2}{\nu^2}E\nu\mathrm{ch}\nu\frac{L}{2}$$

$$0 = A\lambda \mathrm{sh}\lambda\frac{L}{2} + \frac{\lambda^2}{\nu^2}C\nu \mathrm{sh}\nu\frac{L}{2}$$

With (A.10) we get

$$A = C = 0 \qquad -\frac{G\epsilon}{el_D^2} = B\lambda \mathrm{ch}\lambda\frac{L}{2}\left(1 + \frac{\lambda \mathrm{th}\lambda L/2}{\nu \mathrm{th}\nu L/2}\right) = E\lambda \mathrm{ch}\nu\frac{L}{2}\left(\frac{\lambda}{\nu} + \frac{\mathrm{th}\nu L/2}{\mathrm{th}\lambda L/2}\right) \tag{A.11}$$

Electrical impedance

The current intensity is

$$I = e(j_+ - j_-) - i\omega\epsilon\frac{\partial V_{ac}}{\partial x} \tag{A.12}$$

From (A.1)

$$I = -eD\frac{\partial \delta q}{\partial x} - \frac{\partial V_{ac}}{\partial x}(\frac{2e^2 c_o D}{kT} + i\omega\epsilon) = -eD\frac{\partial \delta q}{\partial x} - \epsilon D\nu^2\frac{\partial V_{ac}}{\partial x}$$

With (A.7)

$$I = -GD\epsilon\nu^2 \tag{A.13}$$

The potential drop is

$$U = V_{ac}(-L/2) - V_{ac}(L/2) = -GL + \frac{e}{\epsilon\nu^2}(2E\mathrm{sh}\nu\frac{L}{2})$$

$$U = V_{ac}(-L/2) - V_{ac}(L/2) = -GL - \frac{2G}{l_D^2}\frac{\mathrm{th}\nu L/2\ \mathrm{th}\lambda L/2}{\lambda\nu(\lambda \mathrm{th}\lambda L/2 + \nu \mathrm{th}\nu L/2)} \tag{A.14}$$

The electrical impedance is

$$Z = \frac{U}{I} = \frac{L}{D\epsilon\nu^2} + 2Z_W \tag{A.15}$$

The first term is the bulk impedance, corresponding to the electrolyte conductivity

$$\gamma_{el} = \frac{1}{D\epsilon\nu^2} = \frac{l_D^2}{\epsilon(D + i\omega l_D^2)} \tag{A.16}$$

Note that this conductivity is complex.
The second term is the Warburg impedance

$$Z_W = \frac{\mathrm{th}\nu L/2\ \mathrm{th}\lambda L/2}{D\epsilon\lambda\nu^3 l_D^2(\lambda \mathrm{th}\lambda L/2 + \nu \mathrm{th}\nu L/2)} \tag{A.17}$$

Numerical estimates

For a concentration $c_o = 1mM$ the Debye length is $l_D \simeq 10$ nm. The diffusion coefficient of the K^+ and Cl^- ions is close and is about D=2.5 $10^{-9}\mathrm{m}^2 s^{-1}$. At a frequency of 100 kHz, the value of $\tau = \omega l_D^2/D$ is $\tau \simeq 0.025$. Therefore, in experimental conditions, we have largely $\tau \ll 1$.

A consequence is that $\nu^2 = 1/l_D^2(1+i\tau) \simeq 1/l_D^2 \gg |\lambda|^2$. We also have $\nu L/2 \gg 1$. Therefore the Warburg impedance reduces to

$$Z_W = \frac{\mathrm{th}\lambda L/2}{\gamma_{el}\lambda} = \frac{\mathrm{th}\lambda L/2}{\gamma_{el}(i\omega/D)^{1/2}} \tag{A.18}$$

which is called the finite Warburg impedance.

In the ac experiments (but may be not in the dc) we have also $\lambda L/2 \gg 1$ so that the Warburg impedance reduces to

$$Z_W = \frac{1}{\gamma_{el}(i\omega/D)^{1/2}} = \frac{kT}{e^2 2c_o(i\omega D)^{1/2}} = \frac{kT}{2e\mathcal{F}C_o(i\omega D)^{1/2}} \tag{A.19}$$

With C_o in [M/m^3] and $\mathcal{F}$ the Faraday constant.

The total impedance is

$$Z_R = \frac{L}{\gamma_e} + \sqrt{\frac{D}{2\gamma_e\omega}} \qquad Z_I = -\sqrt{\frac{D}{2\gamma_e\omega}}$$

Therefore, the Nyquist diagram is a straight line whose intercept with the x-axis gives the conductance of the cell, L/γ_e. This conductance should be compared to what is expected on the basis of the distance between the electrodes.

The outcome of this analysis, is that in dc experiments performed on the Nafion membrane, the "cell" resistance is dominated by the Warburg resistance, due to the diffusion layers of the K^+ ions which are not absorbed by the Ag/AgCl electrodes.

Appendix B

Reciprocal theorem

Here is considered electro-diffusio-osmotic transport in linear regime associated to slight deviation from an equilibrium situation. In the following, all mentioned force fields correspond to deviation from fields at equilibrium while concentrations fields are those observed at equilibrium. All fluxes are zero at equilibrium. The local force balance in absence of inertia writes :

$$-\boldsymbol{\nabla}.\boldsymbol{\sigma} - \rho_e \boldsymbol{\nabla} V = 0$$

where ρ_e is the electrical charge density, V the local electrical potential and $\boldsymbol{\sigma}$ the hydrodynamic stress tensor written with the sign convention from Bird *et al.*[106] assuming in absence of volume change:

$$\boldsymbol{\sigma} = p\boldsymbol{I} - \eta(\boldsymbol{\nabla}^t \boldsymbol{v} + \boldsymbol{\nabla}\boldsymbol{v}) = p\boldsymbol{I} - \eta\boldsymbol{\mathcal{E}}$$

The absence of volume change, the velocity fields is divergence free:

$$\boldsymbol{\nabla}.\boldsymbol{v} = 0$$

We focus on steady-state dilute situations where the concentration fields c_i are governed by time independent conservation equations that leads to their fluxes j_i in absence of chemical reaction:

$$\boldsymbol{j}_i = c_i \boldsymbol{v} - m_i c_i \boldsymbol{\nabla}\mu_i = c_i \boldsymbol{v} + \boldsymbol{\varphi}_i$$

where m_i is the mobility of the solute, $\boldsymbol{\varphi}_i = -m_i c_i \boldsymbol{\nabla}\mu_i$ is the diffusion contribution and $c_i\boldsymbol{v}$ the convective contribution to the total flux $\boldsymbol{j}_i$, that is also divergence free due to mass conservation in absence of chemical reaction:

$$\boldsymbol{\nabla}.\boldsymbol{j}_i = 0$$

The reciprocity rely on the equality between the cross-product of fields and fluxes related to two independent forcing in linear regime. The following demonstration is inspired from the work of Brunet *et al.* [14]. The reciprocity of electro-diffusio-osmotic flows is demonstrated starting from an expression inspired from the entropy

production. For a given forcing the entropy production can be expressed locally as the sum of the viscous dissipation and the diffusional transport of electrochemical species. The viscous dissipation is proportional to the dot product of the strain tensor by itself while the diffusional dissipation is equal to the sum on solute species of the product of the chemical potential gradient by the diffusional flux of chemical that is proportional to the dot product of the chemical gradient by itself. Considering two independent forcings, it is possible to express a crossed dissipated power based on the sum of the dot product of the first strain by the second strain and the dot product of the first chemical potential gradient by the second chemical potential gradient. By definition of this crossed dissipated power, its value is preserved by inversion of the two forcings. From this starting point, will be expressed the divergence of the osmo-mechanical and electrochemical supplied power. The successive transformations required to reach this result are based on the above mentioned properties of fields and fluxes and emphasized with different colors:

$$
\begin{aligned}
&\frac{1}{2}\eta\boldsymbol{\mathcal{E}}^{(1)} : \boldsymbol{\mathcal{E}}^{(2)} + \sum m_i c_i \boldsymbol{\nabla}\mu_i^{(1)}.\boldsymbol{\nabla}\mu_i^{(2)} \\
&= -\boldsymbol{\nabla}.\left(\boldsymbol{\sigma}^{(1)}.\boldsymbol{v}^{(2)}\right) + \left(\boldsymbol{\nabla}.\boldsymbol{\sigma}^{(1)}\right).\boldsymbol{v}^{(2)} - \sum \boldsymbol{\nabla}\mu_i^{(1)}.\left(\boldsymbol{\varphi}_i^{(2)} + c_i\boldsymbol{v}^{(2)}\right) + \sum \left(q_i\boldsymbol{\nabla}V^{(1)} + \boldsymbol{\nabla}\mu_{ic}^{(1)}\right).c_i\boldsymbol{v}^{(2)} \\
&= -\boldsymbol{\nabla}.\left(\left(\boldsymbol{\sigma}^{(1)} - \pi\boldsymbol{I}\right).\boldsymbol{v}^{(2)}\right) + \cancel{\left(\boldsymbol{\nabla}.\boldsymbol{\sigma}^{(1)}\right).\boldsymbol{v}^{(2)}} + \cancel{\sum q_i c_i \boldsymbol{\nabla}V^{(1)}\boldsymbol{v}^{(2)}} - \sum \boldsymbol{\nabla}\mu_i^{(1)}.\boldsymbol{j}_i^{(2)} \\
&= -\boldsymbol{\nabla}.\left(\left(\boldsymbol{\sigma}^{(1)} - \pi\boldsymbol{I}\right).\boldsymbol{v}^{(2)}\right) - \sum \boldsymbol{\nabla}\mu_i^{(1)}.\boldsymbol{j}_i^{(2)}
\end{aligned}
$$

The two final terms are symmetrical in the exchange between superscripts 1 and 2. In this demonstration appears the osmotic pressure π whose gradient can be related to the gradient in chemical potential:

$$\boldsymbol{\nabla}\pi = k_B T \sum \boldsymbol{\nabla}c_i = \sum c_i \boldsymbol{\nabla}\mu_i$$

In the framework of electro-diffusio-osmotic transport within nanopores, it is of interest to obtain global relations based on integration on a pore volume. Moreover, within a long nanopore of constant radius, all the fluxes are directed only along the pore axis if its wall is assumed as non permeable. As a result, the component of the electrochemical potential gradient perpendicular to the pore axis is zero $\partial\mu_i/\partial r = 0$: this means that every electrochemical potential is uniform within a section of the pore. Moreover the sum of the concentrations by derivative of the chemical potential with respect to the pore radius is also zero as a result:

$$\rho_e \frac{\partial V}{\partial r} = -k_B T \sum c_i \frac{\partial c_i}{c_i \partial r} = -k_B T \sum \frac{\partial c_i}{\partial r} = -\frac{\partial \pi}{\partial r}$$

where π is the osmotic pressure. Replacing the electrostic force by its expression according to π in the radial component of the momentum balance leads:

$$-\frac{\partial p}{\partial r} + \frac{\partial \pi}{\partial r} = 0$$

this means that the difference $\Pi = p - \pi$ is constant in a section of a pore. The integration on the pore volume is expressed, using the Green-Ostrogradski therorem, as a surface integral. In absence of slip at the wall:

$$\begin{aligned} &- \iiint \boldsymbol{\nabla}.\left(\left(\boldsymbol{\sigma}^{(1)} - \pi \boldsymbol{I}\right).\boldsymbol{v}^{(2)}\right) - \sum \boldsymbol{\nabla}\mu_i^{(1)}.\boldsymbol{j}_i^{(2)} \\ &= \left(\Pi_1 - \Pi_2\right)^{(1)} q_v^{(2)} + \sum \left(\mu_{i1} - \mu_{i2}\right) J_{i^{(2)}} \end{aligned}$$

with q_v the flow rate and J_i the total flux solutes through the nanopore. If concentrations are uniform in the entrance and exit sections the last relation can also be divided into electrical an chemical contributions :

$$\begin{aligned} &\left(\Pi_1 - \Pi_2\right)^{(1)} q_v^{(2)} + \sum \left(\mu_{i1} - \mu_{i2}\right) J_i^{(2)} \\ &= \left(\Pi_1 - \Pi_2\right)^{(1)} q_v^{(2)} + \left(V_1 - V_2\right) I^{(2)} + \left(\mu_{c1} - \mu_{c2}\right) J_s^{(2)} \end{aligned}$$

with I the electrical current and J_s the total flux of solutes assumed at the same concentration at the entrance and exit of the nanopore. This final relation is symmetrical in the exchange between superscripts 1 and 2 that proves that the Onsager matrix expressing the linear dependence of fluxes from force fields is symmetrical.

Appendix C

Full schematic of picoflow cell and set-up

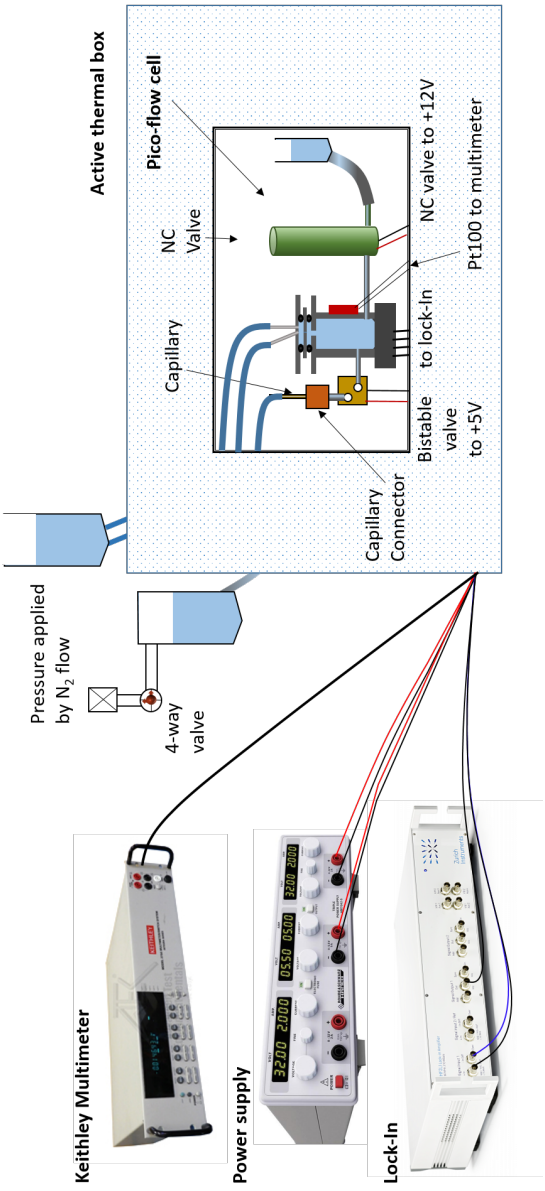

Figure C.1: A full schematic of pico-flow cell and setup. The cell is placed within the thermally regulated box. All the fluidic and electrical connections are passing across the box and are controlled remotely.

Bibliography

[1] Harvey Lodish and S Lawrence Zipursky. Molecular cell biology. *Biochemistry and Molecular Biology Education*, 29:126–133, 2001.

[2] Haixin Sui, Bong-Gyoon Han, John K Lee, Peter Walian, and Bing K Jap. Structural basis of water-specific transport through the aqp1 water channel. *Nature*, 414(6866):872–878, 2001.

[3] R S Norman. Water salination: a source of energy. *Science (New York, N.Y.)*, 186(4161):350–2, October 1974.

[4] S Loeb and R S Norman. Osmotic power plants. *Science (New York, N.Y.)*, 189(4203):654–5, August 1975.

[5] J N Weinstein and F B Leitz. Electric power from differences in salinity: the dialytic battery. *Science (New York, N.Y.)*, 191(4227):557–9, February 1976.

[6] Thor Thorsen and Torleif Holt. The potential for power production from salinity gradients by pressure retarded osmosis. *Journal of Membrane Science*, 335(1–2):103 – 110, 2009.

[7] Andrea Achilli, Tzahi Y. Cath, and Amy E. Childress. Power generation with pressure retarded osmosis: An experimental and theoretical investigation. *Journal of Membrane Science*, 343(1–2):42 – 52, 2009.

[8] David A. Vermaas, Enver Guler, Michel Saakes, and Kitty Nijmeijer. Theoretical power density from salinity gradients using reverse electrodialysis. *Energy Procedia*, 20:170 – 184, 2012.

[9] Jan W. Post, Hubertus V. M. Hamelers, and Cees J. N. Buisman. Energy recovery from controlled mixing salt and fresh water with a reverse electrodialysis system. *Environmental Science & Technology*, 42(15):5785–5790, 2008. PMID: 18754509.

[10] Piotr Długołęcki, Antoine Gambier, Kitty Nijmeijer, and Matthias Wessling. Practical potential of reverse electrodialysis as process for sustainable energy generation. *Environmental Science & Technology*, 43(17):6888–6894, 2009. PMID: 19764265.

[11] Reto Schoch, Jongyoon Han, and Philippe Renaud. Transport phenomena in nanofluidics. *Reviews of Modern Physics*, 80(3):839–883, July 2008.

[12] Frank H. J. van der Heyden, Douwe Jan Bonthuis, Derek Stein, Christine Meyer, and Cees Dekker. Electrokinetic energy conversion efficiency in nanofluidic channels. *Nano Letters*, 6(10):2232–2237, 2006. PMID: 17034089.

[13] Alessandro Siria, Philippe Poncharal, Anne-laure Biance, Rémy Fulcrand, Xavier Blase, Stephen Purcell, and Lydéric Bocquet. Giant osmotic energy conversionmeasured in a single transmembrane boron nitride nanotube. *Nature*, 494:455–458, 2013.

[14] Edouard Brunet and Armand Ajdari. Generalized Onsager relations for electrokinetic effects in anisotropic and heterogeneous geometries. *Physical Review E*, 69(1):016306, January 2004.

[15] Dong-kwon Kim Chuanhua Duan and Yu-feng Chen Arun Majumdar. Power generation from concentration gradient by reverse electrodialysis in ion-selective nanochannels. pages 1215–1224, 2010.

[16] Haixia Zhang Wengang Wu Wei Ouyang, Wei Wang and Zhihong Li. Nanofluidic crystal: a facile, high-efficiency and high-power-density scaling up scheme for energy harvesting based on nanofluidic reverse electrodialysis. *Nanotechnology*, 24(345401), 2013.

[17] Piotr Dlugolecki, Kitty Nymeijer, Sybrand Metz, and Matthias Wessling. Current status of ion exchange membranes for power generation from salinity gradients. *Journal of Membrane Science*, 319(1–2):214 – 222, 2008.

[18] M. Saakesa S.J. Metz G.J. Harmsen J. Veermana, R.M. de Jongb. Reverse electrodialysis: Comparison of six commercial membrane pairs on the thermodynamic efficiency and power density. *Journal of Membrane Science*, 343:7–15, 2009.

[19] Bruce E Logan and Mena Elimelech. Membrane-based processes for sustainable power generation using water. *Nature*, 488(7411):313–9, August 2012.

[20] Rohit Karnik, Chuanhua Duan, Kenneth Castelino, Hirofumi Daiguji, and Arun Majumdar. Rectification of ionic current in a nanofluidic diode. *Nano letters*, 7(3):547–551, 2007.

[21] Chang Wei, Allen J Bard, and Stephen W Feldberg. Current rectification at quartz nanopipet electrodes. *Analytical Chemistry*, 69(22):4627–4633, 1997.

[22] Z Siwy, Y Gu, HA Spohr, D Baur, A Wolf-Reber, R Spohr, P Apel, and YE Korchev. Rectification and voltage gating of ion currents in a nanofabricated pore. *EPL (Europhysics Letters)*, 60(3):349, 2002.

[23] Wei Guo, Ye Tian, and Lei Jiang. Asymmetric Ion Transport through Ion-Channel-Mimic Solid-State Nanopores. *Acc Chem Res.*, 46(12):2834–46, 2013.

[24] Zuzanna S Siwy. Ion-current rectification in nanopores and nanotubes with broken symmetry. *Advanced Functional Materials*, 16(6):735–746, 2006.

[25] Nadanai Laohakunakorn and Ulrich F Keyser. Electroosmotic flow rectification in conical nanopores. *Nanotechnology*, 26(27):275202, 2015.

[26] Clara B. Picallo, Simon Gravelle, Laurent Joly, Elisabeth Charlaix, and Lydéric Bocquet. Nanofluidic osmotic diodes: Theory and molecular dynamics simulations. *Phys. Rev. Lett.*, 111:244501, Dec 2013.

[27] Jacob N. Israelachvili. *Intermolecular and surface forces 2nd edn.* Academic, New York, 1991, 1991.

[28] Robert J Hunter. *Foundations of colloid science.* Oxford University Press, 2001.

[29] DC Prieve, JL Anderson, JP Ebel, and ME Lowell. Motion of a particle generated by chemical gradients. part 2. electrolytes. *Journal of Fluid Mechanics*, 148:247–269, 1984.

[30] J. C. Fair and J. F. Osterle. Reverse electrodialysis in charged capillary membranes. *The Journal of Chemical Physics*, 54(8):3307, 1971.

[31] R J Gross and J F Osterle. Membrane Transport Characteristics of Ultrafine Capillaries. *The journal of Chemical Physics*, 49:228–234, 1968.

[32] Wei Ouyang, Wei Wang, Haixia Zhang, Wengang Wu, and Zhihong Li. Nanofluidic crystal : a facile , scaling up scheme for energy harvesting based on nanofluidic reverse electrodialysis. 24, 2013.

[33] Zuzanna Siwy and Andrzej Fuliński. A nanodevice for rectification and pumping ions. *American Journal of Physics*, 72(5):567–574, 2004.

[34] Frederick George Donnan. Theory of membrane equilibria and membrane potentials in the presence of non-dialysing electrolytes. a contribution to physical-chemical physiology. *Journal of Membrane Science*, 100(1):45–55, 1995.

[35] Pu Jin, Hitomi Mukaibo, Lloyd P. Home, Gregory W. Bishop, and Charles R. Martin. Electroosmotic flow rectification in pyramidal-pore mica membranes. *J. Am. Chem. Soc.*, 132(7):2118–2119, 2010.

[36] Hubert H. Girault. *ANALYTICAL AND PHYSICAL ELECTROCHEMISTRY.* EPFL Press, first edit edition, 2004.

[37] Jacopo Catalano Anders Bentien Bjørn Sjøgren Kilsgaard, Sofie Haldrup. High figure of merit for electrokinetic energy conversion in nafion membranes. *Journal of Power Sources*, 247(016306):235–242, 2014.

[38] A. Sharifi-Viand, M.G. Mahjani, and M. Jafarian. Investigation of anomalous diffusion and multifractal dimensions in polypyrrole film. *Journal of Electroanalytical Chemistry*, 671:51 – 57, 2012.

[39] Carla Heitner-Wirguin. Recent advances in perfluorinated ionomer membranes: structure, properties and applications. *Journal of Membrane Science*, 120(1):1 – 33, 1996.

[40] Anne-Claire Dupuis. Proton exchange membranes for fuel cells operated at medium temperatures: Materials and experimental techniques. *Progress in Materials Science*, 56(3):289 – 327, 2011.

[41] Kenneth A. Mauritz and Robert B. Moore. State of understanding of nafion. *Chemical Reviews*, 104(10):4535–4586, 2004. PMID: 15669162.

[42] T. D. Gierke, G. E. Munn, and F. C. Wilson. The morphology in nafion perfluorinated membrane products, as determined by wide- and small-angle x-ray studies. *Journal of Polymer Science: Polymer Physics Edition*, 19(11):1687–1704, 1981.

[43] William Y. Hsu and Timothy D. Gierke. Ion transport and clustering in nafion perfluorinated membranes. *Journal of Membrane Science*, 13(3):307 – 326, 1983.

[44] G. Gebel. Structural evolution of water swollen perfluorosulfonated ionomers from dry membrane to solution. *Polymer*, 41(15):5829 – 5838, 2000.

[45] Anne-Laure Rollet, Olivier Diat, and Gérard Gebel. A new insight into nafion structure. *The Journal of Physical Chemistry B*, 106(12):3033–3036, 2002.

[46] Klaus Schmidt-Rohr and Qiang Chen. Parallel cylindrical water nanochannels in Nafion fuel-cell membranes. *Nature materials*, 7(345401):75–83, 2007.

[47] S. Slade, S.A. Campbell, T.R. Ralph, and F.C Walsh. Ionic conductivity of an extruded nafion 1100 ew series of membranes. December 2002.

[48] M. Plazanet, P. Bartolini, R. Torre, C. Petrillo, and F. Sacchetti. Structure and acoustic properties of hydrated nafion membranes. *The Journal of Physical Chemistry B*, 113(30):10121–10127, 2009. PMID: 19719280.

[49] David R. Lide. *Handbook of Chemistry and Physics, 85th Edition*. CRC Press, 2004.

[50] A Marques, M.I.A. Ferra, and M.H. Bandeira. No Title. *Portugaliae Electrochimica Acta*, 24:295–303, 2006.

[51] Paul B Hostetler, Alfred H Truesde, and C.L. Christ. Activity Coefficients of Aqueous Potassium Chloride Measured with a Potassium-Sensitive Glass Electrode. *Science*, 155(3769):1537–1539, 1967.

[52] M.A. Izquierdo-Gil, V.M. Barragán, J.P.G. Villaluenga, and M.P. Godino. Water uptake and salt transport through nafion cation-exchange membranes with different thicknesses. *Chemical Engineering Science*, 72:1 – 9, 2012.

[53] Lyderic Bocquet and Elisabeth Charlaix. Nanofluidics, from bulk to interfaces. *Chem. Soc. Rev.*, 39:1073–1095, 2010.

[54] David A. Vermaas, Michel Saakes, and Kitty Nijmeijer. Doubled power density from salinity gradients at reduced intermembrane distance. *Environmental Science & Technology*, 45(16):7089–7095, 2011. PMID: 21736348.

[55] Dimitar M Vlassarev and Jene A Golovchenko. Trapping dna near a solid-state nanopore. *Biophysical journal*, 103(2):352–356, 2012.

[56] Frank HJ van der Heyden, Douwe Jan Bonthuis, Derek Stein, Christine Meyer, and Cees Dekker. Power generation by pressure-driven transport of ions in nanofluidic channels. *Nano letters*, 7(4):1022–1025, 2007.

[57] Byron D Gates, Qiaobing Xu, J Christopher Love, Daniel B Wolfe, and George M Whitesides. Unconventional nanofabrication. *Annu. Rev. Mater. Res.*, 34:339–372, 2004.

[58] D. Mijatovic, J. C. T. Eijkel, and A. van den Berg. Technologies for nanofluidic systems: top-down vs. bottom-up-a review. *Lab Chip*, 5:492–500, 2005.

[59] AJ Storm, JH Chen, XS Ling, HW Zandbergen, and C Dekker. Fabrication of solid-state nanopores with single-nanometre precision. *Nature materials*, 2(8):537–540, 2003.

[60] CT Jan, R Niels, Albertávan den Berg, et al. 1-d nanochannels fabricated in polyimide. *Lab on a Chip*, 4(3):161–163, 2004.

[61] NR Tas, JW Berenschot, P Mela, HV Jansen, M Elwenspoek, and A Van den Berg. 2d-confined nanochannels fabricated by conventional micromachining. *Nano Letters*, 2(9):1031–1032, 2002.

[62] A. Heuberger H. Seidel, L. Csepregi and H. Baumgärtel. Anisotropic etching of crystalline silicon in alkaline solutions i. orientation dependence and behavior of passivation layers. *J. Electrochem. Soc.*, 137(11):3612–3626, 1990.

[63] M. J. Madou. *Fundamentals of Microfabrication: The Science of Miniaturization*. 2nd ed.: Crc press edition, 2002.

[64] B. E. E. Kastenmeier, P. J. Matsuo, J. J. Beulens, and G. S. Oehrlein. Chemical dry etching of silicon nitride and silicon dioxide using $CF_4/O_2/N_2$ gas mixtures. *Journal of Vacuum Science Technology*, 14:2802–2813, September 1996.

[65] Michael Quirk and Julian Serda. Semiconductor manufacturing technology, 2001.

[66] W.M. Zhang, J. Li, L.X. Cao, Y.G. Wang, W. Guo, K.X. Liu, and J.M. Xue. Fabrication of nanoporous silicon dioxide/silicon nitride membranes using etched ion track technique. *Nuclear Instruments and Methods in Physics Research Section B: Beam Interactions with Materials and Atoms*, 266(12–13):3166 – 3169, 2008.

[67] M. J. de Boer, R. W. Tjerkstra, J. W. Berenschot, H. V. Jansen, G. J. Burger, J. G. E. Gardeniers, M. Elwenspoek, and A. van den Berg. Micromachining of buried micro channels in silicon. *Journal of Microelectromechanical Systems*, 9(1):94–103, March 2000.

[68] Maki Suemitsu, Tetsuya Kaneko, and Nobuo Miyamoto. Low Temperature Silicon Surface Cleaning by HF Etching / Ultraviolet Ozone Cleaning (HF / UVOC) Method (I) – Optimization of the HF Treatment –. *Japanese Journal of applied physics*, 28:2421–2424, 1989.

[69] Kenneth E Bean et al. Anisotropic etching of silicon. *IEEE Transactions on Electron Devices*, 25(10):1185–1193, 1978.

[70] Osamu Tabata, Ryoup Asahl, Hirofumf Funabashi, Keuchi Shimaoka, and Susumu Sugfyama. Anisotropic etching of silicon in TMAH solutions *. 34(111):51–57, 1992.

[71] K Biswas and S Kal. Etch characteristics of KOH , TMAH and dual doped TMAH for bulk micromachining of silicon. 37:519–525, 2006.

[72] K Schomburg, W. *Introduction to Microsystem Design*. Rwtheditio edition.

[73] Léo Garcia. *Étude rhéologique des électrolytes confinés en Appareil à Forces de Surfaces dynamique*. PhD thesis, Université Grenoble Alpes, 2016.

[74] ROBERT J. HUNTER, editor. {*COLLOID*} {*SCIENCE*}. Academic Press, 1981.

[75] Juan Liu, Maksim Kvetny, Jingyu Feng, Dengchao Wang, Baohua Wu, Warren Brown, and Gangli Wang. Surface charge density determination of single

conical nanopores based on normalized ion current rectification. *Langmuir*, 28(2):1588–1595, 2012. PMID: 22182684.

[76] Wen-Jie Lan, Martin A. Edwards, Long Luo, Rukshan T. Perera, Xiaojian Wu, Charles R. Martin, and Henry S. White. Voltage-rectified current and fluid flow in conical nanopores. *Accounts of Chemical Research*, 49(11):2605–2613, 2016. PMID: 27689816.

[77] Daniel G Haywood, Anumita Saha-shah, Lane A Baker, and Stephen C Jacobson. Fundamental Studies of Nano fl uidics: Nanopores, Nanochannels, and Nanopipets. *American Chemical Society*, 87:172–187, 2014.

[78] Zhanhua Silber-Li. *Picoliter Flow Calibration*, pages 1650–1653. Springer US, Boston, MA, 2008.

[79] K. V. Sharp and R. J. Adrian. Transition from laminar to turbulent flow in liquid filled microtubes. *Experiments in Fluids*, 36(5):741–747, 2004.

[80] Hai-hang Cui and Shan-nong Zhu. Flow characteristics of liquids in microtubes driven by a high pressure. *Physics of Fluids*, 16, 2004.

[81] Xiaohua Huang, Manuel J Gordon, and Richard N Zare. Current-Monitoring Method for Measuring the Electroosmotic Flow Rate in Capillary Zone Electrophoresis. *American Chemical Society*, 60(8):1837–1838, 1988.

[82] Alice Sze, David Erickson, Liqing Ren, and Dongqing Li. Zeta-potential measurement using the smoluchowski equation and the slope of the current–time relationship in electroosmotic flow. *Journal of Colloid and Interface Science*, 261(2):402 – 410, 2003.

[83] Alessandro Siria, Anne-laure Biance, Christophe Ybert, and Lydéric Bocquet. A flux monitoring method for easy and accurate flow rate measurement in pressure-driven flows. *Lab on a Chip*, pages 872–875.

[84] Ellis Meng, Sascha Gassmann, and Yu-Chong Tai. *A Mems Body Fluid Flow Sensor*, pages 167–168. Springer Netherlands, Dordrecht, 2001.

[85] Herbert Ernst, Artur Jachimowicz, and Gerald A. Urban. High resolution flow characterization in bio-mems. *Sensors and Actuators A: Physical*, 100(1):54 – 62, 2002.

[86] Kari T. Hjelt, Richard van den Doel, Wijnand Lubking, and Michiel J. Vellekoop. High-resolution liquid volume detection in sub-nanoliter reactors. *Sensors and Actuators A: Physical*, 83(1–3):61 – 66, 2000.

[87] John Collins and Abraham P. Lee. Microfluidic flow transducer based on the measurement of electrical admittance. *Lab Chip*, 4:7–10, 2004.

[88] Jian Wu and Jing Ye. Micro flow sensor based on two closely spaced amperometric sensors. *Lab Chip*, 5:1344–1347, 2005.

[89] Klaus Mathwig, Dileep Mampallil, Shuo Kang, and Serge G. Lemay. Electrical cross-correlation spectroscopy: Measuring picoliter-per-minute flows in nanochannels. *Phys. Rev. Lett.*, 109:118302, Sep 2012.

[90] David Sinton, Carlos Escobedo-canseco, Liqing Ren, and Dongqing Li. Direct and Indirect Electroosmotic Flow Velocity Measurements in Microchannels. *Journal of colloid and interface science*, 254:184–189, 2002.

[91] Zeyad A. Almutairi, Tomasz Glawdel, Carolyn L. Ren, and David A. Johnson. A y-channel design for improving zeta potential and surface conductivity measurements using the current monitoring method. *Microfluidics and Nanofluidics*, 6(2):241–251, 2009.

[92] Eleonora Secchi, Sophie Marbach, Antoine Nigués, Derek Stein, Alessandro Siria, and Lydéric Bocquet. Letter. *Nature*, 537(7619):210–213, 2016.

[93] Nadanai Laohakunakorn, Benjamin Gollnick, Fernando Moreno-Herrero, Dirk G. A. L. Aarts, Roel P. A. Dullens, Sandip Ghosal, and Ulrich F. Keyser. A landau–squire nanojet. *Nano Letters*, 13(11):5141–5146, 2013. PMID: 24124664.

[94] L.D. Landau and E.M. Lifshitz. *Fluid Mechanics, Course of Theoretical Physics Volume 6*. 2nd ed.; elsevier edition, 1987.

[95] L.D. Landau. *Dokl. Akad. Nauk SSSR*, 43:286–288, 1944.

[96] H.B. Squire. *Quart. J. Mech. Appl. Math.*, 4:321–329, 1951.

[97] C. Lee, C. Cottin-Bizonne, A.-L. Biance, P. Joseph, L. Bocquet, and C. Ybert. Osmotic flow through fully permeable nanochannels. *Phys. Rev. Lett.*, 112:244501, Jun 2014.

[98] K. Zsdánszky. Precise measurement of small currents. *Nuclear Instruments and Methods*, 112(1):299 – 303, 1973.

[99] Mosaddequr Rahman and Sazzadur Chowdhury. A New Deflection Shape Function for Square Membrane CMUT Design. pages 2019–2022, 2010.

[100] G Mensitieri, A Apicella, J M Kenny, and L Nicolais. Water Sorption Kinetics in Poly (aryl Ether Ether Ketone). *Journal of Applied PolymerScience*, 37:381–392, 1989.

[101] M Keyhani, F A Kulacki, and R N Christensen. Free Convection in a Vertical Annulus With Constant Heat Flux on the Inner Wall. *J. Heat Transfer*, 105(3):454–459, 1983.

[102] H. R. Nagendra, M. A. Tirunarayanan, and A. Ramachandran. Free convection heat transfer in vertical annuli. *Chem. Eng.*, 25:605–610, 1970.

[103] Robert H. Doremus. *Glass Science*. 2nd ed. (wiley, new york) edition, 1994.

[104] F. Devreux, Ph. Barboux, M. Filoche, and B. Sapoval. A simplified model for glass dissolution in water. *Journal of Materials Science*, 36(6):1331–1341, 2001.

[105] Zeev Dagan, Sheldon Weinbaum, and Robert Pfeffer. An infinite-series solution for the creeping motion through an orifice of finite length. *J. Fluid Mech.*, 115:505–523, 1982.

[106] R. Byron Bird, Warren E. Stewart, and Edwin N. Lightfoot. *Transport Phenomena*. John Wiley and Sons, 2002.